How diagenetic rock composition and mineralogical changes associated with water injection affect geomechanics and fluid behaviour in chalk i.e. producibility (IOR)

by

Tine Vigdel Bredal

Thesis submitted in fulfilment of
the requirements for the degree of
PHILOSOPHIAE DOCTOR
(PhD)

University
of Stavanger

Teknisk naturvitenskapelig fakultet
Institutt for energiressurser
2024

Acknowledgements

Summary

Geo-mechanical responses associated with seawater injection for improved oil recovery (IOR) processes have been thoroughly investigated during the last few decades. It has been suggested that the presence of non-carbonate minerals will impact brine-rock interaction processes as water weakening chalk. Moreover, mineralogical processes and geo-mechanical responses associated with seawater injection into fractured chalk and how these processes impact aperture modification and fluid flow have not previously been completely understood. The main objectives of the thesis are to characterize impurities in chalk, which always exist to some extent (quartz, dolomite, pyrite, etc.), and to map brine-rock interaction processes that may be linked with impurities. The second objective is focused on how artificially fractured chalk alters properties during brine injection, in terms of water weakening and mineralogical alteration processes. To reach these objectives, a wide range of methods has been used. A toolbox was developed for providing a guide for selecting an adequate collection of methods for characterization of chalk (**Paper I**).

The newly developed Helium Ion Microscopy combined with Secondary Ion Mass Spectrometry (HIM-SIMS) was used due to the exceptionally high resolution for imaging and chemical identification in-situ. This was the first time that HIM-SIMS was used for IOR research on chalk (**Paper II**). The HIM-SIMS showed that it is possible to discriminate non-carbonate minerals from the calcite surface of micron-sized fossils. Calculations of surface mineral distribution in a synthetic seawater (SSW) flooded outcrop sample, indicated that the clay covered 6.3 % in addition to 39.8 % mixed compound of clay and calcite. On the other hand, the bulk geochemistry showed only a concentration of 5 weight % (Wt.%) non-carbonates (**Paper III**).

Pure dolomite and pure manufactured calcite powder, in addition to three mixes of the two minerals with different ratios were manually compressed to regular cores. Laboratory experiments were performed on these samples using triaxial cells which can mimic reservoir conditions such as temperature and stress while flooding samples with different brines (**Paper IV**). Flooding powdered samples in mixed ratios of dolomite and pure manufactured calcite showed complex chemical processes, with precipitation of new minerals that were not identified when flooding dolomite and manufactured calcite separately. Precipitation of new minerals was dependent on the composition of the injected brine and the ratio of dolomite versus manufactured calcite. These complex chemical processes were for some samples associated with higher total axial strain than observed for the two minerals flooded separately. The total axial strain was dependent also on the porosity and mineral composition present in the sample. A sample with a realistic composition representing the chalk from the Ekofisk oil field on the Norwegian Continental Shelf (NCS) with 5 Wt.% dolomite injected with SSW, showed dissolution of calcite and precipitation of abundant aragonite crystals with sizes ranging up to 20 μm. On the other hand, pure manufactured calcite and dolomite powder showed no significant chemical alteration when SSW was injected in these samples separately. Despite significant dissolution of calcite and precipitation of aragonite in the mixed compound (5 Wt.% dolomite), the precipitation of aragonite did not impact the rate of compaction in the powder samples.

Five Upper Cretaceous outcrop chalk samples from the Obourg quarry, St. Vaast Formation (OBSV), had been flooded in a previous study under comparable conditions as used for the powder experiments. Three of these samples had an artificial fracture of 2.25 (± 0.05) mm that was drilled before the flooding. Here, characterization of mineralogy, chemical, and textural properties on flooded and unflooded samples facilitated interpretation of changes that took place during the flooding experiments. Altered properties as aperture modification were further

associated with the composition of the injected brine, present mineralogy, and geo-mechanical response during flooding (**Paper V**). Three artificially fractured Upper Cretaceous chalk samples showed lower mechanical resilience than unfractured samples flooded with inert brine in the creep phase (above yield stress). During hydrostatic loading there was no significant difference in strength. The water weakening effect was identified after the brine composition changed to reactive brines such as SSW and magnesium chloride. The artificially fractured samples showed a delayed and less significant water weakening effect than observed for unfractured chalk samples for a test duration of two months. This was associated with brine dominantly flowing through the fracture, thus delaying chemical interactions further away from the fracture. An extrapolation of the creep indicated that fractured samples may experience a higher compaction over a prolonged period of 200 days. All apertures were reduced during the flooding experiment. This was dominantly associated with the total axial strain. Matrix (core material) had been forced into void spaces. Precipitation reduced the aperture additionally. The aperture reduction was controlled by the mineralogy present in the matrix as well as the injected brine composition (**Papers V**, **VI**).

The laboratory experiments demonstrated how complex the mineralogical system of chalk can be, by just adding one single mineral such as dolomite to pure calcite. This highlights the necessity to detect and characterize impurities in chalk, even at very low concentrations. The HIM-SIMS results indicated that impurities can be distributed over a significantly larger area than anticipated based on bulk geochemistry. A systematic approach to characterizing impurities in reservoir samples can provide more accurate models for wettability properties, fluid flow and oil recovery. This may improve precision in modelling fluid transportation in the reservoir, as well as a better understanding of rock-fluid interactions with an improved understanding of aperture modification and compaction. Details within this study (Figure 1) also

demonstrate that mineralogical composition and microscopic analyses are paramount to develop IOR applications.

Artificial fractures in chalk

Topic: IOR experiments with fluid injection in fractured carbonate rocks.

Objective: Observe and interpret the geo-mechanical response, mineralogical alteration or precipitation in the open fracture and fracture geometry

Impact: Improved understanding of fracture evolution in chalk, subscience and fluid flow.

Processes in pure mineralogical systems using powder

Topic: IOR experiments using simplified mineralogical systems using pure calcite and dolomite and three mixes.

Objective: Observation and interpretation of mineral dissolution and precipitation associated with brine injected.

Impact: Deciphering processes in pure systems is essential when dealing with more complex systems (clay minerals).

Paper V
Paper VI

Paper IV

Methodologies and Toolbox

Chalk characterization is based on traditional and advanced applications. It needs to be carefully evaluated which method combination rewards the best possible data set for the reserach objective. Imaging and chemical or crystallographic identification on micron and/or nano-scale is often needed and here evaluated.

Paper I
Paper II
Paper III
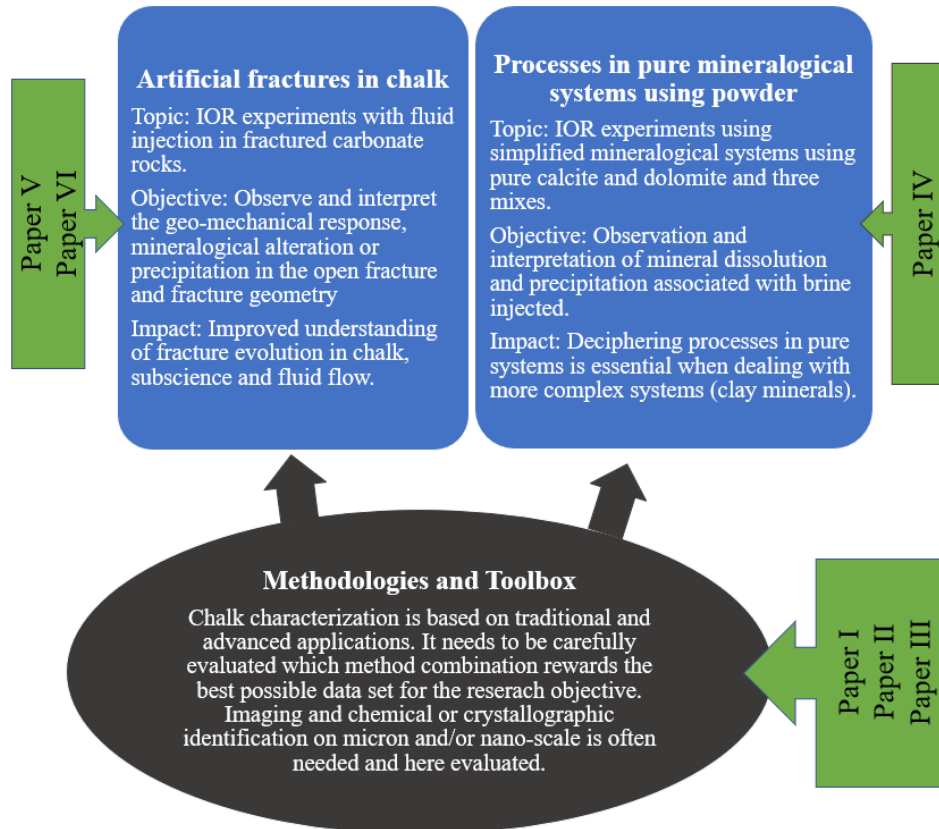
Figure 1) Overview of different sub-projects within this study and how they are linked to each other.

List of publications

Paper I:

Zimmermann, U., Minde, M. W., Madland, M. V., and Bredal, T. V., 2022, "An Analytical TOOLBOX for the Characterization of Chalks and Other Fine-Grained Rock Types within Enhanced Oil Recovery Research and Its Application – Guideline": Energies, v. 15, no. 11, p. 4060.

Paper II:

Bredal, T. V., Zimmermann, U., Madland, M. V., Minde, M. W., Ost, A. D., Wirtz, T., Audinot, J.-N., and Korsnes, R. I., 2022, "High-Resolution Topographic and Chemical Surface Imaging of Chalk for Oil Recovery Improvement Applications": Minerals, v. 12, no. 3, p. 356.

Paper III:

Bredal, T. V., Ost, A. D, Wirtz, T., Audinot, J.-N., Zimmermann, U., Madland, M. V., Minde, M. W., Puntervold, T., 2023, "4D surface reconstruction of micron-sized organic calcite for characterization of chemical heterogeneity of chalk surfaces". Energy and Fuels

Paper IV:

Bredal, T. V., Zimmermann, U., Korsnes, I.R, Madland, M. V., Minde, M. "Unconsolidated artificial calcite and dolomite core flooding tests under reservoir conditions" Under review in Geoenergy Science and Engineering.

Paper V:

Bredal, T. V., Korsnes, R. I., Zimmermann, U., Minde, M. W., and Madland, M. V., 2022, "Water Weakening of Artificially Fractured

Chalk, Fracture Modification and Mineral Precipitation during Water Injection; An Experimental Study": Energies, v. 15, no. 10, p. 3817.

Paper VI:

Bredal, T.V., Zimmermann, U., Korsnes, I.R, Minde, M., Tucho, W.M. Audinot, J.-N., Madland M. V., 2023 "Comprehensive Characterization of Mineral Precipitation in Artificially Fractured Chalk during flooding Experiments" Journal of Petroleum Science Engineering.

Contributions

2021

Bredal, T.V., 2021 "IOR research and reservoir characterization on Eldfisk cores on micron and nanoscale." Digital presentation. September 8th, Stavanger, Norway

Bredal, T.V., Zimmermann, U., Minde, M., Korsnes, I.R., Madland M. V., Audinot, J.-N., 2021 "Dolomite Flooding Experiments for Enhanced Oil Recovery Purposes at Reservoir Conditions - A Study of Mineralogical changes at micro and nano scale using novel methods. Abstract SPE's 58th Annual Conference, March, Denver, USA

Bredal, T.V., 2021 "Brine-rock interaction processes in pure mineralogical systems for IOR purposes in chalk reservoirs." Presentation. IOR conference April 26-28, Stavanger, Norway

Bredal, T.V., Zimmermann, U., Korsnes, I.R., Minde, M., Madland M. V., 2021 "Alteration of sample properties on reworked reservoir chalk in laboratory flooding experiments." Abstract. Tekna Conference January 13,14 Trondheim, Norway

2020

Bredal, T.V., 2020 "Dissolution of minerals dependent on flooding brine and linked precipitation and distribution in porous media. Mineralogical alteration in carbonate reservoir." Digital presentation. IOR Delivery Forum Kick -Off. May 26, Stavanger, Norway

2019

Bredal, T.V., Minde, M. W., 2019 "Rock and the fluid: Applied sciences using a toolbox for material characterization." Presentation. University ISTerre November 25, Grenoble, France

Bredal, T.V., 2019 "*Imaging and analysis of artificial fractured chalk in laboratory EOR experiments*." Poster and presentation. November Conference, November 11-13, Rio De Janeiro, Brazil

Bredal, T.V., Zimmermann, U., Minde, M. W., and Madland, M. V., 2019 "*Mineralogical changes in EOR experiments in fractured chalk.*" Poster. Goldschmidt, European association of geochemistry August 19-23, Barcelona, Spain

Bredal, T.V., Madland, M. V., Minde, M. W, Zimmermann, U., 2019 "*Mineralogical understanding of rock composition and mineralogical changes before and after EOR experiments*." Poster. IOR Conference, March 19-20, Stavanger, Norway

Table of contents

List of abbreviations

ACS	American Chemical Society
AF	Artifical Fracture
AFM	Atomic Force Microscopy
BET	Brunauer–Emmett–Teller
BSE	Backscattered Electron
CT	X-ray Computed Tomography
DOL.LOV	Dolomite, Løvgavlen Formation
EDS	Energy Dispersive X-ray Spectroscopy
EOR	Enhanced Oil Recovery
FIB	Focused Ion Beam
FIB-SEM	Focused Ion Beam- Scanning Electron Microscopy
GFIS	Gas Field Ion Source
HIM	Helium Ion Microscopy
HIM-SIMS	Helium Ion Microscopy-Secondary Ion Mass Spectrometry
IC	Ion Chromatography
ICP-MS	Inductive Coupled Plasma-Mass Spectrometry
IOR	Improved Oil Recovery
IPS	Intragranular Pressure Solution
LIST	Luxembourg Institute of Science and Technology
LOI	Loss on Ignition
LVDT	Linear Voltage Displacement Transducer
MLA	Mineral Liberation Analysis
NCS	Norwegiean Continental Shelf
OBSV	Obourg quarry, St. Vaast Formation
PDI	Potential-determining ions
PPM	Part per million
PV/day	Pore volume per day
REF	Reference sample (unflooded)
ROI	Region of Interest
SE	Secondary Electron
SEM	Scanning Electron Microscopy
SIMS	Secondary Ion Mass Spectrometry
SSA	Spesific Surface Area
SSW	Syntetic Seawater
TEM	Transmission Electron Microscopy
TOT/C	Total carbon
TOT/S	Total sulfur
U.Eq	Un equlibriated
VPDB	Vienna Pee Dee Belemnite
Wt.%	Weight %
XRD	X-ray diffraction

Table of figures

xxii

List of Tables

1 Motivation and objective

Changes in the porosity and the effective overburden stress during hydrocarbon production are essential properties for predicting compaction and subsidence in reservoirs as Ekofisk and Valhall which are two giant hydrocarbon reservoirs at the Norwegian Continental Shelf (NCS). Ekofisk is naturally fractured (Agarwal et al., 2000) which complicates prediction and modeling subsidence. Subsidence has several consequences, like casing deformations which can pose a challenge for well completion. At the same time, the compaction can steer to additional drainage of the reservoir and thereby increase the oil recovery. Current simulation models based on experimental data for predicting compaction, still suffer from inaccuracy (Amour et al., 2023; Keszthelyi et al., 2016).

The presence of fractures and their impact on strain can challenge accuracy in predicting compaction and subsidence. They can be modelled by modifying the bulk rock properties to adjust for the fracture porosity and permeability. These models provide average values based on two-dimensional block models representing different fracture densities (Gutierrez et al., 2013). For years, mechanisms of fluid flow through fractured carbonate reservoirs have been studied, including Improved Oil Recovery (IOR) modelling on multi-phase systems (Andersen, 2019). However, less attention has been given to their impact on compaction, subsidence, and mineralogical alterations in and adjacent to fractures or aperture modification during brine injection.

The effects of non-calcite minerals present on compaction and fluid flow in chalk associated with brine injection have still not been completely understood. The question has been raised by several authors (Amour et al., 2021; Andersen et al., 2018; Madland et al., 2011; Puntervold et al., 2007; Romanuka et al., 2012; Shariatpanahi et al., 2016). Most available methods challenge to image and chemically characterize these minerals

in-situ with high enough resolution, due to the small size often ranging below micron scale. Several authors have pointed out that the presence of impurities may impact the strain (Austad et al., 2008; Fabricius, 2007; Kallesten et al., 2021a; Madland et al., 2011; Minde et al., 2018). Dolomite is one example of a non-calcite mineral present in chalk on the NCS (Kallesten et al., 2021b) which may impact modeling of oil recovery.

In this context, the presented research aims at answering the following questions:

- What role does the presence of dolomite play in brine-rock interaction processes of chalk?
- How will an artificial fracture impact geo-mechanical behaviour associated with different compositions of brine?
- How will a fracture and the adjacent core material alter during brine-injection in terms of mineralogical and textural changes?
- How are impurities of non-calcite minerals distributed in chalk?
- How will the presence of impurities impact precipitation of minerals and its distribution during fluid injection?

To characterize these impurities, a segment of the objective was to evaluate a newly combined instrument: Helium Ion Microscopy (HIM) combined with Secondary Ion Mass Spectrometry (SIMS) as this could resolve the challenge mentioned above, due to its high resolution of both imaging and chemical detection. A better understanding of the link between mineralogical and mechanical processes during fluid injection can increase accuracy of the input data for extrapolation and simulation of future reservoir behaviour. Data may in the next phase help when designing the optimal brine for Enhanced Oil Recovery (EOR), yet this is not part of the scope here.

2

2   Introduction

Carbonate reservoirs at the NCS, and specifically chalk, have great potential to accumulate oil due to the very high storage capacity caused by the porosity often reaching 40–50 % (Sulak and Danielsen, 1989). About 40 % of the world's oil is produced from chalk and carbonate rocks (Tanner et al., 1991). However, chalk reservoirs are often characterized by low matrix (core material) permeability and depend on a connected fractured network to transport fluids through the reservoir effectively. The grain surfaces in chalk tend not to be water-wet, which challenges primary oil production. IOR strategies are implemented for hydrocarbon reservoirs to increase the oil recovery when primary production by pressure depletion is declining. The initial purpose of seawater injection at Ekofisk in 1987 was to stabilize the pore-pressure to prevent seafloor subsidence following declining hydrocarbon production (Doornhof et al., 2006; Hermansen et al., 2000; Teufel et al., 1991). And at the same time, it was intended to drive remaining hydrocarbons towards the production well. However, seawater injection allowed not only to sustain but to increase the oil production beyond initial predictions (Sylte et al., 1999). The seawater injection did, however, not prevent further seabed subsidence as intended but stimulated compaction due to water weakening of chalk (Cook and Jewell, 1996; Hermansen et al., 2000; Sulak and Danielsen, 1989; Sylte et al., 1999). IOR methods allow for additional hydrocarbon production from existing reservoirs instead of developing new fields (Newman, 1983).

The physio-chemical effects of fluid-rock interactions during brine injection have been widely studied (Korsnes et al., 2008; Korsnes et al., 2006b; Megawati et al., 2013; Risnes et al., 2005). High-quality reservoir chalk on the NCS is normally pure with less than five weight % (Wt.%) impurities which refers to non-calcite components (clay, dolomite, quartz, etc.). Fluid injection may trigger dissolution of present minerals

and precipitation of secondary minerals. These processes have been of specific interests as those may alter reservoir properties that may in turn improve oil recovery (Andersen et al., 2018; Heggheim et al., 2005; Minde et al., 2018). However, the impact of impurities (non-calcite minerals) in these fluid-rock interactions is still not completely understood.

A better understanding of brine-rock interactions in chalk with presence of impurities can help to develop the ideal or "smart" water composition which is a major focus within IOR research. Decoding fluid-rock interaction processes is essential to predict wettability alteration and water weakening effect. Linking those chemical processes taking place in chalk with geo-mechanical alterations is therefore paramount to develop successful reservoir management. This will demand necessary analytical tools to produce sound and sufficient data. To establish knowledge of the relationship between mineralogical changes and geo-mechanical alteration is therefore the first step to establish the ideal brine. The very small grain size of coccolith fragments and the new grown secondary minerals during fluid injection (Skovbjerg et al., 2012; Skovbjerg et al., 2013; Zimmermann et al., 2015) challenged detailed mineralogical characterization from the 1970s to 2000s significantly. Methods which provide in-situ imaging and chemical identification with high enough resolution have been challenging but have improved during the last two decades. New methods allow future research road maps to secure models and predictions for recovery or further use of reservoirs like storage spaces.

Previous studies have discussed in detail the process of dissolution and precipitation during EOR experiments (Andersen et al., 2018; Minde et al., 2019; Minde et al., 2020) and emphasized the role of temperature during flooding experiments with constant pressure (Minde et al., 2018; Nermoen et al., 2016; Wang et al., 2015). The different brine recipes have been the same in numerous experiments over the last decades and are described in Chapter 3.2. The following introductory chapters aim to

pinpoint the major aspects and clarify background of the research with a focus on the selected topics.

2.1 Improved Oil Recovery (IOR)

Primary recovery refers to pore pressure depletion of the reservoir by natural drive mechanisms. IOR, often synonymous with secondary recovery, is a general term which implies to improve the oil recovery by any practice. EOR or tertiary recovery is more specific. It implies a reduction in oil saturation below the residual oil saturation (Thomas, 2008). Both terms refer to processes related to seawater injection, yet EOR is used when the brine composition is changed from the original seawater to increase the recovery beyond what may be produced by seawater (Kokal and Al-Kaabi, 2010). The term IOR is most frequently used in the thesis.

IOR has been applied with great success on chalk reservoir at the NCS, wherefore the strategy gained a high recognition within hydrocarbon industry in Norway. Currently, IOR is a major tool in more sustainable hydrocarbon exploitation and is of importance for CO_2 and hydrogen storage strategies, which depend on an effective use of reservoirs.

2.2 Chalk and impurities

Chalk is a deep marine sedimentary rock formed mainly by highly porous calcareous micro- and nano-fossils, predominantly coccolithophores, which degrade to individual skeletal plates of micron-sized coccoliths with increasing burial. Individual coccolith plates can be as small as 0.3 μm (Scholle and Kinsman, 1973). The small constituents of the rock generate specific surface area (SSA) often ranging between 1–2 m²/g for pure chalk (Hjuler and Fabricius, 2009). Hjuler and Fabricius (2009) found in a larger chalk study that the non-carbonate fraction displayed a wider range of SSA values between 0.2–

79.5 m²/g. As the rock is highly porous and soft, it is sensitive to compaction during diagenesis (Scholle et al., 1974).

Due to its depositional environment distal to the shore, presence of detrital grains is normally minor and mostly introduced by aerial transport like pyroclastic fall deposits (Simonsen and Toft, 2006). Chalk is rather homogeneous in terms of its mineralogy, with one major constituent being calcite with minor occurrences between 0-10 Wt.% of other minerals (e.g. dolomite, quartz, opal, apatite, feldspar, pyrite, oxides, or different clay minerals) depending on location, age, and degree of diagenesis (Hjuler and Fabricius, 2009). With increasing overburden, pressure and subsequent fluid expulsion lead to compaction, porosity reduction, pore-filling cementation, and lithification, resulting in a fine-grained sedimentary rock (Bjørlykke and Høeg, 1997). Early incoming fluids (e.g., oil) lower the formation water concentration and inhibit compaction. Over-pressurized chalk will reduce grain-to-grain stresses (contact dissolution) and the porosity will remain higher than expected for the specific depth where these processes occur. Tectonic processes may cause increased solution and cementation (Scholle, 1977). Pressure solution and local secondary precipitation of carbonate are dominant factors for cementation. These processes can vary controlled by grain size distributions, faunal composition (aragonite versus low magnesium calcite), or concentrations and abundance of non-carbonate material. Cementation during diagenesis is dependent on the burial depth and pore-water chemistry. If fresh pore water flushes through the rock before major burial, the chalk is subject to a higher porosity loss than the burial depth would suggest (Scholle, 1977). During diagenesis authigenic clays such as kaolinite, illite and chlorite can precipitate directly from aqueous solution, instead of being altered by the precursor lattice (Curtis et al., 1985; Zhao et al., 2023). Accessory silicates in chalk are predominantly represented by clay minerals originated from pyroclastic sources transported by wind (Lindgreen, 2002; Simonsen and Toft, 2006) and flint (Drits et al., 2017). These authigenic clays can be

mixed-layer clays of mainly illite and smectite, chlorite, and in some cases, serpentine (Lindgreen et al., 2008; Lindgreen, 2002) or to mixed-layered clays such as illite-smectite (Fabricius, 2007). Further mineral dissolution and pore-filling cementation is dependent on parameters during diagenesis such as pore-water chemistry, organic matter, soluble molecular mass, and thermal maturation. Dolomite is one of the minerals that has been formed in many reservoir and non-reservoir chalk successions on the NCS during diagenetic processes (Kallesten et al., 2021a; Kallesten et al., 2021b).

2.3 Formation of dolomite and presence in chalk

Dolomite ($CaMg(CO_3)_2$) is predominantly a result of diagenetic processes which can be divided into two groups based on the mode of formation (Davies, 1979). Primary dolomite precipitates directly from aqueous solution whereas secondary dolomite is formed by replacing the precursor mineral calcite by ion exchange. Primary dolomite has been suggested to precipitate in sabkhas which are regions characterized by relatively high ambient temperature, high salinity, and light intensity (Alsharhan and Kendall, 2003). More recent studies indicate that in addition to evaporation, certain microbial processes facilitate nucleation of primary dolomite in shallow depositional environment (Petrash et al., 2017). The most common dolomite, however, is secondary dolomite. The process of dolomitization is characterized by replacement of calcium ions by magnesium ions. This process requires certain conditions like sufficient supply of Mg^{2+} from brine, a certain permeability to allow dolomitizing brines to flow through the muddy facies in addition to elevated temperatures often around 60°C to 70°C (Machel, 2004). The mechanisms of fluid transportation in the subsurface are generally assigned to density differences of the solutions and the permeability through the precursor sediment, driven either by glacio-eustacy or by

thermal convection. These solutions can be seawater or brines concentrated by evaporation, connate water, or meteoric water.

The stoichiometric dolomite has a 50:50 ratio of Ca to Mg with the near-perfect ordering of the Mg and Ca in alternate cation layers. A gradual increase in Mg concentration during dolomitization allows the dolomite to be classified depending on the ratio of the Mg in the crystal lattice. Table 1 presents dolomite groups developed by (Chilingar, 1957). The dolomite of most dolostones is granular, with individual grains ranging from micron-sized up to a few millimeters.

Table 1) Dolomite characterization based on Ca/Mg ratio by Chilingar (1957)

Name	Ca/Mg ratio
Magnesian dolomite	1 - 1.5
Dolomite	1.5 -1.7
Slightly calcareous dolomite	1.7 -2
Calcareous dolomite	2 - 3.5
Highly dolomitic limestone	3.5 - 16
Dolomitic limestone	16 - 60
Slightly dolomitic limestone	60 - 105
Calcific limestone	> 105

The mole-by-mole conversion of calcite to dolomite necessarily results in a 12 % increase in porosity reflecting the difference in specific density (as Mg-containing dolomite has a higher specific density than calcite) causing an overall volume decrease. Dolomitization can enhance, preserve, or destroy porosity (Sun, 1995). High primary porosities in limestones can be conserved during the dolomitization process, but may also be significantly reduced by the growth of pore-filling dolomite cement during diagenesis (Braithwaite et al., 2004). The initial crystal structure and cementation during burial will determine the petrophysical properties of dolomite petroleum reservoirs (Woody et al., 1996).

Abundance of dolomite is facilitated by higher porosity, as mentioned before, but fractured rocks are even more inclined to alteration by fluid migration during diagenesis. At the NCS, caused by its geological evolution, tectonic processes contributed to post-depositional fracturing processes (Wrona et al., 2017; Ziegler, 1975). The relation between dolomite precipitation and fracturing of chalk successions has not been studied in detail yet. However, at Ekofisk dolomite has been formed as in other chalk reservoirs at the NCS (Kallesten et al., 2021b) and those deposits are also fractured. Nevertheless, faulting and fracturing of carbonate reservoirs have major implications for hydrocarbon fluid pathways (Agosta et al., 2007; Wu et al., 2016).

2.4   Fractured chalk

Since chalk reservoirs have a combination of high porosity but rather low matrix permeability, fractures and related high permeable zones are of great importance to sustain an effective fluid flow (Snow and Brownlee, 1989). The naturally fractured system on Ekofisk Field is believed to increase reservoir permeability by a factor of 50 (Sulak and Danielsen, 1989). A high intensity of fractures can create a spatially distinct, permeable zone (Michie et al., 2014). The contribution of a single fracture to reservoir fluid flow depends on its geometry, which includes length, height, and aperture size (Philip et al., 2005). The fault core is a narrow zone that commonly forms between major slip surfaces (Figure 2). The original host rock is destroyed in the fault core by mechanical and chemical processes. The inner core of the fault zone has experienced the highest strain and where the permeability is decreased to such an extent that the inner core acts as a barrier for fluid transport (Caine et al., 1996; Goddard and Evans, 1995). The adjacent destruction zone is a wider zone of deformation with numerous fractures and smaller faults (Figure 2). The fracture network, fracture density, and orientation will control bulk permeability in these damage zones.
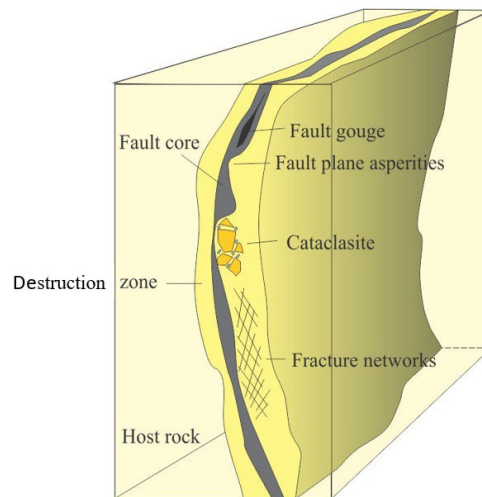
Figure 2) A schematic of a single fault, with variable thickness and extent of the core and adjacent fracture networks (modified from Caine et al 1996).

To better understand the complexity of reservoir fluid behaviour and petrophysical properties, it is beneficial to consider the details of a fault zone, and to categorize the zones with distinct hydrogeological units as barriers, conduits, or combined conduits and barriers (Chester et al., 1993). A simplified fracture-matrix model composed of several parallel regions with homogeneous distribution of fracture-matrix properties and cross-section has been developed (Andersen, 2019). Andersen (2019) simulated oil recovery by spontaneous imbibition of injected fluids in a multiphase system. The author predicted that regions with frequent and wide fractures receive more fluids and produce faster yet with high water production. Regions with lower fracture frequency and narrow apertures receive less water, produce slower, and the injected seawater is more likely left in the matrix. This demands precise mapping of the fractures and a study of possible precipitation of minerals within fractures depending on the injected fluid.

During pressure depletion of reservoirs, as in the Valhall reservoir, experience increased effective overburden stresses, seabed subsidence

(Barkved et al., 2003), and reduced matrix permeability (Bisdom et al., 2016; Laubach et al., 2019). On the other hand, compaction may also induce fractures (Mukherjee et al., 1995). Properties of the fracture can change (Egeberg and Saigal, 1991) and, in turn, alter the fluid flow.

2.5 Water-weakening effect

Seawater injection for IOR purposes will deform the chalk matrix and lead to reservoir compaction. The deformation is a consequence of processes associated with surface-active ions present in seawater such as Ca^{2+}, Mg^{2+}, and SO_4^{2-} (Korsnes et al., 2008). Compaction during seawater injection is dependent on initial porosity (Nermoen, 2018). This geo-mechanical response is often referred to as water weakening of chalk. There are several simultaneous processes leading to water weakening in chalk and these were widely studied in laboratory experiments (Andersen et al., 2018; Heggheim et al., 2005; Korsnes et al., 2008; Korsnes et al., 2006a). Water weakening is associated with SO_4^{2-} adsorbing to the calcite surface which will reduce the bulk modulus and yield points and cause compaction. The disjoining pressure in granular contacts is increased by the interactions between charged surfaces. The net repulsive forces that act as normal forces in the vicinity of the grains will counteract the cohesive forces and enhance pore collapse during loading (Megawati et al., 2013).

Geo-mechanical responses related to the water weakening of chalk are results of surface chemistry and chemical alterations, which may lead to calcite dissolution and precipitation of new minerals (Amour et al., 2021; Heggheim et al., 2005; Korsnes et al., 2008; Strand et al., 2003). Dissolution and precipitation processes are also dependent on effective stresses, temperatures, porosity, chemistry, and diagenetic processes such as cementation (Bjørlykke and Høeg, 1997). Precipitated magnesite ($MgCO_3$) is identified in experiments where Mg^{2+} is present in the injected brine such as $MgCl_2$ (Minde et al., 2018) or synthetic seawater (SSW) (Madland et al., 2011). Magnesite has a smaller crystal size

compared to dissolved calcite, and thereby it may reduce the solid volume of the rock. Morphological changes such as the smoothing of grain surfaces when injected with NaCl have been identified (Andersen et al., 2018). Surface grain rounding has been suggested to weaken mechanical intergranular friction and provoke additional compaction (Megawati et al., 2011).

Brine-rock interaction processes are likely dependent on the non-carbonate minerals (Madland et al., 2011). Madland et al. (2011) observed that pure chalk experienced a lower compaction rate compared to chalk with impurities of silicate and clay minerals. It has been suggested that reprecipitation of Si-bearing minerals enhances the dissolution of calcite, which may explain the high level of compaction observed in chalk flooded with $MgCl_2$ brine (Andersen et al., 2018).

Currently, the role of non-calcite or non-carbonate minerals present within chalk during IOR processes is yet underexplored. Therefore, characterization of the mineral composition of reservoir chalk and the abundance of precipitated minerals during brine injection is of high importance. However, not only the abundance but also the distribution of these phases may be important as the area they cover (when attached to calcite minerals) also influence surface charge thus the wettability properties. Consequently, the distribution of those phases is a very important parameter for wettability modelling.

2.6 Ekofisk

The Ekofisk Field is located within the Norwegian Central Graben which represents the southern branch of the North Sea triple rift system in the southern part of the Norwegian North Sea (Gennaro, 2011). The Ekofisk structure is an elongated anticline or dome structure with a main fold axis in a north-south direction (Van Den Bark and Thomas, 1981). The reservoir depth is approximately 2900 meters subsea. The reservoir consists of two chalk intervals: the Ekofisk Formation deposited during

Danian and the reworked chalk sediments of the Tor Formation deposited during Maastrichtian (Gennaro et al., 2013). A relatively impermeable layer of argillaceous, siliceous, and cherty chalk separates the two producing formations.

Ekofisk and Tor formations have an average porosity of 30 to 40 %, despite the significant overburden. The diagenesis of chalk in general includes mechanical compaction and reduction in porosity due to compaction during early burial, followed by later pore-filling cementation associated with pressure dissolution (Fabricius, 2007). The final porosity will depend on the maximum depth of burial and pore water chemistry (Scholle and Kinsman, 1973). Some exceptions can cause a higher porosity (Scholle, 1977). It is suggested that the preserved porosity in Ekofisk field can be associated with over-pressuring of the reservoir, magnesium rich pore fluids, and early introduction of hydrocarbons (Van Den Bark and Thomas, 1981). Porosity and permeability are also associated with presence of clay and/or silica where pure chalk (>90 % $CaCO_3$) will normally have a higher quality (Blinkenberg et al., 2020; Fabricius, 2007). The Danian Ekofisk Formation is rich in silica compared to the underlying Maastrichtian Tor Formation and forms a more heterogeneous and overall poorer reservoir interval in many of the producing fields in the Danish Central Graben (Blinkenberg et al., 2020; Fabricius and Borre, 2007; Gennaro et al., 2013). The poorer quality identified in intervals with more than 5 % silica in an Ekofisk fabric is interpreted to be the result of local calcite dissolution and cementation related to release of silica-rich brines associated with opal phases which caused pervasive silicification and cementation of the calcite microcrystals (Blinkenberg et al., 2021).

The Ekofisk structure has most likely been formed because of several subsequent tectonic events (Gennaro, 2011). Among them were Permo-Triassic extension and the deposition of the Zechstein successions, Early Jurassic doming, followed by Late Jurassic rifting. Early Cretaceous was dominated by compression (inversion) and transpressive movement

along Triassic-Jurassic faults, followed by Late Cretaceous to Eocene thermal subsidence accompanied by compression and inversion of major basement faults and salt movement. The halokinesis developed 4-way dip anticlines (Boersma et al., 2020).

Tectonics resulted in a dense fractured reservoir. Its distribution, orientation, and interconnectivity of the natural fractures govern fluid flow (Chapter 2.4). Interpretation of seismic discontinuity created by a 3D seismic cube combined with higher resolution borehole image log indicated that most small-scale fractures occur close to large faults (Boersma et al., 2020). The authors in Boersma et al. (2020) also characterized Lower Ekofisk Formation by more widespread small-scale seismic discontinuities with high intensity.

3   Methodologies

Despite the rather simple mineralogy of chalk, which consists predominantly of coccolithophores, rock properties may vary depending on the presence of non-calcite minerals (Chapter 2.2). Characterization of the non-calcite minerals is particularly interesting as those will impact processes related to fluid injections. These processes may include sorption (Risnes et al., 2003), dissolution, and precipitation on the surface or in the porous media at sub-micron scale. Non-carbonate minerals and their distribution may additionally affect rock mechanical parameters, which may in turn impact the oil recovery (Andersen et al., 2018; Minde et al., 2018).

Mineralogical alterations take place mainly at a very small scale (< 2 µm) during IOR related experiments. The small constituents of chalk, which can be as small as 0.3 µm (Scholle and Kinsman, 1973) challenges the resolution of instruments used for imaging and chemical detection. Chemical and textural alterations need to be mapped throughout the core, to determine the distribution, homogeneity, and quantity of newly precipitated minerals. The timing and rate of chemical alteration can provide a more accurate link to geo-mechanical behaviour. A range of methods is required to detect present non-carbonate minerals and brine-rock interaction processes associated with seawater injection, like what, where and when these processes occurred.

To model processes during fluid injection for IOR, an in-depth characterization of the reservoir properties from submicron level on pore scale, to core scale, and reservoir scale is essential. However, upscaling is a very complex task. To tackle this challenge, the reservoir rocks need to be studied as extensively as possible. The following subchapters describe in-depth samples and brines compositions and preparations, workflow and experimental procedures using the triaxial cell. The toolbox briefly describes the application of various methods used for

characterization of chalk and small grained constituents, divided into three information levels.

3.1   Sample preparations

The powder samples, described in **Paper IV**, were prepared in a plastic cylinder to fit in a heat shrink sleeve to replicate a standard core. The mixed mineral samples were scaled, mixed, and hand shaken for a few minutes before adding the powder into the heat shrink sleeve. The cylinder was filled with powder, stamped, and twisted stepwise. Drainage discs allowed the brine to be evenly distributed. A 45 µm polypropylene screen filter was surrounded by two 0.22 µm filter placed between the drainage disc and the mantled core to prevent particles from escaping the core and enter the hydraulic system. Pure and mixed powder were collected for reference purposes.

On-shore cores from the St. Vaast Formation were extracted from a non-weathered chalk block in addition to several cores for reference sampling. Five samples were cored parallel from the same outcrop block with a diameter of 38.1 mm and a length of about 70 mm (**Paper V**). A 2 mm drill bit was used to produce cylindrical holes along the flooding axis, mimicking fractures in three cores (Figure 3). The size of the fractures measured 2.25 (± 0.05) mm in diameter. Two supplementary intact cores were added to the experiment as reference. Fresh samples (unflooded) were used for analysis in **Paper III**, and a sample flooded with SSW in **Paper II**. A fractured outcrop sample from Obourg quarry, St. Vaast Formation (OBSV) flooded with $MgCl_2$ was investigated in **Paper VI**.
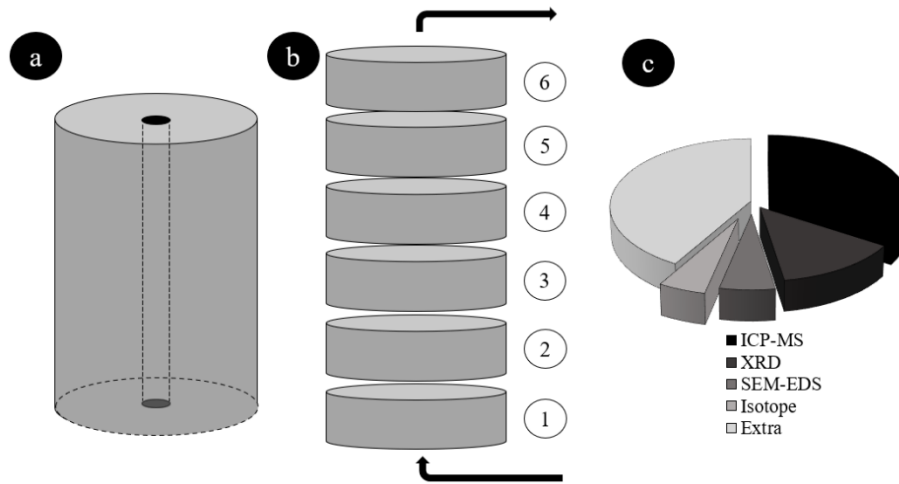
Figure 3) Sample preparation pre and post experiments. a) A sketch of a core with a central drilled hole which measured 2.25 (± 0.05) mm. The diameter of the core was 3.81 cm and the length around 7 cm. (NB the figure is not in scale). b) The samples were sliced post experiments. The inlet is slice 1 and the outlet is slice 6 (sometimes 5 or 7 slices depending on the length of the sample). The arrows indicate the flow direction of the injected brine. c) Each slice was divided into several pieces for further investigation by various methods.

Samples were mounted in epoxy to allow imaging of the sample in a cross-sectional view. Epoxy was mixed and heated to 40°C and added to the sample under vacuum. After 24 hours the surface of the mounts was manually ground (dry) in several steps using coarse scale of 250 and 500 grits before using 1000 grits combined with ethanol. A final polish was performed with 3 microns Diapro on Dac performed by Struers Roto Pol-35. All samples, mounted as well as fresh surface samples, went through a final step of coating with either palladium, carbon or gold, to prevent charging when using Scanning Electron Microscopy (SEM), Mineral Liberation Analysis (MLA) or Helium Ion Microscopy (HIM).

3.2 Brines

Several compositions of brines were used in these experiments to detect processes linked to different concentration of ions present in natural seawater. A total of five different brines were used: SSW, LowSal (low salinity), $MgCl_2$, $MgCl_2$ U.Eq (Un-equilibrated $MgCl_2$) and NaCl.

All the brines were made from distilled water in either one or two steps. The brines that were equilibrated went through a preparation step. 0.1 g/L $CaCO_3$ powder was added to distilled water to achieve equilibrium with the chalk. The brine was stirred for two hours, degassed, and filtered with a 0.22 µm filter. All brines went through the final step where the ions (Table 2) were added to the distilled water or the equilibrated brine. The brines were stirred for two hours, degassed, and filtered with a 0.65 µm filter.

SSW is one of these in-house laboratory mixed brines, which match the ion concentration in natural seawater used for IOR purposes in North Sea chalk reservoirs. The composition of this brine comprises Na^+, Cl^-, Mg^{2+}, Ca^{2+}, K^+, and SO_4^{2-} (Table 2). LowSal is ten times diluted SSW. LowSal was chosen because it showed potential for enhanced oil recovery in dolomitic reservoir samples (Puntervold et al., 2018). $MgCl_2$ was selected since Mg^{2+} is one of the most reactive ions in SSW. By isolating the $MgCl_2$ in a separate brine used in flooding experiment helps understanding its impact during brine rock interaction processes and its role in SSW. $MgCl_2$ brine mixed without $CaCO_3$ equilibrated water is referred to "$MgCl_2$ U.Eq". Another $MgCl_2$ brine was used which was equilibrated to carbonate to underline the role of equilibration during brine injection experiments. NaCl is the major component in SSW and used as a reference as it is not expected to interact with chalk (Megawati et al., 2015). The concentrations of $MgCl_2$, $MgCl_2$ U.Eq, and NaCl were selected such that the brines have equal ion strength to SSW (Table 2).

Table 2) Ion concentration of the brine used in the experiments.

Ions [mol/L] Brines	Cl^-	Na^+	K^+	Mg^{2+}	Ca^{2+}	$SO_4{}^{2-}$	$HCO_3{}^-$
SSW	0.525	0.45	0.01	0.0445	0.013	0.024	0.002
LowSal	0.0525	0.045	0.001	0.0045	0.0013	0.0024	0.0002
$MgCl_2$*	0.438	*	*	0.219	*	*	*
$MgCl_2$ U.Eq	0.438	*	*	0.219	*	*	*
NaCl*	0.657	0.657	*	*	*	*	*

* The ion is not present in the brine.

3.3   Workflow

Flooding experiments like those performed within this research project have been carried out routinely over decades at the University of Stavanger. Procedures are developed, yet some adjustments were required. First, samples were prepared (Chapter 3.2) and dimension recorded. The samples were uploaded to the triaxial cell (Figure 4a). The brines were prepared (Chapter 3.2) shortly before the test started. The planned test duration was aimed to last for approximately three months for the powder experiments and two months for fractured samples. Physical limitations such as clogging of the system occasionally resulted in a shorter test duration. Effluent samples were frequently collected (Figure 4b) during fluid injection and analyzed in batches via Ion Chromatography (IC) described in Appendix 8.1. The cores were flushed with four pore volumes of distilled water before dismantling (Figure 4c).

Post measurements were performed after dismantling in wet-condition and repeated in dry condition after 24 hours kept in a heating cabinet that kept 70°C. The samples were cut in one cm thick slices and therefore the number of total slices varied depending on the sample length. Each slice was divided into several pieces such that every slice could be analyzed by several methods.
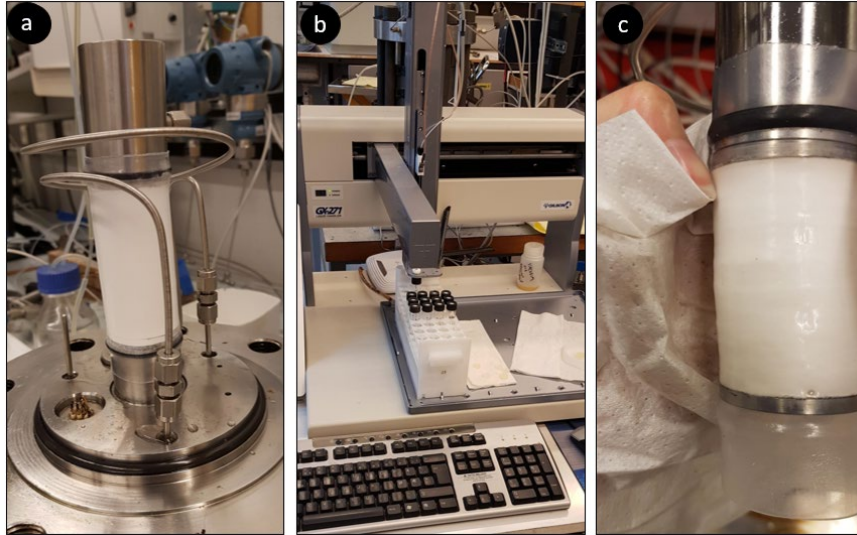
Figure 4) Workflow in lab. a) Sample prepared and mantled in the triaxial cell. b) Automatic effluent sampler. c) A flooded sample still surrounded by the heat shrinkage sleeve.

For all experiments the flooded samples were sliced from inlet to outlet, where "1" is inlet and outlet is "5", "6" or "7" (Figure 3). Sample material was analyzed in three steps described in the toolbox (Chapter 3.2) as performed on unflooded sample material normally performed before the experiment as the final step in the workflow (Figure 5).
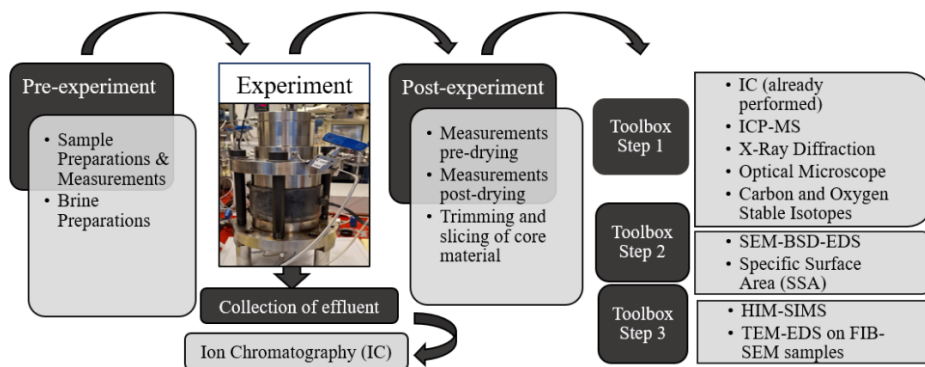
Figure 5) Workflow throughout projects. From preparations, via experiments with effluent collection and water analysis, to post-experiment measurements, and finally application of various methods on different levels described in the toolbox (Chapter 3.5).

3.4   Triaxial cell test

The triaxial cell can simulate reservoir conditions and measure mechanical properties of deformable solids (e.g., powder or reservoir rocks) at temperatures and stresses resembling for instance North Sea chalk reservoirs. A heat shrink sleeve surrounded the specimen and separated it from the confining oil. An extensometer which enclosed the circumference of the core allowed radial strain measurements. A Linear Voltage Displacement Transducer (LVDT) was located on top of the cell for axial displacement measurements. A heating jacket surrounding the triaxial cell allowed a constant temperature while running the experiment. The Ekofisk reservoir temperature of 130°C was used in all experiments. The top section and confining chamber were mounted with bolts to the underbody. Triaxial cell stresses were controlled by two high-pressure pumps: Quizix QX Pump 1 and Quizix QX pump 2 regulating axial and confining pressure, respectively (Figure 6). A few rigs were equipped with two Vindum VP1-12K-HC. The flow rate of the injection brine was controlled by a Gilson 307 pump. A back pressure regulator controlled the pore pressure and prevented boiling of the pore fluid at elevated temperatures. Computer software (Lab View) logged data throughout the test, i.e., axial, and radial deformation, temperatures, and various pressures (Figure 6). The prepared brine was filled into a separate piston cell chamber, with distilled water in the adjacent chamber, separated by a piston.

The brine was injected through the cores with a rate corresponding to one pore volume/day for both powder samples and outcrop chalk cores, OBSV. Continuous brine injection through the core during the entire experimental program, allowed for continuous measurement of the differential pressure, such that the sample permeability change could be calculated.
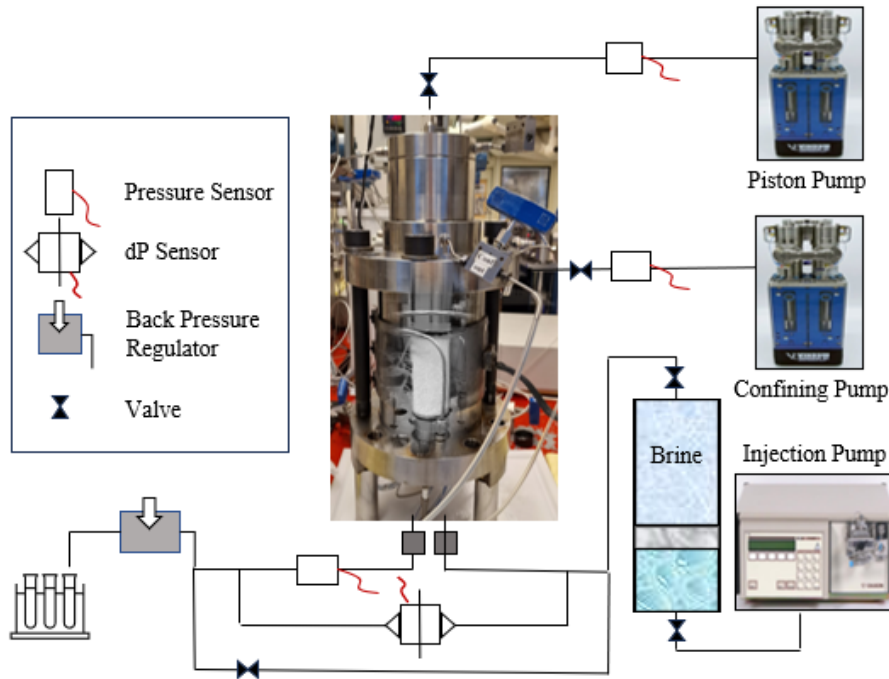
Figure 6) A simplified sketch of the triaxial cell set-up. The system is controlled by a piston and a confining pump to keep the overburden pressure. Backing fluid is pumped into a piston cell by the injection pump which allows the brine to flow into the triaxial cell. The back pressure regulator controls the pore pressure. The system is monitored by pressure sensors.

The experiments were performed under either uniaxial strain conditions or hydrostatic test conditions as described for each case in detail in the different publication (**Paper IV), (Paper V**). The axial strain was calculated from recording the change in length of the core; thus, the stress-strain development of the framework (matrix) was acquired. The axial strain (ϵ_{ax}) was calculated (Equation 1) where L is the sample length and ΔL is the change in length. The loading phase was followed by the creep phase, where the material slowly deforms under the constant load.

$$\epsilon_{ax} = \frac{\Delta L}{L_0} \times 100 \tag{1}$$

A logarithmic formula (Equation 2) was used for extrapolation of the creep, where A and t_0 are constants that were determined by adjustment to the experimental creep curve. $\mathcal{E}_{creep}$ is the logarithmic creep behaviour and t is the endpoint of the observed creep phase. For detailed descriptions, the reader is referred to Madland et al. (2006).

$$\mathcal{E}_{creep} = A \ln (1 + t/t_0) \tag{2}$$

For consolidated samples, the yield point and bulk modulus can be determined from the hydrostatic loading period. The yield point reflects the limit of the elastic behaviour and the start of plastic behaviour. In this thesis it is determined by the intersection of two tangent lines which follows the elastic and the plastic phase of the loading curve.

The triaxial test procedure was tailored for cemented and consolidated chalk. Multiple failures of triaxial tests on unconsolidated powder samples were caused by the absence of adjusted methods. Failures were initiated by loose grains flooding into the tubing system causing clogging, often in the backpressure regulator. Procedures for unconsolidated samples were adjusted to prevent powder from escaping the core and the triaxial cell. By adding a 45 µm polypropylene screen filter in addition to the filter 0.22 µm. Additionally, the injection rate was significantly reduced during the saturation phase to avoid high differential pressure. Those changes prevented powder from moving into the tubing system.

3.5   Toolbox

A compilation for analytical tools has been presented by Zimmermann et al. (2017) and established as a 'toolbox' for mineralogical research on chalk (**Paper I**). A detailed workflow is paramount when characterizing

chalk composition where the methods have been divided into three different steps (Figure 7).

TOOLBOX for chalk analysis

FIRST STEP	SECOND STEP	THIRD STEP
Basic background tools for fundamental database information (core scale)	Advanced tools for extended database information (pore-scale µm)	Specialized tools for complete data base (sub-micron)

•X-Ray Diffraction
•Optical microscope
•Whole rock geochemistry
•Effluent geochemistry
•Traditional stable isotope geochemistry
•Pycnometry
	•Electron Microscopy
	  •SEM-BSE-EDS
	  •MLA
	•Raman
	•Specific Surface Area (SSA)
		•Nano-SIMS (lack of optimal imaging)
		•TERS-AFM (challenging sample preparation)
		•TEM-EDS om FIB-SEM samples
		•Current:HIM-SIMS
		•Future: Raman-SEM

Figure 7) Methodologies divided into three categories with three different levels of information provided in the toolbox.

The first step in chalk characterization or other fine-grained material, includes collecting basic data with background tools for fundamental database information. This includes characterization using basic routine analytical tools such as X-ray diffraction (XRD) for mineralogical identification, Inductive Coupled Plasma-Mass Spectrometry (ICP-MS) for whole rock geochemistry, stable isotope measurements (C-O isotopes), and optical microscopy (Appendices 8.2-8.5). The second step incorporates extended data collection with advanced tools for comprehensive database information. This includes either grain or

textural information as SSA (Appendix 8.6). The third and final step includes application of key analytical techniques to reach the highest level of details using highly specialized tools which can reach the highest resolution on sub-micron level. Several methods are listed on each step; however, some data may partly overlap and support results. Suggested methods on the first step are paramount for understanding the composition of the reservoir rock or sample. Complementing with the methods from the second step would build up a powerful database for interpretation and decision-making. Methods on the third step have advantages when characterizing on sub-micron scale is requested. A complementary approach can deliver the requested data set for feasible interpretation. Methods and instruments used in this thesis are described in detail in Appendix 8.

During IOR and EOR experiments (Chapter 3.3) brines are injected into rock samples. The effluent is then studied using IC. The data can identify which ions are expelled from the core during flooding, and which are left in the core by comparing to the influent. Analysis of the brine provides data linked to a time which can be linked to the strain behaviour and helps determine the impact of ion exchange. The main limitation of water analysis is related to processes where for instance a calcium rich mineral dissolves at the inlet and another precipitate at the outlet which balance the total calcium concentration and thereby mask the process. Further core analysis is therefore essential.

ICP-MS provides bulk geochemistry. XRD enables phase identification based on the crystal lattice and therefore support the chemical concentration obtained by geochemistry. The limitation of these two methods is related to absence of texture information (images) of the analyzed area.

More detailed characterization such as sample imaging and chemical identification using common instruments, as Scanning Electron Microscopy coupled with Energy Dispersive X-ray Spectroscopy (SEM-

EDS) described in Appendix 8.7 is recommended for characterization on the second step described in the toolbox. However, it strives to determine element distribution on such small particles as the minimum spot size for EDS is normally around 1 µm² (Priebe et al., 2019) and analyses are mostly semi-quantitative. MLA (Appendix 8.8) measurements are based on BSE image analysis and may determine pore and grain boundaries on polished specimens. The method quantifies different mineral phases (or group of minerals) and assigns each group a color, and thus produces a mineral distribution map. Grain size distribution can also be imaged, and pore space calculated which may be ideally combined with SSA data to gain more in-depth information about textural properties of the samples. A significant change in SSA for instance, may indicate dissolution or precipitation of new mineral phases.

Highly specialized tools are proposed for detailed characterization at the third step of the toolbox. Transmission Electron Microscope (TEM) resolves the issue to gain images and identify the different phases on sub-micron scale (Appendix 8.9). TEM coupled with EDS provides very high magnification images and identification of the chemical composition and crystal orientation. The disadvantage of the TEM-EDS is related to sample preparation using Focused Ion Beam - Secondary Electron Microscopy (FIB-SEM) which is time consuming, expensive and carries a high risk to destroy the small sample measuring only 10*10*0.1 µm (Appendix 8.10). TEM-EDS provides a cross-sectional view of a FIB-SEM sample and carries some obstacles regarding surface and cement characterization (Hjuler et al., 2018). Nevertheless, a method with easier sample preparation can procedure quicker analyses which will benefit research progress.

HIM combined with SIMS is a newly developed combination of two high resolution instruments and has not previously been reported for chalk analysis before (Appendix 8.11 and **Papers II, III).** The combined HIM-SIMS instrument has been developed by a group of scientists at Luxembourg Institute of Science and Technology (LIST). Currently,

only a few instruments are available worldwide. Applying this technique to chalk is therefore considered unique. The major advantage of the HIM-SIMS is that it overcomes the challenge previously described regarding the need of high-resolution imaging combined with in-situ chemical identification on sub-micron scale. The value of high-resolution imaging obtained by HIM without linking the surface topography of a sample to its chemical composition of the specimen (obtained by SIMS), has been limited. Conversely, a high-resolution chemical identification obtained by SIMS without knowing the accurate location because of poor imaging is not satisfying (Zimmermann et al., 2015). The combination of the two instruments allowed an in-situ detection of surface imaging and chemical detection on nanoscale without moving the sample and without costly and time-consuming sample preparation. HIM-SIMS allows the identification and mapping of different phases in a sample material.

Application of HIM-SIMS is therefore an advantageous tool when investigating reservoir core material for increased comprehension of brine-rock interaction processes, thus complementing existing methods. Nevertheless, the methodology has a few limitations. For instance, the compound of ^{40}Ca and ^{16}O is not yet possible to differentiate from ^{56}Fe, due to mass interference. Additionally, certain elements are more easily ionized during the sputtering process. Therefore, the ratio of ion concentrations limits mineral interpretation. A method that can normalize ionization for each element is currently being developed and may in the future provide more accurate mineral characterization to interpret the genesis of minerals in terms of their protolith.

Despite HIM-SIMS providing novel information of surface chemistry on nanoscale linked to the coccolith`s topography, characterization must still be complemented by additional methods for further information on different scales. Using complementary methods on different steps presented in the toolbox and being aware of their limitations such that

the final collection of methods chosen gain the maximum effectivity and thus solve the research objective.

4 Materials

Properties of the sample materials used in the experimental work are described in the following sub-chapters.

4.1 Dolomite powder

Dolomite was selected as the second mineral for the investigation due to the abundance in chalk formations at the NCS (Kallesten et al., 2021b). The dolomite powder was provided by Norwegian Talc AS. The dolomite is a mid- to late Cambrian marble deposit in the fourth subset of the Leivset Formation, extracted from the Løvgavlen quarry in Fauske (Norway). The marble deposits are located in the Salten Region on the Fauske nappe and are particularly complex structural unit (Melezhik et al., 2013). Dolomite samples were also collected from the Løvgavlen quarry with subsequent analysis of geochemistry and isotopic data to compare the powder to the actual exposed rock. The provided dolomite powder was identified successfully as one of the subset formations of the Leivset Formation based on bulk geochemistry and stable isotope data (Table 3). A complete geochemistry table is provided for all samples used in the thesis and is found in Appendix 8.12.

Table 3) Selected elements and $\delta^{13}C$ and $\delta^{18}O$ for dolomite powder (Dol REF) where Dol indicates dolomite and REF is reference and dolomite samples of the Løvgavlen Formation at Fauske (DOL.LOV). VPDB means Vienna Pee Dee Belemnite. PPM is part per million.

Element	SiO_2	Al_2O_3	MgO	CaO	Sr	$\delta^{13}C$	$\delta^{18}O$	CaO/MgO
Sample	Wt.%	Wt.%	Wt.%	Wt.%	PPM	VPDB [‰]	VPDB [‰]	
Dol REF 0	0.31	0.05	21.61	30.85	57.8	-0.2	-9.45	1.43
Dol REF 1	0.26	0.03	21.46	31.00	50.3	-0.2	-9.48	1.44
Dol REF 2	0.28	0.03	21.61	30.63	50.8	-0.2	-9.36	1.42
Dol REF 3	0.24	0.03	21.47	31.01	49.8	-0.2	-9.44	1.44
DOL.LOV.1	0.35	0.08	21.63	30.78	52.3	-0.2	-8.87	1.42
DOL.LOV.2	0.29	0.07	21.68	30.90	52.3	-0.2	-8.97	1.43
DOL.LOV.3	0.28	0.11	21.45	31.10	66.1	0.26	-9.00	1.45

The powdered dolomite had an average size of 16 μm, where 90 % of the grains were in the interval of 5-50 μm (Figure 8). The CaO/MgO ratio acquired from whole-rock geochemical measurements (Appendix 8.6) was calculated to 1.43 (± 0.03) which classify the dolomite (Table 1) as a magnesian dolomite (Chilingar, 1957). Porosity was calculated to 33.9 (± 2.6) % for dolomite samples (Table 3 in **Paper IV**). Porosity calculation is provided in Appendix 8.13.

Dolomite powder was used as experimental material in **Paper IV**. Five dolomite samples were flooded with different compositions of brines. The samples were labeled by the mineral composition, followed by a core number, the slice number (Figure 3), and the brine used in the experiment: e.g., Dol 3.5 SSW, where "Dol" is dolomite, "3" is the test number, "5" indicates the outlet slice and "SSW" is the brine used during flooding.
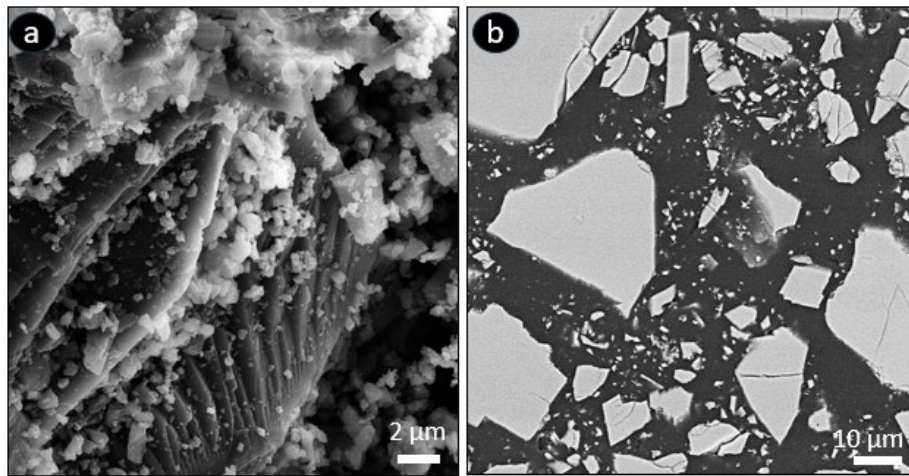
Figure 8) Secondary Electron (SE) images of unflooded dolomite powder. a) A fresh surface sample exhibits a "stepped" topography. b) Dolomite grains in cross sectional view of an unflooded polished powder sample. The powdered dolomite had an average size of 16 μm, where 90 % of the grains were in the interval between 5-50 μm (the numbers were provided by MLA).

4.2   Manufactured calcite powder

Manufactured calcite was selected as the study objective as chalk always has some impurities. The manufactured calcite powder is 99.95 Suprapur® with the chemical formula $CaCO_3$ and is provided by Merck Millipore. The particles showed mainly subhedral crystals, with a frequent grain size of 10 µm and occasional presence of clustered small grains of 2 (± 1.5) µm (Figure 9).

The samples were labeled by the mineral composition, followed by a core number, the slice number (Figure 3), as well as the brine used in the experiment. The porosity of calcite samples was calculated to 55.5 (± 2.7) %.
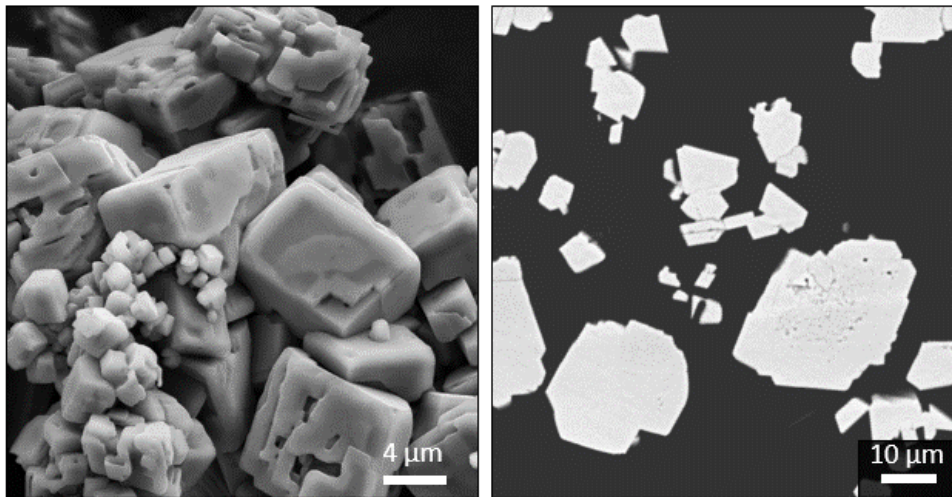
Figure 9) SEM-SE images of unflooded manufactured calcite. a) Fresh surface SEM-SE image. b) Polished sample. The most common grainsize is around 10 µm.

4.3   Mixed powder (dolomite/calcite)

Dolomite and calcite were mixed in different ratios to match a realistic ratio of 5 % Wt. dolomite, two mixes were added to increase understanding how the concentration of dolomite among chalk may

impact brine rock interaction processes. Three different ratios of dolomites-calcite mixes were selected: 50 to 50 %, 20 to 80 %, and 5 to 95 %. In contrast to samples of pure materials which were flooded with five different compositions of brines, only two different brines were used including the most realistic brine (SSW) in addition to $MgCl_2$ U.Eq. which showed the highest dissolution rate of calcite and precipitation of magnesite. The samples were labelled as following: e.g., "Mix 1.5 50-50 $MgCl_2$ U.Eq" represents a two-component sample of dolomite and calcite, 1 is the core number, 5 indicates the outlet slice (Figure 3), "50-50" is the mixing ratio, and "$MgCl_2$ U.Eq" is the brine used during flooding.

4.4 Outcrop chalk samples

Due to the difficulty of collecting reservoir samples, analogue outcropping chalk is frequently used to study IOR processes and labelled in numerous publications 'on-shore chalk' (Andersen et al., 2018; Hjuler and Fabricius, 2009; Kallesten et al., 2021b). Chalk from an Upper Cretaceous succession (Coniacian) from the Obourg quarry, which contains chalk successions deposited in the Mons basin, located in Belgium (Figure 10) was used for analyses documented in **Paper II**, **Paper III**, **Paper V** and **Paper VI**. The chalk was sampled from the St. Vaast Formation (Dusar and Lagrou, 2007; Robaszynski et al., 2001; Schroeder, 2006). The depositional basin for the St. Vaast Formation rocks can be described as a gentle syncline developed on a folded and faulted Paleozoic basement (Pirson et al., 2008). The St. Vaast Formation contains > 95 % calcium carbonate, with impurities of quartz and traces of glauconite, chlorite and pyrite (Cornet and Briart, 2000). This chalk formation had a high SSA of 4.52 ($\pm$ 0.14) g/m² compared to other reservoir and outcrop chalk often ranging between 1.65 and 3.88 g/m² (Wen, 2018). The average porosity was 41 ($\pm$ 1) %, and the permeability ranged around 0.56 mD for intact cores (Table 2 **Paper V**). All samples from this formation are labeled OBSV followed by a core number and

the brine it was flooded with. The samples with an artificial fracture are additionally labeled AF indicating "artificial fracture". The final number represents the slice number, where # 1 is the "inlet" and # 6 or 7 represents the "outlet" (Figure 3). Unflooded material is marked with "REF" indicating unflooded or reference.
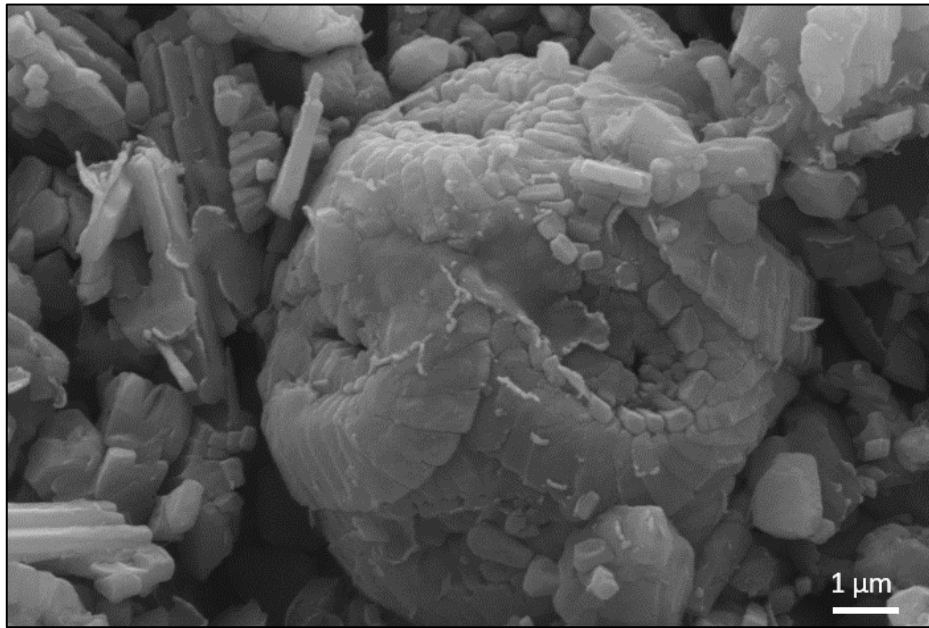
Figure 10) An SEM-SE image of a coccolith from the Upper Cretaceous Coniacian, St. Vaast Formation, Obourg quarry.

5   Main results

5.1   Chemical and geo-mechanical processes in pure and mixed powdered samples

To increase comprehension of brine-rock interaction processes during seawater injection, experiments with pure and mixed mineralogical powder samples were flooded in triaxial cells (Chapter 3.4) under reservoir conditions with a temperature of 130°C, effective overburden stress of 13.1 MPa and 0.7 MPa pore pressure (**Paper IV**). Five dolomite powder samples, five manufactured calcite samples (99.95 % Suprapur®), in addition to six mixed samples of dolomite and calcite powders (in three different ratios) were flooded with five different composition of brines (Table 2). After flooding samples in triaxial cells under reservoir conditions, a selection of methods described in the toolbox (Chapter 3.5) were used for identification of chemical alteration processes. Three standard deviation is used when data is provided with a range (e.g., porosity showed an average of 55.5 ($\pm$ 2.7) %).

5.1.1   Dolomite powder samples flooded with different compositions of brine

The five flooded dolomite powder samples flooded with five different brines showed distinct compaction during loading and creep. During loading of the dolomite samples, Dol 3 SSW showed axial strain of 6.7 % which was higher compared to dolomite tests flooded with other brines showing axial strains ranging between 4.8 % - 5.3 % (Figure 11a). The porosities for dolomite samples ranged between 33.0 % and 35.6 % (Table 4).

Table 4) Porosities pre-and post-experiments and axial strain during loading and creep for dolomite, calcite, and mixed powder samples. The numbers in brackets for Cal 4F LowSal represent a repeated test set up without issues with pumps during loading (see text for details).

Sample	Porosity			Axial Strain			Duration
	Pre-test	Post-test	Δ	Loading	Creep	Total	
	[%]	[%]		[%]	[%]	[%]	[Days]
Dol 1B MgCl$_2$	33.0	25.7	7.3	5.3	2.9	8.2	93
Dol 2 NaCl	33.7	25.4	8.3	5.4	1.9	7.3	92
Dol 3 SSW	33.8	25.5	8.3	7.0	1.6	8.6	20
Dol 4C LowSal	33.6	25.8	7.8	4.8	1.6	6.4	28
Dol 6 MgCl$_2$ U.Eq	35.6	23.1	12.5	5.3	3.0	8.3	86
Cal 1 MgCl$_2$	58.2	38.2	20	12.6	4.3	16.9	90
Cal 2D NaCl	55.1	*	*	9.7	7.8	17.5	54
Cal 3B SSW	53.4	40.9	12.5	12.8	1.1	13.9	31
Cal 4F LowSal	56.2	38.2	18.0	17.0 (10.3)	3.4 (4.2)	20.4 (14.5)	85
Cal 6B MgCl$_2$ U.Eq	54.7	40.8	13.9	10.8	4.7	15.5	85
Mix 1 50-50 MgCl$_2$ U.Eq	42.0	31.3	10.7	5.9	5.7	11.6	82
Mix 2 50-50 SSW	44.4	29.0	15.4	7.5	4.2	11.7	28
Mix 3 5-95 MgCl$_2$ U.Eq	55.4	38.1	17.3	8.0	6.8	14.8	85
Mix 4 5-95 SSW	54.7	40.2	14.5	15.7	1.1	16.8	4
Mix 5 20-80 MgCl$_2$ U.Eq	50.5	37.2	13.3	11.0	7.0	18.0	84
Mix 6B 20-80 SSW	51.7	24.1	27.6	12.7	1.1	13.8	13

*Sample collapsed in the triaxial test

Under constant stress conditions during creep, the compaction rates for the MgCl$_2$ flooded samples were 0.14 % per week (from after the tenth day when the samples showed stable compaction) for both Dol 1B MgCl$_2$ and Dol 6 MgCl$_2$ U.Eq (Figure 11b). This was two times higher than for the sample flooded with NaCl (Dol 2 NaCl) showing 0.06 % axial strain per week (Table 5). Extrapolation of Dol 4C LowSal estimated a compaction rate of 0.09 % per week (Table 4).

Table 5) Compaction rates during creep for dolomite samples.

Sample	Dol 1B MgCl$_2$	Dol 2 NaCl	Dol 3 SSW	Dol 4C LowSal	Dol 6 MgCl$_2$ U.Eq
Compaction rate [%/week]	0.14	0.06	*	0.09	0.14

*Not calculated (it was flooded too short to show a constant rate).
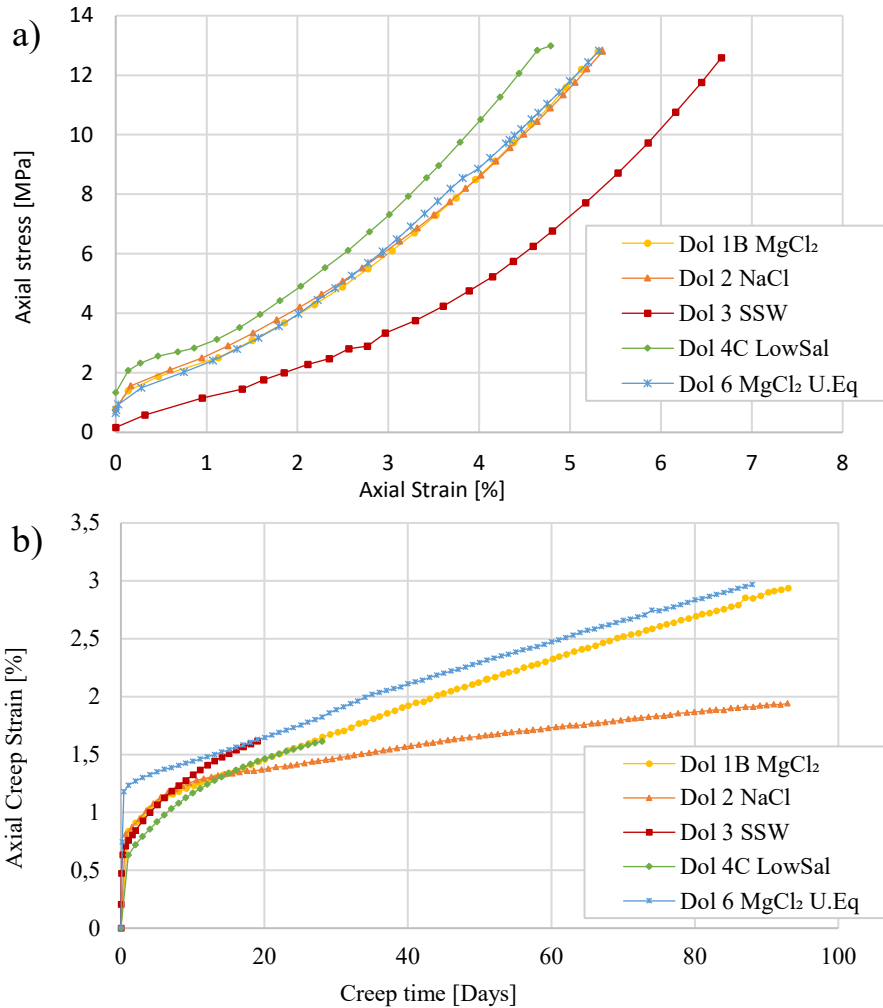
Figure 11) Dolomite powder samples flooded in triaxial cell tests under reservoir conditions of 130°C with a flooding rate of one pore volume/day. a) Loading b) Creep

All five dolomite samples showed insignificant chemical alterations characterized by the absence of mineral precipitation (Table 6). This was supported by SEM-EDS (Figure 5 **Paper IV**), XRD (Figure 4 **Paper IV**) and geochemistry (Table 4 **Paper IV**). IC data showed instant and temporary loss of Mg^{2+} ions during temperature increase for Dol 1B

MgCl$_2$, Dol 6 MgCl$_2$. U.Eq, and Dol 3 SSW (Figure 3a **Paper IV**). Dol 3 SSW also experienced an initial loss of SO$_4^{2-}$ identified in the first few effluent samples (Figure 3b **Paper IV**).

Table 6) Mineral precipitation associated with the injected brine and sample material.

Brine composition/ Sample mineral	MgCl$_2$	NaCl	SSW	LowSal	MgCl$_2$ U.Eq
Dolomite	0	0	0	0	0
Calcite	Magnesite	0	0	0	Magnesite
Mix 5-95	*	*	Aragonite	*	Magnesite
Mix 20-80	*	*	Aragonite (traces of anhydrite)	*	Magnesite High-magnesium calcite
Mix 50-50	*	*	Anhydrite	*	Magnesite High-magnesium calcite

" 0 " Indicates no newly precipitated minerals identified.
" * " Not tested

5.1.2 *Manufactured calcite powder flooded with different compositions of brine*

The compaction identified during loading for the five calcite powder samples, ranged between 9.7 % and 12.8 % axial strain (Figure 12a). A compaction of 17.0 % for Cal 4F LowSal was an outlier due to pump issues. Repeated tests for Cal 4F LowSal showed an axial strain of 10.3 % (Table 7, Appendix 2 **Paper IV**). The initital sample porosity was calculated to 55.5 ($\pm$ 2.7) % (Table 4).

The axial creep rates for calcite powdered samples showed distinct creep strains. The calcite powder sample flooded with NaCl (Cal 2D NaCl) showed a significant compaction the first three days, which stabilized at an axial strain of 7.0 % after the first week (Figure 12b). The Cal 4F LowSal showed a similar behaviour with significant compaction the first two days which stabilized at 3.2 % after three days (Figure 12b). The

sample Cal 3B SSW instantly reduced the compactionrate in the creep phase, and ceased at an axial strain of only 1.15 % (Figure 12b). Cal 1 $MgCl_2$ and Cal 6B $MgCl_2$ U.Eq showed constant creep rates of around 0.350 %/week (Table 7). The final axial strains were 4.2 % and 4.7 % for Cal 1 $MgCl_2$ and Cal 6B $MgCl_2$ U.Eq, respectively (Table 4).

Table 7) Compaction rates during creep for manufactured calcite samples.

Sample	Cal 1 $MgCl_2$	Cal 2D NaCl	Cal 3B SSW	Cal 4F LowSal	Cal 6B $MgCl_2$ U.Eq
Compaction rate [%/week]	0.350	*	*	*	0.350

*Not calculated due to completely flat curves/constant after a certain time

Precipitation of magnesite was detected in Cal 1 $MgCl_2$ and Cal 6B $MgCl_2$ U.Eq (Table 6). A constant excess of Ca^{2+} with corresponding decrease of Mg^{2+} were identified in effluent samples compared to the composition of the injection fluid, obtained by IC (Figure 7a, **Paper IV**). The retention of Mg^{2+} in the core was reflected in the geochemistry result. Cal 6B $MgCl_2$ U.Eq showed a MgO concentration of 17.35 Wt.% and 0.65 Wt.% for inlet and oulet slices, respectively. For Cal 1 $MgCl_2$ the MgO concentrations were 8.49 Wt.% and 0.33 Wt.% for the inlet slice and the outlet slice, respectively (Appendix 8.1). Magnesite was identified by XRD thus supported the above mentioned observations (Figure 8 **Paper IV**). SEM-EDS data also supported the presence of magnesium-rich minerals.

Cal 3B SSW showed absence of dissolution, precipitation, and morphological changes (Table 6). The geochemistry data, for instance, showed only trace values of 0.09 Wt.% and 0.18 Wt.% MgO (Appendix 8.1) for inlet and outlet slices, respectively. Insignificant chemical (Appendix 8.1) and textural alterations (Figure 9 **Paper IV**) were identified for Cal 3B NaCl and Cal 4F LowSal.
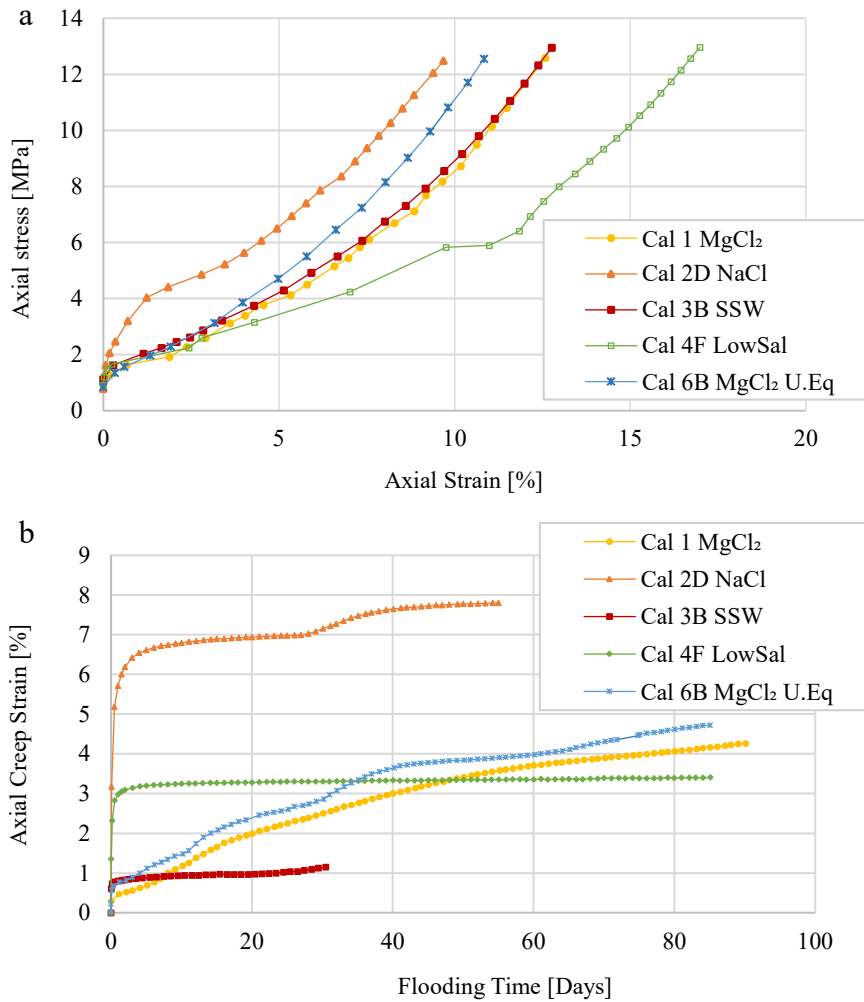
Figure 12) Calcite powder samples flooded in triaxial cells under reservoir conditions of 130°C with an injection rate of one pore volume/day. a) Loading. Cal 4F LowSal experienced unstable pump conditions (see repeated test in appendix 2, **Paper IV**). b) Creep

5.1.3   Mixed dolomite and calcite powder flooded with MgCl₂ U.Eq and SSW

The mixed samples with different ratios of dolomite and calcite showed higher strain for the three SSW than the three MgCl₂ U.Eq flooded

samples during loading. The axial strains during loading for SSW flooded samples were 7.6 %, 12.7 %, and 15.7 % for Mix 2 50-50 SSW, Mix 6B 20-80 SSW and Mix 4 5-95 SSW, respectively (Table 4, Figure 13a). The axial strains for $MgCl_2$ U.Eq flooded samples were 5.5 %, 11.0 %, and 8.0 % for Mix 1 50-50 $MgCl_2$ U.Eq, Mix 5 20-80 $MgCl_2$ U.Eq, Mix 3 5-95 $MgCl_2$ U.Eq, respectively (Table 4, Figure 13a). Mix 5 20-80 $MgCl_2$ U.Eq experienced pump instability which caused a jump in axial strain. Porosities ranged between 42.0 % and 55.4 % (Table 4).

During constant overburden, two SSW flooded mixed samples showed axial compaction which ceased at around 1.1 % axial strain under less than a day into the creep for Mix 4 5-95 SSW and Mix 6B 20-80 SSW (Figure 13b). Mix 2 50-50 SSW showed a total strain of 4.2 % after four weeks. SSW flooded tests were shorter than tests flooded with $MgCl_2$ U.Eq. because of clogging.

On the contrary to trends observed during loading, all three mixed samples flooded with $MgCl_2$ U.Eq experienced higher axial strains than SSW flooded mixed samples during creep. The most significant compaction was observed the first week (Figure 13b). The axial strain rates significantly reduced and showed 0.02 %, 0.25 %, and 0.12 % per/week (after the 4th week) for Mix 1 50-50 $MgCl_2$ U.Eq, Mix 3 5-95 $MgCl_2$ U.Eq, and Mix 5 20-80 $MgCl_2$ U.Eq, respectively (Table 8). The total axial strains for the $MgCl_2$ flooded mixed samples during creep were 5.7 %, 6.8 %, and 7.0 % for Mix 1 50-50 $MgCl_2$ U.Eq, Mix 3 5-95 $MgCl_2$ U.Eq and Mix 5 20-80 $MgCl_2$ U.Eq, respectively (Table 4).

Table 8) Compaction rates during creep for mixed dolomite and calcite samples. The rates represent the period after the 4th week.

Sample	Mix 1 50-50 $MgCl_2$ U.Eq	Mix 2 50-50 SSW	Mix 3 5-95 $MgCl_2$ U.Eq	Mix 4 5-95 SSW	Mix 5 20-80 $MgCl_2$ U.Eq	Mix 6B 20-80 SSW
Compaction rate [%/week]	0.02	*	0.25	*	0.12	*

*The sample stagnated the compaction rate early.

41
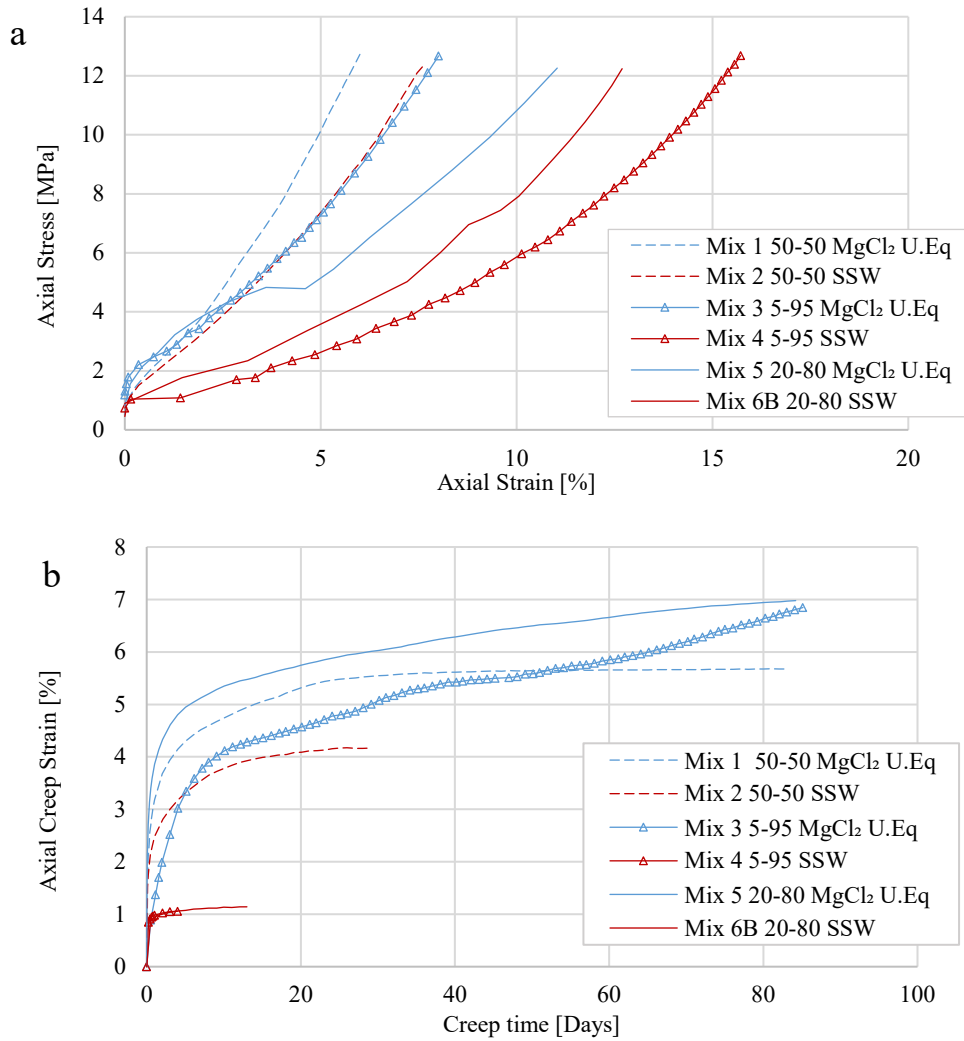
Figure 13) Axial strain during loading and creep for all mixed dolomite-calcite tests flooded with MgCl₂ U.Eq and SSW. a) Axial strain during loading of Mixed dolomite-calcite tests. b) Axial strain during creep for mixed dolomite-calcite tests.

Mixed samples experienced significant chemical alterations with subsequent precipitation of new minerals (Table 4). The three mixed SSW flooded samples showed precipitation of aragonite ($CaCO_3$) and

anhydrite ($CaSO_4$). Aragonite was abundant in Mix 4 5-95 SSW (Figure 14), and present in Mix 6B 20-80 SSW. Anhydrite was identified in Mix 2 50-50 SSW (Figure 15) and traces were identified in Mix 6B 20-80 SSW (Table 4). The following results lead to the mineral identification:

Aragonite was clearly identified by XRD (Figure 13 **Paper IV**). The aragonite concentration in Mix 6B 20-80 SSW was 4.1 Wt.% in the inlet and 13.6 Wt.% in the outlet (Appendix 3 **Paper IV**). The elongated/ needle shaped mineral was identified by SEM-EDS (Figure 14). The maximum grain sizes identified was 20 μm in Mix 4 5-95 SSW.
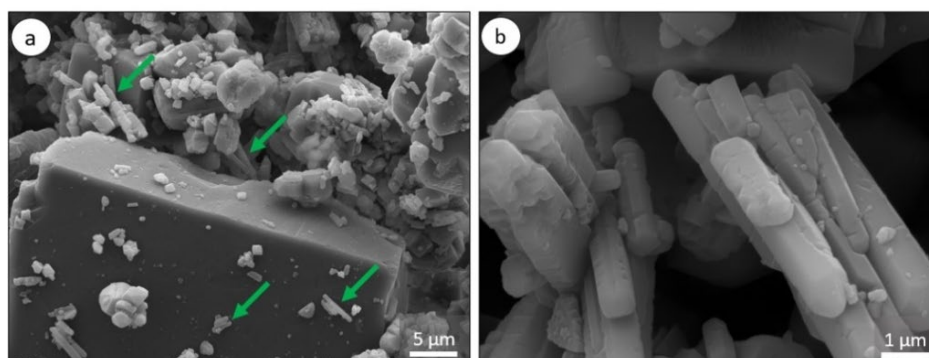
Figure 14) SEM-SE images of precipitated aragonite ($CaCO_3$) in Mix 4.1 5-95 SSW. a) A low magnification SEM-SE image distributes aragonite on the surface of a dolomite crystal highlighted by green arrows. The size ranged from 5-10 μm. b) Aragonite cluster of elongated/needle shaped crystals measuring < 20 μm.

Anhydrite was identified by XRD, predominantly in sample Mix 2 50-50 SSW. Slice three held 1.3 Wt.%, whereas only trace values were detected in the inlet and oulet slices (Appendix 3 **Paper IV**). Geochemistry obtained from Mix 2 50-50 SSW showed an increased sulfur (TOT/S) concentration, thus supporting precipitation of anhydrite. The highest concentration was identified in the second slice with 0.45 Wt.% TOT/S (Appendix 8.1). Mix 6B 20-80 SSW showed trace values of 0.06 Wt.% TOT/S in the outlet slice (data was not acquired for all slices). IC data documented a loss of 0.018 M SO_4^{2-} for Mix 2 50-50 SSW (Figure 11 **Paper IV**). Anhydrite crystals identified by SEM-EDS

measured up to five μm. Single elemental maps showed overlap of S and Ca (Figure 15).
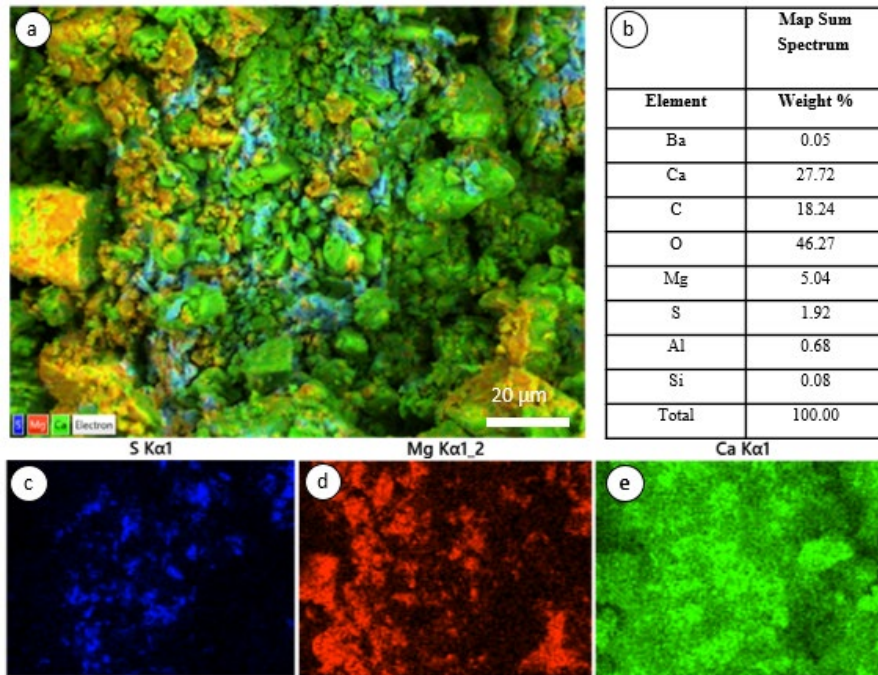
Figure 15) SEM and EDS for Mix 2.2 50-50 SSW. a) A combined SEM-SE image overlayed by single EDS maps of S (blue) Mg (red) and Ca (green). b) EDS sum spectrum acquired in a). c) Single map distribution of S. d) Single map distribution of Mg. e) Single map distribution of Ca.

The three mixed samples flooded with $MgCl_2$ U.Eq showed significant chemical interaction. This was reflected in IC data which showed significant Ca^{2+} excess and Mg^{2+} loss in effluent (Figure 11 **Paper IV**). Geochemistry data of tested samples revealed increased MgO concentration compared to unflooded mixed samples. The most significant increases were 8.2 Wt.% and 10.7 Wt.% averagely for Mix 1 50-50 $MgCl_2$ U.Eq and Mix 5 20-80 $MgCl_2$ U.Eq, respectively (Table 8, **Paper IV**). For the two latter tests, an MgO increase was identified throughout the entire core length. On the other hand, only 4.3 Wt.% and 0.5 Wt.% increases were detected in the inlet and outlet of Mix 3 5-95 $MgCl_2$ U.Eq, respectively. High-magnesium calcite was identified by

XRD in outletslices of Mix 1 50-50 $MgCl_2$ U.Eq, Mix 5 20-80 $MgCl_2$ U.Eq, and only traces in Mix 3 5-95 $MgCl_2$ U.Eq in addition to magnesite in the inlet of all three mixed samples flooded with $MgCl_2$ U.Eq (Figure 12 **Paper IV**). Rhombohedral magnesium-rich minerals were identified by SEM-EDS (Figure 16) pointing to precipitation of magnesite in the inlet slices of Mix 1.1 50-50 $MgCl_2$ and Mix 3.1 5-95 $MgCl_2$ U.Eq.
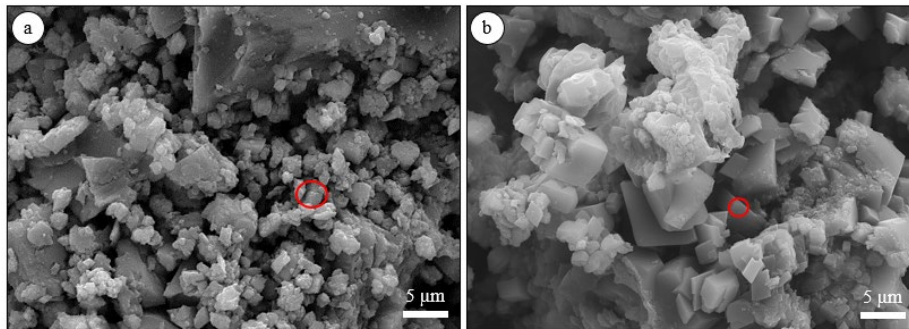
Figure 16) Precipitation of magnesite in inlet slices of mixed dolomite and calcite samples flooded with $MgCl_2$ U.Eq. a) A red circle highlights precipitation of magnesite in Mix 1.1 50-50 $MgCl_2$ U.Eq. The crystal size was around 1 μm. b) Red circle highlights precipitation of magnesite in Mix 3.1 5-95 $MgCl_2$ U.Eq. The magnesite crystals were abundant and measured frequently 3-8 μm.

5.2   Artificially fractured outcrop chalk

Three artificially fractured outcrop samples (OBSV) were flooded under reservoir conditions of 130°C. Hydrostatic loading above yield followed by a creep phase with an effective overburden stress of 11.3 MPa. Descriptions of sample preparations are found in Chapter 3.1. Two additional intact (unfractured) samples were flooded for reference purposes. The average porosity and permeability of all five samples were 41.8 % and 0.56 mD, respectively. The diameter of artificial fractures measured 2.25 ($\pm$ 0.05) mm before flooding. The chalk samples held around 5 Wt.% non-carbonate phases (Appendix 8.1), including glauconite, illite, and pyrite (**Paper V**). The samples were flooded with NaCl (Creep 1) for six days with a flooding rate of one pore volume per day (PV/day). The brine composition injected changed to SSW and $MgCl_2$ for two fractured samples as well as for two reference samples (Creep 2). The third artificially fractured sample was flooded with NaCl during the entire creep phase. Mineralogical processes and fracture modification are presented, but the reader is referred to **Papers V and IV** for additional information. Details for the set up can also be found in (Abubeker, 2013; Geitle, 2013).

5.2.1   Artificial fracture and geo-mechanical responses

All samples showed comparable axial strains during hydrostatic loading which ranged between 0.79 % and 1.07 % (Figure 2 **Paper V**). During Creep 1 (NaCl injection), the average axial creep strain was 1.11 ($\pm$ 0.17) % and 1.41 ($\pm$ 0.42) % for unfractured and fractured samples, respectively (Figure 17a). When the brine composition changed in Creep 2, all $MgCl_2$ and SSW flooded samples showed enhanced compaction rates compared to the NaCl flooded core (Figure 17b). The unfractured samples showed a more instant and significant compaction after the brine change compared to artificially fractured samples. The maximum strain rate/day was 0.07 for OBSV 6 $MgCl_2$ and 0.30 OBSV 9 SSW, at the 6th

day and 2nd day after brine change, respectively (Table 9). The fractured samples experienced a later onset of an increasing strain rate. The highest compaction rate/day were 0.05 for OBSV 4 AF-MgCl$_2$ and 0.09 for OBSV 12 AF-SSW, on the 7th and the 5th day after brine change respectively (Table 9). OBSV 18 AF-NaCl showed for comparison an average strain rate/day of 0.02 during Creep 2 (Figure 17).
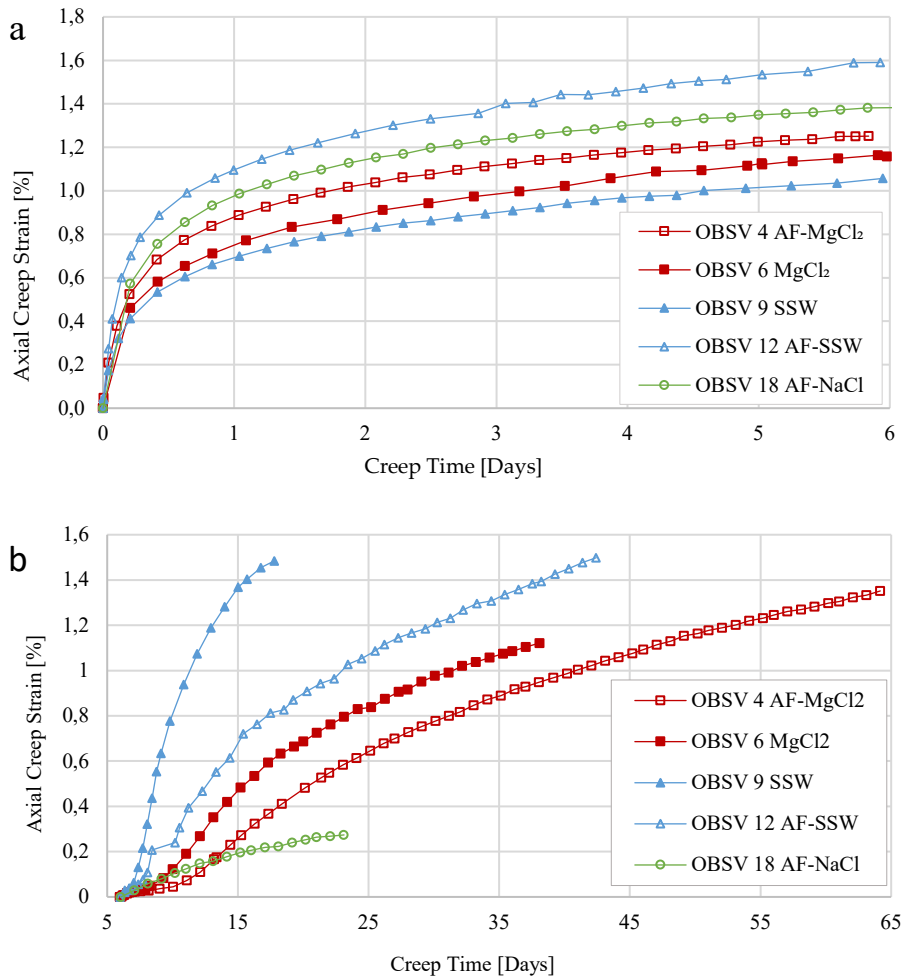
Figure 17) Axial creep strain for five OBSV samples, three samples with an artificial fracture and two unfractured reference samples. a) Primary creep phase (Creep 1) during injection of NaCl. b) Secondary creep (Creep 2) with injection of MgCl$_2$, SSW or NaCl.

47

Table 9) Maximum compaction rates given in [%]/day for five OBSV samples, and at which time the maximum creep-rate was identified given in days after brine change (Creep 2).

	Un-fractured		Artificially fractured		
	OBSV 6 $MgCl_2$	OBSV 9 SSW	OBSV 4 AF-$MgCl_2$	OBSV 12 AF-SSW	OBSV 18 AF-NaCl
Maxiumum creep rate [%] /day	0.07	0.30	0.05	0.09	0.02
Day after brine change	6	2	7	5	*

*The test continued with the same brine throughout the test.

5.2.2 Mineral dissolution and precipitation in artificial fracture flooded with MgCl₂

During the flooding test, the artificial fractures changed, and mineral precipitation took place. OBSV 4 AF-MgCl₂ was selected for in-depth analysis of the fracture and the adjacent regions (**Paper VI**). Calcite was dissolved along fracture wall, and precipitation of magnesite was identified in the artificial fracture by SEM-EDS (Figures 18 and 19).
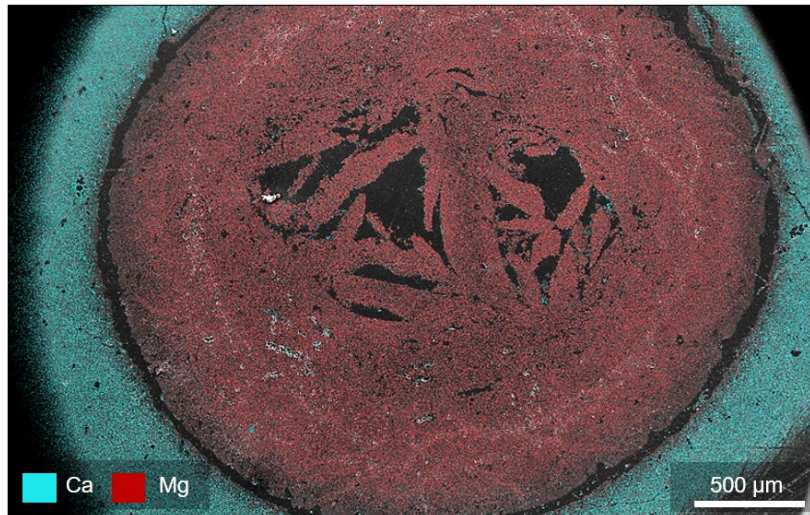
Figure 18) An SEM-EDS map acquired perpendicular to the flood direction, showing Ca (predominantly present in the matrix) and Mg (predominantly present in the fracture fill) distribution in an artificially fractured OBSV sample injected by MgCl₂ (OBSV 4 AF-MgCl₂).

Dissolution of calcite and precipitation of magnesite during $MgCl_2$ injection were documented by several methods. The effluent data obtained by IC supported Mg^{2+} retention and Ca^{2+} production throughout the test (Figure 4a in **Paper V**). Precipitation of magnesite was supported by XRD and TEM (Figures 5, 12 **Paper VI**). Trigonal shaped magnesite crystals were identified by SEM-EDS which frequently precipitated in the fracture along with a sheetlike mineral identified by TEM and interpreted as chlorite based on EDS (Figures 9, 11 **Paper VI**). Geochemistry results acquired from the fracture fill showed 41.1 Wt.% MgO and only 2.0 Wt.% CaO in the inlet slice (Appendix 8.1). The presence of CaO was linked to fragments and circular shapes of coccoliths. Additional elements identified were SiO_2, Al_2O_3, Fe_2O_3, and K_2O with concentrations of 8.8 Wt.%, 1.6 Wt.%, 0.8 Wt.% and 2.0 Wt.%, respectively. A chlorite-illite compound was frequently identified surrounding magnesite (Figure 19). The presence of magnesite and clay in the fracture fill, was supported by HIM-SIMS (Figure 10 **Paper VI**).
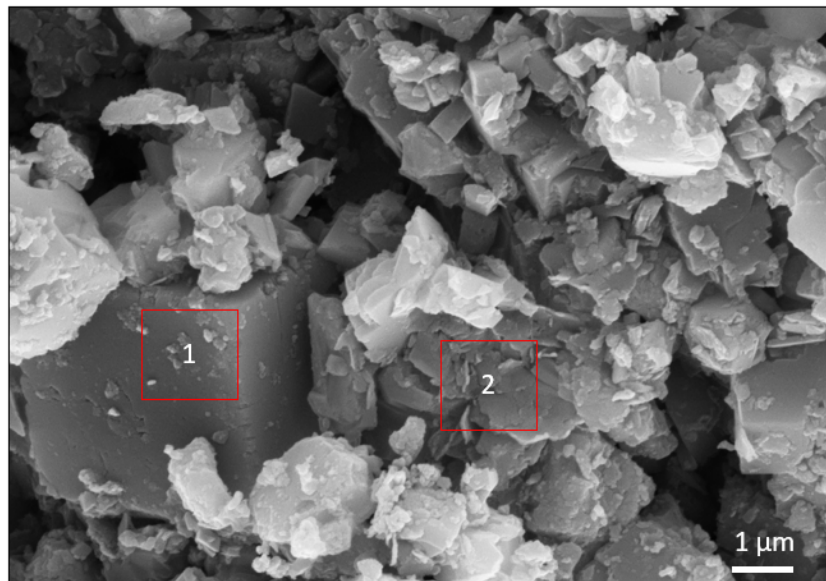
Figure 19) An SEM-SE image (OBSV 4 AF-MgCl₂ #3) acquired within the fracture fill showing a magnesite (1) and sheetlike clay possible chlorite (-illite) (2). Chemistry data is acquired within the area of the red boxes.

5.2.3 Aperture modification

All three artificially fractured samples experienced an aperture reduction. The fracture aperture diameters were reduced by 84 %, 76 %, and 44 % for OBSV 12 AF-SSW, OBSV 4 AF-MgCl$_2$, and OBSV 18 AF-NaCl flooded tests, respectively (Table 10). OBSV 12 AF-SSW showed complete closure of the fracture aperture for the first four slices (Figure 7, **Paper V**). The non-carbonate phase (chlorite-illite compound) cemented the central part of the fracture and measured approximately 1 mm in diameter (Figure 6, **Paper V**). Chlorite covered the inside surface of OBSV 18 AF-NaCl (Figure 6, **Paper V**). Aperture modification was not only linked to precipitation or dissolution, see discussion (6.3) for details.

Table 10) Average aperture reduction for three artificially fractured samples.

Sample	OBSV 12 AF-SSW	OBSV 4 AF-MgCl$_2$	OBSV 18 AF-NaCl
Average aperture reduction [%]	84	76	44

5.3 Surface characterization using HIM-SIMS

Precipitation of new minerals takes place on micron and sub-micron scale during seawater injection of chalk. A novel method was applied in this research project to test if the high-resolution HIM-SIMS can provide data which can help understand mineralogical alterations. The HIM-SIMS was able to determine the coccolith`s surface topography combined with its chemistry in-situ and is recommended as a supplementary method for chalk characterization on nanoscale (**Papers II, III**)

5.3.1 Chemical and textural identification of surface fragments in chalk

The HIM provided a high-resolution SE image (HIM-SE image) of a fresh surface chalk sample (OBSV 12.4 SSW) with detailed topographical features of the coccolith grains (Figure 20a). Single elemental maps from the same region of interest (ROI) were acquired using SIMS (Figure 20b–h).
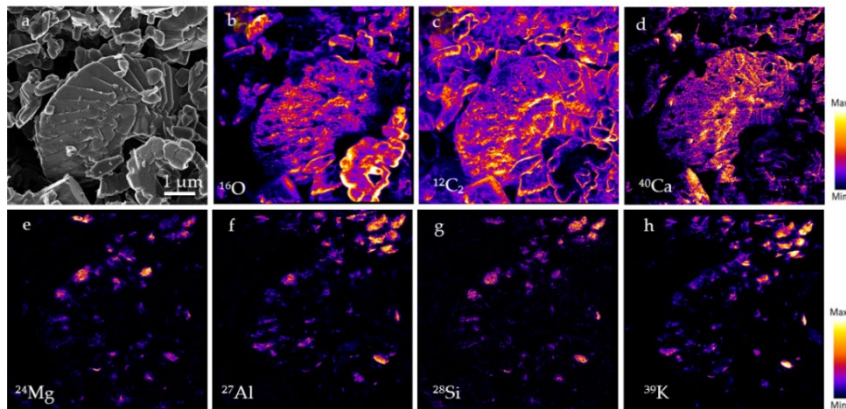
Figure 20) HIM-SIMS images of sample OBSV 12.4 SSW. (a) HIM-SE image of a ROI obtained by HIM focusing on a coccolith fragment. (b-d) Chemical images obtained by SIMS of ^{16}O, $^{12}C_2$, and ^{40}Ca are presented with a scalebar at the right, representing the intensity of each element. (e-h) Elemental distribution of ^{24}Mg, ^{27}Al, ^{28}Si, and ^{39}K.

Single elemental maps of ^{40}Ca, $^{12}C_2$ and ^{16}O were merged, to represent calcite ($CaCO_3$) distribution on the coccolith surface. ^{24}Mg, ^{27}Al, ^{28}Si, and ^{39}K were merged to represent the presence of clay (most probably chlorite-illite) coating the coccoliths surface. A HIM-SE image overlayed the merged single elemental SIMS maps of ^{24}Mg, ^{27}Al, ^{28}Si, and ^{39}K, allocated a red color which highlighted locations of clay coating the coccolith surface (Figure 20).
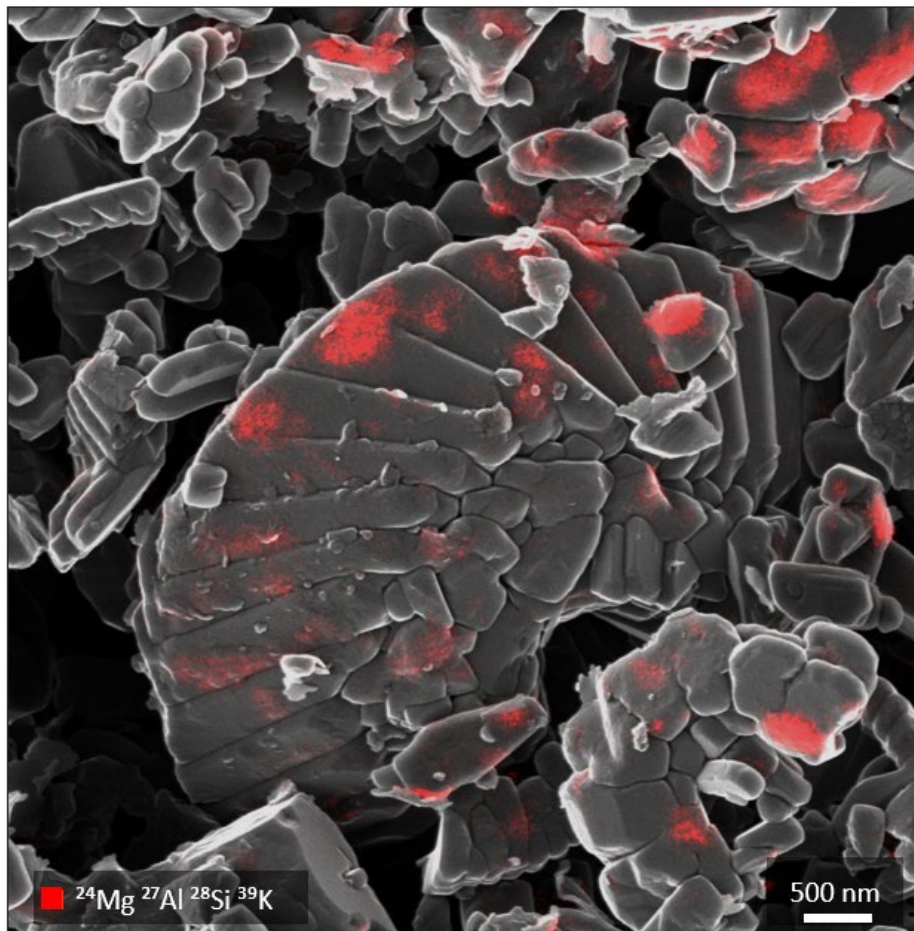
Figure 21) A combined HIM-SIMS map highlights the presence of clay on the coccolith surface (OBSV 12 AF-SSW #4). The distribution of ^{24}Mg, ^{27}Al, ^{28}Si, and ^{39}K were first assigned a red colour and then combined with the original HIM-SE image obtained by HIM.

5.3.2 *Quantification and distribution of surface clay*

HIM-SIMS acquisitions were performed on a coccolith plate from an unflooded OBSV chalk sample (see Chapter 4.4 for details). The aim was to link its topography with the distribution of single elements and thus quantify the distribution of non-calcite minerals (**Paper III**). HIM-SE images were acquired from different angles around the grain which allowed a 3D construction. Chemical data was acquired by SIMS at the same ROI and projected onto the 3D surface model to create a 4D surface reconstruction (Figure 22).
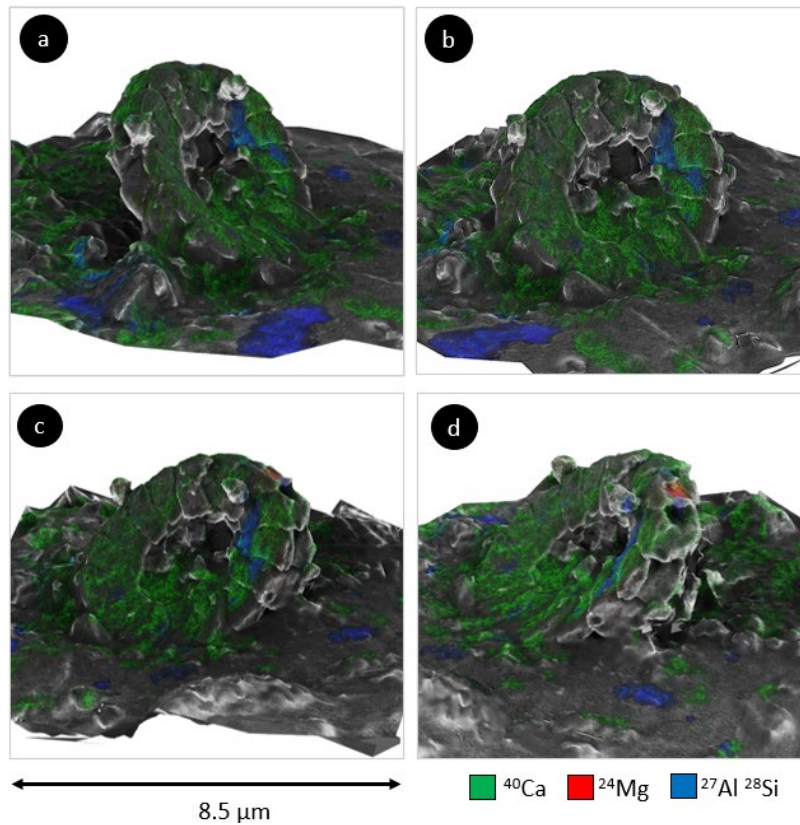
Figure 22) 4D surface reconstruction of the coccolith grain presented from different perspectives with azimuthal angles of 0°, 45°, 60° and 90° (a-d). ^{40}Ca is represented by green, ^{24}Mg by red and the ^{27}Al - ^{28}Si by blue.

The total number of pixels in the selected raw SIMS images was 512x512 which covered 72.25 μm² of the surface. The isotopes: ^{40}Ca, ^{24}Mg, ^{27}Al and ^{28}Si were identified. ^{40}Ca covered a total area of 89.8 %. In 46.1 % of the pixels ^{24}Mg, ^{27}Al, ^{28}Si, or all three elements were present. As each pixel can contain several ions, the data set is categorized into groups:

(i) ^{40}Ca (locations occupied by calcite only),
(ii) ^{24}Mg hotspot
(iii) ^{27}Al and/or ^{28}Si (locations without occupation of calcite)
(iv)   'mix' composed of ^{40}Ca and ^{27}Al/^{28}Si.

The mix (iv) covered 39.8 % of the area, while calcite (i) covered 50.0 % of the ROI (Table 11). ^{24}Mg hotspot (ii) was detected in 1.4 % of the pixels. Surface distribution calculations showed 6.3 % coverage by non-carbonate. The bulk geochemistry for unflooded OBSV showed around 5 Wt.% non-carbonate (Appendix 8.1).

Table 11) Relative surface distribution of detected elements with respect to the surface of the coccolith grain imaged in Figure 22 (the exact angle is provided in Figure 2, **Paper III**).

	Area	%
^{40}Ca only	50.00	%
^{24}Mg (dominantly present at hotspot)	1.40	%
^{27}Al and/or ^{28}Si (non-carbonate only/without occupation of calcite)	6.30	%
"Mix": ^{40}Ca and ^{27}Al and/or ^{28}Si (or all)	39.80	%
Locations with no detection (^{40}Ca, ^{27}Al, ^{28}Si, ^{24}Mg)	2.50	%
Total field of view	100.00	%

5.3.3 Characterization of manufactured calcite powder on nano scale

Data presented here is linked to Paper IV and Chapter 5.1 but have not been published in any of the papers. The data is presented to support mineral precipitation identified with the high resolution HIM-SIMS.

Surface characterization of single manufactured calcite grains was performed by HIM-SIMS. Four flooded samples were selected (Cal 1.1 $MgCl_2$, Cal 2.1D NaCl, Cal 3.1B SSW and Cal 6.1B $MgCl_2$ U.Eq) in addition to an unflooded reference. The HIM-SE images showed accumulations of sub-micron sized grains on the surface of Cal 1.1 $MgCl_2$ (Figure 23). These particles showed high intensities of ^{24}Mg. The surface of Cal 3B SSW and Cal 6B.1 $MgCl_2$ U.Eq showed ^{24}Mg in low intensities covering the surface. Patches of accumulated high ^{24}Mg signals were identified as nanosized magnesite nucleus. The low ^{24}Mg intensity coating the surfaces were remains of ^{24}Mg adsorption.
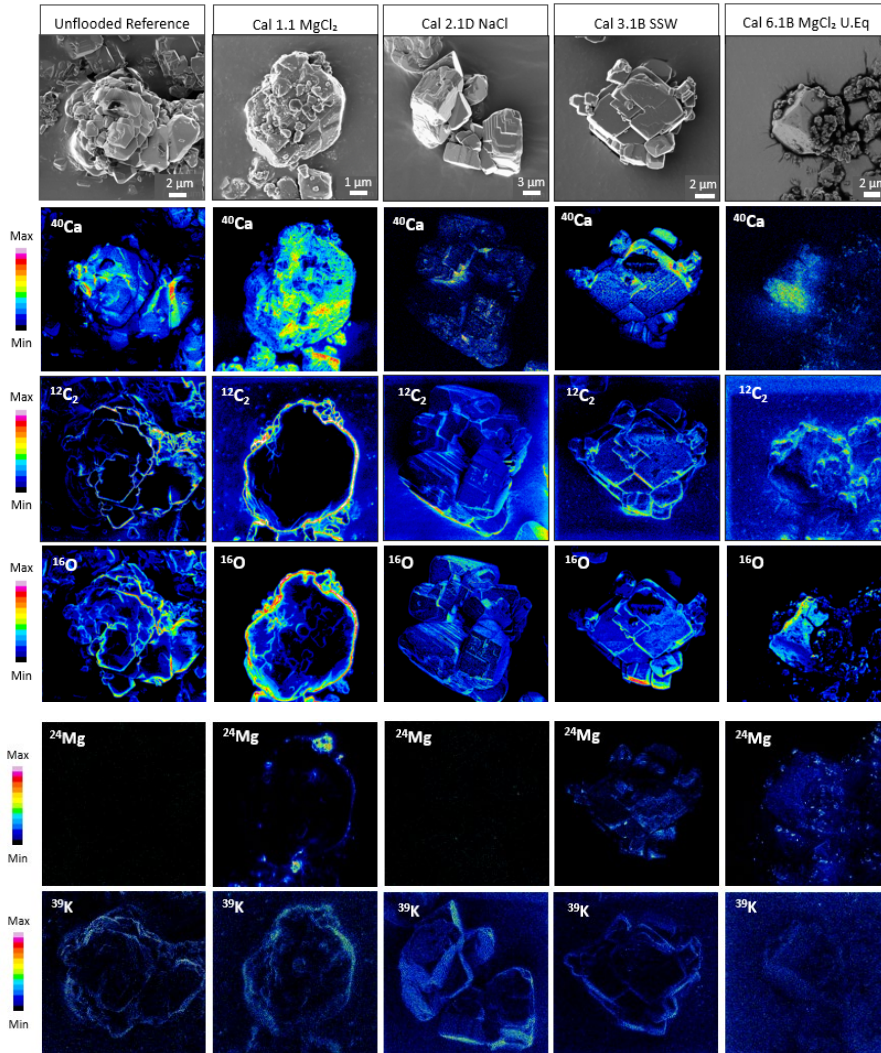
Figure 23) Distribution of single elements on the surface of flooded manufactured calcite presented in "fire-maps". Low distribution is represented by blue, gradually increasing to high distribution represented by red. The unflooded reference sample is presented in the left column, Cal 1.1 MgCl$_2$ in the second, Cal 2.1D NaCl in the third column, Cal 3.1B SSW in the fourth and Cal 6B.1 MgCl$_2$ U.Eq in the fifth. The data is not normalized. Cal 4F LowSal was not analyzed.

6   Discussions

Water weakening of chalk is a well-documented process during brine injection (Chapter 2.5). Routine experiments using triaxial cells have been performed at the University of Stavanger for decades where water weakening of chalk has been linked to properties as brine composition (Andersen et al., 2018; Heggheim et al., 2005; Korsnes et al., 2008; Korsnes et al., 2006a) and porosity. The role of non-calcite phases and fractures in reservoir chalk in IOR research has been underexplored. This research is one of the first approaches to link impurities and fractures in chalk with geo-mechanical response during brine injection (Figure 24). Despite using traditional in-house triaxial cell set-up (e.g., Andersen et al 2018 and references therein), the research implements novel approaches which implies certain experimental limitations (Chapter 6.1).
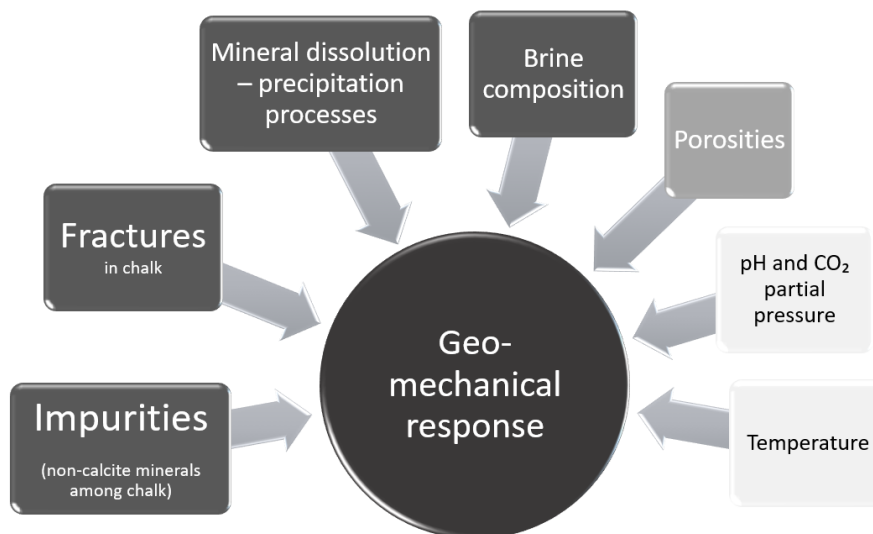
Figure 24) Properties and processes pointing to geo-mechanical compaction can impact strain during seawater injection. The discussion focuses on the properties as impurities (e.g., dolomite), fractures and mineral dissolution and precipitation in chalk as well as brine composition marked in dark grey. Porosities will also be mentioned as these are properties which significantly impact geo-mechanical processes but have not been highlighted as they are already well documented (light grey). pH and CO_2 partial pressure in addition to temperature are properties that impact these processes but are not the scope in this discussion (white boxes).

6.1 Study limitations

Statistical significance and repeatability in the experimental data are limited. Tests were repeated only a few times in the laboratory (due to time limitation), however these showed high repeatability. It needs to be considered that the experiments presented in chapter 5 were mostly pilot studies and first of its kind under reservoir conditions. The axial strain during loading for Cal 4 LowSal and Cal 4E LowSal showed very comparable responses with a strain of 10.3 ($\pm$ 0.04) % (Appendix 2 **Paper IV**).

6.1.1 *Manufactured calcite and milled natural dolomite versus natural chalk*

Manufactured calcite was used because natural chalk will always have presence of impurities to some extent. However, using pure manufactured calcite powder faces a few limitations when replacing natural chalk, which needs to be considered when comparing powder to natural chalk. The major properties of powder which are distinct from chalk, are associated with lack of consolidation and cemented grain contacts. Grain sizes, surface topography, and SSA of manufactured calcite and milled dolomite with natural origin may differ from coccoliths properties. Manufactured calcite is inorganic, but its valuable advantage is the homogeneous mineralogical composition. Adhesion forces are strongly dependent on surface topography. These properties may determine the total area available for brine-rock interactions and affect porosity, thus the total strain.

Natural chalk consists of biomineralized low-magnesium calcite (Rinderknecht et al., 2021). Biofilms, natural presence of MgO in biomineralized chalk, and presence of residual oil are properties that cannot be replicated using powders. Biogenetic calcite has a more negative surface charge than synthetic calcite, which is associated with adsorbed anionic organic matter on the surface (Madsen, 2015). The

presence of organic material on particle surfaces among chalk is suggested to modify the onset of dissolution (Hassenkam et al., 2011). Despite high purities for manufactured calcite (< 99 %), it may contain organic compounds associated with additives in the production for inhibiting crystal growth, thus enhancing nucleation. The use of additives varies between suppliers. The incorporation of organic compounds inhibit dissolution of manufactured calcite making it behave comparable to biogenic calcite (Hassenkam et al., 2011). Still, Hassenkam et al. (2011) showed in their laboratory experiment that modern and fossil coccoliths were both more resistant to dissolution than inorganic calcite. However, not all calcite particles in natural chalk are biogenetic. The relation between originally organic and secondary precipitation of inorganic cements is barely studied, maybe impossible considering the small grain sizes.

6.1.2 Temperature

All experiments have been executed under the same temperature of 130°C (realistic Ekofisk temperature), therefore mineral dissolution and precipitation kinetics allocated to temperature variations have not been highlighted. Temperature has been suggested to be a more important mechanism affecting calcite dissolution than the composition of the brine e.g., (Minde et al., 2018). An increased temperature will enhance the dissolution rate (Zahid et al., 2010). As the emphasis here is focused on the impact from the present mineralogy associated with the brine composition in brine-rock interaction processes, temperature effects have been granted a disproportionately small part in the discussion.

6.1.3 Artificial fractures in laboratory versus reservoir

Reservoir fractures (Chapter 2.4) may be associated with fractured surfaces caused by faulting where waterflow, compaction and sealing may develop differently than in artificially produced circular fractures of 2.25 (± 0.05) mm in diameter. The artificial hole was produced under

ambient conditions for the laboratory experiments. The nature of these fractures will differ from natural fractures, but the experiment was performed as a starting point for further studies on fractured chalk. Modification of the hole was not possible to monitor during the test. Pre-test diameters were compared to the post-test diameters. If the fracture aperture reduced during hydrostatic loading in the laboratory test or at which exact moment is not known. The main objective within this experiment, as mentioned above, was not upscaling of the results, but simple observations of mineralogical and geo-mechanical processes. Sound experimental set-ups can be developed for future research for the purpose of upscaling, which is obviously an important feature to resolve this issue.

6.1.4 Reservoir chalk versus outcrop samples

HIM-SIMS characterization was performed on outcrop samples of chalk, due to limited access of reservoir chalk. Reservoir chalk may have different mineral composition and distribution due to different diagenetic processes. Moreover, early incoming hydrocarbons in chalk at the NCS may have diminished diagenetic processes (Kallesten et al., 2021b). Therefore, IOR research on reservoir chalk is highly recommended if accessible.

6.2 Brine-rock interaction processes in pure and mixed mineralogical mixes - powder samples

The rationale behind experimenting with pure and mixed mineral samples is described in Chapter 1. Pure indicates single mineral samples composed of either dolomite or calcite. 'Mixed' powder samples have different ratios of dolomite versus calcite which are 5:95, 20:80, and 50:50 (Chapter 4). The following sub-chapters cover discussions of results and mechanisms related to strain during increasing stresses (Chapter 6.2.1), followed by a discussion of processes associated with different strain results during constant stress conditions in manufactured calcite (Chapter 6.2.2). Chapter 6.2.3 discusses the link between dissolution and precipitation of new mineral phases to the mineralogical composition of samples and the ion composition of the brine in mixed samples. A focus is laid on the most realistic sample which is aimed to represent Ekofisk. Then, in Chapter 6.2.4, the link between the mineral dissolution and precipitation processes discussed (Chapter 6.2.3) are associated with geo-mechanical responses. Surface energy is a property that impacts processes in the flooding experiments of powder especially. Analysis of surface properties was not the scope of thesis and has not been performed. A few terms used in the following discussion not previously introduced involving surface energy are briefly described in Table 12.

Table 12) Descriptions of terms used in discussion involving surface chemistry.

Terms	Descriptions
Adsorption	Adsorption is when atoms, ions, or molecules adhere to a surface. It adsorbs because of surface energy and creates a film on the mineral surface. The surface bonding depends on the crystal structure of the sample. The adsorption process is generally classified as physisorption (characteristic of weak van der Waals forces) or chemisorption (Dąbrowski, 2001). It may also occur due to electrostatic attraction.
Surface charge	Adsorption of ions creates an electrical surface charge. While all ions participate, their concentrations and different affinities for complexation (the covalent or non-covalent interactions between two or more compounds) determine the net surface charge, which can be positive, negative, or zero (Groenendijk and van Wunnik, 2021).
Disjoining pressure	Disjoining pressure comprises of three main types of repulsive and attractive forces including electric double layer, van der Waals and structural force (Adeyemi et al., 2023). Disjoining pressure is calculated by summing the three forces. Their magnitudes and directions depend on the surface properties of the rock as well as the composition of the brine.
Repulsion forces	Repulsion forces often refer to positive disjoining pressure (attractive forces are negative disjoining pressure). They are strong but short ranged forces between calcite surfaces attributed adsorption of water molecules (Røyne et al., 2015).
Zeta potential	Zeta potential is the electrical potential at the slipping plane diffuse (outer) layer (Derkani et al., 2019) This plane is the interface which separates mobile fluid from fluid that remains attached to the surface. The magnitude of the zeta potential indicates the degree of electrostatic repulsion between adjacent, similarly charged particles in a dispersion.
Potential determining ions	Ca^{2+}, Mg^{2+} and SO_4^{2-} that adsorb strongly onto the surface and control mineral surface charge (Derkani et al., 2019).

6.2.1 Stress-strain relationship in powder samples during loading from ambient to constant stress condition

Compaction rates reduced with increasing stress during loading of pure dolomite, pure manufactured calcite, and mixed powder tests (Figures 11a, 12a and 13a). This was interpreted to be associated with a rapid reorganization of unconsolidated grains and loss of porosity which consequently generated a stiffer sample. Compaction processes during the flooding experiments with powder showed therefore some

discrepancies from mechanisms normally observed for chalk (discussed in 6.1.1) (Fabricius, 2007).

Compaction during loading of stress is dependent on initial porosity. The axial strain identified during loading of the manufactured dolomite tests, showed in general lower compaction compared to calcite powder tests where axial strains were in average 5.6 % and 11.5 % for pure dolomite and pure calcite flooded tests, respecitvely (Table 4). This was associated with the different initial porosity which measured averagely 33.9 % and 55.5 % for dolomite and calcite samples, respectively (Table 4). The average porosities for mixed samples were 43.2 %, 51.1 %, 55.1 %, and the strains during loading were 6.7 %, 11.6 % and 11.9 % for the mixes of 5:95, 20:80 and 50:50 dolomite and calcite ratio respectively. The mixed samples of dolomite and calcite therefore demonstrated that the higher the initial porosity, the higher the compaction during loading proceeded. Water weakening of chalk is dependent on the porosity (Amour et al., 2021). The distinct initial porosities may further be related to different crystal size distribution. A wider range in grain size distribution is associated with a lower porosity (Fabricius et al., 2002). The grain size for powdered dolomite was averagely 16 µm, where 90 % of the grains were in the interval of 5-50 µm (Figure 8) and the most frequent grain size was around 10 µm with some abundant grainsize of 2 (± 1.5) µm for manufactured calcite (Figure 9). This supported the lower porosity of dolomite of 33.9 % versus 55.5 % for calcite samples.

Powder samples of pure and mixed mineralogy flooded under reservoir conditions showed a compaction rate with dependency on the brine composition. The high compaction observed for SSW during loading compared to NaCl and LowSal flooded samples for dolomite and mixed samples (Figures 11 and 13) can be associated with SO_4^{2-} adsorption to the mineral surface facilitating repulsive forces (Madland et al., 2011; Megawati et al., 2013). High-magnitude short range repulsive forces exist between calcite surfaces in presence of water (Røyne et al., 2015). AFM measurements of forces between mineral surfaces allow the effects

of surface forces to be isolated from possible competing mechanisms during compaction of chalk. Water weakening in chalk is a chalk-fluid interaction process where the strain depends on the strength of adsorption of the fluid molecules to the calcite surfaces (Risnes et al., 2003). These repulsion forces are normally correlated with water weakening of chalk (Megawati et al., 2013; Meireles et al., 2021; Risnes, 2001; Risnes et al., 2005; Røyne et al., 2011). The higher compaction observed during loading for SSW powder samples may be associated with the disjoining forces and reduced friction between particles (Meireles et al., 2019) allowing improved reorganization.

Adsorption of Mg^{2+} to calcite and dolomite mineral surfaces tends to have a comparable impact on compaction during loading of stress, like adsorption of SO_4^{2-} has, as just discussed. The two $MgCl_2$ flooded calcite samples (Cal 1 $MgCl_2$ and Cal 6B $MgCl_2$ U.Eq) showed higher axial strain than Cal 2D NaCl and the corrected axial strain (described in Chapter 5.1.2) for Cal 4F LowSal during loading (Table 4). Adsorption of Mg^{2+} to the calcite surface has potentially reorganized grains more efficiently, thus enhanced compaction during loading similarly as observed for SO_4^{2-}. The calcite surface can be positively or negatively charged (Madsen, 2015). Higher surface charge caused by adsorption of positive ions such as Mg^{2+} on the calcite surface will increase the disjoining pressure (Katika et al., 2018). NaCl and LowSal have, on the other hand, none or low concentrations of potential determining ions (PDI) in calcite powder samples can be associated with the lower strain during loading of stresses.

Adsorption of molecules present in a brine to mineral surfaces may not necessarily be related to chemistry and temperature alone but can also be dependent on surface geometry. Dol 3 SSW showed an initial loss of SO_4^{2-} which was higher than for Cal 3B SSW during the temperature increase before creep initiated (Figure 25). The loss of SO_4^{2-} from the injected fluid was retained in the samples. This could be linked to greater adsorption of SO_4^{2-} to the dolomite surface. Dolomite and calcite have

similar crystal coordination but have distinct surface geometries in the used pure powders for the presented experiment. Dolomite exhibited a rough topography whereas calcite displayed a more smooth and uniform surface texture (Figures 8a and 9a). Dominant mechanisms responsible for the surface charge are crystal structure (Pokrovsky et al., 2000), ion adsorption, and the electrical double-layer effect due to ionic strength (Groenendijk and van Wunnik, 2021). The lower adsorption of SO_4^{2-} to manufactured calcite surfaces than to dolomite mineral surfaces can be explained by the larger grain size and smoother grain surfaces of manufactured calcite powder than normally observed for chalk and coccolith fragments (Figure 10). Zeta potential measurements of dolomite surface have shown positive surface charge in presence of seawater. Of cations, Ca^{2+} had a significant effect on surface charge for dolomite, whereas Mg^{2+} was found to have a negligible effect (Mohammed et al., 2022).
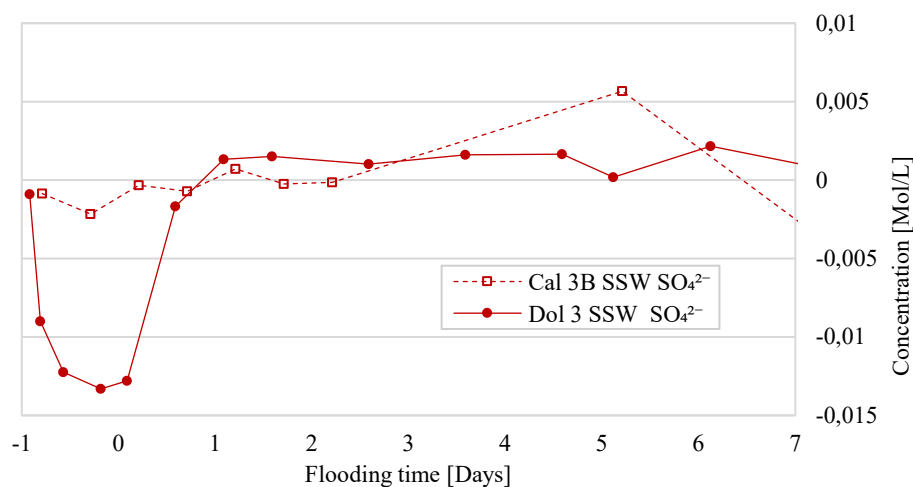
Figure 25) Deviation of the SO_4^{2-} concentration in the effluent from the original injected brines for samples Cal 3B SSW and Dol 3 SSW. The creep starts at time zero. The temperature increased the day before creep started (-1). The loss of ions during temperature increase is interpreted as ion adsorption as no new minerals were detected post flooding.

The processes observed for unconsolidated powder during loading was dependent on porosity, water chemistry, as well as the surface geometry

of the grains. This may not have any direct implication for subsidence during seawater injection in chalk reservoirs, as the grain contacts in chalk are potentially cemented. However, surface chemistry will play a role in plastic deformation when the stress condition surpasses the yield point, which will be specifically relevant for chalk with high porosity and low yield point.

6.2.2 Compaction of manufactured calcite powder samples during creep

The composition of the brine plays a key role for the compaction mechanism in unconsolidated calcite powder when flooded under constant stress condition. Surface complexation models have shown that divalent ions such as Ca^{2+}, Mg^{2+} and CO_3^{2-} have a significant impact on the surface charge. Na^+ and Cl^-, which are present in considerable concentrations in seawater, have negligible impact on surface complexation reactions (Groenendijk and van Wunnik, 2021). Interpretation of trends in compaction of powder under constant flow in triaxial cell experiments, may be divided in three different phases. The first phase is during loading stresses as discussed in 6.2.1. The creep (constant pressure) can be divided into two phases, where the first phase is interpreted to be controlled predominantly by surface chemistry (one to five days depending on brine composition) and the second phase is most likely dominated by dissolution and precipitation processes. The following subchapter focuses mainly on calcite samples flooded with $MgCl_2$ and NaCl to highlight the difference in these two creep phases when a sample is flooded with a PDI (Table 12) and an indifferent ion. Other pure calcite and dolomite samples not discussed in detail can be found in **Paper IV**. Processes observed in mixed powder samples are discussed separately in Chapters 6.2.3 and 6.2.4.

6.2.2.1   Compaction of calcite in the initial phase of creep

During the first three days of the creep, the two calcite samples injected with $MgCl_2$ showed low creep strain of 0.6 % and 0.9 % for Cal 1 $MgCl_2$ and Cal 6B $MgCl_2$ U.Eq, respectively. Adsorption of Mg^{2+} to the calcite surface created repulsive forces (Chapter 6.2.1) which inhibited additional compaction when the grains were already well packed, and the stress condition was stable. Cal 2D NaCl on the other hand, reached a significant strain of 6.4 % after the initial three days of the creep (Figure 12b) which ceased shortly after. The rapid compaction observed during the first three days may be attributed to the absence of cemented contacts combined with negligeable ion adsorption of Na^+. Since Na^+ is an indifferent ion, (Derkani et al., 2019; Pierre et al., 1990) it is therefore inactive at the calcite-fluid interface (Austad et al., 2015; Hiorth et al., 2010; Puntervold et al., 2015).

These observations for pure calcite samples flooded with NaCl and $MgCl_2$ showed partly comparable observations as identified for outcrop chalk the three first days (flooded under comparable conditions as powder samples). The outcrop chalk samples (different analogues to Ekofisk) flooded with $MgCl_2$ showed a rather low compaction from start reaching around 0.5 - 1.25 % strain during the first three days whereas five NaCl samples continued to compact (Andersen et al., 2018). The stagnating compaction for $MgCl_2$ and the continous compaction for NaCl flooded samples the first three days in powder and outcrop chalk are therefore comparable. The main difference between the outcrop samples analyzed in Andersen et al. (2018) and powder samples analyzed here, is the significantly higher compaction observed for the NaCl flooded powder samples. The different creep behaviour between powder and outcrop samples is interpreted to be associated with the absence of consolidated grain contacts in powder sample. As Na^+ is normally considered an indifferent ion (Pierre et al., 1990), it is commonly accepted that Na^+ is inactive at the calcite-fluid interface (Austad et al., 2015; Hiorth et al., 2010; Puntervold et al., 2015). Meireles et al. (2019)

showed that calcite powder settled in seawater (21°C), had 10 % higher porosity than calcite powder settled in inert fluid which supports that the presence of PDI in the settling phase help conserve porosity. They also argued that divalent ions present in seawater (Ca^{2+} and Mg^{2+}) lead to higher repulsive forces between grains whereas adsorption of SO_4^{2-} counteracts the initial positive surface charge, thus lowering the repulsive forces.

In a comparable study using analytical grade calcite powder under 150°C and with stress between < 20 – 40 > MPa, two samples injected with different compositions of brines were compared (Zhang et al., 2011). A solution of $CaCO_3$ (equilibrium) was mixed with 0.05 mol/L $MgCl_2$ and injected in one sample and a second sample was injected with a solution of $CaCO_3$ mixed with 0.5 mol/L NaCl. The authors in Zhang et al. (2011) suggested that the lower compaction identified for the sample with presence of Mg^{2+} had an inhibiting effect on intergranular pressure solution (IPS). Based on the interpretation in Zhang et al. (2011) it is possible that the released pressure on grain contacts could be associated with adsorption of Mg^{2+} causing repulsive force which therefore stagnated the IPS thus the compaction identified during the first three days (Figure 12b). The second sample flooded with NaCl in the study by Zhang et al. (2011) showed a significantly higher strain, in the order of 1-2.5, than for the sample with $MgCl_2$, which was in line with data identified for the NaCl flooded sample (Cal 2 NaCl) in this experimental set up. The experiments performed by Zhang et al. (2011) were predominately performed without flowing through the samples. This could have caused equilibrium with the sample thus prevented dissolution and precipitation processes. Nevertheless, the experiments performed here were tested under constant flow of brine through the samples allowing a continuous new supply of Mg^{2+}.

6.2.2.2 Compaction of manufactured calcite in creep after the three first days

After the first three days, the compaction rate for Cal 2D NaCl stabilized and almost ceased (Figure 12b). The absence of a continuous compaction rate is interpreted to be associated with the absence of dissolution and precipitation in the unconsolidated system. Nevertheless, the two $MgCl_2$ U.Eq flooded calcite samples showed an increasing compaction rate (Figure 12b). The increasing compaction is associated with dissolution of calcite and precipitation of magnesite; further discussed in Chapter 6.2.3. The increasing compaction rate for the $MgCl_2$ flooded sample was absent in the study performed by Zhang et al. (2011). The equilibrated $(CaCO_3)$ $MgCl_2$ brine, along with a near static test conditions could have caused equilibrium which prevented dissolution and precipitation processes.

The manufactured calcite sample flooded with SSW (Cal 3B SSW) experienced a rapid stagnation of the creep which almost ceased after about a day (Figure 12b). Due to surface charge and repulsive forces a rapid compaction commenced during loading (Chapter 6.2.1). During constant stress, repulsive forces may prevent IPS as discussed for Mg^{2+}. Due to the absence of constant dissolution and precipitation, further compaction did not commence which therefore supports processes discussed associated with presence of PDI and compaction associated with dissolution and precipitation.

6.2.3 *Mineral dissolution and precipitation associated with sample and brine composition in mixed mineral samples*

Mineral precipitation in mixed powder samples composed of dolomite and calcite flooded with $MgCl_2$ U.Eq or SSW showed with both brines surprisingly complex chemical processes, compared to those when pure

dolomite and pure manufactured calcite samples were flooded separately. Flooded pure dolomite powder showed in general insignificant chemical alterations independent of the composition of the brine injected which were identified by geochemistry (Appendix 8.12) and supported by IC (Figure 3, Paper IV). Magnesite was the only mineral that precipitated among all five calcite samples flooded with five different compositions of brine. The following two sub-chapters discuss mineralogical processes during injection of $MgCl_2$ U.Eq followed by SSW in pure and mixed mineral systems.

6.2.3.1 Mineral dissolution and precipitation during $MgCl_2$ U.Eq injection

Pure manufactured calcite showed precipitation of magnesite at the inlet for samples flooded with $MgCl_2$ (Cal 1 $MgCl_2$ and Cal 6B $MgCl_2$ U.Eq), which is commonly observed for outcrop chalk injected with $MgCl_2$ (Andersen et al., 2018; Minde et al., 2018; Minde et al., 2020). $MgCl_2$ injection into mixed compounds of dolomite and calcite caused significant chemical interaction e.g., higher concentration of Mg^{2+} retention than identified for pure manufactured calcite detected in effluent by IC (Figure 26). The highest exchange rates were in the order of 2-4 times higher for the two compounds with highest ratio of dolomite (Mix 1 50-50 $MgCl_2$ U.Eq and Mix 5 20-80 $MgCl_2$ U.Eq).
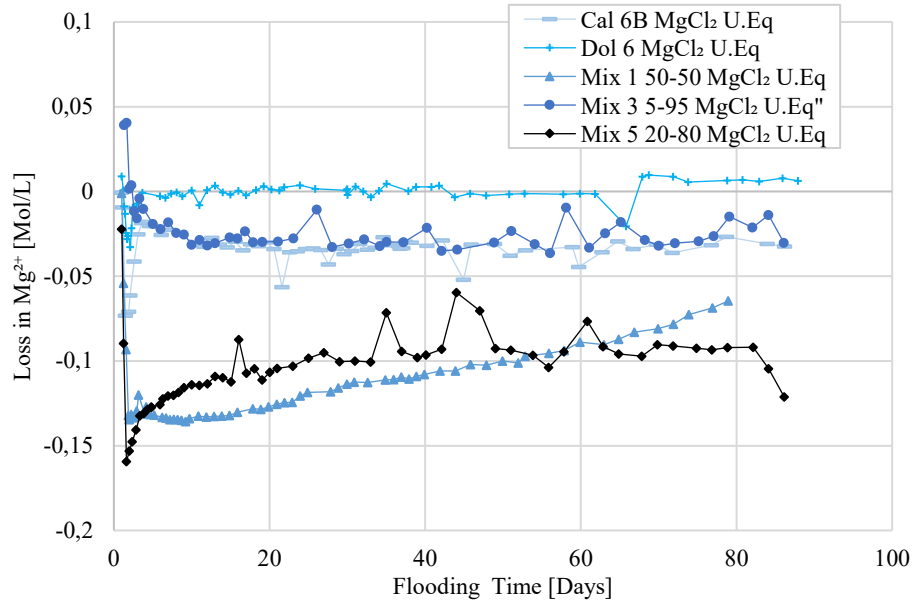
Figure 26) Deviation of Mg²⁺ concentration in the effluent from the injected concentration in five samples flooded with 0.219 mol/L MgCl₂ U.Eq.

Precipitation of magnesite and high-magnesium calcite (Figure 27) justified the significant loss of Mg^{2+}. It has been suggested that precipitation of high-magnesium calcite will only occur if the Mg^{2+}/Ca^{2+} ratio is low (< 0.2) (Abdollahpour et al., 2022). Based on the hypothesis stated in Abdollahpour et al. (2022), it may imply that precipitation of magnesite in the inlet slice (and dissolution of calcite) of mixed samples flooded with MgCl₂, reduced the Mg^{2+}/Ca^{2+} ratio in the solution; and subsequently allowed only high-magnesium calcite to precipitate towards the outlet of the samples. High-magnesium calcite was not identified in the pure calcite and dolomite samples flooded separately, and only in traces for Mix 3 5-95 MgCl₂ U.Eq (Figure 27). This indicates that the precipitation of high-magnesium calcite is also dependent on the magnesium concentration bound in the present mineralogy. High-magnesium calcite was not identified when MgCl₂ U.Eq was flooded in neither of the pure samples of dolomite and calcite (Dol 6 MgCl₂ U.Eq and Cal 6B MgCl₂ U.Eq).

71
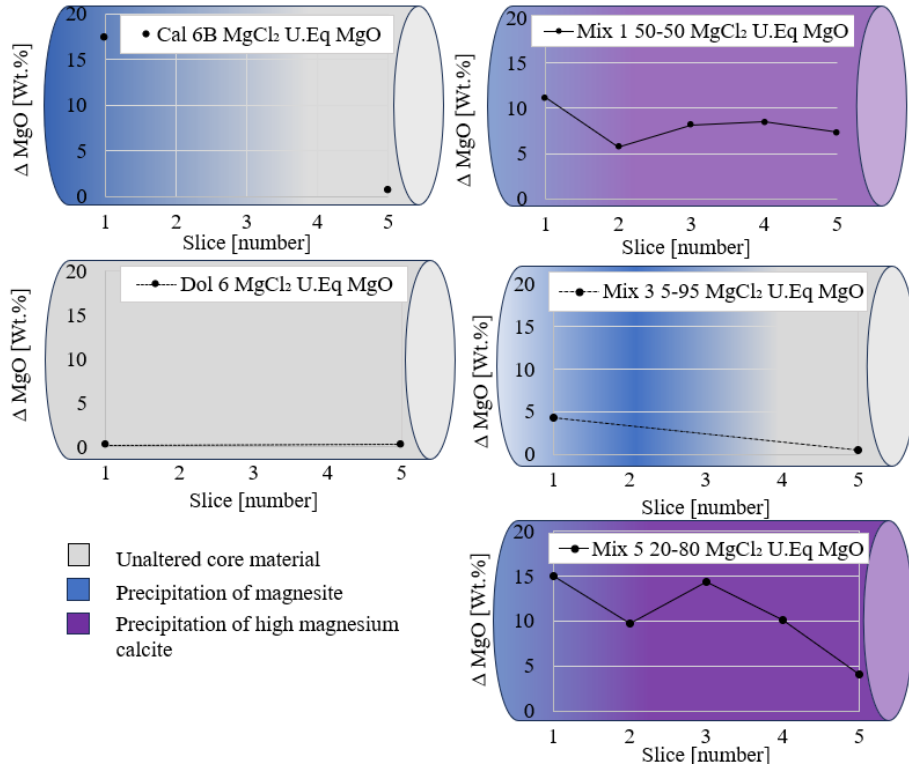
Figure 27) Visualization of mineral distribution for five samples flooded with MgCl₂ U.Eq. The samples are presented with the deviation of MgO in Wt.% from pre-test concentrations throughout the cores based on ICP-MS. The visual distributions represented by colors are based on identification and interpretations of additional data as SEM-EDS and XRD (Appendix 3, **Paper IV**). Slice one is inlet and five is outlet (Chapter 3.1)

6.2.3.2 Mineral dissolution and precipitation associated with SSW injection

Pure manufactured calcite (Cal 3B SSW) showed interestingly no significant chemical alteration when flooded with SSW (Figure 28). Coccoliths in chalk being millions of years old, are normally not significantly dissolved or recrystallized. Based on the theory of Ostwald ripening (Voorhees, 1985) calcite particles are expected to merge and grow into larger particles over time (Japsen et al., 2011). Absence of

merging and growing calcite particles in the powder experiment can be associated with organic inhibitors (Zhang and Spiers, 2005).

In mixed samples with dolomite and calcite, two minerals precipitated during SSW injection: (i) anhydrite ($CaSO_4$) and (ii) aragonite ($CaCO_3$). These minerals were, however, not identified in dolomite and manufactured calcite samples flooded separately with SSW. Anhydrite precipitated in small quantities in mixed samples flooded with SSW. The higher the dolomite concentration in the sample, the more anhydrite was detected (Table 6, Figure 28). It was suggested that anhydrite precipitated in Liège chalk flooded with SSW (Madland et al., 2011; Madland et al., 2008). Outcrop chalk from Liège had a non-carbonate concentration of around 2.5 Wt.% and possible traces of dolomite (Andersen et al., 2018). Precipitation of anhydrite (in general) might be associated with presence of dolomite or other impurities among chalk given the presence of SO_4^{2-} in the brine, because anhydrite did not precipitate when dolomite and manufactured calcite were flooded separately (Figure 28).

Besides precipitation of anhydrite in mixed samples flooded with SSW, aragonite precipitated predominantly in the Mix 4 5-95 SSW despite a short test duration of only 4 days. The test stopped when it was no longer possible to inject brine through the sample. The crystal sizes of the new grown aragonite ranged typically between 5 to 20 μm. Less abundant and smaller aragonite crystals which measured up to a maximum of 5 μm were observed in Mix 6B 20-80 SSW. Aragonite was not identified in Mix 2 50-50 SSW. Aragonite seemed therefore more prone to precipitate in low ratios of pure dolomite to pure calcite and did not precipitate when dolomite and calcite were flooded separately. Kinetics of aragonite precipitation is controlled by Mg^{2+}/Ca^{2+} ratio in brine, where low ratios will favor calcite precipitation and brine with higher ratios will dominantly favor aragonite (Morse et al., 1997). Above a given saturation (i.e. $\Omega c >/ 2.6$) at 25°C, aragonite precipitates more rapidly than calcite (Zhong and Mucci, 1989). The temperature in this study was,

by contrast, 130°C. An increasing accumulation of aragonite (interpreted based on SEM-EDS and XRD data) towards the outlet in Mix 3 5-95 MgCl$_2$ U.Eq (Figure 28) may indicate a change in the Mg^{2+}/Ca^{2+} ratio in the brine while being transported through the sample.
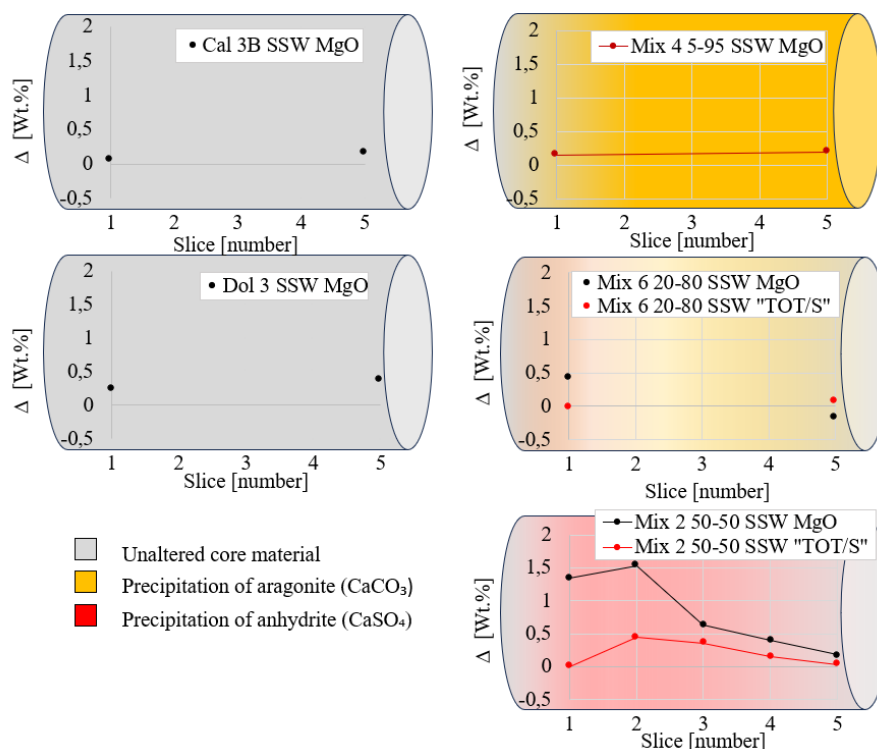
Figure 28) The sketch visualizes presence of new mineral phases in five powder samples flooded with SSW presented with a change in Wt.% of MgO and TOT/S identified by ICP-MS. The darker the coloring the higher the estimated amount of the precipitated mineral. The color saturation is not accurately scaled. The presented distribution presented by color grading is based on identification and interpretations of SEM-EDS, XRD, in addition to ICP-MS results. Slice 1 is the inlet and 5 is outlet.

A ratio of 5-95 Wt.% dolomite to calcite within the carbonate fraction in reservoir chalk at Ekofisk is realistic (Kallesten et al., 2021b). The powder sample with this composition (Mix 4 5-95 SSW) exhibited precipitation of aragonite (Figure 14, Figure 13 **Paper IV**). The Ca^{2+} concentration in SSW is not higher than 0.013 mol/L (Table 2) which

cannot ascribe the significant precipitation. Additionally, ion chromatography results showed Ca^{2+} excess in the effluent for Mix 4 5-95 SSW (Figure 11a **Paper IV**) indicating dissolution of calcite. The kinetics of calcite dissolution are rather fast, and the equilibration time for calcite dissolution is in the order of seconds thus limited to the surface of grains and immediate to injection (Hao et al., 2020). The instant dissolution close to the inlet may be associated with precipitation further into the sample (Figure 28).

The 'realistic' sample (Mix 4 5-95 SSW) showed a rapid dissolution of calcite in the laboratory experiment. If properties of the powder calcite-dolomite mix are comparable to reservoir chalk, then it may indicate that seawater injection in chalk with a 5 % dolomite could release more oil from the reservoir. Hassenkam et al. (2011) suggested that organic material present among biogenic calcite inhibited dissolution of calcite in conditions where calcite would normally dissolve, as previously discussed. Japsen et al. (2011) argued that recrystallization of calcite in the North Sea chalk is inhibited most likely by an organic component. Despite different properties, calcite may be vulnerable for dissolution in the reservoir attributed to the presence of dolomite during seawater injection. Hiorth et al. (2010) suggested that calcite dissolution could be a controlling factor for increased oil recovery. The authors based their interpretation on experimental studies using pure Stevns Klint outcrop chalk and argued that the surface potential changes (spontaneous imbibition) could not explain the observed increases in oil recovery. Moreover, calcite dissolution may improve pore connectivity thus increasing the permeability (Gachuz-Muro et al., 2017). However, the precipitation of aragonite can reduce permeability, which in turn may reduce production rates.

6.2.4 Compaction associated with mineral dissolution, precipitation, and distribution

Flooding experiments using mixed mineral compounds flooded with different brines showed more complex chemical interaction compared to mineral systems flooded separately (Chapter 6.2.3). These complex chemical processes were on a few occasions reflected in geo-mechanical responses. The following chapters discuss the link between geo-mechanical response associated with precipitation of new minerals (Chapter 6.2.4.1) and how the presence of dolomite impact precipitation and strain (Chapter 6.2.4.2).

6.2.4.1   Geo-mechanical response associated with precipitation of minerals when flooding with SSW

Precipitation of anhydrite may be associated with a higher strain in unconsolidated samples. The highest axial strain observed under constant stress for the five SSW flooded powder samples was Mix 2 50-50 SSW which compacted 4.2 % whereas the other four samples flooded with SSW showed final axial strains ranging between 1.1 % and 1.6 % (Figure 29). The final axial strains were not dependent on the initial porosity as Mix 2 50-50 SSW had the next lowest initial porosity of 44.4 % (Table 4). The higher compaction observed for Mix 2 50-50 SSW may be associated with precipitation of anhydrite. The reason for inducing a higher axial strain is here not fully understood, but it indicates that porosity alone is not the major factor determining compaction in unconsolidated samples. Andersen et al. (2018) suggested that reprecipitation of Si-bearing minerals advances the dissolution of calcite in chalk. However, in this experiment silica is absent. Dissolution of calcite in unconsolidated samples did not cause increased compaction (see Mix 4 5-95 SSW, Figure 29). The absence of increased strain during calcite dissolution could be associated with absence of cemented grain contacts in the powders. However, more experimental work needs to be done in this field to define clear trends based on a larger data set.

Precipitation of aragonite in mixed powders flooded with SSW did not seem to impact geo-mechanical response in powder samples. Mix 4 5-95 SSW, as previously mentioned, is the most 'realistic' mineralogical composition for some chalk reservoirs at the NCS with up to 5 % dolomite (Kallesten et al., 2021b), and this sample showed comparable compaction as observed for pure calcite powder (Cal 3B SSW). The dissolution of calcite and precipitation of aragonite was interpreted to have negligible effects on compaction in unconsolidated samples (Figure 29). However, a potential dissolution of calcite in reservoir chalk could have other consequences, such as weakening or the reservoir may suffer from a reducing permeability attributed to the precipitation of aragonite which may possibly migrate and clog pores.
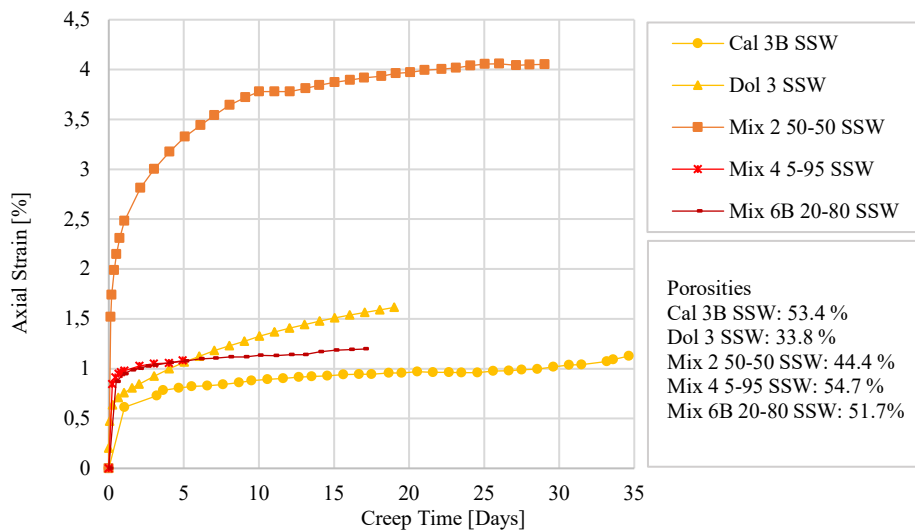
Figure 29) Compaction during creep for five pure and mixed mineral samples flooded with SSW under constant reservoir conditions resembling Ekofisk.

6.2.4.2 Geo-mechanical response associated with mineral distribution and precipitation of minerals throughout the sample when flooded with MgCl₂ U.Eq

It is possible that the uniform distribution of dolomite throughout the core controls compaction, in addition to precipitation of new minerals. The three mixed samples flooded with MgCl₂ U.Eq. showed axial strains ranging between 5.7 % - 7.0 % which exceeds the compaction identified for pure dolomite and pure calcite samples flooded separately, with only 2.9 % and 4.3 % axial strains for Dol 6 MgCl₂ U.Eq for Cal 6B MgCl₂ U.Eq, respectively (Figure 30). The higher compaction rates for mixed mineral samples during the primary week may be attributed the superior Ca^{2+} excess and Mg^{2+} retention in the effluent which was 2-4 times higher than for pure calcite (Figure 26). The significant compaction included also Mix 3 5-95 MgCl₂ U.Eq. This sample showed comparable Ca^{2+} excess and Mg^{2+} retention as observed for Cal 6B MgCl₂ U.Eq (Figure 26) and magnesite precipitation (Appendix 3, **Paper IV**). The significant compaction observed the first week is therefore predominantly associated with the presence of dolomite throughout the samples. After three weeks the compaction rate decreased and nearly ceased for Mix 1 50-50 MgCl₂ U.Eq (Figure 30). Despite of an almost completely flattened creep for Mix 1 50-50 MgCl₂ U.Eq, it still showed higher excess Ca^{2+} and retention of Mg^{2+} excess in the effluent than observed for Cal 6B MgCl₂ U.Eq. The absence of compaction despite dissolution of calcite may be allocated to the significant precipitation of magnesium-rich minerals throughout the sample. The precipitation eventually cemented grain contacts enhancing the mechanical strength. This process strengthened the sample core thus prevented further compaction despite of on-going dissolution of calcite. Moreover, Mix 1 50-50 MgCl₂ U.Eq preserved the highest porosity (Table 4) of the five samples flooded with MgCl₂ U.Eq (Figure 26).
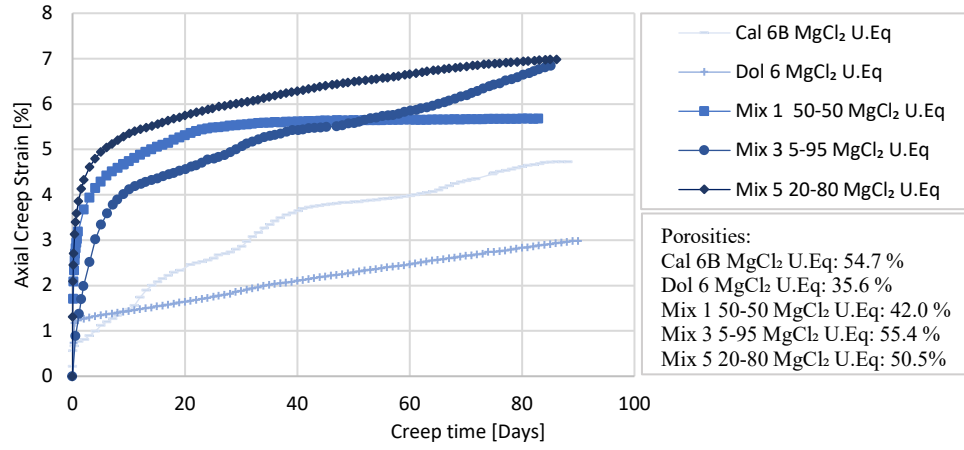
Figure 30) Compaction during creep for five powder samples flooded with MgCl₂ U.Eq under reservoir conditions resembling Ekofisk.

6.3   Water weakening and aperture modification in fractured chalk

Three artificially fractured outcrop samples were flooded under reservoir conditions with different compositions of brines which were compared to two intact samples without artificial fractures. The rationale behind this approach is described in Chapter 1. Sample preparations are described in Chapter 3.1 and sample material in Chapter 4.5. Detailed descriptions and results can be found in **Paper V** and **Paper VI**. The following sub-chapters cover discussions of results and mechanisms behind precipitation of minerals in the artificial fractures and how this may be associated with the brine composition (Chapter 6.3.1). Chapter 6.3.2 covers a discussion related to mechanical responses associated with the artificial fracture which is dependent on the composition of the brine injected and the test duration. Chapter 6.3.3 covers a discussion of how sealing (Chapter 6.3.1) and water weakening mechanisms (Chapter 6.3.2) impact aperture modification. Possible consequences for fractured chalk reservoirs injected with seawater are also discussed.

6.3.1   Sealing of fracture apertures

Artificially fractured samples reduced the fracture aperture during the flooding experiment under reservoir conditions (Table 10). A chlorite compound occasionally intermingled with illite was identified in all three fractured samples within the fracture fill (OBSV 4 AF-MgCl$_2$, OBSV 12 AF-SSW, OBSV 18 AF-NaCl). Brine-rock interaction processes contributed to formation of cement in the artificial fracture apertures. The three artificial fractured samples showed distinct composition and quantity of the cement/precipitation. Chlorite was most abundant in OBSV 12 AF-SSW where it cemented and sealed the fracture aperture (Figure 6 **Paper V**). It was also identified in the fracture of OBSV 18 AF-NaCl, but the extent was limited to covering the inside fracture surface (Figure 6 **Paper V**). Chlorite was also identified intermingled with illite among the precipitate mixture (dominated by magnesite) in the

fracture fill of OBSV 4 AF-MgCl$_2$, interpreted by data acquired by XRD, SEM-EDS, TEM-EDS, and HIM-SIMS (Figures 4, 6i, 10, and 9 respectively in **Paper VI**). Thus, all samples exhibited precipitates of chlorite (-illite), independent of the brine injected. The precipitation had to be sourced from the non-carbonate minerals present in the matrix, since elements as Fe, Si and Al were not present in the injected brines (Table 2). Chlorite is a diagenetic mineral that may coat grains or fill and cement pores (Laczkó-Dobos et al., 2020). It can typically occur in stylolites in green color bands along with smectite and opal-A (Fabricius and Borre, 2007).

In addition to chlorite (-illite) precipitation, OBSV 4 AF-MgCl$_2$ experienced multiple chemical processes which caused a final reduction of the aperture with an average reduction of 76 % for all slices (Table 10). These processes were associated with both decreasing as well as increasing the final fracture aperture (Figure 31a). The contribution of increasing the aperture for OBSV 4 AF-MgCl$_2$ was attributed to the dissolution of calcite along the fracture wall (Figure 3 **Paper VI**). The major dissolution-precipitation commenced along the fracture wall because the brine was dominantly transported through the fracture (further discussed in Chapter 6.3.2). Precipitation of magnesite in addition to the chlorite (-illite) in the fracture contributed to sealing the rock. Precipitation of magnesite is commonly detected when injecting MgCl$_2$ in chalk and calcite (Minde et al., 2019).

Calcite precipitation was not observed in any of the three artificially fractured OBSV samples. Calcite present within the fracture fill in OBSV 12 AF-SSW and OBSV 18 AF-NaCl (Figure 31) was sourced from the matrix and further discussed in Chapter 6.3.3.

Cementing and sealing will contribute to reduced apertures in the reservoir. Fracture connectivity may be reduced by closing small fractures and narrow tips of fractures in addition to the cement reducing the overall open-fracture length (Philip et al., 2005).
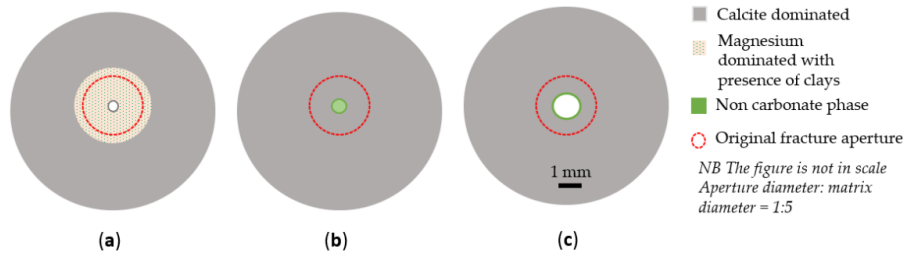
Figure 31) The sketch simplifies aperture modification and mineralogy in a cross-section for the three artificially fractured cores. All samples represent the third slice, where the apertures were most significantly reduced. The red circle symbolizes the original aperture size. a) OBSV 4 AF-$MgCl_2$, b) OBSV 12 AF-SSW, c) OBSV 18 AF-NaCl.

6.3.2 Mechanical resilience and presence of fractures

Flooding artificially fractured samples and unfractured matrix samples (for reference purpose) in laboratory experiments using triaxial cells indicated in this study that the creep behaviour is affected by the presence of fractures. A significantly higher compaction for artificially fractured samples than unfractured matrix samples was observed using NaCl brine during the first week of the experiment called "Creep 1" (Figure 17a). There was however not a significant difference before the samples reached hydrostatic yield (Figure 2 **Paper V**).

The effect of changing the brine composition to $MgCl_2$ or SSW during "Creep 2" (after Creep 1 when the composition of the injected brine had been changed), highlighted the water weakening associated with the brine composition in line with observations normally observed in water weakening experiments (Andersen et al., 2018; Kallesten et al., 2021a; Korsnes et al., 2006a; Madland et al., 2008; Minde et al., 2018; Nermoen et al., 2016). The creep behaviors changed when entering Creep 2 (Figure 17). The water weakening effect on the matrix sample flooded with SSW (OBSV 9 SSW) was 0.30 %/day the 2nd day after the brine change (Table 9). Whereas the artificially fractured sample flooded with SSW (OBSV 12 AF-SSW) showed a maximum compaction rate of 0.09 %/day the 5th day after the brine change. A comparable delay with less significant

compaction was also observed for the $MgCl_2$ injection samples where the maximum compaction rates were 0.07 %/day and 0.05 %/day after the 6th and 7th day after the brine change for OBSV 6 $MgCl_2$ and OBSV 4 AF-$MgCl_2$, respectively (Table 9). The delayed onset of increased compaction for artificially fractured samples observed, supported that the fracture acted as the main highway for the injected brine, with restricted flow of brine into the matrix. The effluent data supported this interpretation of brine flowing through for artificially fractured samples. Almost instantly (hours) after the brine changed from NaCl to either $MgCl_2$ or SSW, the new concentration of the injected brine was identified in the effluent. The un-fractured samples showed in contrast traces of the concentration of the new brine in the effluent after one day, which is in line with one pore volume a day (Figures 4, 5 **Paper V**). Nevertheless, a significant increase in compaction was observed for artificially fractured samples after the brine change (OBSV 12 AF-SSW and OBSV 4 AF-$MgCl_2$), compared to sample OBSV 18 AF-NaCl which is expected to experience minimal water weakening. The artificially fractured samples (OBSV 12 AF-SSW and OBSV 4 AF-$MgCl_2$) must have experienced water weakening despite that the fractures transported most of the brine. The water weakening that was present for the fractured samples, indicates that water molecules also reached the matrix, later than for unfractured samples (Figure 17).

Despite less significant and delayed compaction for artificially fractured samples observed during Creep 2 (Figure 17), an extrapolation of the creep indicated that over time the fractured samples may experience a compaction beyond the unfractured samples (OBSV 6 and OBSV 12) (Figure 32). A complete description of methods used for extrapolation can be found in (Madland et al., 2006). The extrapolation is calculated for a long period, which may weaken the strength of the interpretation, but there is a clear trend. Moreover, the main point here is to discuss the possibility that the final axial strain for artificially fractured samples may surpass the axial strain observed for intact samples. If artificially

83

fractured samples over time show a higher compaction than unfractured samples, it would be associated with the presence of the void space in fractures reducing the overall mechanical resistance. This interpretation would then be in line with axial strain observed during Creep 1 under NaCl injection, where the artificially fractured samples showed significantly higher axial strain than unfractured samples. If samples with artificial fractures will surpass compaction over time, can only be verified in future laboratory experiments that last for a minimum of 6-12 months with the same set-up as used here.
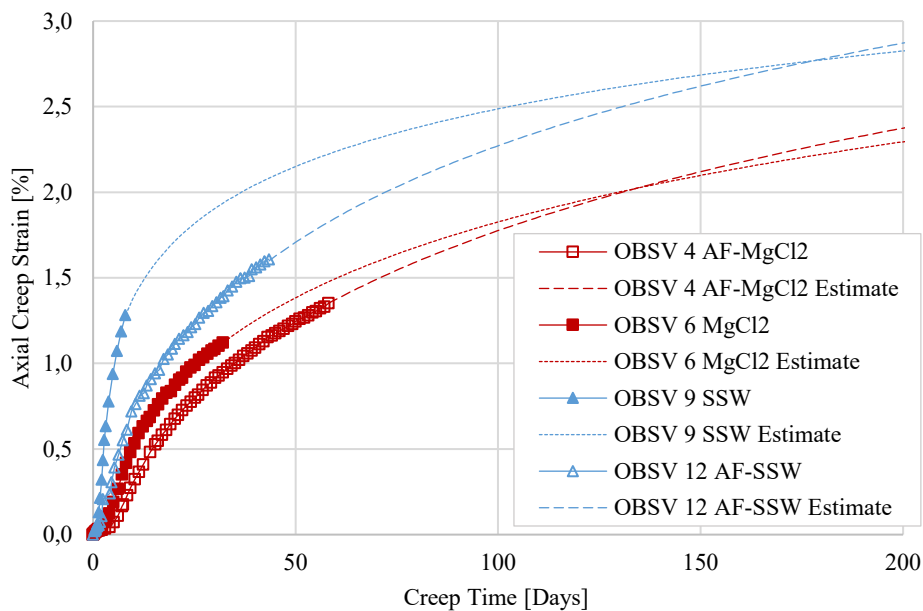
Figure 32) Extrapolation of axial creep strain for four samples whereof two had an artificial fracture and two were intact samples flooded for reference purposes.

A delayed water weakening process was as discussed identified for the fractured samples compared to unfractured samples during brine injection in this laboratory experiment. This could imply a more rapid compaction in the Lower Ekofisk Formation at Ekofisk which is

characterized by small scaled discontinuities (Boersma et al., 2020). Additionally, it is possible that the Lower Ekofisk Formation may become stable at an earlier stage than a formation with larger tectonic fractures which may experience a later onset of water weakening and potentially experience a totally higher compaction. Improved understanding providing more accurate predictions may help increase wellbore stability and avoid drilling challenges in the shale overburden related to subsidence at for instance Valhall (Kristiansen and Flatebø, 2010). However, this speculative up-scaling is important but needs substantial data and modelling techniques. This study is, nevertheless, a first step in this direction.

6.3.3 Processes controlling aperture modification in chalk during brine injection and possible consequences for permeability

Integrating data from mechanical and chemical processes within the laboratory experimental results implies that there are several mechanisms that alter the fracture aperture during brine injection. The following chapter discusses the link between aperture reduction and total strain for three compositions of brine.

All three samples experienced a fracture aperture reduction which measured 84 %, 76 %, and 44 % for OBSV 12 AF-SSW, OBSV 4 AF-MgCl$_2$, and OBSV 18 AF-NaCl tests, respectively (Figure 31) as discussed (Chapter 6.3.1). Matrix materials (coccolith platelets and fragments) were identified within the original aperture in two artificial fractures. The volume of matrix material identified within the original fracture was most significant for OBSV 12 AF-SSW but was also observed within OBSV 18 AF-NaCl. The presence of matrix material in the original aperture indicated that matrix was forced into vacant spaces (Figure 6 **Paper V**). The total axial strains (loading, Creep 1 plus Creep 2) were 4.16 %, 3.41 % and 2.51 % for OBSV 12 AF-SSW, OBSV 4

AF-MgCl$_2$, and OBSV 18 AF-NaCl respectively (Figure 33). The main mechanism of fracture aperture reduction was interpreted to be associated with water weakening. Grain contacts that weakened during brine injection (Chapter 2.5) must have facilitated grain sliding forcing coccoliths and fragments into the void space inside the fracture. The higher the identified strain, the more prominent was the aperture reduction (Figure 33). The sealing, discussed in Chapter 6.3.1, caused additional reduction of the fracture aperture by accumulation of minerals. The contribution to aperture reduction caused by sealing is roughly estimated by black arrows, indicating that MgCl$_2$ contributed more to the sealing than SSW (and NaCl).

For an ideal comparison, tests could have been performed with the same test duration. However, the experiments had different durations (42 days, 64 days, and 23 days for OBSV 12 AF-SSW, OBSV 4 AF-MgCl$_2$, and OBSV 18 AF-NaCl, respectively). Sealing processes are dependent on the injected volume of brine, which is therefore a time dependent process. Since strain versus aperture reduction here showed a strong link, different duration may not significantly impact the interpretation. It is expected that the base line for OBSV 18 AF-NaCl with a longer test duration would be unaltered as the main mechanism for this reference is only linked to strain versus aperture reduction with negligible sealing effect. A longer test duration could have shown a larger deviation from the green baseline indicated by the rate of increase shown by a blue and a red stippled line representing the rate of sealing associated with the rate of compaction for OBSV 12 AF-SSW and OBSV 4 AF-MgCl$_2$ respectively (Figure 33).
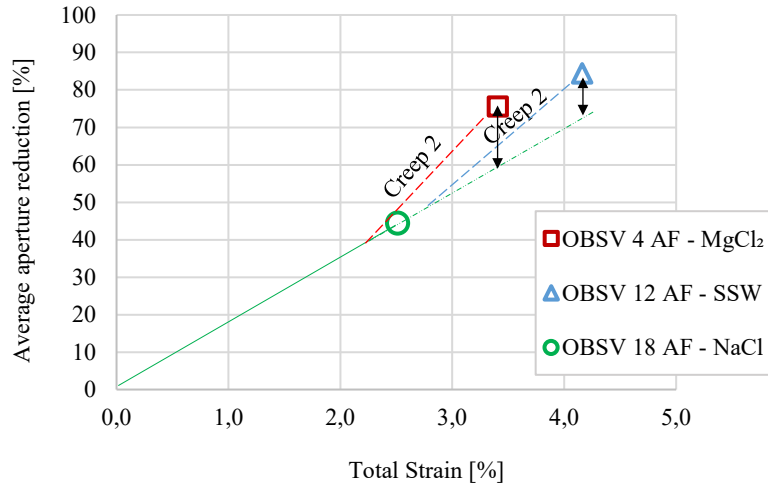
Figure 33) The figure presents the aperture reduction associated with the total axial strain (Loading, Creep 1, and Creep 2) for three artificially fractured outcrop samples flooded under reservoir conditions. OBSV 18 AF-NaCl was flooded for reference purpose. The green line indicates the expected aperture reduction when only the total strain caused aperture reduction (the reference showed coating of chlorite which had negligible effect on aperture reduction). OBSV 12 AF-SSW and OBSV AF- MgCl$_2$ experienced a higher total strain than OBSV AF-NaCl (X-axis). At the same time these two samples experienced a more significant aperture reduction than OBSV AF-NaCl (Y-axis). The distance between the green base line and the red square and blue triangle indicates that the aperture reduction is caused by precipitation or sealing of the fractures. The two stippled lines represent the strain identified in Creep 2, and thereby the deviations (black arrows) from the green line provide an estimate of how much the sealing alone reduced the aperture. This is a simplified model that can be used in future projects, but more data is required like creating a more accurate baseline.

Permeable fractures are important for effective oil production. However, constant modification of fracture apertures through compaction, dissolution, and precipitation of mineral processes will complicate reservoir simulation models. The dynamic fracture aperture modification during brine injection is a complicated process which gives rise to under- or overestimating recoveries and reserves in naturally fractured reservoirs. An increased understanding of these processes can contribute to a smarter planning of fluid injection, which is a key factor for successful and improved oil recovery without large uncertainties, since small variations in aperture can have large implication to flow. Modeling flow behaviour in fractured porous media is a mature research field, still it faces substantial challenges regarding multi-phase flow and multi-

physics couplings as mechanics and chemistry (Berre et al., 2019). Newer elastic fracture modeling which includes changes in fracture properties during production, has shown that more water will be produced than previously anticipated (Soleimani, 2017). Structural and diagenetic observations of fracture properties can be used for upscaling and predicting the capability of larger fractures to transport fluid (Laubach, 2003). As an example, imaging techniques such as X-ray computed tomography (CT) on fractured core samples will visualize the internal fracture geometry, connectivity, and intensity in three dimensions. This will facilitate fracture intensity and permeability calculations (Glad et al., 2023) for small-scaled discontinuities as in the Lower Ekofisk Formation (Boersma et al., 2020).

Glad et al., (2023) identified presence of numerous microfractures using CT, previously not recorded in the Lower Cretaceous of the Danish North Sea. Observations of the artificially fractured outcrop samples indicated that minor fracture apertures readily reduce during water injection at reservoir overburden stress resembling Ekofisk. Small fractures that can be characterized by CT (Glad et al., 2023) may in the Lower Ekofisk Formation diminish or close during seawater injection and thus reduce permeability which has previously not been documented. Compaction and reduction of permeability could thus force more injected brine to the surrounding matrix and thereby increase the hydrocarbon production. Compaction and closure of microfractures in heterogeneous chalk during a laboratory experiment was suggested to be a potential mechanism for additional oil production however with limited efficiency (Hao and Shapiro, 2019).

6.4 Characterization of chalk surfaces on submicron scale using HIM-SIMS

Chalk characterization using the high resolution HIM-SIMS has not previously been reported. The background for testing this method is associated with the challenges met when characterizing chalk due to the very small grain size as described in e.g., Chapter 3.5. Technical descriptions of the method are explained in Appendix 8.11, advantages and limitations are discussed in Chapter 3.5 (Toolbox). An unflooded outcrop OBSV sample (Chapter 4.4) and manufactured calcite powders (Chapter 4.2) were used in this very first analytical examination. This chapter discusses how characterization of chalk on nanoscale using the high-resolution HIM-SIMS instrument (**Paper II**) can contribute to better understanding of brine-rock interactions on nano scale.

The HIM-SIMS demonstrated its ability to determine the chemistry of the surface of coccoliths and to create high resolution images without moving the sample. HIM-SE images showed that it is possible to identify well-defined crystal boundaries or coating on the surface of the coccolith fragments. The surface chemistry distribution (obtained by SIMS) was combined with surface topography (obtained by HIM) of nanosized grains (Figure 7 **Paper II**). Based on the composition of chemistry detected on the surface of the unflooded OBSV sample, illite was interpreted to be the coating mineral on calcite grains. The coating was detected in patches with frequently well-defined boundaries. This non-carbonate phase has not previously been visualized at this resolution by more traditional methods. The observations may be correlated with the heterogeneous distribution of adhesion properties on calcite surfaces obtained by AFM studies (Hassenkam et al., 2009; Okhrimenko et al., 2014; Skovbjerg et al., 2012). Hassenkam et al. (2009) found that wettability and elasticity were heterogeneously distributed over scales of 10s of nanometers on the surface of chalk. They suggested that these patches were relics from material originally present during sedimentation or a result of diagenesis. In a later study, also performed

by AFM concluded that these laths, which were solely of 1-4 nanometer thick layering on calcite surfaces, were clay (Skovbjerg et al., 2012). The authors argued that they were clay based on parameters such as size and shape of the laths. In a similar study using chalk samples from the gas and water zones of the Danish sector in the North Sea Basin, laths on the surface were interpreted as illite (Skovbjerg et al., 2013). The authors based their interpretation on the diagenetic history of the sediment, their shape and size using AFM in addition to chemical force mapping. The HIM-SIMS facilitates chemical detection of these phases in-situ combined with high resolution imaging and can thus confirm that the composition of these phases could match with illite.

HIM-SIMS is also valuable when characterizing mineral nucleation on sub-micron scale (e.g., Figure 23) associated with brine injection. Nanosized magnesite crystals were identified on the manufactured calcite surface. Precipitation of separate crystals have previously been proposed by Madland et al. (2011) where they ruled out that the loss of Mg^{2+} to the core, identified by ion chromatography, was not solely an exchange process of Ca^{2+} and Mg^{2+} on the calcite surface. Numerous research has since then documented nucleation and precipitation of magnesite in experiments under reservoir conditions for the NCS (Andersen et al., 2018; Minde et al., 2018; Minde et al., 2020). However, methods to identify and visualize chemical compositions of micron-sized surface grains, without a time-consuming sample preparation, have not previously been available. HIM-SIMS as an analytical technique has therefore the potential to play an extraordinary role in the investigation of the abundance of mineral phases at this scale in the future.

6.5 Clay distribution and brine-rock interaction processes in chalk

An SSW flooded outcrop OBSV sample (OBSV 12 AF-SSW) was used in a follow up study using the HIM-SIMS (Chapter 5.3.2) with the aim of focusing on the distribution of the clay, identified on the surface of coccolith grains (**Paper II**). This chapter covers a method to visualize the non-carbonate distribution on the calcite surface. The distribution of the non-carbonate phase was calculated. Further it discusses how distribution of impurities in chalk reservoirs may impact processes during seawater injection at the reservoir for IOR purposes, by implementing processes discussed in the powder sample experiments (Chapter 6.2) and the OBSV outcrop samples (Chapter 6.3).

An unflooded OBSV sample was analysed to detect and quantify the distribution of mineral phases covering particles in chalk and present it in a 4D surface reconstruction (**Paper III**). A 4D surface reconstruction is a 3D model with an added fourth dimension representing the surface chemistry (Chapter 5.3.2). 6.3 % of the coccolith grain surface was covered by a non-carbonate phase in addition to a 39.8 % chemically mixed area (predominantly silicate phases) including minute Mg-rich carbonate (Table 11). However, the bulk geo-chemistry showed abundance of 5 Wt.% of non-carbonates within the rocks (Table 1 **Paper III**). The "mix" of 39.8 % significantly exceeds estimates of non-carbonate mineral abundance based on bulk geochemistry. The more widespread distribution of clay than anticipated based on bulk data is attributed to clay as thin films on calcite surfaces (Figures 21, 22). This widespread distribution of non-carbonate phases underestimates strongly the non-carbonate surface distribution in this chalk.

It is therefore essential to complement bulk geochemistry with additional data when modeling non-carbonate distribution for reservoir chalk because the abundance will impact modelling brine-rock interaction processes. Surface mineral composition, charge, and ion exchange

capacity as well as brine pH and ionic composition, are some of the rock and fluid properties that impact initial wettability, its alteration and the spontaneous imbibition potential during seawater injection (Puntervold et al., 2021). The reservoir may be heterogeneous with fractional, spotted or dalmatian wettability (Anderson, 1986). The surface rock is then either strongly oil-wet, or strongly water-wet. Fractional wettability has been defined as "mixed" wettability (Salathiel, 1973). Current models for wettability alterations are based on simplified models which consider the calcite surface as either water wet, oil wet, fractional or mixed wet (Yang et al., 1999). These models use estimated mineralogical abundance mostly determined based on bulk geochemistry and subsequently bulk mineralogy. Here, we imaged submicron-sized non-carbonate phases in patches on the 4D surface reconstruction (Figures 21, 22) that are smaller than a single droplet of water (Mercado et al., 2016). The presence of these distinct patches of non-carbonate distribution on the calcite surface will impact wettability alteration processes and the potential for spontaneous imbibition. Quantification of the abundance of non-carbonate phases covering calcite surfaces in carbonate reservoirs can improve the understanding of brine-rock interaction mechanisms.

The presence of natural organic adlayers on grain surfaces has been argued to be responsible for the partial water wettability (when water sorptivity is anomalously low) of limestones (Ioannou et al., 2004). Therefore, even hydrophilic minerals can attract oil molecules caused by the organic material adsorbed to the mineral surface thus effect the wettability substantially, even more than the covered minerals (Matthiesen et al., 2014).

Likewise, if the thin layers of clay covering the calcite surface in patches (Figure 21) are not covered by an organic adlayer, they will have a different wetting condition than calcite which can potentially affect mechanical properties (Sachdeva et al., 2020). The mechanical strength may become weaker when water wetness decreases. The chemistry of

the thin water film is determined by the wettability and therefore the content of silica and clay among calcite thus the water weakening (Strand et al., 2007). Madland et al. (2011) highlighted that pure chalk had a slower reaction rate in terms of compaction, than chalk with higher content of non-carbonate (particularly silicates and clays). Nevertheless, the presence and distribution of silica and clay minerals in chalk and its impact on the mechanical strength has not been completely understood. The significant difference in chemical processes identified when flooding pure calcite versus the mixed samples containing dolomite and calcite, proved that more complex chemical reactions commence when calcite is not pure (Chapter 6.2.3). The study also documented complex chemical processes which in some cases impact compaction in the unconsolidated powders depending on the nature of the new mineral phase (Chapter 6.2.4). The 'realistic' sample with 5 Wt.% dolomite in the sample Mix 4 5-95 SSW experienced calcite dissolution. If manufactured calcite has comparable properties as chalk containing biomineralized calcite, the dissolution of calcite and precipitation of aragonite could potentially weaken the rock if the overburden stress is so high that the reservoir has reached the yield point and is compacting in the plastic phase (Chapter 6.1.1). Mix 4 5-95 SSW did not show any additional compaction compared to Cal 3B SSW in the experiment as mentioned, which could be attributed to the absence of consolidation.

Water weakening data obtained from laboratory experiments have been upscaled to field scale using reservoir porewater chemistry data (Minde and Hiorth, 2020). Water chemistry data collected at a production well 400 meters apart from an injection well helped to determine water breakthrough based on the concentration of chlorine (Hiorth et al., 2011). Chlorine was used as a natural tracer as it does not react with sediments, and it has a lower concentration in seawater than the Ekofisk formation water (Hiorth et al., 2011). Five to six years after injection, the water composition had the same chlorine concentration as seawater. Loss of other ions was seen as associated with mineral precipitation in the

reservoir. The model presented by Minde and Hiorth (2020) demonstrated that the dissolution/precipitation mechanisms studied in the laboratory was likely to propagate at a much lower speed and mainly affect compaction near the well region and close to the temperature front. They suggested that the more rapid transport of sulphate changing the surface charge through the reservoir could significantly have contributed to the observed water weakening effect. They also concluded that present impurities in chalk could eliminate the delay in alteration-induced creep. The results obtained in the powder experiment here can support their conclusion. The mineralogical alterations, with precipitation of aragonite predominantly in the central parts and towards the outlet observed for Mix 4 5-95 SSW as well as observations of high magnesium towards the outlet of Mix 1 50-50 $MgCl_2$ U.Eq and Mix 5 20-80 $MgCl_2$ U.Eq. On the contrary, precipitation of magnesite in the pure calcite sample (Cal 6 $MgCl_2$ U.Eq) showed that the precipitates were predominantly identified in the inlet slice. This different pattern of distribution of newly precipitated minerals is directly linked with the sample mineralogy. The consequence of injecting seawater in a pure reservoir would be dominated by mineral precipitation close to the injection well (or no mineralogical alterations at all) with a delay front as discussed in Minde and Hiorth, (2020). Oppositely could a reservoir with impurities (eg., dolomite) initiate dissolution and precipitation instantly thus follow more closely the injected seawater front and therefore move more rapidly towards the production well.

Compaction and subsidence associated with calcite dissolution can force remaining oil towards the production wells and thereby enhance recovery. A more extensive chemical acquisition and topographical mapping of the grain surfaces within chalk, can provide more accurate input to modeling wettability, chemical alterations, thus weakening during seawater injection. Then IOR methodologies can be altered in a favorable direction. HIM-SIMS is the first approach to solve this challenge as described, yet it needs further development to achieve the

necessary feasibility in terms of velocity for analysis by, for example, automatization. This has been achieved within other methodologies like electron microscopy (Schulz et al., 2020) and Raman spectroscopy (Lünsdorf et al., 2019) in the past.

7 Conclusions

Laboratory experiments were performed in triaxial cells under reservoir conditions (in terms of temperature and pressures) replicating Ekofisk at the NCS to better understand the impact of impurities and fractures among chalk in brine-rock interaction processes. Those parameters are important when evaluating IOR strategies for the future.

Pure dolomite and manufactured calcite powders samples were flooded separately in addition to several mixed compounds of the two minerals in different ratios. The in-depth analysis of results from flooding experiments using triaxial cells to acquire geo-mechanical data, effluent analysis, and sample material analysis, facilitated identification of brine-rock interactions attributed to the presence of dolomite among calcites by comparing those processes to results from experiments with pure calcite. Additionally, artificially fractured outcrop chalk samples have been flooded with different compositions of brines in triaxial cells under reservoir conditions also typical for the Ekofisk reservoir. The purpose of the experimental research was to study the geo-mechanical response associated with the presence of fractures, mineralogical alterations in the fractured area, and modification of fracture geometry. The samples in both projects were thoroughly characterized by complementary methods, described in an analytical "toolbox", to detect geochemical and mineralogical alterations. A special emphasis was laid on the application of HIM-SIMS for surface characterization of chalk. This novel method can both image and detect the surface chemistry in-situ at very high resolution down to nanoscale. It was here used for the first time ever on chalk.

Results showed that powder samples with mixed compositions of two minerals (calcite and dolomite) experienced surprisingly more complicated chemical interactions compared to experiments where pure dolomite and pure manufactured calcite were flooded separately. No new

mineral phases were identified when pure dolomite was flooded in five different tests using different composition of brines, with SSW as one of them. Magnesite precipitated in pure manufactured calcite when samples were flooded with 0.219 mol/L $MgCl_2$. Yet, no other minerals were detected in pure manufactured calcite, including samples that were flooded with SSW. The complicated processes, when flooding mixed compounds (of pure dolomite and manufactured calcite), included dissolution of calcite and precipitation of new minerals which were strongly dependent on the composition of the brine as well as the ratio of dolomite to calcite in the mixed samples. Secondary minerals that precipitated only in samples with mixed mineralogy were anhydrite and aragonite when SSW was injected and magnesite and high magnesium calcite when $MgCl_2$ was injected. The most 'realistic' (referring to a ratio of dolomite to calcite comparable to reservoir chalk at the NCS), Kallesten et al. (2021) sample was a 5-95 Wt.% dolomite to calcite ratio. When the sample was flooded with SSW, it experienced dissolution of calcite and precipitation of aragonite. The test lasted only four days. It was proposed that if an instant surface dissolution of calcite grain dissolves in chalk at the NCS due to presence of dolomite or other impurities, the reservoir will potentially release oil previously adhered to the surface more efficiently. However, a production rate may suffer from a reducing permeability attributed to the precipitation of aragonite which may possibly migrate and clog pores. The dissolution-precipitation process in the 5-95 Wt.% SSW unconsolidated sample, did not impact the axial strain rate during creep. Calcite dissolution in reservoir (where chalk is consolidated) may however reduce mechanical strength thus increase the compaction. The proposed mechanisms are valid if manufactured calcite properties do not vary significantly from chalk containing biomineralized calcite, and that impurities are not covered by organic adlayers.

Artificially fractured samples showed significantly higher compaction during the initial six days of creep when flooded with NaCl in the triaxial

cell tests, compared to intact samples without an artificial fracture. The higher compaction observed for fractured samples was attributed to the matrix being forced into the void spaces. This weakening was however not observed during loading of stresses, which indicated that the process commenced only after the samples reached the yield point. A change in the composition of the injected brine after six days caused a rapid and significant compaction, associated with water weakening for samples without the artificial fractures, when brines as SSW and $MgCl_2$ were injected. The later and less significant onset for artificially fractured samples were associated with brine mainly passing through the fractures. Extrapolation of the creep indicated that artificially fractured samples may over a longer timespan (at least six months) be mechanically weaker than intact samples. This was in line with data obtained during an initial phase of the experiment under injection of NaCl, which as mentioned concluded that the presence of artificial fractures caused enhanced compaction. The seawater injected at Ekofisk most likely flows predominantly through the fractures with the highest permeability, yet ions will be transported into the adjacent matrix despite low matrix permeability often under 1 mD. This causes weakening of the chalk, yet the compaction rate will, potentially, be lower in a highly dense fractured location than a location with low fracture densities. Eventually, the compaction may stagnate in locations with low fracture densities but continue and compact beyond in high fracture density locations.

All three artificially fractured outcrop samples reduced the apertures during the flooding experiment. The main mechanism of fracture aperture reduction was therefore interpreted to be dominantly associated with compaction forcing matrix material into the fracture. The higher axial strain observed, the more significant reduction of the aperture was identified. Precipitation and cementation in the fracture aperture caused additional reductions of the fracture apertures. The clay (chlorite) identified covering the inside surface of the fracture must have been sourced from the matrix, as these elements (Si, Al, and Fe etc.) did not

exist in the injected brine. In the reservoir, the non-carbonate minerals present in the chalk may determine brine-rock interaction processes affecting water weakening, source precipitation and cementing which likely reduce smaller apertures. Aperture reduction and closure of smaller fractures in the reservoir, e.g., Lower Ekofisk Formation, may force seawater into the chalk matrix and thus expel more hydrocarbons out of the reservoir.

Application of the high resolution HIM-SIMS showed great potential to detect chemical impurities on nano-meter scale with in-situ imaging. HIM-SIMS demonstrated for the first-time abundant clay minerals in patches covering calcite surfaces. Bulk geochemistry for an unflooded outcrop chalk sample (OBSV) measured only around 5 Wt.% non-carbonate concentration, whereas the surface was covered by 6.3 % clay in addition to a fraction of 39.8 % of the total area where the surface was mixed with calcite and clay. As impurities were broadly distributed on coccolith surfaces in the outcrop OBSV chalk samples, they cover a large surface area available for brine and rock to interact. The impurities present as thin films in patches on the coccolith surface implies a larger inhomogeneity in terms of surface charges. They will therefore play a significant role in brine-rock interaction processes during seawater injection if they are not covered by an adlayer of organic material. The manufactured calcite may have different properties, like solubility, than natural biomineralized calcite in chalk. However, assuming they have comparable properties, dolomite or impurities of other non-carbonate minerals present among chalk will facilitate dissolution of calcite and precipitation of new minerals thus enhance the oil release and possibly reduce permeability. Calcite dissolution may also cause additional compaction.

Characterization of reservoir chalk samples down to nanoscale can facilitate a more profound understanding of brine-rock interactions and increase accuracy of input data for modelling fractional wettability and alterations, mineral dissolution, and precipitation thus compaction,

subsidence, sealing capability and fluid flow in chalk reservoirs. HIM-SIMS is an ultimate complementary method which can identify surface chemistry and quantify the distribution of impurities coating calcite fragments in patches.

The laboratory experiments demonstrated that presence of dolomite distributed within the mineralogically mixed two-component samples, caused precipitation of new minerals distributed throughout the cores. Precipitation of aragonite in the "realistic" mixed compound (Mix 4 5-95 SSW) did not precipitate in pure calcite (Cal 3 SSW). Precipitation of minerals in the reservoir with present impurities may travel with a faster front towards the production well during seawater injection, compared to reservoir with pure chalk. The faster front of precipitation will be attributed to the presence of impurities. The presence of impurities such as dolomite or potentially other non-carbonates may consequently cause a more significant and rapid compaction than reservoirs with high calcite purities.

7.1 Application and future work

Parts of the thesis included completely new approaches to understand the impact of non-calcite minerals present among chalk by using single mineral systems (calcite and dolomite tested separately) and mixing them in definite ratios. Mixing calcite with a specific mineral such as dolomite in controlled ratios was a useful method to detect and study chemical processes which are attributed to the presence of the specific mineral in the mixed compound. A follow-up study performing flooding tests under reservoir conditions using samples with mixed calcite and silica e.g., quartz flooded under reservoir conditions, may provide useful data related to chemical alterations. This can also be extended with clays such as chlorite which can be present in chalk. Then, tests using three components (clays, dolomite, and calcite) could be developed. These tests with mixed compounds are simplified, therefore they help to

understand chemical processes. If and how those results can be upscaled to reservoir level is another very interesting and important question.

These tests facilitate comprehension of geo-mechanical responses related to those impurities only in unconsolidated powder samples. To approach testing powder samples having properties being closer to a consolidated rock sample, all samples can be flooded with one selected brine during a primary week before changing the brine composition. In this way the samples will experience a comparable compaction during the settling phase (loading phase) and the three to five days into the creep until reaching a stabile compaction. This change of procedure will provide a more realistic interpretation of brine-rock interactions in triaxial cells when using powder samples. Constant acquisition of the ratio of compressional-wave velocity (V_p) to shear-wave velocity (V_s) could be added to support changes in rock conditions as porosity and consolidation.

Parts of this research project was a continuation of an earlier project which included detailed characterization of artificially fractured outcrop chalk. Several properties that control modification of minor fracture apertures have been pointed out. This data may be applicable for better understanding aperture modification and geo-mechanical response within reservoirs when implementing new methodologies for improved production. More precise input from laboratory experiments to model these processes can help predict more accurately near wellbore compaction associated with wormhole acidizing.

The analytical toolbox described (Chapter 3.5) was an update of previous work and may be applied by anyone who requests characterization of rock materials especially on fine grained material (included shale and diatomite). The thesis highlighted specifically the advantage of mapping the chemistry on surfaces of calcite in chalk by utilizing HIM-SIMS as a complementary method when characterizing chalk. Availability is still limited; the cost is high and mapping larger areas will be time-

consuming. However, like the developments of electron microscopic techniques, a similar advance can be expected for HIM-SIMS in the future.

The identification of the surface chemistry of coccolith grains using HIM-SIMS for reservoir chalk could be performed with a purpose to alter the composition of the injecting brine to create the 'ideal' composition. An ideal composition of an injecting brine for a specific reservoir rock could increase recovery by an optimization of wettability alteration or aperture reduction in network of small fractures to force injected seawater into the matrix and more effectively expel remaining hydrocarbons. This could potentially increase sweep efficiency and the recovery factor. These processes may also depend on biofilms adhered to calcite surfaces, which needs to be accounted for in future research.

This new research proposed could be implemented in the future to improve understanding brine-rock interactions, help developing the optimal brine and thereby improve the recovery factor in mature chalk reservoirs.

8 Appendices

The following methods for experimental set-up and sample analysis described have been utilized in the thesis, however, it does not include the exact same methods previously described in the "toolbox".

8.1 Ion Chromatography (IC)

Effluent samples were prepared by diluting the samples by 100, 500, or 1000 times depending on original concentration by using a Gilson Gx-271 Liquid Handler and filtered with a (0.20 μm) sieve. Chemical analyses were performed by using either Dionex ICS 3000 or Dionex ICS 5000+ Ion Chromatography System. Ion Chromatography (IC) separates and quantifies anions and cations in an ionic solution. The quantity of an anion/cation was measured by the change in conductivity when the sample passed through the detector. The data from the detector was presented in a chromatogram which is a plot showing ion abundance versus time. Each specific ion was identified based on the position of the peak, and the size reflects the concentration of the ion detected. The ion concentrations of the produced fluid analysed were verified by external standards.

8.2 X-Ray Diffraction (XRD)

Two different instruments were used for mineral identification. A D-8000 Bruker analysed 5-90 grader 2-theta with 1-degree per minute and with EVA V4.0 software for mineral identification. It provides a database of X-ray diffraction patterns. Phase analysis was also performed using powder X-ray diffractograms recorded on Bruker D8 Endeavor X-Ray diffraction with a Lynxeye XE-T detector. The diffractograms were recorded between 5° and 70° 2-theta at a step size of 0.015° 2-theta at a time step of 0.5 per second. ICDD PDF-4+ - is an available database

(Powder Diffraction Files) and MDI Jade Pro – software was used for interpretation.

8.3 Whole rock geochemistry (Inductive Coupled Plasma Mass Spectrometry, ICP-MS)

Sample material was milled in an agate beaker to a fine mesh. The geochemical data was obtained by Inductive Coupled Plasma-Mass Spectrometry (ICP-MS) analysis. The milled sample was mixed with $LiBO_2/Li_2B_4O_7$ flux in crucibles and fused in a furnace. The cooled bead was dissolved in the American Chemical Society (ACS) grade nitric acid and analyzed by ICP-MS. Loss on ignition (LOI) was determined by igniting a sample split then measuring the weight loss after being ignited at 1000°C for 1 hour, then cooled and weighed again. Total Carbon and Sulphur concentrations were determined by the LECO® method. Here, induction flux was added to the prepared sample then ignited in an induction furnace. A carrier gas swap up released carbon which was measured by adsorption in an infrared spectrometric cell. An additional 14 elements were measured after dilution in Aqua Regia. The prepared sample was digested with a modified Aqua Regia solution of equal parts concentrated HCl, HNO_3, and DI-H_2O for 1 hour in a heating block. The sample volume was increased with dilute HCl-solutions and splits of 0.5 g were analyzed. Accuracy and precision are between 2-3 % per element.

8.4 Carbon and Oxygen Stable Isotopes

Stable isotope analysis was performed by Isotopic Ratio Mass Spectrometry (IRMS) at the stable Isotope Laboratory at the University of Tromsø. A Thermo-Fisher MAT253 IRMS with a Gasbench II for the determination of $\delta^{13}C$ and $\delta^{18}O$ in carbonates. Isotopic values were quoted relative to the Vienna Pee Dee Belemnite (VPDB). The analysis was performed on crushed sample material of minimum 1.0 mg. $\delta^{13}C$ and

δ¹⁸O isotopic analysis of chalk samples reflect paleoclimate and post-depositional alterations. The relative abundance of the stable isotopes of an element in a mineral depends on fractionation by mass, temperature and/or biological processes during mineralization. The temperature at the time of precipitation can be determined during diagenesis and in flooding experiments. Based on the δ¹⁸O an estimated temperature (T) at precipitation can be estimated according to Equation 3 where δw = (-1) and δc is δ¹⁸O (Anderson et al., 1983; Gómez et al., 2008).

$$T = 16.0 - 4.14 (\delta c - \delta w) + 0.13 (\delta c - \delta w)^2 \qquad (3)$$

Carbon isotopes may reveal information about primary depositional conditions and are usually not subject to strong diagenetic alteration. Oxygen isotopes, in contrast, are more sensitive to environmental and post-depositional processes and need to be treated very carefully for interpretation.

8.5 Binocular Light Microscopy

A Zeiss Stemi DV4 has a maximum of 20 times magnification. It helped evaluating texture and color variation for artificially fractured outcrop samples.

8.6 Specific Surface Area (SSA)

Approximately two grams of sample material were ground in an agate mortar. The samples were heated in a tube at a temperature of 80°C and kept under vacuum for 4.5 hours. A Micromeritics TriStar II was utilized for the purpose of measuring Brunauer–Emmett–Teller (BET) surface area based on the BET theory (Brunauer et al., 1938). Nitrogen gas was introduced to the sample continuously under a vacuum of around 20 - 30 mTorr. The sample tube was submerged in liquid nitrogen (LN_2) for cooling during measurement. At increased partial pressures, nitrogen gas filled a greater area of the micro-pores, which adsorbed as a monolayer

on the surface of the grains. The change in pressure is a measure of the amount of gas that was adsorbed on the surface. When including the exact sample weight, the SSA was calculated by TriStar II 3020 Software, and the resulting surface extension is given in m^2/g.

8.7 Secondary Electron Microscopy (SEM) coupled with Energy Dispersive X-ray Spectroscopy (EDS)

A selection of samples was molded epoxy under a vacuum. The samples were first polished by hand (320, 500, 1000 grit paper) using ethanol, followed by machine polishing by Struers Tegramin-30 us. The final polishing medium and suspension was MD-Nap 1 µm from Struers. These mounted samples were also used for Focused Ion Beam – Secondary Electron Microscopy (FIB- SEM), Transmission Electron Microscopy (TEM) coupled with Energy Dispersive X-ray Spectroscopy (EDS), Helium Ion Microscopy (HIM) combined with Secondary Ion Mass Spectrometry (SIMS) investigations.

Samples were mounted on aluminum holders followed by coating with palladium (Pd) or gold (Au). A Zeiss Supra 35-VP SEM was used for high magnification of morphological differences and to obtain elemental composition by using an EDS detector. Images were acquired using the secondary electron (SE) detector and backscatter electron detector (BSE) at a fixed working distance of 10 mm, accelerating voltage of 15.00 kV and using an aperture size of 30 µm. Energy Dispersive X-ray Spectroscopy (EDS) was performed either as point analysis line scan, area of 2x2 µm² or complete map analysis. The interaction volume in the sample is ~ 1 µm³ (Priebe et al., 2019).

8.8 Mineral Liberation Analysis (MLA)

A FEI Quanta 600 F Mineral Liberation Analyzer (MLA) is a Scanning Electron Microscope (SEM) equipped with Energy Dispersive X-ray

(EDX) spectrometers, and computer software that automates microscope operation. MLA measurements are based on Backscattered Electron (BSE) image analysis and may determine grain boundaries on polished and coated specimens. It locates and classifies the characteristic X-ray spectra of mineral species by comparing these to a library of reference spectra (Sylvester, 2012). The spectrum is further classified as a specific mineral or group of minerals, assigned a color, and saved in a database. Standard greyscale is calibrated to copper and is unique for each mineral. Bright greyscale reflects heavier minerals (atomic number) while the darker end of the greyscale represents lighter minerals. The average greyscale of the mineral in the BSE image is linked to a database of EDS-spectrum for comparison and hence produces a color map based on the variation in greyscale of the BSE-image. The automated operation of the MLA analysis allows a high number of mineral grains to be examined and provides a statistically representative analysis of a sample. It is capable of distinguishing fine-grained and complex intergrown minerals down to micrometer scale (Sylvester, 2012). However, similar mineral compositions may be challenging to distinguish (e.g., hematite and magnetite) and the MLA is unable to distinguish polymorphs like calcite, aragonite and vaterite. An SEM-generated electron beam scans the sample in a raster pattern, often called a frame, with a resolution depending on the magnification; increased magnification decreases the size of the frame (Krinsley and Doornkamp, 1973). During acquisition, 15 kV acceleration voltage and a beam current of 10 nA were used. The smallest particle size that can be identified and mapped visually by MLA software is 0.2 μm (Sylvester, 2012). Distinguishing smaller minerals may cause spectral interferences. A software, GXMAP, was used for the purpose of discriminating the grain boundaries determined by the greyscale of the BSE image.

8.9 Transmission Electron Microscopy (TEM) coupled with Energy Dispersive X-ray Spectroscopy (EDS)

Analysis of FIB-SEM samples with TEM was performed using a JEM-2100 connected with an EDAX Apollo XLT2 EDS. The electrons have an energy typically between 100 to 200 keV. The electron microscope produced an image formed by the interactions of electrons with the sample when the ion beam passed through the specimen. The transmitted beam was projected onto a fluorescent screen where the internal microstructures were observed, and a single column of atoms could be recognized. The electrons behave as Broglie waves which define the limit to the resolution of the same order of magnitude at 0.2 to 0.4 nm (Hull and Bacon, 2011) and gain magnifications up to 1 million times (Callister, 2007). Contrasts were imaged at low magnification due to the variation in the materials composition, followed by differential absorption of electrons. TEM studies on FIB-SEM samples allowed for high-magnification images and identification of the chemical composition and crystal orientation.

8.10 Focused Ion Beam - Secondary Electron Microscopy (FIB-SEM)

Samples were prepared for TEM analysis using a Focused Ion Beam-Secondary Electron Microscopy (FIB-SEM) (a Helios G4 UX FEI) instrument. The FIB-SEM combination allowed simultaneous monitoring of the preparation process of ultrathin focused ion beam (FIB) - samples (100 nm). The sample was coated with 30 nm gold (Au) to create electrical conductivity. The beam of ionized gallium (Ga^+) was accelerated (30 keV) and focused onto the specimen surface. This initiated atom sputtering and removal of layer by layer which produced a pool around the area of interest. A sharp wolfram needle was attached to a carbon cord on top of the sample (Figure 29). Naphthalene, $C_{10}H_8$,

diffused into the chamber, enhanced the needle welding to the sample. The sample (2 μm) was pulled out at a speed of 1 μm/sec and attached to an omniprobe (sample holder) of copper (Cu). A final thickness of 100 nm was achieved by a time-consuming sputtering process at a constant working distance of 4 mm.
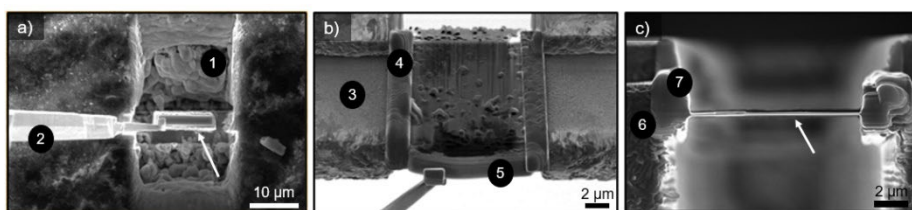
Figure 34) An image series that visualizes the steps in FIB preparation. a) The white arrow indicates the chalk sample. A pool (1) was formed around the sample by sputtering around it using a beam of gallium ions attached to a tungsten needle (2); b) the tungsten needle moved the sample to an omniprobe (3); applied carbon (4) connected the sample to the omniprobe and a carboncord (5) to attach the sample to the needle; c) the white arrow points to the final result after thinning the sample by sputtering. The sample reached a thickness of 100 nm, has a dimension of 10 x 12 μm, and is glued to carbon (7) which connects the sample to the omniprobe (6).

8.11 Helium Ion Microscopy (HIM) combined with Secondary Ion Mass Spectrometry (SIMS)

A Zeiss ORION NanoFab Helium Ion Microscope (HIM) (Hlawacek and Gölzhäuser, 2016) was used for Secondary Electron (SE) image acquisitions. HIM uses a very finely focused He^+ or Ne^+ ion beam, produced by a gas field ion source (GFIS), to raster-scan the sample under investigation and to create SEs collected by an Everhart–Thornley (ET) detector. He^+ ions are typically used as source to produce HIM-SE images to limit sputtering of the surface during the imaging process due to the low sputtering yield of He^+ versus Ne^+ (Pillatsch et al., 2013). This provides spatial resolutions down to 0.5 nm (Dowsett and Wirtz, 2017; Kim et al., 2019) related to the high brightness of the GFIS and the

very small interaction volume between the impinging He$^+$ ions and the sample in the near surface region, from which SEs were emitted (Hlawacek and Gölzhäuser, 2016; Wirtz et al., 2019). Chemical images were acquired by using a Secondary Ion Mass Spectrometer (SIMS) system installed on the HIM, which provided analytical information of specimen (called "HIM-SIMS") (Audinot et al., 2021; Dowsett and Wirtz, 2017; Wirtz et al., 2019). For SIMS, Ne$^+$ primary ions were used to enhance sputtering of the surface (up to a few nanometers of depth) and therefore to increase the secondary ion (SI) yield to achieve adequate signal statistics. The spatial resolution of the SIMS mode is better than 20 nm (Audinot et al., 2021; Wirtz et al., 2019).
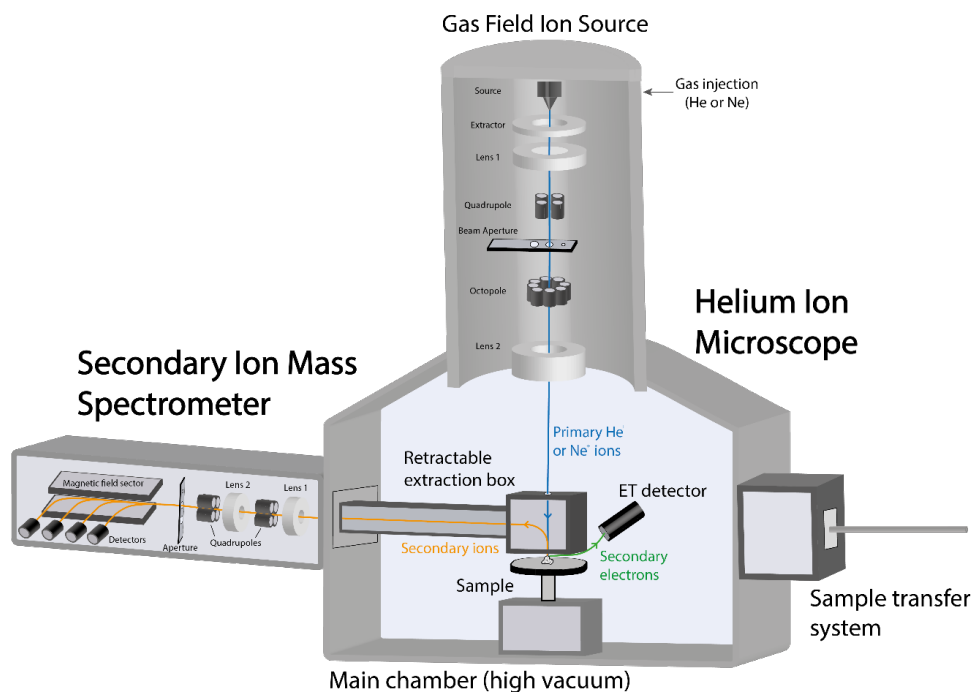
Figure 35) Schematic cross-sectional view of the HIM-SIMS instrument. The central part consists of the Helium Ion Microscope (HIM) used primarily for topographic SE imaging, while the left part shows the coupled Secondary Ion Mass Spectrometer (SIMS) add-on system dedicated for elemental analysis.

8.12 Geochemistry tables

Loss on ignition (LOI)

Element (Wt%/PPM)	SiO$_2$	Al$_2$O$_3$	Fe$_2$O$_3$	MgO	CaO	Na$_2$O	K$_2$O	TiO$_2$	P$_2$O5	MnO	Cr$_2$O$_3$	Ba	Ni	Sc	LOI	Sum
Sample	%	%	%	%	%	%	%	%	%	%	%	PPM	PPM	PPM	%	%
Cal Ref 1	0.0	<0.01	<0.04	<0.01	55.9	<0.01	<0.01	<0.01	0.0	<0.01	<0.002	<1	<20	<1	44.1	100.0
Cal Ref 2	0.0	<0.01	<0.04	<0.01	56.0	<0.01	<0.01	<0.01	<0.01	<0.01	<0.002	<1	<20	<1	44.1	100.0
Cal Ref 3	0.0	<0.01	<0.04	<0.01	55.9	<0.01	<0.01	<0.01	<0.01	<0.01	0.0	<1	<20	<1	44.1	100.0
Cal 1.1 MgCl$_2$	0.0	<0.01	<0.04	8.5	43.8	<0.01	<0.01	<0.01	<0.01	<0.01	0.0	1.0	<20	<1	47.7	100.0
Cal 1.5 MgCl$_2$	0.1	<0.01	0.1	0.3	55.2	<0.01	0.02	0.03	0.04	0.05	0.0	<1	<20	<1	44.4	100.0
Cal 2.1D NaCl	0.0	<0.01	<0.04	<0.01	53.8	0.0	<0.01	<0.01	<0.01	<0.01	<0.002	<1	<20	<1	46.1	100.0
Cal 2.5D NaCl	0.1	<0.01	<0.04	<0.01	53.7	<0.01	<0.01	<0.01	<0.01	<0.01	<0.002	<1	<20	<1	46.3	100.0
Cal 3.1 SSW	0.0	<0.01	0.1	0.1	54.4	0.0	<0.01	<0.01	<0.01	<0.01	<0.002	1.0	<20	<1	45.4	100.0
Cal 3.5 SSW	0.0	<0.01	<0.04	0.2	55.5	0.0	<0.01	<0.01	<0.01	<0.01	<0.002	1.0	<20	<1	44.3	100.0
Cal 4.1F LowSal	0.2	0.0	<0.04	0.0	54.9	<0.01	<0.01	<0.01	<0.01	<0.01	<0.002	3.0	<20	<1	44.8	100.0
Cal 4.5F LowSal	0.1	0.0	<0.04	0.0	56.1	<0.01	<0.01	<0.01	<0.01	<0.01	<0.002	5.0	<20	<1	43.8	100.0
Cal 6.1B MgCl$_2$ U.Eq	0.1	<0.01	<0.04	17.4	36.0	0.0	<0.01	<0.01	<0.01	<0.01	<0.002	<1	30.0	<1	46.6	100.0
Cal 6.5B MgCl$_2$ U.Eq	0.0	<0.01	<0.04	0.7	55.1	0.0	<0.01	<0.01	<0.01	<0.01	0.0	<1	248.0	<1	44.2	100.0
Dol Ref 1	0.3	0.1	0.1	21.6	30.9	0.0	0.1	<0.01	0.0	<0.01	<0.002	13.0	<20	<1	47.0	100.0
Dol Ref 2	0.3	0.0	0.1	21.5	31.0	<0.01	0.0	<0.01	0.0	<0.01	0.0	11.0	<20	<1	47.1	100.0
Dol Ref 3	0.3	0.0	<0.04	21.6	30.6	<0.01	0.0	<0.01	0.0	<0.01	0.0	12.0	<20	<1	47.3	100.0
Dol Ref 4	0.2	0.0	0.0	21.5	31.0	<0.01	0.0	<0.01	0.0	<0.01	0.0	12.0	<20	<1	47.1	100.0
Dol 1.1B MgCl$_2$	0.3	0.0	0.1	21.9	30.0	<0.01	<0.01	<0.01	0.0	<0.01	<0.002	8.5	<20	<1	47.8	100.0
Dol 1.5B MgCl$_2$	0.2	0.0	0.1	21.8	30.2	<0.01	<0.01	<0.01	<0.01	<0.01	<0.002	7.5	<20	<1	47.7	100.0
Dol 2.1 NaCl	0.2	0.0	0.1	21.8	30.4	<0.01	<0.01	<0.01	<0.01	<0.01	<0.002	7.0	<20	<1	47.5	100.0
Dol 2.5 NaCl	0.3	0.0	0.1	21.7	30.6	<0.01	<0.01	<0.01	0.0	<0.01	<0.002	9.5	<20	<1	47.3	100.0
Dol 3.1 SSW	0.2	0.0	0.1	21.8	30.6	<0.01	<0.01	<0.01	<0.01	<0.01	<0.002	12.5	<20	<1	47.3	100.0
Dol 3.5 SSW	0.3	0.0	0.1	21.9	30.4	<0.01	<0.01	<0.01	<0.01	<0.01	<0.002	12.5	<20	<1	47.3	100.0
Dol 4.1C LowSal	0.3	0.0	0.1	21.4	30.8	<0.01	0.0	<0.01	0.0	<0.01	0.0	11.5	<20	<1	47.4	100.0
Dol 4.5C LowSal	0.3	0.0	0.1	21.5	30.8	0.0	0.0	<0.01	<0.01	<0.01	0.0	12.0	<20	<1	47.2	100.0
Dol 6.1 MgCl$_2$ U.Eq	0.2	0.0	0.1	21.8	30.6	<0.01	<0.01	<0.01	0.0	<0.01	0.0	8.0	<20	<1	47.3	100.0
Dol 6.5 MgCl$_2$ U.Eq	0.2	0.0	0.1	21.8	30.8	<0.01	<0.01	<0.01	<0.01	<0.01	0.0	6.0	<20	<1	47.1	100.0
Mix1.In.REF	0.2	0.0	<0.04	11.6	42.2	<0.01	0.0	<0.01	<0.01	<0.01	<0.002	7.0	<20	<1	45.8	99.8
Mix1.Out.REF	0.2	0.0	0.1	11.3	42.5	<0.01	0.0	<0.01	<0.01	<0.01	<0.002	6.0	<20	<1	45.8	99.8
Mix2.In.REF	0.2	0.0	<0.04	12.3	41.4	<0.01	0.0	<0.01	<0.01	<0.01	<0.002	7.0	<20	<1	45.8	99.8
Mix2.Out.REF	0.1	0.0	0.1	10.9	43.1	<0.01	0.0	<0.01	<0.01	<0.01	<0.002	6.0	<20	<1	45.6	99.8
Mix3.In.REF	0.1	<0.01	<0.04	1.1	54.7	<0.01	<0.01	<0.01	<0.01	<0.01	<0.002	<1	<20	<1	44.2	100.0
Mix3.Out.REF	0.06	<0.01	<0.04	1.10	54.59	<0.01	<0.01	<0.01	<0.01	<0.01	<0.002	3	<20	<1	44.3	99.95
Mix4.In.REF	0.04	<0.01	<0.04	1.18	54.16	<0.01	<0.01	<0.01	<0.01	<0.01	<0.002	1	<20	<1	44.6	99.96
Mix4.Out.REF	0.03	<0.01	<0.04	1.20	54.21	<0.01	<0.01	<0.01	<0.01	<0.01	<0.002	<1	<20	<1	44.5	99.97
Mix5.In.REF	0.06	<0.01	<0.04	4.11	50.75	<0.01	<0.01	<0.01	<0.01	<0.01	<0.002	3	<20	<1	45.0	99.92
Mix5.Out.REF	0.13	<0.01	0.05	4.75	50.20	<0.01	<0.01	<0.01	<0.01	<0.01	<0.002	4	<20	<1	44.8	99.92
Mix6.In.REF	0.08	<0.01	<0.04	4.89	50.20	<0.01	<0.01	<0.01	<0.01	<0.01	<0.002	3	<20	<1	44.7	99.92
Mix6.Out.REF	0.08	<0.01	0.07	4.70	50.18	<0.01	<0.01	<0.01	<0.01	<0.01	<0.002	3	<20	<1	44.9	99.91
Mix 1.1 50-50 MgCl$_2$	0.18	0.03	0.08	22.68	27.45	<0.01	<0.01	<0.01	<0.01	<0.01	<0.002	7	<20	<1	49.2	99.63
Mix 1.2 50-50 MgCl$_2$	0.14	0.02	0.05	17.28	34.71	<0.01	0.01	<0.01	<0.01	<0.01	<0.002	6	<20	<1	47.5	99.71
Mix 1.3 50-50 MgCl$_2$	0.47	0.14	0.09	19.71	31.65	<0.01	0.03	<0.01	<0.01	<0.01	<0.002	9	<20	<1	47.6	99.68
Mix 1.4 50-50 MgCl$_2$	0.27	0.08	0.07	19.99	31.60	<0.01	0.02	<0.01	<0.01	<0.01	<0.002	6	<20	<1	47.6	99.67
Mix 1.5 50-50 MgCl$_2$	0.21	0.06	0.06	18.85	33.42	<0.01	0.02	<0.01	<0.01	<0.01	<0.002	7	<20	<1	47.1	99.69
Mix 2.1 50-50 SSW	0.22	0.05	0.07	12.86	39.11	<0.01	0.02	<0.01	<0.01	<0.01	<0.002	6	<20	<1	47.4	99.78
Mix 2.2 50-50 SSW	0.23	0.05	0.05	13.04	40.15	<0.01	0.02	<0.01	<0.01	<0.01	<0.002	9	<20	<1	46.2	99.78
Mix 2.3 50-50 SSW	0.20	0.04	0.07	12.14	41.72	<0.01	0.02	<0.01	<0.01	<0.01	<0.002	10	<20	<1	45.6	99.79
Mix 2.4 50-50 SSW	0.18	0.04	0.07	11.91	42.07	<0.01	0.02	<0.01	<0.01	<0.01	<0.002	6	<20	<1	45.5	99.80
Mix 2.5 50-50 SSW	0.21	0.03	0.06	11.69	42.34	<0.01	0.02	<0.01	<0.01	<0.01	<0.002	8	<20	<1	45.4	99.80

Element (Wt%/PPM)	Be	Co	Cs	Ga	Hf	Nb	Rb	Sn	Sr	Ta	Th	U	V	W	Zr	Y	La
Sample	PPM	PPM	PPM	PPM	PPM	PPM	PPM	PPM	PPM	PPM	PPM	PPM	PPM	PPM	PPM	PPM	PPM
Cal Ref 1	<1	<0.2	<0.1	<0.5	<0.1	<0.1	<0.1	<1	46.5	<0.1	<0.2	<0.1	<8	2.5	1.2	<0.1	0.2
Cal Ref 2	<1	<0.2	<0.1	<0.5	<0.1	<0.1	<0.1	<1	58.9	<0.1	<0.2	<0.1	<8	<0.5	0.2	<0.1	0.2
Cal Ref 3	<1	<0.2	<0.1	<0.5	<0.1	<0.1	<0.1	<1	49	<0.1	<0.2	<0.1	<8	<0.5	1.1	<0.1	0.1
Cal 1.1 MgCl₂	<1	<0.2	<0.1	<0.5	<0.1	<0.1	<0.1	<1	32.15	<0.1	<0.2	<0.1	<8	<0.5	1.2	<0.1	0.15
Cal 1.5 MgCl₂	<1	<0.2	<0.1	<0.5	<0.1	<0.1	<0.1	<1	40.95	<0.1	<0.2	<0.1	<8	<0.5	0.55	<0.1	0.3
Cal 2.1D NaCl	<1	<0.2	<0.1	<0.5	<0.1	<0.1	<0.1	<1	48.5	<0.1	<0.2	<0.1	<8	<0.5	2.7	<0.1	<0.1
Cal 2.5D NaCl	1.0	0.2	<0.1	<0.5	<0.1	<0.1	<0.1	<1	47.2	<0.1	<0.2	<0.1	<8	<0.5	1.5	<0.1	0.2
Cal 3.1 SSW	<1	<0.2	<0.1	<0.5	<0.1	<0.1	<0.1	<1	41	<0.1	<0.2	<0.1	<8	<0.5	0.8	<0.1	<0.1
Cal 3.5 SSW	<1	<0.2	<0.1	<0.5	<0.1	<0.1	<0.1	<1	40.8	<0.1	<0.2	<0.1	<8	<0.5	1.8	<0.1	0.2
Cal 4.1F LowSal	<1	0.4	<0.1	<0.5	<0.1	<0.1	<0.1	<1	62.4	<0.1	<0.2	<0.1	12	<0.5	1.8	0.2	0.2
Cal 4.5F LowSal	<1	0.2	<0.1	<0.5	<0.1	<0.1	<0.1	<1	56.1	<0.1	<0.2	<0.1	<8	<0.5	0.6	0.3	<0.1
Cal 6.1B MgCl₂ U.Eq	<1	0.2	<0.1	<0.5	<0.1	<0.1	<0.1	<1	26.3	<0.1	<0.2	<0.1	<8	<0.5	0.7	<0.1	0.6
Cal 6.5B MgCl₂ U.Eq	<1	2.5	<0.1	<0.5	<0.1	<0.1	<0.1	<1	42.9	<0.1	<0.2	<0.1	<8	<0.5	1.7	<0.1	0.1
Dol Ref 1	<1	<0.2	<0.1	<0.5	<0.1	0.3	1	<1	57.8	<0.1	0.3	1.6	<8	0.8	1.8	1.8	1.1
Dol Ref 2	<1	<0.2	<0.1	<0.5	<0.1	0.4	0.8	<1	50.3	<0.1	0.3	1.3	<8	<0.5	2.8	2	1.2
Dol Ref 3	<1	<0.2	<0.1	<0.5	<0.1	<0.1	0.8	<1	50.8	<0.1	0.4	1.6	<8	<0.5	1.8	1.9	1.2
Dol Ref 4	<1	<0.2	<0.1	<0.5	<0.1	0.1	0.7	<1	49.8	<0.1	0.9	1.1	<8	<0.5	2	1.7	1
Dol 1.1B MgCl₂	<1	0.3	<0.1	<0.5	<0.1	0.15	0.1	<1	55.35	<0.1	0.3	1.15	<8	<0.5	1.6	2	1.45
Dol 1.5B MgCl₂	<1	<0.2	<0.1	<0.5	<0.1	0.2	0.7	<1	56.75	<0.1	0.3	1.45	<8	0.6	2.05	2.15	1.7
Dol 2.1 NaCl	<1	<0.2	<0.1	<0.5	<0.1	0.2	<0.1	<1	54.15	<0.1	0.25	1.55	<8	<0.5	1.65	2.1	1.4
Dol 2.5 NaCl	<1	<0.2	<0.1	<0.5	<0.1	0.2	0.1	<1	55.8	<0.1	0.3	1.4	<8	<0.5	1.7	1.9	1.3
Dol 3.1 SSW	<1	0.6	<0.1	<0.5	<0.1	0.2	0.85	<1	57.4	<0.1	0.3	1.3	<8	<0.5	1.85	2.1	1.3
Dol 3.5 SSW	<1	<0.2	<0.1	<0.5	<0.1	0.2	0.95	<1	56.4	<0.1	0.25	1.25	<8	<0.5	1.9	2.05	1.25
Dol 4.1C LowSal	<1	<0.2	<0.1	<0.5	<0.1	0.2	0.85	<1	52.95	<0.1	0.3	1.4	<8	<0.5	2.35	1.95	1.3
Dol 4.5C LowSal	<1	<0.2	<0.1	<0.5	<0.1	0.25	0.85	<1	51.35	<0.1	0.3	1.25	9	<0.5	3.65	2.1	1.1
Dol 6.1 MgCl₂ U.Eq	<1	<0.2	<0.1	<0.5	<0.1	0.2	<0.1	<1	53	<0.1	0.2	1.3	<8	<0.5	1.7	1.9	1.2
Dol 6.5 MgCl₂ U.Eq	<1	<0.2	<0.1	<0.5	<0.1	0.2	<0.1	<1	49.8	<0.1	0.3	1.5	<8	<0.5	2.7	1.8	1.2
Mix1.In.REF	<1	<0.2	<0.1	<0.5	<0.1	0.2	0.5	<1	50.1	<0.1	<0.2	0.6	<8	<0.5	2.0	0.9	0.8
Mix1.Out.REF	<1	0.2	<0.1	<0.5	<0.1	0.3	0.5	<1	52.7	<0.1	<0.2	0.7	<8	<0.5	3.7	1.1	0.7
Mix2.In.REF	<1	<0.2	<0.1	<0.5	<0.1	0.3	0.7	<1	52.1	<0.1	<0.2	1.2	<8	<0.5	4.4	1.0	0.5
Mix2.Out.REF	<1	<0.2	<0.1	<0.5	<0.1	0.2	0.5	<1	50.8	<0.1	<0.2	0.6	<8	<0.5	3.0	1.0	0.5
Mix3.In.REF	<1	<0.2	<0.1	<0.5	<0.1	0.4	<0.1	<1	52.9	0.1	<0.2	<0.1	<8	<0.5	2.4	0.7	0.3
Mix3.Out.REF	<1	<0.2	<0.1	<0.5	<0.1	0.2	<0.1	<1	48.5	0.2	<0.2	0.1	<8	<0.5	2.1	1.2	0.2
Mix4.In.REF	<1	<0.2	<0.1	<0.5	<0.1	<0.1	0.2	<1	54.7	<0.1	<0.2	<0.1	<8	<0.5	1.5	0.1	<0.1
Mix4.Out.REF	<1	<0.2	<0.1	<0.5	<0.1	<0.1	<0.1	<1	53.7	<0.1	<0.2	<0.1	<8	<0.5	1.1	<0.1	<0.1
Mix5.In.REF	<1	<0.2	<0.1	<0.5	<0.1	<0.1	0.3	<1	55.1	<0.1	<0.2	0.2	<8	<0.5	2.4	0.4	0.2
Mix5.Out.REF	<1	0.3	<0.1	<0.5	<0.1	0.1	0.2	<1	55.9	<0.1	<0.2	0.3	<8	<0.5	2.6	0.4	0.2
Mix6.In.REF	<1	<0.2	<0.1	<0.5	<0.1	<0.1	0.2	<1	52.8	<0.1	<0.2	0.2	<8	13.3	2.2	0.4	0.2
Mix6.Out.REF	<1	0.3	<0.1	<0.5	<0.1	<0.1	0.3	<1	55.4	<0.1	<0.2	0.3	<8	<0.5	1.2	0.4	<0.1
Mix 1.1 50-50 MgCl₂	<1	0.3	<0.1	<0.5	<0.1	0.1	0.2	<1	33.2	<0.1	0.2	0.8	<8	<0.5	2.9	1.0	0.4
Mix 1.2 50-50 MgCl₂	<1	<0.2	<0.1	<0.5	<0.1	<0.1	0.4	<1	38.6	<0.1	<0.2	0.6	<8	<0.5	1.5	0.9	0.4
Mix 1.3 50-50 MgCl₂	<1	<0.2	0.1	<0.5	0.1	0.1	1.5	<1	31.2	<0.1	0.3	0.7	<8	<0.5	4.5	1.0	0.6
Mix 1.4 50-50 MgCl₂	<1	<0.2	<0.1	<0.5	<0.1	<0.1	0.7	<1	28.9	<0.1	<0.2	0.7	<8	<0.5	3.5	1.0	0.5
Mix 1.5 50-50 MgCl₂	<1	<0.2	<0.1	<0.5	<0.1	<0.1	0.6	<1	34.7	<0.1	<0.2	0.7	<8	<0.5	3.3	1.0	0.5
Mix 2.1 50-50 SSW	<1	0.2	<0.1	<0.5	<0.1	<0.1	0.6	<1	47.8	<0.1	<0.2	0.6	<8	<0.5	1.6	1.0	0.5
Mix 2.2 50-50 SSW	<1	<0.2	<0.1	<0.5	<0.1	<0.1	0.7	<1	51.1	<0.1	<0.2	1.0	<8	<0.5	1.8	0.9	0.5
Mix 2.3 50-50 SSW	<1	<0.2	<0.1	<0.5	<0.1	<0.1	0.6	<1	50.4	<0.1	0.2	0.8	<8	<0.5	2.8	1.0	0.4
Mix 2.4 50-50 SSW	<1	<0.2	<0.1	<0.5	0.1	<0.1	0.5	<1	49.6	<0.1	<0.2	0.6	<8	1.2	5.2	1.0	0.3
Mix 2.5 50-50 SSW	<1	<0.2	<0.1	<0.5	0.1	0.3	0.6	<1	52.8	<0.1	<0.2	0.8	<8	<0.5	4.0	0.9	0.5

Element (Wt%/PPM)	Ce	Pr	Nd	Sm	Eu	Gd	Tb	Dy	Ho	Er	Tm	Yb	Lu
Sample	PPM	PPM	PPM	PPM	PPM	PPM	PPM	PPM	PPM	PPM	PPM	PPM	PPM
Cal Ref 1	<0.1	<0.02	<0.3	<0.05	<0.02	<0.05	<0.01	<0.05	<0.02	<0.03	<0.01	<0.05	<0.01
Cal Ref 2	0.2	0.05	<0.3	<0.05	0.02	<0.05	0.02	<0.05	<0.02	<0.03	0.02	<0.05	0.01
Cal Ref 3	<0.1	<0.02	<0.3	<0.05	<0.02	<0.05	<0.01	<0.05	<0.02	<0.03	<0.01	<0.05	<0.01
Cal 1.1 MgCl₂	<0.1	<0.02	<0.3	<0.05	<0.02	<0.05	<0.01	<0.05	<0.02	<0.03	<0.01	<0.05	<0.01
Cal 1.5 MgCl₂	<0.1	<0.02	<0.3	<0.05	<0.02	<0.05	<0.01	<0.05	<0.02	<0.03	<0.01	<0.05	<0.01
Cal 2.1D NaCl	<0.1	<0.02	<0.3	<0.05	<0.02	<0.05	<0.01	<0.05	<0.02	<0.03	<0.01	<0.05	<0.01
Cal 2.5D NaCl	0.3	0.09	0.3	<0.05	<0.02	<0.05	<0.01	<0.05	<0.02	<0.03	<0.01	<0.05	<0.01
Cal 3.1 SSW	<0.1	<0.02	<0.3	<0.05	<0.02	<0.05	<0.01	<0.05	<0.02	<0.03	<0.01	<0.05	<0.01
Cal 3.5 SSW	0.2	<0.02	<0.3	<0.05	<0.02	<0.05	<0.01	<0.05	<0.02	<0.03	<0.01	<0.05	<0.01
Cal 4.1F LowSal	0.5	0.03	<0.3	<0.05	<0.02	0.06	<0.01	<0.05	<0.02	<0.03	<0.01	<0.05	<0.01
Cal 4.5F LowSal	0.2	<0.02	<0.3	<0.05	<0.02	<0.05	<0.01	<0.05	<0.02	<0.03	<0.01	<0.05	<0.01
Cal 6.1B MgCl₂ U.Eq	0.2	<0.02	<0.3	<0.05	<0.02	<0.05	<0.01	<0.05	<0.02	<0.03	<0.01	<0.05	<0.01
Cal 6.5BMgCl₂ U.Eq	<0.1	<0.02	<0.3	<0.05	<0.02	<0.05	<0.01	<0.05	<0.02	<0.03	<0.01	<0.05	<0.01
Dol Ref 1	1.9	0.26	1.2	0.13	0.05	0.28	0.03	0.17	0.04	0.11	0.01	0.07	0.02
Dol Ref 2	1.8	0.24	0.9	0.19	0.05	0.21	0.03	0.17	0.03	0.12	0.01	0.09	0.01
Dol Ref 3	1.8	0.22	0.9	0.17	0.04	0.2	0.02	0.16	0.04	0.11	0.02	0.08	0.01
Dol Ref 4	1.6	0.22	1	0.13	0.04	0.19	0.03	0.18	0.03	0.12	0.02	0.09	0.01
Dol 1.1B MgCl₂	1.95	0.28	1.1	0.19	0.065	0.26	0.045	0.195	0.05	0.095	0.025	0.095	0.02
Dol 1.5B MgCl₂	1.95	0.265	1.05	0.195	0.05	0.225	0.04	0.24	0.05	0.125	0.02	0.09	0.015
Dol 2.1 NaCl	2	0.25	1.1	0.155	0.055	0.25	0.04	0.205	0.05	0.135	0.02	0.095	0.015
Dol 2.5 NaCl	1.85	0.24	0.9	0.175	0.05	0.24	0.03	0.24	0.05	0.105	0.02	0.065	0.015
Dol 3.1 SSW	1.9	0.22	0.85	0.19	0.055	0.25	0.035	0.195	0.04	0.125	0.015	0.08	0.02
Dol 3.5 SSW	2	0.245	1.1	0.205	0.05	0.25	0.03	0.175	0.035	0.125	0.01	0.09	0.01
Dol 4.1C LowSal	1.95	0.255	1.1	0.195	0.065	0.23	0.04	0.205	0.04	0.125	0.03	0.1	0.02
Dol 4.5C LowSal	1.85	0.245	1	0.185	0.05	0.205	0.04	0.215	0.045	0.125	0.02	0.08	0.015
Dol 6.1 MgCl₂ U.Eq	1.9	0.24	1	0.17	0.04	0.19	0.03	0.17	0.04	0.12	0.02	0.11	0.01
Dol 6.5 MgCl₂ U.Eq	1.8	0.24	1	0.13	0.04	0.21	0.03	0.18	0.03	0.1	0.02	0.11	<0.01
Mix1.In.REF	1.1	0.13	0.7	0.10	0.03	0.12	0.01	0.11	<0.02	0.05	<0.01	<0.05	0.01
Mix1.Out.REF	1.2	0.16	0.6	0.10	0.03	0.10	0.01	0.11	0.03	0.06	<0.01	<0.05	<0.01
Mix2.In.REF	1.1	0.16	0.7	0.06	0.02	0.11	0.02	0.12	<0.02	0.05	0.01	0.06	<0.01
Mix2.Out.REF	1.1	0.13	0.5	0.07	0.03	0.10	0.01	0.11	<0.02	0.05	<0.01	0.05	<0.01
Mix3.In.REF	0.4	0.12	<0.3	<0.05	<0.02	<0.05	<0.01	<0.05	<0.02	<0.03	<0.01	<0.05	<0.01
Mix3.Out.REF	0.5	0.12	<0.3	<0.05	<0.02	<0.05	0.01	<0.05	<0.02	<0.03	0.01	<0.05	<0.01
Mix4.In.REF	0.2	<0.02	<0.3	<0.05	<0.02	<0.05	<0.01	<0.05	<0.02	<0.03	<0.01	<0.05	<0.01
Mix4.Out.REF	<0.1	<0.02	<0.3	<0.05	<0.02	<0.05	<0.01	<0.05	<0.02	<0.03	<0.01	<0.05	<0.01
Mix5.In.REF	0.4	0.03	<0.3	<0.05	<0.02	<0.05	<0.01	<0.05	<0.02	<0.03	<0.01	<0.05	<0.01
Mix5.Out.REF	0.2	<0.02	<0.3	<0.05	<0.02	0.05	<0.01	<0.05	<0.02	<0.03	<0.01	<0.05	<0.01
Mix6.In.REF	0.5	0.02	<0.3	<0.05	<0.02	0.05	<0.01	<0.05	<0.02	<0.03	<0.01	<0.05	<0.01
Mix6.Out.REF	0.4	<0.02	<0.3	<0.05	<0.02	<0.05	<0.01	<0.05	<0.02	<0.03	<0.01	<0.05	<0.01
Mix 1.1 50-50 MgCl₂	1.0	0.09	0.6	0.08	<0.02	0.12	<0.01	0.09	0.02	0.04	<0.01	<0.05	<0.01
Mix 1.2 50-50 MgCl₂	1.0	0.07	0.4	0.06	<0.02	0.09	<0.01	0.08	<0.02	0.05	<0.01	0.05	<0.01
Mix 1.3 50-50 MgCl₂	1.3	0.11	0.7	0.08	0.03	0.12	0.01	0.15	<0.02	0.07	<0.01	<0.05	<0.01
Mix 1.4 50-50 MgCl₂	1.0	0.07	0.6	0.05	<0.02	0.07	<0.01	0.12	<0.02	0.04	<0.01	<0.05	<0.01
Mix 1.5 50-50 MgCl₂	1.0	0.05	0.6	0.08	<0.02	0.11	<0.01	0.09	<0.02	0.06	<0.01	<0.05	<0.01
Mix 2.1 50-50 SSW	0.9	0.08	0.6	0.06	<0.02	0.10	<0.01	0.10	<0.02	0.05	<0.01	<0.05	<0.01
Mix 2.2 50-50 SSW	1.0	0.07	0.5	0.05	<0.02	0.10	<0.01	0.09	<0.02	0.06	<0.01	<0.05	<0.01
Mix 2.3 50-50 SSW	0.9	0.06	0.4	0.07	<0.02	0.08	<0.01	0.12	<0.02	0.05	<0.01	<0.05	<0.01
Mix 2.4 50-50 SSW	1.1	0.05	0.3	0.06	<0.02	0.11	<0.01	0.10	<0.02	0.03	<0.01	<0.05	<0.01
Mix 2.5 50-50 SSW	<0.1	<0.02	<0.3	<0.05	<0.02	0.10	<0.01	0.10	<0.02	0.05	<0.01	<0.05	<0.01

Element (Wt%/PPM) Sample	TOT/C %	TOT/S %	Mo PPM	Cu PPM	Pb PPM	Zn PPM	Ni PPM	As PPM	Cd PPM	Sb PPM	Bi PPM	Ag PPM	Au PPB	Hg PPM	Tl PPM	Se PPM
Cal Ref 1	11.85	<0.02	<0.1	<0.1	<0.1	<1	<0.1	0.9	<0.1	<0.1	<0.1	<0.1	<0.5	<0.01	<0.1	<0.5
Cal Ref 2	12.27	<0.02	<0.1	<0.1	<0.1	<1	<0.1	0.8	<0.1	<0.1	<0.1	<0.1	<0.5	<0.01	<0.1	<0.5
Cal Ref 3	11.86	<0.02	<0.1	<0.1	<0.1	<1	<0.1	0.6	<0.1	<0.1	<0.1	<0.1	<0.5	<0.01	<0.1	<0.5
Cal 1.1 MgCl₂	15.27	<0.02	<0.1	0.3	<0.1	1.5	0.95	0.7	<0.1	<0.1	<0.1	<0.1	2.6	<0.01	<0.1	<0.5
Cal 1.5 MgCl₂	12.365	<0.02	<0.1	0.1	<0.1	<1	<0.1	0.5	<0.1	<0.1	<0.1	<0.1	<0.5	<0.01	<0.1	<0.5
Cal 2.1D NaCl	14.64	<0.02	<0.1	<0.1	<0.1	<1	0.2	<0.5	<0.1	<0.1	<0.1	<0.1	0.9	<0.01	<0.1	<0.5
Cal 2.5D NaCl	14.85	<0.02	<0.1	<0.1	<0.1	<1	0.8	0.7	<0.1	<0.1	<0.1	<0.1	<0.5	<0.01	<0.1	<0.5
Cal 3.1 SSW	13.79	<0.02	<0.1	0.2	<0.1	<1	0.2	0.8	<0.1	<0.1	<0.1	<0.1	<0.5	<0.01	<0.1	<0.5
Cal 3.5 SSW	12.04	<0.02	<0.1	<0.1	<0.1	<1	<0.1	<0.5	<0.1	<0.1	<0.1	<0.1	<0.5	<0.01	<0.1	<0.5
Cal 4.1F LowSal	13.22	<0.02	<0.1	0.4	0.8	<1	3.2	1.0	<0.1	<0.1	<0.1	<0.1	<0.5	<0.01	<0.1	<0.5
Cal 4.5F LowSal	12.05	<0.02	<0.1	0.9	1.6	2	1.1	0.8	<0.1	<0.1	<0.1	<0.1	<0.5	<0.01	<0.1	<0.5
Cal 6.1B MgCl₂ U.Eq	14.92	<0.02	<0.1	0.5	<0.1	4	20.5	<0.5	<0.1	<0.1	<0.1	<0.1	<0.5	<0.01	<0.1	<0.5
Cal 6.5BMgCl₂ U.Eq	12.56	<0.02	<0.1	<0.1	<0.1	<1	<0.1	<0.5	<0.1	<0.1	<0.1	<0.1	<0.5	<0.01	<0.1	<0.5
Dol Ref 1	12.82	<0.02	<0.1	<0.1	1.3	<1	1.1	<0.5	<0.1	<0.1	<0.1	<0.1	<0.5	<0.01	<0.1	<0.5
Dol Ref 2	12.91	<0.02	0.1	<0.1	1.4	1	<0.1	0.7	<0.1	<0.1	<0.1	<0.1	<0.5	<0.01	<0.1	<0.5
Dol Ref 3	12.93	<0.02	0.1	<0.1	1.5	1	<0.1	1	<0.1	<0.1	<0.1	<0.1	<0.5	<0.01	<0.1	<0.5
Dol Ref 4	12.8	<0.02	0.2	<0.1	1.7	2	<0.1	1.1	<0.1	<0.1	<0.1	<0.1	<0.5	<0.01	<0.1	<0.5
Dol 1.1B MgCl₂	13.735	<0.02	0.3	0.5	1.45	<1	6.1	0.8	<0.1	<0.1	<0.1	<0.1	2.85	<0.01	<0.1	<0.5
Dol 1.5B MgCl₂	13.66	<0.02	0.1	0.2	1.4	<1	2.1	<0.5	<0.1	<0.1	<0.1	<0.1	1.35	<0.01	<0.1	<0.5
Dol 2.1 NaCl	13.47	<0.02	<0.1	1	1.35	<1	0.35	<0.5	<0.1	<0.1	<0.1	<0.1	0.7	<0.01	<0.1	<0.5
Dol 2.5 NaCl	13.35	<0.02	0.1	0.35	1.3	<1	0.5	0.5	<0.1	<0.1	<0.1	<0.1	1.1	<0.01	<0.1	<0.5
Dol 3.1 SSW	13.73	<0.02	0.25	0.45	1.3	<1	17.6	<0.5	<0.1	<0.1	<0.1	<0.1	0.8	<0.01	<0.1	<0.5
Dol 3.5 SSW	13.545	<0.02	0.2	0.1	1.3	<1	0.6	<0.5	<0.1	<0.1	<0.1	<0.1	<0.5	<0.01	<0.1	<0.5
Dol 4.1C LowSal	12.905	<0.02	<0.1	0.95	1.4	2	0.1	0.65	<0.1	<0.1	<0.1	<0.1	0.9	<0.01	<0.1	<0.5
Dol 4.5C LowSal	12.885	<0.02	0.1	<0.1	1.4	2.5	<0.1	1.4	<0.1	<0.1	<0.1	<0.1	<0.5	<0.01	<0.1	<0.5
Dol 6.1 MgCl₂ U.Eq	13.05	<0.02	0.1	2.4	1.4	2	8.4	<0.5	<0.1	<0.1	<0.1	<0.1	1.9	<0.01	<0.1	<0.5
Dol 6.5 MgCl₂ U.Eq	12.86	<0.02	0.1	1.4	1.5	1	0.9	0.7	<0.1	<0.1	<0.1	<0.1	<0.5	<0.01	<0.1	<0.5
Mix1.In.REF	12.14	<0.02	<0.1	<0.1	0.8	<1	0.7	<0.5	<0.1	<0.1	<0.1	<0.1	<0.5	<0.01	<0.1	<0.5
Mix1.Out.REF	10.37	<0.02	<0.1	<0.1	0.7	<1	<0.1	0.7	<0.1	<0.1	<0.1	<0.1	<0.5	<0.01	<0.1	<0.5
Mix2.In.REF	12.31	<0.02	<0.1	0.1	0.8	<1	<0.1	<0.5	<0.1	<0.1	<0.1	<0.1	<0.5	<0.01	<0.1	<0.5
Mix2.Out.REF	9.47	<0.02	<0.1	<0.1	0.8	<1	0.2	<0.5	<0.1	<0.1	<0.1	<0.1	<0.5	<0.01	<0.1	<0.5
Mix3.In.REF	10.03	<0.02	<0.1	0.1	<0.1	<1	<0.1	<0.5	<0.1	<0.1	<0.1	<0.1	<0.5	<0.01	<0.1	<0.5
Mix3.Out.REF	9.35	<0.02	<0.1	<0.1	<0.1	<1	0.4	<0.5	<0.1	<0.1	<0.1	<0.1	<0.5	<0.01	<0.1	<0.5
Mix4.In.REF	11.33	<0.02	<0.1	<0.1	<0.1	<1	<0.1	<0.5	<0.1	<0.1	<0.1	<0.1	<0.5	<0.01	<0.1	<0.5
Mix4.Out.REF	11.69	<0.02	<0.1	<0.1	<0.1	<1	<0.1	0.8	<0.1	<0.1	<0.1	<0.1	<0.5	<0.01	<0.1	<0.5
Mix5.In.REF	11.81	<0.02	<0.1	<0.1	0.2	<1	<0.1	<0.5	<0.1	<0.1	<0.1	<0.1	<0.5	<0.01	<0.1	<0.5
Mix5.Out.REF	12.34	<0.02	<0.1	<0.1	0.3	<1	<0.1	<0.5	<0.1	<0.1	<0.1	<0.1	<0.5	<0.01	<0.1	<0.5
Mix6.In.REF	12.00	<0.02	<0.1	0.1	0.3	<1	0.4	1.0	<0.1	<0.1	<0.1	<0.1	0.7	<0.01	<0.1	<0.5
Mix6.Out.REF	12.31	<0.02	<0.1	<0.1	0.3	<1	<0.1	1.2	<0.1	<0.1	<0.1	<0.1	0.8	<0.01	<0.1	<0.5
Mix 1.1 50-50 MgCl₂	14.50	<0.02	<0.1	1.7	0.9	1	15.1	1.1	<0.1	<0.1	<0.1	<0.1	1.0	<0.01	<0.1	<0.5
Mix 1.2 50-50 MgCl₂	13.73	<0.02	<0.1	0.2	0.8	<1	0.8	1.5	<0.1	<0.1	<0.1	<0.1	<0.5	<0.01	<0.1	<0.5
Mix 1.3 50-50 MgCl₂	13.10	<0.02	<0.1	1.1	1.4	2	1.6	0.7	<0.1	<0.1	<0.1	<0.1	<0.5	<0.01	<0.1	<0.5
Mix 1.4 50-50 MgCl₂	13.38	<0.02	<0.1	0.6	2.2	2	1.5	1.1	<0.1	<0.1	<0.1	<0.1	1.5	<0.01	<0.1	<0.5
Mix 1.5 50-50 MgCl₂	12.94	<0.02	0.2	0.8	3.9	3	1.7	1.3	<0.1	<0.1	<0.1	<0.1	<0.5	<0.01	<0.1	<0.5
Mix 2.1 50-50 SSW	14.27	<0.02	<0.1	1.7	5.2	5	4.3	1.3	<0.1	<0.1	<0.1	<0.1	0.6	<0.01	<0.1	<0.5
Mix 2.2 50-50 SSW	13.01	0.45	0.1	0.8	3.5	3	0.8	0.6	<0.1	<0.1	<0.1	<0.1	0.8	<0.01	<0.1	<0.5
Mix 2.3 50-50 SSW	11.96	0.35	<0.1	1.5	4.1	3	1.8	0.5	<0.1	<0.1	<0.1	<0.1	<0.5	<0.01	<0.1	<0.5
Mix 2.4 50-50 SSW	12.68	0.15	<0.1	1.0	4.0	3	2.2	0.8	<0.1	<0.1	<0.1	<0.1	0.5	<0.01	<0.1	<0.5
Mix 2.5 50-50 SSW	12.85	0.03	0.1	1.3	4.7	4	2.7	0.7	<0.1	<0.1	<0.1	<0.1	<0.5	<0.01	<0.1	<0.5

Element (Wt%/PPM) Sample	SiO₂ %	Al₂O₃ %	Fe₂O₃ %	MgO %	CaO %	Na₂O %	K₂O %	TiO₂ %	P₂O5 %	MnO %	Cr₂O₃ %	Ba PPM	Ni PPM	Sc PPM	LOI %	Sum %
Mix 3.1 5-95 MgCl₂	0.10	<0.01	<0.04	5.43	48.48	<0.01	<0.01	<0.01	<0.01	<0.01	<0.002	2	<20	<1	45.9	99.91
Mix 3.5 5-95 MgCl₂	0.07	0.02	0.05	1.68	53.65	<0.01	<0.01	<0.01	<0.01	<0.01	<0.002	<1	<20	<1	44.5	99.97
Mix 4.1 5-95 SSW	0.09	0.01	<0.04	1.30	53.99	<0.01	<0.01	<0.01	<0.01	<0.01	<0.002	3	<20	<1	44.6	99.94
Mix 4.5 5-95 SSW	0.09	0.01	<0.04	1.34	54.12	<0.01	<0.01	<0.01	<0.01	<0.01	<0.002	2	<20	<1	44.4	99.97
Mix 5.1 20-80 MgCl₂	0.11	0.02	0.08	19.59	30.42	<0.01	<0.01	<0.01	<0.01	<0.01	<0.002	3	48	<1	49.5	99.68
Mix 5.2 20-80 MgCl₂	0.09	<0.01	<0.04	14.35	38.54	<0.01	<0.01	<0.01	0.01	<0.01	<0.002	3	<20	<1	47.0	100.01
Mix 5.3 20-80 MgCl₂	0.12	0.02	<0.04	18.98	33.44	<0.01	<0.01	<0.01	0.02	<0.01	<0.002	4	<20	<1	47.1	99.66
Mix 5.4 20-80 MgCl₂	0.10	0.02	<0.04	14.73	38.49	<0.01	<0.01	<0.01	0.01	<0.01	<0.002	4	<20	<1	46.4	99.73
Mix 5.5 20-80 MgCl₂	0.10	0.02	<0.04	8.72	45.44	<0.01	<0.01	<0.01	<0.05	<0.01	<0.002	3	<20	<1	45.6	99.82
Mix 6.1B 20-80 SSW	0.11	<0.01	<0.04	5.02	47.97	<0.01	<0.01	<0.01	<0.01	<0.01	<0.002	3	23	<1	46.8	99.88
Mix 6.5B 20-80 SSW	0.10	<0.01	<0.04	4.44	47.31	<0.01	<0.01	<0.01	0.01	<0.01	<0.002	2	<20	<1	48.1	99.89
OBSV 4 REF IN	3.32	0.97	0.34	0.29	52.06	0.04	0.22	0.04	0.06	0.02	<0.002	23	<20	1	42.5	99.85
OBSV 4 AF - MgCl₂ #1	3.38	0.99	0.31	0.66	51.81	0.03	0.18	0.04	0.05	0.02	<0.002	22	<20	1	42.4	99.84
OBSV 4 AF - MgCl₂ #3	3.39	1.00	0.36	0.97	51.37	0.03	0.16	0.05	0.07	0.02	<0.002	22	<20	1	42.4	99.85
OBSV 4 AF - MgCl₂ #4	3.32	0.98	0.34	0.99	51.73	0.03	0.15	0.04	0.09	0.02	<0.002	19	<20	1	42.1	99.84
OBSV 4 AF - MgCl₂ #6	3.37	0.98	0.34	0.98	51.67	0.03	0.16	0.04	0.06	0.02	<0.002	22	<20	1	42.2	99.84
OBSV 4 AF - MgCl₂ #7	3.32	0.98	0.35	0.95	51.68	0.03	0.15	0.04	0.06	0.02	<0.002	19	<20	1	42.2	99.84
OBSV 4 REF OUT	3.50	1.03	0.37	0.28	52.01	0.04	0.23	0.05	0.05	0.02	<0.002	25	<20	1	42.3	99.85
OBSV 6 REF IN	3.38	1.00	0.34	0.28	52.29	0.04	0.22	0.05	0.06	0.02	<0.002	26	<20	<1	42.2	99.84
OBSV 6 MgCl₂ #2	3.19	1.00	0.34	1.50	51.24	0.03	0.15	0.05	0.07	0.02	<0.002	22	<20	1	42.2	99.83
OBSV 6 MgCl₂ #3	3.37	1.02	0.36	1.43	51.21	0.03	0.15	0.05	0.08	0.02	<0.002	19	<20	<1	42.1	99.83
OBSV 6 MgCl₂ #4	3.27	1.00	0.34	1.28	51.38	0.04	0.16	0.05	0.09	0.02	<0.002	21	<20	1	42.2	99.83
OBSV 6 MgCl₂ #5	3.31	1.02	0.41	1.08	51.68	0.03	0.17	0.05	0.08	0.02	<0.002	23	<20	1	42.0	99.83
OBSV 6 MgCl₂ #6	3.52	1.05	0.38	0.96	51.50	0.04	0.17	0.05	0.10	0.02	<0.002	23	<20	1	42.0	99.84
OBSV 6 MgCl₂ #7	3.54	1.03	0.40	1.01	51.86	0.04	0.18	0.05	0.08	0.02	<0.002	24	<20	1	41.6	99.83
OBSV 6 REF OUT	3.40	1.03	0.33	0.30	51.89	0.04	0.23	0.05	0.09	0.02	<0.002	24	<20	1	42.5	99.84
OBSV 9 REF IN	3.44	1.01	0.39	0.29	51.97	0.04	0.22	0.05	0.10	0.02	<0.002	25	<20	1	42.3	99.85
OBSV 9 SSW #1	3.37	1.04	0.36	0.55	51.88	0.04	0.21	0.05	0.10	0.02	<0.002	23	<20	1	42.2	99.81
OBSV 9 SSW #2	3.43	1.03	0.40	0.51	51.64	0.04	0.22	0.05	0.09	0.02	<0.002	25	<20	1	42.4	99.84
OBSV 9 SSW #3	3.52	1.04	0.38	0.48	51.50	0.04	0.23	0.05	0.08	0.02	<0.002	23	<20	1	42.5	99.84
OBSV9 SSW #4	3.45	1.04	0.39	0.45	51.65	0.05	0.22	0.05	0.08	0.02	<0.002	23	<20	1	42.5	99.84
OBSV 9 SSW #5	3.49	1.02	0.42	0.43	51.80	0.05	0.23	0.05	0.07	0.02	<0.002	23	<20	1	42.3	99.85
OBSV 9 SSW #6	3.55	1.04	0.42	0.40	51.60	0.05	0.24	0.05	0.06	0.02	<0.002	23	<20	1	42.4	99.85
OBSV 9 REF OUT	3.59	1.05	0.47	0.28	52.00	0.04	0.23	0.05	0.07	0.02	<0.002	27	<20	1	42.0	99.84
OBSV 12 REF IN	3.58	1.05	0.40	0.28	51.89	0.04	0.24	0.05	0.06	0.02	<0.002	26	<20	1	42.2	99.84
OBSV 12 AF-SSW #1	3.61	1.07	0.47	0.44	51.93	0.04	0.24	0.05	0.08	0.02	<0.002	23	<20	2	41.9	99.85
OBSV 12 AF-SSW #2	3.52	1.05	0.38	0.48	52.05	0.04	0.22	0.05	0.07	0.02	<0.002	21	<20	1	42.0	99.84
OBSV 12 AF-SSW #3	3.56	1.07	0.40	0.53	51.93	0.03	0.23	0.05	0.08	0.02	<0.002	27	<20	1	41.9	99.82
OBSV 12 AF-SSW #4	3.64	1.08	0.43	0.52	51.88	0.04	0.22	0.05	0.06	0.02	<0.002	24	<20	1	41.9	99.84
OBSV 12 AF-SSW #5	3.60	1.06	0.39	0.49	51.67	0.04	0.23	0.05	0.07	0.02	<0.002	24	<20	1	42.2	99.84
OBSV 12 AF-SSW #6	3.62	1.08	0.43	0.40	51.94	0.04	0.24	0.05	0.08	0.02	<0.002	23	<20	1	42.0	99.85
OBSV 18 REF IN	3.39	1.00	0.54	0.27	51.90	0.04	0.22	0.05	0.10	0.02	<0.002	65	<20	1	42.3	99.83
OBSV 18 AF-NaCl #1	3.49	1.02	0.39	0.28	52.21	0.06	0.22	0.05	0.09	0.02	<0.002	23	<20	1	42.0	99.85
OBSV 18 AF-NaCl #2	3.30	0.98	0.38	0.27	52.52	0.06	0.21	0.04	0.10	0.02	<0.002	23	<20	1	42.0	99.85
OBSV 18 AF-NaCl #3	3.21	0.98	0.36	0.27	52.46	0.06	0.21	0.04	0.09	0.02	<0.002	24	<20	<1	42.1	99.86
OBSV 18 AF-NaCl #4	3.30	1.00	0.38	0.27	52.46	0.07	0.21	0.04	0.07	0.02	<0.002	27	<20	1	42.0	99.85
OBSV 18 AF-NaCl #5	3.28	0.99	0.39	0.27	52.38	0.07	0.21	0.04	0.07	0.02	<0.002	22	<20	1	42.1	99.85

Element (Wt%/PPM)	Be	Co	Cs	Ga	Hf	Nb	Rb	Sn	Sr	Ta	Th	U	V	W	Zr	Y	La
Sample	PPM	PPM	PPM	PPM	PPM	PPM	PPM	PPM	PPM	PPM	PPM	PPM	PPM	PPM	PPM	PPM	PPM
Mix 3.1 5-95 MgCl₂	<1	<0.2	<0.1	<0.5	0.3	<0.1	<0.1	<1	45.4	<0.1	<0.2	<0.1	<8	<0.5	2.4	0.1	<0.1
Mix 3.5 5-95 MgCl₂	<1	<0.2	<0.1	<0.5	<0.1	<0.1	<0.1	<1	51.3	<0.1	<0.2	<0.1	<8	<0.5	1.7	<0.1	<0.1
Mix 4.1 5-95 SSW	<1	<0.2	<0.1	<0.5	<0.1	0.2	<0.1	<1	48.8	<0.1	<0.2	<0.1	<8	<0.5	1.4	0.3	0.3
Mix 4.5 5-95 SSW	<1	<0.2	<0.1	<0.5	<0.1	<0.1	0.1	<1	53.5	<0.1	<0.2	<0.1	<8	1.2	3.0	0.1	<0.1
Mix 5.1 20-80 MgCl₂	<1	0.7	<0.1	<0.5	<0.1	<0.1	<0.1	<1	26.0	<0.1	<0.2	0.2	<8	<0.5	1.6	0.3	<0.1
Mix 5.2 20-80 MgCl₂	1	<0.2	<0.1	<0.5	<0.1	0.3	<0.1	<1	28.2	0.1	<0.2	0.4	<8	<0.5	2.4	0.2	0.3
Mix 5.3 20-80 MgCl₂	<1	<0.2	<0.1	<0.5	<0.1	<0.1	<0.1	<1	15.5	<0.1	<0.2	0.3	9	25.6	1.6	0.5	0.2
Mix 5.4 20-80 MgCl₂	<1	<0.2	<0.1	<0.5	<0.1	<0.1	<0.1	<1	22.2	<0.1	<0.2	0.3	<8	24.7	1.0	0.6	0.2
Mix 5.5 20-80 MgCl₂	<1	<0.2	<0.1	<0.5	<0.1	<0.1	<0.1	<1	33.2	<0.1	<0.2	0.4	11	3.7	0.9	0.4	0.1
Mix 6.1B 20-80 SSW	2	<0.2	<0.1	<0.5	0.2	<0.1	<0.1	<1	50.7	<0.1	<0.2	0.3	<8	5.0	7.4	0.4	0.2
Mix 6.5B 20-80 SSW	<1	<0.2	<0.1	<0.5	<0.1	<0.1	0.2	<1	48.7	<0.1	<0.2	0.1	<8	1.1	2.2	0.5	<0.1
OBSV 4 REF IN	3	0.5	0.6	<0.5	0.3	0.9	8.4	<1	1189.8	<0.1	0.7	0.4	16	<0.5	10.5	7.8	10.8
OBSV 4 AF - MgCl₂ #1	<1	0.5	0.5	<0.5	0.2	0.8	8.2	<1	1152.4	<0.1	0.8	0.5	14	<0.5	9.3	6.8	9.7
OBSV 4 AF - MgCl₂ #3	<1	0.5	0.6	<0.5	0.3	0.8	7.7	<1	1115.2	<0.1	0.6	0.5	15	<0.5	9.2	7.8	9.3
OBSV 4 AF - MgCl₂ #4	<1	0.4	0.5	<0.5	0.3	0.8	7.9	<1	1157.9	0.1	0.6	0.5	15	<0.5	10.2	7.5	10.5
OBSV 4 AF - MgCl₂ #6	<1	1.4	0.4	<0.5	0.3	0.9	7.7	<1	1127.3	<0.1	0.6	0.5	17	<0.5	10.2	7.0	9.5
OBSV 4 AF - MgCl₂ #7	<1	0.4	0.4	<0.5	0.3	0.8	7.6	<1	1128.5	0.2	0.5	0.5	18	<0.5	10.1	6.6	10.0
OBSV 4 REF OUT	<1	0.3	0.6	<0.5	0.2	0.9	8.9	<1	1181.1	<0.1	0.7	0.4	17	<0.5	9.3	6.5	9.4
OBSV 6 REF IN	<1	0.5	0.6	<0.5	0.2	0.7	8.5	<1	1199.0	<0.1	0.7	0.5	13	<0.5	10.0	7.5	9.6
OBSV 6 MgCl₂ #2	1	1.5	0.5	<0.5	0.3	0.9	7.4	<1	1165.3	<0.1	0.7	0.5	13	0.6	11.3	7.8	10.3
OBSV 6 MgCl₂ #3	<1	0.5	0.6	<0.5	0.3	0.8	7.8	<1	1154.9	<0.1	0.8	1.3	15	<0.5	9.8	7.6	10.3
OBSV 6 MgCl₂ #4	<1	1.6	0.7	<0.5	0.2	0.8	7.6	<1	1165.9	0.1	0.6	0.5	13	<0.5	10.4	7.5	9.9
OBSV 6 MgCl₂ #5	<1	0.5	0.6	<0.5	0.3	0.8	8.0	<1	1138.4	<0.1	0.7	0.5	16	<0.5	10.3	7.9	10.1
OBSV 6 MgCl₂ #6	1	0.5	0.5	<0.5	0.2	0.9	8.6	<1	1186.7	<0.1	0.7	0.5	14	<0.5	10.4	7.7	10.9
OBSV 6 MgCl₂ #7	3	<0.2	0.6	<0.5	0.2	1.1	8.4	<1	1171.8	<0.1	0.6	0.6	16	<0.5	10.8	7.9	10.5
OBSV 6 REF OUT	<1	0.5	0.6	<0.5	0.3	1.0	8.4	<1	1156.4	0.1	1.0	0.5	16	<0.5	9.9	7.7	11.2
OBSV 9 REF IN	1	1.1	0.5	<0.5	0.3	0.8	8.5	<1	1128.1	<0.1	0.9	0.9	17	<0.5	10.2	8.1	12.1
OBSV 9 SSW #1	<1	0.3	0.5	1.5	0.2	0.9	7.6	<1	1202.8	<0.1	0.7	0.6	26	<0.5	11.2	8.1	10.6
OBSV 9 SSW #2	<1	1.1	0.5	<0.5	0.3	0.9	8.4	<1	1184.8	<0.1	0.6	0.6	14	<0.5	10.0	8.3	10.4
OBSV 9 SSW #3	<1	1.4	0.6	<0.5	0.6	1.0	8.6	<1	1189.7	0.1	0.7	0.6	14	<0.5	22.8	8.0	10.7
OBSV9 SSW #4	<1	0.6	0.6	<0.5	0.3	1.0	8.5	<1	1159.9	<0.1	0.7	0.7	14	<0.5	10.8	7.2	10.1
OBSV 9 SSW #5	2	0.4	0.6	<0.5	0.2	0.9	8.6	<1	1139.9	<0.1	0.7	0.7	14	0.5	10.1	6.9	10.0
OBSV 9 SSW #6	1	0.5	0.6	<0.5	0.3	0.9	9.0	<1	1176.6	0.1	0.8	0.5	16	<0.5	11.3	7.3	10.2
OBSV 9 REF OUT	1	0.5	0.8	<0.5	0.2	0.8	9.2	<1	1224.8	<0.1	0.7	0.6	17	<0.5	10.8	7.4	10.6
OBSV 12 REF IN	<1	1.4	0.7	<0.5	0.3	0.8	8.9	<1	1158.0	<0.1	0.9	0.6	20	<0.5	10.4	7.2	9.6
OBSV 12 AF-SSW #1	<1	0.6	0.6	<0.5	0.3	0.8	8.9	<1	1146.9	0.1	0.7	0.5	24	1.4	11.4	8.1	10.4
OBSV 12 AF-SSW #2	1	0.4	0.7	<0.5	0.4	0.8	8.6	<1	1150.9	<0.1	0.7	0.6	17	<0.5	9.9	8.0	11.3
OBSV 12 AF-SSW #3	1	0.2	0.5	1.7	0.3	1.0	9.1	<1	1202.7	<0.1	0.8	0.8	33	<0.5	11.2	7.6	11.0
OBSV 12 AF-SSW #4	<1	0.3	0.7	<0.5	0.3	0.9	9.2	<1	1182.2	<0.1	0.8	0.6	28	1.5	10.9	7.5	11.0
OBSV 12 AF-SSW #5	1	0.6	0.6	<0.5	0.2	1.0	8.8	<1	1156.6	0.1	0.8	0.6	23	<0.5	10.2	7.8	11.3
OBSV 12 AF-SSW #6	3	0.5	0.7	<0.5	0.3	0.9	8.9	4	1147.1	<0.1	0.6	0.6	18	<0.5	10.9	7.9	11.0
OBSV 18 REF IN	<1	1.2	0.7	<0.5	0.5	1.1	9.2	<1	1172.7	0.2	0.8	0.6	21	0.5	18.7	8.1	11.9
OBSV 18 AF-NaCl #1	<1	0.5	0.5	<0.5	0.3	0.9	8.3	<1	1147.3	<0.1	0.8	0.5	21	<0.5	9.8	7.6	10.7
OBSV 18 AF-NaCl #2	<1	<0.2	0.6	0.5	0.2	1.0	8.2	<1	1121.7	<0.1	0.8	0.7	19	<0.5	10.3	7.6	12.1
OBSV 18 AF-NaCl #3	<1	<0.2	0.5	0.7	0.3	1.1	8.4	<1	1148.9	<0.1	0.9	0.5	15	<0.5	11.0	7.8	10.2
OBSV 18 AF-NaCl #4	<1	0.5	0.5	0.5	0.3	0.9	8.7	<1	1156.4	<0.1	0.7	0.5	13	<0.5	11.2	7.0	10.0
OBSV 18 AF-NaCl #5	<1	0.4	0.5	<0.5	0.3	1.0	8.7	<1	1158.4	<0.1	0.6	0.5	17	<0.5	10.8	7.2	10.1

| Element (Wt%/PPM) | Ce | Pr | Nd | Sm | Eu | Gd | Tb | Dy | Ho | Er | Tm | Yb | Lu |
Sample	PPM	PPM	PPM	PPM	PPM	PPM	PPM	PPM	PPM	PPM	PPM	PPM	PPM
Mix 3.1 5-95 MgCl₂	<0.1	<0.02	<0.3	<0.05	<0.02	<0.05	<0.01	<0.05	<0.02	<0.03	<0.01	<0.05	<0.01
Mix 3.5 5-95 MgCl₂	0.1	<0.02	<0.3	<0.05	<0.02	<0.05	<0.01	<0.05	<0.02	<0.03	<0.01	<0.05	<0.01
Mix 4.1 5-95 SSW	0.3	0.10	0.3	<0.05	<0.02	<0.05	<0.01	<0.05	<0.02	<0.03	<0.01	<0.05	<0.01
Mix 4.5 5-95 SSW	0.1	<0.02	<0.3	<0.05	<0.02	<0.05	<0.01	<0.05	<0.02	<0.03	<0.01	<0.05	<0.01
Mix 5.1 20-80 MgCl₂	0.3	<0.02	<0.3	<0.05	<0.02	<0.05	<0.01	<0.05	<0.02	<0.03	<0.01	<0.05	<0.01
Mix 5.2 20-80 MgCl₂	<0.1	<0.02	<0.3	<0.05	<0.02	0.07	<0.01	<0.05	<0.02	<0.03	<0.01	<0.05	<0.01
Mix 5.3 20-80 MgCl₂	0.6	0.07	0.3	<0.05	<0.02	<0.05	<0.01	0.05	<0.02	0.04	<0.01	<0.05	<0.01
Mix 5.4 20-80 MgCl₂	0.5	0.08	<0.3	<0.05	<0.02	0.08	<0.01	<0.05	<0.02	<0.03	<0.01	<0.05	<0.01
Mix 5.5 20-80 MgCl₂	0.5	0.06	<0.3	<0.05	<0.02	0.09	<0.01	<0.05	<0.02	0.05	<0.01	0.05	<0.01
Mix 6.1B 20-80 SSW	0.4	0.05	<0.3	<0.05	<0.02	<0.05	<0.01	<0.05	<0.02	<0.03	<0.01	<0.05	<0.01
Mix 6.5B 20-80 SSW	0.5	0.06	<0.3	<0.05	<0.02	0.05	<0.01	0.06	<0.02	<0.03	<0.01	<0.05	<0.01
OBSV 4 REF IN	8.0	1.47	5.5	0.94	0.22	1.10	0.15	0.98	0.18	0.60	0.08	0.45	0.07
OBSV 4 AF - MgCl₂ #1	7.9	1.43	5.5	0.93	0.19	1.02	0.14	0.83	0.20	0.52	0.07	0.49	0.06
OBSV 4 AF - MgCl₂ #3	7.7	1.44	5.7	1.02	0.21	1.03	0.15	0.88	0.21	0.57	0.08	0.43	0.07
OBSV 4 AF - MgCl₂ #4	8.1	1.57	5.7	1.09	0.21	1.14	0.17	0.97	0.20	0.63	0.07	0.50	0.07
OBSV 4 AF - MgCl₂ #6	7.7	1.37	5.1	0.91	0.24	1.05	0.14	0.80	0.20	0.61	0.06	0.35	0.06
OBSV 4 AF - MgCl₂ #7	7.2	1.38	5.4	0.80	0.20	1.01	0.13	0.88	0.18	0.49	0.06	0.48	0.06
OBSV 4 REF OUT	7.4	1.32	5.1	0.78	0.18	1.01	0.14	0.88	0.18	0.52	0.06	0.41	0.05
OBSV 6 REF IN	7.9	1.47	5.7	0.94	0.21	1.02	0.14	0.87	0.18	0.57	0.06	0.49	0.06
OBSV 6 MgCl₂ #2	7.7	1.49	6.0	1.00	0.23	1.06	0.16	0.85	0.19	0.51	0.07	0.47	0.06
OBSV 6 MgCl₂ #3	8.0	1.62	6.1	1.00	0.23	1.19	0.16	1.01	0.20	0.60	0.07	0.51	0.07
OBSV 6 MgCl₂ #4	8.1	1.58	5.7	1.06	0.22	1.18	0.15	0.93	0.20	0.56	0.07	0.50	0.06
OBSV 6 MgCl₂ #5	8.1	1.62	5.8	1.14	0.24	1.15	0.15	1.01	0.21	0.58	0.07	0.44	0.07
OBSV 6 MgCl₂ #6	8.9	1.66	6.3	1.05	0.28	1.14	0.18	1.01	0.21	0.61	0.08	0.53	0.08
OBSV 6 MgCl₂ #7	8.1	1.57	5.8	0.96	0.24	1.13	0.16	0.90	0.20	0.57	0.08	0.51	0.06
OBSV 6 REF OUT	8.0	1.60	5.3	1.00	0.25	1.07	0.15	1.00	0.20	0.59	0.07	0.48	0.07
OBSV 9 REF IN	8.1	1.63	7.0	1.09	0.24	1.21	0.16	1.02	0.23	0.62	0.07	0.50	0.08
OBSV 9 SSW #1	8.6	1.71	6.6	1.20	0.26	1.17	0.18	0.95	0.25	0.57	0.09	0.52	0.08
OBSV 9 SSW #2	8.6	1.65	6.3	1.05	0.24	1.15	0.16	1.04	0.22	0.61	0.07	0.50	0.07
OBSV 9 SSW #3	8.8	1.66	6.2	1.05	0.23	1.10	0.16	0.98	0.19	0.59	0.08	0.49	0.07
OBSV9 SSW #4	8.3	1.52	5.8	1.11	0.25	1.10	0.15	1.02	0.20	0.56	0.07	0.45	0.07
OBSV 9 SSW #5	7.8	1.52	6.0	1.03	0.21	1.10	0.14	0.92	0.21	0.59	0.07	0.52	0.06
OBSV 9 SSW #6	7.8	1.51	6.1	0.93	0.23	1.03	0.15	0.86	0.19	0.54	0.07	0.48	0.07
OBSV 9 REF OUT	8.2	1.55	5.9	1.03	0.21	1.07	0.14	0.81	0.20	0.51	0.07	0.48	0.07
OBSV 12 REF IN	7.8	1.46	5.7	0.89	0.22	1.06	0.14	0.92	0.20	0.51	0.07	0.50	0.07
OBSV 12 AF-SSW #1	8.3	1.51	5.7	1.01	0.21	1.01	0.15	0.92	0.19	0.48	0.07	0.48	0.08
OBSV 12 AF-SSW #2	8.7	1.56	5.9	0.97	0.23	1.11	0.15	1.04	0.21	0.64	0.07	0.59	0.06
OBSV 12 AF-SSW #3	8.2	1.64	6.3	1.03	0.22	1.17	0.18	0.99	0.20	0.59	0.09	0.51	0.07
OBSV 12 AF-SSW #4	8.2	1.48	5.1	0.85	0.21	1.10	0.15	0.81	0.19	0.57	0.10	0.47	0.07
OBSV 12 AF-SSW #5	8.6	1.61	6.1	0.98	0.22	1.19	0.15	1.12	0.22	0.62	0.06	0.46	0.08
OBSV 12 AF-SSW #6	8.6	1.57	6.3	1.11	0.23	1.10	0.16	1.05	0.20	0.56	0.08	0.50	0.07
OBSV 18 REF IN	9.6	1.80	6.7	1.19	0.25	1.34	0.17	0.97	0.18	0.63	0.07	0.55	0.08
OBSV 18 AF-NaCl #1	7.9	1.52	5.9	0.99	0.23	1.04	0.15	1.00	0.18	0.61	0.07	0.43	0.06
OBSV 18 AF-NaCl #2	8.8	1.66	6.3	1.11	0.26	1.23	0.17	1.08	0.21	0.56	0.08	0.45	0.09
OBSV 18 AF-NaCl #3	7.9	1.64	6.4	1.06	0.26	1.08	0.17	0.93	0.19	0.55	0.09	0.50	0.08
OBSV 18 AF-NaCl #4	7.7	1.51	5.8	0.99	0.21	1.07	0.15	0.87	0.19	0.53	0.08	0.46	0.07
OBSV 18 AF-NaCl #5	7.8	1.54	6.1	0.96	0.22	0.99	0.14	0.84	0.19	0.60	0.07	0.51	0.07

Element (Wt%/PPM)	TOT/C	TOT/S	Mo	Cu	Pb	Zn	Ni	As	Cd	Sb	Bi	Ag	Au	Hg	Tl	Se
Sample	%	%	PPM	PPM	PPM	PPM	PPM	PPM	PPM	PPM	PPM	PPM	PPB	PPM	PPM	PPM
Mix 3.1 5-95 MgCl₂	11.80	<0.02	<0.1	1.6	1.7	2	16.3	0.6	<0.1	<0.1	<0.1	<0.1	<0.5	<0.01	<0.1	<0.5
Mix 3.5 5-95 MgCl₂	12.32	<0.02	<0.1	1.1	2.3	2	0.8	1.4	<0.1	<0.1	<0.1	<0.1	<0.5	<0.01	<0.1	<0.5
Mix 4.1 5-95 SSW	12.75	<0.02	<0.1	2.0	4.8	5	2.3	1.1	<0.1	<0.1	<0.1	<0.1	<0.5	<0.01	<0.1	<0.5
Mix 4.5 5-95 SSW	12.38	<0.02	<0.1	1.3	3.0	2	4.3	<0.5	<0.1	<0.1	<0.1	<0.1	0.9	<0.01	<0.1	<0.5
Mix 5.1 20-80 MgCl₂	15.83	<0.02	<0.1	3.8	1.4	2	43.6	1.3	<0.1	<0.1	<0.1	<0.1	<0.5	<0.01	<0.1	<0.5
Mix 5.2 20-80 MgCl₂	13.52	<0.02	<0.1	1.0	1.5	2	0.8	<0.5	<0.1	<0.1	<0.1	<0.1	0.7	<0.01	<0.1	<0.5
Mix 5.3 20-80 MgCl₂	12.85	<0.02	<0.1	0.4	1.5	2	0.8	<0.5	<0.1	<0.1	<0.1	<0.1	<0.5	<0.01	<0.1	<0.5
Mix 5.4 20-80 MgCl₂	12.25	<0.02	<0.1	0.5	1.1	1	0.3	<0.5	<0.1	<0.1	<0.1	<0.1	<0.5	<0.01	<0.1	<0.5
Mix 5.5 20-80 MgCl₂	12.43	<0.02	<0.1	0.9	2.3	2	1.1	<0.5	<0.1	<0.1	<0.1	<0.1	0.5	<0.01	<0.1	<0.5
Mix 6.1B 20-80 SSW	14.99	<0.02	<0.1	1.0	1.1	<1	1.6	<0.5	<0.1	<0.1	<0.1	<0.1	0.9	<0.01	<0.1	<0.5
Mix 6.5B 20-80 SSW	16.44	0.06	<0.1	0.8	1.8	2	0.5	0.5	<0.1	<0.1	<0.1	<0.1	1.3	<0.01	<0.1	<0.5
OBSV 4 REF IN	11.93	<0.02	<0.1	1.9	3.1	15	3.6	0.7	0.2	<0.1	<0.1	0.3	1.6	<0.01	<0.1	<0.5
OBSV 4 AF - MgCl₂ #1	11.89	<0.02	<0.1	1.8	2.2	13	3.9	0.8	0.2	<0.1	<0.1	0.2	<0.5	<0.01	<0.1	<0.5
OBSV 4 AF - MgCl₂ #3	11.83	<0.02	<0.1	1.7	2.5	16	2.6	0.7	0.2	<0.1	<0.1	0.2	<0.5	<0.01	<0.1	0.7
OBSV 4 AF - MgCl₂ #4	11.78	<0.02	0.2	2.1	2.5	15	4.2	<0.5	0.1	<0.1	<0.1	0.2	1.1	<0.01	<0.1	<0.5
OBSV 4 AF - MgCl₂ #6	11.81	<0.02	0.1	1.9	2.2	13	2.6	0.9	0.1	<0.1	<0.1	0.2	1.1	<0.01	<0.1	0.7
OBSV 4 AF - MgCl₂ #7	11.78	<0.02	<0.1	1.7	2.4	15	2.2	0.8	0.1	<0.1	<0.1	0.2	1.1	<0.01	<0.1	0.6
OBSV 4 REF OUT	11.86	<0.02	0.2	2.3	2.6	17	3.0	<0.5	0.1	<0.1	<0.1	0.2	1.1	<0.01	<0.1	0.7
OBSV 6 REF IN	11.76	<0.02	0.1	1.4	3.3	19	2.6	0.5	0.1	<0.1	<0.1	0.3	0.7	<0.01	<0.1	<0.5
OBSV 6 MgCl₂ #2	11.85	0.05	0.2	1.5	7.8	40	2.6	0.8	0.3	<0.1	<0.1	0.3	2.6	<0.01	<0.1	0.6
OBSV 6 MgCl₂ #3	11.68	0.05	0.1	1.6	5.7	32	3.6	0.5	0.3	<0.1	<0.1	0.3	<0.5	<0.01	<0.1	<0.5
OBSV 6 MgCl₂ #4	11.81	0.06	<0.1	1.5	4.3	24	2.8	<0.5	0.2	<0.1	<0.1	0.3	2.1	<0.01	<0.1	<0.5
OBSV 6 MgCl₂ #5	11.98	0.08	0.1	1.8	3.9	22	4.2	1.4	0.2	<0.1	<0.1	0.3	1.4	<0.01	<0.1	<0.5
OBSV 6 MgCl₂ #6	11.76	0.08	<0.1	1.7	3.0	18	3.0	<0.5	0.4	<0.1	<0.1	0.3	0.7	<0.01	<0.1	<0.5
OBSV 6 MgCl₂ #7	11.80	0.10	<0.1	1.9	3.5	20	3.9	0.7	0.3	<0.1	<0.1	0.3	<0.5	<0.01	<0.1	0.7
OBSV 6 REF OUT	11.89	<0.02	<0.1	1.7	7.8	40	2.5	0.9	0.3	<0.1	<0.1	0.3	1.0	<0.01	<0.1	<0.5
OBSV 9 REF IN	11.92	<0.02	0.1	2.3	3.0	22	4.0	1.1	0.2	<0.1	<0.1	0.3	1.4	<0.01	<0.1	0.5
OBSV 9 SSW #1	12.09	<0.02	<0.1	2.3	2.9	19	12.7	1.7	0.1	<0.1	<0.1	0.2	0.9	<0.01	0.1	<0.5
OBSV 9 SSW #2	12.08	<0.02	0.1	1.8	3.1	19	3.5	1.6	0.3	<0.1	<0.1	0.2	0.8	<0.01	<0.1	0.7
OBSV 9 SSW #3	12.09	<0.02	<0.1	1.7	2.4	15	1.9	0.9	0.1	<0.1	<0.1	0.2	1.8	<0.01	<0.1	1.0
OBSV9 SSW #4	11.94	<0.02	0.1	2.1	3.0	19	3.5	0.9	0.2	<0.1	<0.1	0.3	<0.5	<0.01	<0.1	<0.5
OBSV 9 SSW #5	12.13	<0.02	0.2	2.0	2.6	18	2.2	1.5	0.1	<0.1	<0.1	0.3	<0.5	<0.01	<0.1	0.9
OBSV 9 SSW #6	12.13	<0.02	0.2	2.2	2.4	14	3.7	0.7	0.2	<0.1	<0.1	0.3	1.0	<0.01	<0.1	1.1
OBSV 9 REF OUT	11.92	<0.02	0.2	2.2	3.3	23	4.0	2.1	0.2	<0.1	<0.1	0.3	0.8	<0.01	<0.1	1.2
OBSV 12 REF IN	11.82	<0.02	0.2	2.1	2.5	16	3.4	1.1	0.2	<0.1	<0.1	0.3	<0.5	<0.01	<0.1	<0.5
OBSV 12 AF-SSW #1	11.80	0.13	0.2	2.2	2.8	18	6.8	0.8	0.2	<0.1	<0.1	0.2	<0.5	<0.01	<0.1	0.9
OBSV 12 AF-SSW #2	11.84	0.09	0.2	1.7	2.3	13	3.9	0.8	0.2	<0.1	<0.1	0.2	<0.5	0.01	<0.1	0.8
OBSV12 AF-SSW #3	11.86	0.10	0.3	2.1	2.3	17	3.7	1.4	0.2	<0.1	<0.1	0.2	2.1	<0.01	<0.1	0.6
OBSV 12 AF-SSW #4	11.83	0.12	0.2	2.3	3.2	20	4.9	1.4	0.2	<0.1	<0.1	0.2	0.7	<0.01	<0.1	0.6
OBSV 12 AF-SSW #5	11.75	0.10	0.2	2.0	2.7	17	4.7	1.0	0.1	<0.1	<0.1	0.2	<0.5	<0.01	<0.1	<0.5
OBSV 12 AF-SSW #6	11.75	0.10	0.2	2.3	2.7	14	4.7	1.0	0.1	<0.1	<0.1	0.2	1.4	0.01	<0.1	<0.5
OBSV 18 REF IN	11.91	0.02	0.1	2.0	2.0	11	<0.1	<0.5	0.2	<0.1	<0.1	<0.1	<0.5	<0.01	<0.1	<0.5
OBSV 18 AF-NaCl #1	11.79	<0.02	0.1	1.6	2.1	13	2.4	<0.5	0.2	<0.1	<0.1	0.2	1.3	<0.01	<0.1	0.6
OBSV 18 AF-NaCl #2	11.83	<0.02	0.2	1.5	2.4	14	2.5	1.3	0.2	<0.1	<0.1	0.2	<0.5	<0.01	<0.1	<0.5
OBSV 18 AF-NaCl #3	11.92	<0.02	0.1	1.2	1.6	11	3.1	0.7	0.1	<0.1	<0.1	0.3	7.5	<0.01	<0.1	<0.5
OBSV 18 AF-NaCl #4	11.93	<0.02	0.1	1.9	2.2	13	2.6	2.1	0.2	<0.1	<0.1	<0.1	27.7	<0.01	<0.1	<0.5
OBSV 18 AF-NaCl #5	12.03	<0.02	0.1	1.6	4.9	12	2.4	<0.5	0.2	0.2	<0.1	<0.1	<0.5	<0.01	<0.1	<0.5

8.13 Porosity calculations

Core length and diameter of OBSV samples were measured to calculate bulk volume (V_b). The pore volume (V_p) was calculated from the difference between the dry (M_{dry}) and saturated mass (M_{sat}) divided by saturation fluid density (ρ_{fluid}) given in Equation 4.

$$\phi_{core.pre-test} = \frac{V_p}{V_b} = \frac{M_{sat} - M_{dry}}{\rho_{fluid} V_b} \qquad \text{(Equation 4)}$$

Post-test porosity was calculated based on new V_b on post core length and diameter. The saturated volume (V_s) was determined based on cores post-test dry mass (M_s) and post-test density (ρ_s) which is provided in Equation 5.

$$\phi_{core.post-test} = \frac{V_p}{V_b} = \frac{V_b - V_s}{V_b} = 1 - \frac{V_s}{V_b} = 1 - \frac{M_s}{\rho_s V_b} \qquad \text{(Equation 5)}$$

Porosity powder core was acquired by measuring the length and diameter of powder core to determine V_b. The solid mass (M_s) and powder density were used to calculate V_s given in Equation 6.

$$\phi_{powder.pre-test} = \frac{V_p}{V_b} = \frac{V_b - V_s}{V_b} = 1 - \frac{V_s}{V_b} = 1 - \frac{M_s}{\rho_s V_b} \qquad \text{(Equation 6)}$$

Post-test porosity of powder samples was measured by acquiring post-test saturated (M_{sat}) and dry (M_{dry}) mass of powder core divided by fluid density (ρ_{fluid}) to determine V_p. V_b was calculated by measuring post-test length and diameter given in Equation 7.

$$\phi_{powder.post-test} = \frac{V_p}{V_b} = \frac{M_{sat} - M_{dry}}{\rho_{fluid} V_b} \qquad \text{(Equation 7)}$$

9 References

Abdollahpour. M.. Heberling. F.. Schild. D.. and Rahnemaie. R.. 2022. Magnesium Coprecipitation with Calcite at Low Supersaturation: Implications for Mg-Enriched Water in Calcareous Soils: Minerals. v. 12. no. 2. p. 265.

Abubeker. E.. 2013. Water weakening of chalks - comparsion of intact and fractured cores [Master Thesis]: University of Stavanger. 88 p.

Adeyemi. B. J.. Jadhawar. P.. and Akanji. L.. 2023. Evolution and Interfacial Dynamics of Thin Electrolyte Films in Oil–Brine–Carbonate Rock Systems due to Chemical Equilibrium Disruptions: Energy & Fuels. v. 37. no. 1. p. 175-190.

Agarwal. B.. Hermansen. H.. Sylte. J. E.. and Thomas. L. K.. 2000. Reservoir Characterization of Ekofisk Field: A Giant. Fractured Chalk Reservoir in the Norwegian North Sea-History Match: SPE Reservoir Evaluation & Engineering. v. 3. no. 06. p. 534-543.

Agosta. F.. Prasad. M.. and Aydin. A.. 2007. Physical properties of carbonate fault rocks. fucino basin (Central Italy): implications for fault seal in platform carbonates: Geofluids. v. 7. no. 1. p. 19-32.

Alsharhan. A. S.. and Kendall. C. G. S. C.. 2003. Holocene coastal carbonates and evaporites of the southern Arabian Gulf and their ancient analogues: Earth-Science Reviews. v. 61. no. 3. p. 191-243.

Amour. F.. Bonto. M.. Hajiabadi. M. R.. and Nick. H. M.. Sensitivity Study of Chemical Effects on the Compaction Behavior of Reservoir Chalk (Dan Field. Danish North Sea). *in* Proceedings 55th U.S. Rock Mechanics/Geomechanics Symposium2021. Volume All Days: ARMA-2021-1998.

Amour. F.. Hajiabadi. M. R.. and Nick. H. M.. 2023. Impact of uncertainties associated with the choice of the yield stress on the prediction of subsurface reservoir compaction: A field study:

International Journal of Rock Mechanics and Mining Sciences. v. 161. p. 105280.

Andersen. P. Ø.. 2019. A simplified modelling approach for petroleum recovery by spontaneous imbibition in naturally fractured reservoirs: Journal of Natural Gas Science and Engineering. v. 63. p. 95-114.

Andersen. P. Ø.. Wang. W.. Madland. M. V.. Zimmermann. U.. Korsnes. R. I.. Bertolino. S.. Schulz. B.. Gilbricht. S.. and Minde. M. W.. 2018. Comparative Study of Five Outcrop Chalks Flooded at Reservoir Conditions: Chemo-mechanical Behaviour and Profiles of Compositional Alteration: Transport in Porous Media. v. 121. no. 1. p. 135-181.

Anderson. T. F.. Arthur. M. A.. Arthur. M. A.. Anderson. T. F.. Kaplan. I. R.. Veizer. J.. and Land. L. S.. 1983. Stable Isotopes of Oxygen and Carbon and their Application to Sedimentologic and Paleoenvironmental Problems. Stable Isotopes in Sedimentary Geology. Volume 10. SEPM Society for Sedimentary Geology. p. 0.

Anderson. W. G.. 1986. Wettability Literature Survey- Part 1: Rock/Oil/Brine Interactions and the Effects of Core Handling on Wettability: Journal of Petroleum Technology. v. 38. no. 10. p. 1125-1144.

Audinot. J.-N.. Philipp. P.. De Castro. O.. Biesemeier. A.. Hoang. Q. H.. and Wirtz. T.. 2021. Highest resolution chemical imaging based on secondary ion mass spectrometry performed on the helium ion microscope: Reports on progress in physics. Physical Society (Great Britain). v. 84. no. 10.

Austad. T.. Shariatpanahi. S. F.. Strand. S.. Aksulu. H.. and Puntervold. T.. 2015. Low Salinity EOR Effects in Limestone Reservoir Cores Containing Anhydrite: A Discussion of the Chemical Mechanism: Energy & Fuels. v. 29. no. 11. p. 6903-6911.

Austad. T.. Strand. S.. Madland. M. V.. Puntervold. T.. and Korsnes. R. I.. 2008. Seawater in Chalk: An EOR and Compaction Fluid: SPE Reservoir Evaluation & Engineering. v. 11. no. 04. p. 648-654.

Barkved. O.. Pete. H.. Roar. K.. Tore. K.. and Kristiansen. T.. 2003. Valhall Field - Still on Plateau after 20 Years of Production. v. 11.

124

Berre. I.. Doster. F.. and Keilegavlen. E.. 2019. Flow in Fractured Porous Media: A Review of Conceptual Models and Discretization Approaches: Transport in Porous Media. v. 130. no. 1. p. 215-236.

Bisdom. K.. Bertotti. G.. and Nick. H. M.. 2016. The impact of different aperture distribution models and critical stress criteria on equivalent permeability in fractured rocks: Journal of Geophysical Research: Solid Earth. v. 121. no. 5. p. 4045-4063.

Bjørlykke. K.. and Høeg. K.. 1997. Effects on burial diagenesis of stress. compaction and fluid flow in sedimentary basins. 267-276 p.:

Blinkenberg. K. H.. Anderskouv. K.. Sheldon. E.. Bjerrum. C. J.. and Stemmerik. L.. 2020. Stratigraphically controlled silicification in Danian chalk and its implications for reservoir properties. southern Danish Central Graben: Marine and Petroleum Geology. v. 115. p. 104134.

Blinkenberg. K. H.. Anderskouv. K.. Sølling. T. I.. Al-Ramadan. K.. and Stemmerik. L.. 2021. The influence of silica on carbonate diagenesis in chalk – Ekofisk Formation. Danish Central Graben: Sedimentary Geology. v. 415. p. 105846.

Boersma. Q.. Athmer. W.. Haege. M.. Etchebes. M.. Haukås. J.. and Bertotti. G.. 2020. Natural fault and fracture network characterization for the southern Ekofisk field: A case study integrating seismic attribute analysis with image log interpretation: Journal of Structural Geology. v. 141. p. 104197.

Braithwaite. C.. Rizzi. G.. and Darke. G.. 2004. The Geometry and Petrogenesis of Dolomite Hydrocarbon Reservoirs. Geological Society. Special Publications. Edited by CJR Braithwaite. G. Rizzi. and G. Darke ….

Brunauer. S.. Emmett. P. H.. and Teller. E.. 1938. Adsorption of Gases in Multimolecular Layers: Journal of the American Chemical Society. v. 60. no. 2. p. 309-319.

Caine. J. S.. Evans. J. P.. and Forster. C. B.. 1996. Fault zone architecture and permeability structure: Geology. v. 24. no. 11. p. 1025-1028.

Callister. J. W. D.. 2007. Material Science and Engineering. An Introduction.. New York. Department of Metalurgical Engieering. The University of Utah.

Chester. F. M.. Evans. J. P.. and Biegel. R. L.. 1993. Internal structure and weakening mechanisms of the San Andreas Fault: Journal of Geophysical Research: Solid Earth. v. 98. no. B1. p. 771-786.

Chilingar. G. V.. 1957. Classification of limestones and dolomites on basis of Ca/Mg ratio: Journal of Sedimentary Research. v. 27. no. 2. p. 187-189.

Cook. C. C.. and Jewell. S.. 1996. Simulation of a North Sea Field Experiencing Significant Compaction Drive: SPE Reservoir Engineering. v. 11. no. 01. p. 48-53.

Cornet. and Briart. 2000. Saint-Vaast Chalk Formation - SVA. Volume 2022: National Commission for Stratigraphy Belgium.

Curtis. C. D.. Murchison. D. G.. Berner. R. A.. Shaw. H.. Sarnthein. M.. Durand. B.. Eglinton. G.. Mackenzie. A. S.. Surdam. R. C.. Eglinton. G.. Curtis. C. D.. McKenzie. D. P.. and Murchison. D. G.. 1985. Clay mineral precipitation and transformation during burial diagenesis: Philosophical Transactions of the Royal Society of London. Series A. Mathematical and Physical Sciences. v. 315. no. 1531. p. 91-105.

Dąbrowski. A.. 2001. Adsorption — from theory to practice: Advances in Colloid and Interface Science. v. 93. no. 1. p. 135-224.

Davies. G. R.. 1979. Dolomite reservoir rocks: processes. controls. porosity development.

Derkani. M. H.. Fletcher. A. J.. Fedorov. M.. Abdallah. W.. Sauerer. B.. Anderson. J. and Zhang. Z. J.. 2019. Mechanisms of Surface Charge Modification of Carbonates in Aqueous Electrolyte Solutions: Colloids and Interfaces. v. 3. no. 4. p. 62.

Doornhof. D.. Kristiansen. T. G.. Nagel. N. B.. Pattillo. P. D.. and Sayers. C.. 2006. Compaction and subsidence: Oilfield Review. v. 18. no. 3. p. 50-68.

Dowsett. D.. and Wirtz. T.. 2017. Co-registered in situ secondary electron and mass spectral imaging on the helium ion microscope demonstrated using lithium titanate and magnesium oxide nanoparticles: Analytical chemistry. v. 89. no. 17. p. 8957-8965.

Drits. V. A.. Skibsted. J.. Dorzhieva. O. V.. Fallick. A. E.. and Lindgreen. H.. 2017. Structural characterization of marine nano-quartz in chalk and flint from North Sea Tertiary chalk reservoirs for oil and gas: American Mineralogist. v. 102. no. 7. p. 1402-1417.

Dusar. M.. and Lagrou. D.. 2007. Cretaceous flooding of the Brabant Massif and the lithostratigraphic characteristics of its chalk cover in northern Belgium: Geologica Belgica. v. 10. p. 27-38.

Egeberg. P. K.. and Saigal. G. C.. 1991. North Sea chalk diagenesis: cementation of chalks and healing of fractures: Chemical Geology. v. 92. no. 4. p. 339-354.

Fabricius. I. L.. 2007. Chalk: composition. diagenesis and physical properties: Bulletin of the Geological Society of Denmark. v. 55. p. 97-128.

Fabricius. I. L.. and Borre. M. K.. 2007. Stylolites. porosity. depositional texture. and silicates in chalk facies sediments. Ontong Java Plateau – Gorm and Tyra fields. North Sea: Sedimentology. v. 54. no. 1. p. 183-205.

Fabricius. I. L.. Mavko. G.. Mogensen. C.. and Japsen. P.. 2002. Elastic moduli of chalk as a reflection of porosity. sorting. and irreducible water saturation. SEG Technical Program Expanded Abstracts 2002. p. 1903-1906.

Gachuz-Muro. H.. Sohrabi. M.. and Pemex. E.. Prediction. control and validation of rock dissolution during smart water injection and its impact on waterflood performance in heavy oil carbonate reservoirs. *in* Proceedings International Symposium of the Society of Core Analyst. Vienna. Austria2017.

Geitle. K.. 2013. Chemically induced compaction in fractured and intact chalk cores [Master Thesis]: University of Stavanger. 78 p.

Gennaro. M.. 2011. 3D seismic stratigraphy and reservoir characterization of the Chalk Group in the Norwegian Central Graben. North Sea [PhD Thesis]: University of Bergen.

Gennaro. M.. Wonham. J. P.. Sælen. G.. Walgenwitz. F.. Caline. B.. and Faÿ-Gomord. O.. 2013. Characterization of dense zones within the Danian chalks of the Ekofisk Field. Norwegian North Sea: Petroleum Geoscience. v. 19. no. 1. p. 39-64.

Glad. A. C.. Afrough. A.. Amour. F.. Ferreira. C. A. S.. Price. N.. Clausen. O. R.. and Nick. H. M.. 2023. Anatomy of fractures: Quantifying fracture geometry utilizing X-ray computed tomography in a chalk-marl reservoir; the Lower Cretaceous Valdemar Field (Danish Central Graben): Journal of Structural Geology. v. 174. p. 104936.

Goddard. J. V.. and Evans. J. P.. 1995. Chemical changes and fluid-rock interaction in faults of crystalline thrust sheets. northwestern Wyoming. U.S.A: Journal of Structural Geology. v. 17. no. 4. p. 533-547.

Gómez. J.. Goy. A.. and Canales. M.. 2008. Seawater temperature and carbon isotope variations in belemnites linked to mass extinction during the Toarcian (Early Jurassic) in Central and Northern Spain. Comparison with other European sections: Palaeogeography. Palaeoclimatology. Palaeoecology. v. 258. no. 1-2. p. 28-58.

Groenendijk. D. J.. and van Wunnik. J. N. M.. 2021. Surfactant Adsorption and Ion Exchange on Calcite Surfaces: Energy & Fuels. v. 35. no. 10. p. 8763-8772.

Gutierrez. M.. Tunbridge. L. W.. Hansteen. H.. Makurat. A.. Barton. N.. and Landa. G.. 2013. Modelling of the Compaction Behaviour of Fractured Chalk.

Hao. J.. Feilberg. K. L.. and Shapiro. A.. 2020. Kinetics of calcite dissolution and Ca–Mg ion exchange on the surfaces of north sea chalk powders: ACS omega. v. 5. no. 28. p. 17506-17520.

Hao. J.. and Shapiro. A.. 2019. Effect of Compaction on Oil Recovery Under Low Salinity Flooding in Homogeneous and Heterogeneous Chalk.

Hassenkam. T.. Johnsson. A.. Bechgaard. K.. and Stipp. S. L. S.. 2011. Tracking single coccolith dissolution with picogram resolution and implications for CO2 sequestration and ocean acidification: Proceedings of the National Academy of Sciences. v. 108. no. 21. p. 8571-8576.

Hassenkam. T.. Skovbjerg. L.. and Stipp. S.. 2009. Probing the intrinsically oil-wet surfaces of pores in North Sea chalk at subpore resolution: Proceedings of the National Academy of Sciences of the United States of America. v. 106. p. 6071-6076.

Heggheim. T.. Madland. M. V.. Risnes. R.. and Austad. T.. 2005. A chemical induced enhanced weakening of chalk by seawater: Journal of Petroleum Science and Engineering. v. 46. p. 171-184.

Hermansen. H.. Landa. G. H.. Sylte. J. E.. and Thomas. L. K.. 2000. Experiences after 10 years of waterflooding the Ekofisk Field. Norway: Journal of Petroleum Science and Engineering. v. 26. no. 1. p. 11-18.

Hiorth. A.. Bache. Ø.. Jettestuen. E.. Cathles. L. M.. Moe. R. W.. Omdal. E.. Korsnes. R. I.. and Madland. M. V.. 2011. A Simplified Approach to Translate Chemical Alteration in Core Experiments to Field Conditions. . International Symposium of the Society of Core Analysts.: Austin. TX. USA.

Hiorth. A.. Cathles. L. M.. and Madland. M. V.. 2010. The Impact of Pore Water Chemistry on Carbonate Surface Charge and Oil Wettability: Transport in Porous Media. v. 85. no. 1. p. 1-21.

Hjuler. M.. and Fabricius. I. L.. 2009. Engineering properties of chalk related to diagenetic variations of Upper Cretaceous onshore and offshore chalk in the North Sea area: Journal of Petroleum Science and Engineering. v. 68. no. 3-4. p. 151-170.

Hjuler. M.. Hansen. V.. and Fabricius. I.. 2018. Interpretational challenges related to studies of chalk particle surfaces in scanning and transmission electron microscopy: Bulletin of the Geological Society of Denmark. v. 66. p. 151-165.

Hlawacek. G.. and Gölzhäuser. A.. 2016. Helium Ion Microscopy. *in* Hlawacek. G.. and Gölzhäuser. A.. eds.. Springer International Publishing. p. 526.

Hull. D.. and Bacon. D. J.. 2011. Chapter 2 - Observation of Dislocations. *in* Hull. D.. and Bacon. D. J.. eds.. Introduction to Dislocations (Fifth Edition): Oxford. Butterworth-Heinemann. p. 21-41.

Ioannou. I.. Hoff. W.. and Hall. C.. 2004. On the role of organic adlayers in the anomalous water sorptivity of Lepine limestone: Journal of colloid and interface science. v. 279. p. 228-234.

Japsen. P.. Dysthe. D. K.. Hartz. E. H.. Stipp. S. L. S.. Yarushina. V. M.. and Jamtveit. B.. 2011. A compaction front in North Sea chalk: Journal of Geophysical Research: Solid Earth. v. 116. no. B11.

Kallesten. E. I.. Cherif. Y.. Madland. M. V.. Korsnes. R. I.. Omdal. E.. Andersen. P. Ø.. and Zimmermann. U.. 2021a. Validation study of water weakening research from outcrop chalks performed on Eldfisk reservoir cores: Journal of Petroleum Science and Engineering. v. 198. p. 108164.

Kallesten. E. I.. Zimmermann. U.. Madland. M. V.. Bertolino. S.. Omdal. E.. and Andersen. P. Ø.. 2021b. Mineralogy and geochemistry of reservoir and non-reservoir chalk from the Norwegian

continental shelf: Journal of Petroleum Science and Engineering. v. 205. p. 108914.

Katika. K.. Alam. M. M.. Alexeev. A.. Chakravarty. K. H.. Fosbøl. P. L.. Revil. A.. Stenby. E.. Xiarchos. I.. Yousefi. A.. and Fabricius. I. L.. 2018. Elasticity and electrical resistivity of chalk and greensand during water flooding with selective ions: Journal of Petroleum Science and Engineering. v. 161. p. 204-218.

Keszthelyi. D.. Dysthe. D. K.. and Jamtveit. B.. 2016. Compaction of North-Sea Chalk by Pore-Failure and Pressure Solution in a Producing Reservoir: Frontiers in Physics. v. 4.

Kim. S.. Trofimov. A.. Khanom. F.. Stern. L.. Lamberti. W.. Colby. R.. Abmayr. D.. Belianinov. A.. and Ovchinnikova. O. S.. 2019. High Resolution Multimodal Chemical Imaging Platform for Organics and Inorganics: Anal Chem. v. 91. no. 19. p. 12142-12148.

Kokal. S.. and Al-Kaabi. A.. 2010. Enhanced oil recovery: challenges & opportunities: World Petroleum Council: Official Publication. v. 64. p. 64-69.

Korsnes. R.. Madland. M. V.. Austad. T.. Haver. S.. and Røsland. G.. 2008. The effects of temperature on the water weakening of chalk by seawater: Journal of Petroleum Science and Engineering. v. 60. p. 183-193.

Korsnes. R. I.. Madland. M. V.. and Austad. T.. 2006a. Impact of brine composition on the mechanical strength of chalk at high Temperature. Taylor & Francis. p. 133-140.

Korsnes. R. I.. Strand. S.. Hoff. Ø.. Pedersen. T.. Madland. M. V.. and Austad. T.. 2006b. Does the chemical interaction between seawater and chalk affect the mechanical properties of chalk?. Multiphysics Coupling and Long Term Behaviour in Rock Mechanics: https://doi.org/10.1201/9781439833469.ch61.. Taylor & Francis. p. 427-434.

Krinsley. D. H.. and Doornkamp. J. C.. 1973. Atlas of Quartz Sand Surface Textures. London. Press. Cambridge Univ.

Kristiansen. T. G.. and Flatebø. R. E.. 2010. Sixty Days Ahead of Schedule: Reducing Drilling Risk at Valhall Using Computational Geomechanics: SPE Drilling & Completion. v. 25. no. 04. p. 544-554.

Laczkó-Dobos. E.. Gier. S.. Sztanó. O.. Milovský. R.. and Hips. K.. 2020. Porosity Development Controlled by Deep-Burial Diagenetic Process in Lacustrine Sandstones Deposited in a Back-Arc Basin (Makó Trough. Pannonian Basin. Hungary): Geofluids. v. 2020. p. 9020684.

Laubach. S. E.. 2003. Practical approaches to identifying sealed and open fractures: AAPG Bulletin. v. 87. no. 4. p. 561-579.

Laubach. S. E.. Lander. R. H.. Criscenti. L. J.. Anovitz. L. M.. Urai. J. L.. Pollyea. R. M.. Hooker. J. N.. Narr. W.. Evans. M. A.. Kerisit. S. N.. Olson. J. E.. Dewers. T.. Fisher. D.. Bodnar. R.. Evans. B.. Dove. P.. Bonnell. L. M.. Marder. M. P.. and Pyrak-Nolte. L.. 2019. The Role of Chemistry in Fracture Pattern Development and Opportunities to Advance Interpretations of Geological Materials: Reviews of Geophysics. v. 57. no. 3. p. 1065-1111.

Lindgreen. H.. Drits. V. A.. Jakobsen. F. C.. and Sakharov. B. A.. 2008. Clay mineralogy of the central north Sea upper Cretaceous—Tertiary chalk and the formation of clay-rich layers: Clays and Clay Minerals. v. 56. no. 6. p. 693-710.

Lindgreen. H.. Drits. V. Sakharov. Boris Jakobsen. H. Salyn. A. Dainyak. L. Krøyer. H.. 2002. The structure and diagenetic transformation of illite-smectite and chlorite-smectite from North Sea Cretaceous-Tertiary chalk: Clay Minerals - CLAY MINER. v. 37. p. 429-450.

Lünsdorf. N. K.. Kalies. J.. Ahlers. P.. Dunkl. I.. and von Eynatten. H.. 2019. Semi-Automated Heavy-Mineral Analysis by Raman Spectroscopy: Minerals. v. 9. no. 7. p. 385.

Machel. H.. 2004. Concepts and models of dolomitization: A critical reappraisal: Geological Society. London. Special Publications. v. 235. p. 7-63.

Madland. M. V.. Finsnes. A.. Alkafadgi. A.. Risnes. R.. and Austad. T.. 2006. The influence of CO2 gas and carbonate water on the mechanical stability of chalk: Journal of Petroleum Science and Engineering. v. 51. p. 149-168.

Madland. M. V.. Hiorth. A.. Omdal. E.. Megawati. M.. Hildebrand-Habel. T.. Korsnes. R. I.. Evje. S.. and Cathles. L. M.. 2011. Chemical Alterations Induced by Rock–Fluid Interactions When Injecting Brines in High Porosity Chalks: Transport in Porous Media. v. 87. no. 3. p. 679-702.

131

Madland. M. V.. Midtgarden. K.. Manafov. R.. Korsnes. R. I.. Kristiansen. T. G.. and Hjort. A.. 2008. The effect of temperature and brine composition on the mechanical strength of Kansas chalk. International Symposium of the Society of Core Analysts: Abu Dhabi. p. 6.

Madsen. L.. 2015. Calcite: Surface Charge: Encyclopedia of Surface and Colloid Science. Third Edition. CRC Press.

Matthiesen. J.. Bovet. N.. Hilner. E.. Andersson. M. P.. Schmidt. D. A.. Webb. K. J.. Dalby. K. N.. Hassenkam. T.. Crouch. J.. Collins. I. R.. and Stipp. S. L. S.. 2014. How Naturally Adsorbed Material on Minerals Affects Low Salinity Enhanced Oil Recovery: Energy & Fuels. v. 28. no. 8. p. 4849-4858.

Megawati. M.. Andersen. P. Ø.. Korsnes. R. I. E.. Steinar. Hiorth. A.. and Madland. M. V.. 2011. The Effect of Aqueous Chemistry pH on the Time-Dependent Deformation Behaviour of Chalk-Experimental and Modelling Study. Les Rencontres scientifiques d'IFP Energies Nouvelles. Flows and mechanics in natural porous media from pore to field scale Paris. 16-18 November. Pore2Fluid IFP Energ. Nouv.

Megawati. M.. Hiorth. A.. and Madland. M. V.. 2013. The Impact of Surface Charge on the Mechanical Behavior of High-Porosity Chalk: Rock Mechanics and Rock Engineering. v. 46. p. 1073-1090.

Megawati. M.. Madland. M. V.. and Hiorth. A.. 2015. Mechanical and physical behavior of high-porosity chalks exposed to chemical perturbation: Journal of Petroleum Science and Engineering. v. 133. p. 313-327.

Meireles. L. T. P.. Storebø. E. M.. and Lykke Fabricius. I.. 2019. Effect of electrostatic forces on the porosity of saturated mineral powder samples and implications for chalk strength: Geophysics. v. 85. no. 1. p. MR37-MR50.

Meireles. L. T. P.. Storebø. E. M.. Welch. M. J.. and Fabricius. I. L.. 2021. Water weakening of soft and stiff outcrop chalk induced by electrical double layer disjoining pressure: International Journal of Rock Mechanics and Mining Sciences. v. 141. p. 104700.

Melezhik. V.. Roberts. D.. Gjelle. S.. Solli. A.. Fallick. A. E.. Kuznetsov. A.. and Gorokhov. I.. 2013. Isotope chemostratigraphy of high-

grade marbles in the Rognan area. North-Central Norwegian Caledonides: A new geological map. and tectonostratigraphic and palaeogeographic implications: Norsk Geologisk Tidsskrift. v. 93. p. 107-139.

Mercado. K. P.. Radhakrishnan. K.. Stewart. K.. Snider. L.. Ryan. D.. and Haworth. K. J.. 2016. Size-isolation of ultrasound-mediated phase change perfluorocarbon droplets using differential centrifugation: The Journal of the Acoustical Society of America. v. 139. no. 5. p. EL142-EL142.

Michie. E. A. H.. Haines. T. J.. Healy. D.. Neilson. J. E.. Timms. N. E.. and Wibberley. C. A. J.. 2014. Influence of carbonate facies on fault zone architecture: Journal of Structural Geology. v. 65. p. 82-99.

Minde. M. W.. and Hiorth. A.. 2020. Compaction and Fluid—Rock Interaction in Chalk Insight from Modelling and Data at Pore-. Core-. and Field-Scale: Geosciences. v. 10. no. 1. p. 6.

Minde. M. W.. Madland. M. V.. Zimmermann. U.. Egeland. N.. Korsnes. R. I.. Nakamura. E.. Kobayashi. K.. and Ota. T.. 2019. Mineralogical alterations in calcite powder flooded with MgCl2 to study Enhanced Oil Recovery (EOR) mechanisms at pore scale: Microporous and Mesoporous Materials. v. 304. p. 109402.

Minde. M. W.. Wang. W.. Madland. M. V.. Zimmermann. U.. Korsnes. R. I.. Bertolino. S.. and Andersen. P. Ø.. 2018. Temperature effects on rock engineering properties and rock-fluid chemistry in opal-CT-bearing chalk: Journal of Petroleum Science and Engineering. v. 169. p. Pages 454-470.

Minde. M. W.. Zimmermann. U.. Madland. M. V.. Korsnes. R. I.. Schulz. B.. and Gilbricht. S.. 2020. Mineral replacement in long-term flooded porous carbonate rocks: Geochimica et Cosmochimica Acta. v. 268. p. 485-508.

Mohammed. I.. Al Shehri. D.. Mahmoud. M.. Kamal. M. S.. Arif. M.. Alade. O. S.. and Patil. S.. 2022. Investigation of Surface Charge at the Mineral/Brine Interface: Implications for Wettability Alteration: Frontiers in Materials. v. 9.

Morse. J. W.. Wang. Q.. and Tsio. M. Y.. 1997. Influences of temperature and Mg:Ca ratio on CaCO3 precipitates from seawater: Geology. v. 25. no. 1. p. 85-87.

133

Mukherjee. H.. Poe. B.. Heidt. H.. Watson. T.. and Barree. R. D.. 1995. Effect of Pressure Depletion on Fracture Geometry Evolution and Production Performance. SPE Annual Technical Conference and Exhibition: Dallas. Texas. Society of Petroleum Engineers. p. 8.

Mustafa. A.. Alzaki. T.. Aljawad. M.. Solling. T.. and Dvorkin. J.. 2022. Impact of acid wormhole on the mechanical properties of chalk. limestone. and dolomite: Experimental and modeling studies: Energy Reports. v. 8. p. 605-616.

Nermoen. A.. 2018. Porosity Evolution during Chemo-Mechanical Compaction. *in* Taher Hcine. G.. ed.. Porosity: Rijeka. IntechOpen. p. Ch. 9.

Nermoen. A.. Korsnes. R. I.. Aursjø. O.. Madland. M. V.. Kjørslevik. T. A. C.. and Østensen. G.. 2016. How Stress and Temperature Conditions Affect Rock-Fluid Chemistry and Mechanical Deformation: Frontiers in Physics. v. 4. no. 2.

Nermoen. A.. Korsnes. R. I.. Hiorth. A.. and Madland. M. V.. 2015. Porosity and permeability development in compacting chalks during flooding of nonequilibrium brines: Insights from long-term experiment: Journal of Geophysical Research: Solid Earth. v. 120. no. 5. p. 2935-2960.

Newman. G. H.. 1983. The Effect of Water Chemistry on the Laboratory Compression and Permeability Characteristics of Some North Sea Chalks: Journal of Petroleum Technology. v. 35. no. 05. p. 976-980.

Nogués. J.. Fitts. J.. Celia. M.. and Peters. C.. 2013. Permeability evolution due to dissolution and precipitation of carbonates using reactive transport modeling in pore networks: Water Resources Research. v. 49.

Okhrimenko. D.. Dalby. K.. Skovbjerg. L.. Bovet. N.. Christensen. J.. and Stipp. S.. 2014. The surface reactivity of chalk (biogenic calcite) with hydrophilic and hydrophobic functional groups: Geochimica et Cosmochimica Acta. v. 128. p. 212–224.

Petrash. D. A.. Bialik. O. M.. Bontognali. T. R. R.. Vasconcelos. C.. Roberts. J. A.. McKenzie. J. A.. and Konhauser. K. O.. 2017. Microbially catalyzed dolomite formation: From near-surface to burial: Earth-Science Reviews. v. 171. p. 558-582.

Philip. Z. G.. Jennings. J. W.. Olson. J. E.. Laubach. S. E.. and Holder. J.. 2005. Modeling Coupled Fracture-Matrix Fluid Flow in Geomechanically Simulated Fracture Networks: SPE Reservoir Evaluation & Engineering. v. 8. no. 04. p. 300-309.

Pierre. A. C.. Lamarche. J. M.. Mercier. R.. Foissy. A.. and Persello. J.. 1990. Calcium as a potential determining ion in aqueous calcite suspension: Journal of Dispersion Science and Technology. v. 11. p. 611-635.

Pillatsch. L.. Vanhove. N.. Dowsett. D.. Sijbrandij. S.. Notte. J.. and Wirtz. T.. 2013. Study and optimisation of SIMS performed with He+ and Ne+ bombardment: Applied Surface Science. v. 282. p. 908.

Pirson. S.. Spagna. P.. Baele. J.-M.. Damblon. F.. Gerrienne. P.. Vanbrabant. Y.. and Yans. J.. 2008. An overview of the Geology of Belgium. 5-25 p.:

Pokrovsky. O.. Mielczarski. J.. and Barres. O.. 2000. Surface Speciation Models of Calcite and Dolomite/Aqueous Solution Interfaces and Their Spectroscopic Evaluation: Langmuir. v. 16. p. 2677-2688.

Priebe. A.. Barnes. J.-P.. Edwards. T. E. J.. Pethö. L.. Balogh. I.. and Michler. J.. 2019. 3D Imaging of Nanoparticles in an Inorganic Matrix Using TOF-SIMS Validated with STEM and EDX: Analytical Chemistry. v. 91. no. 18. p. 11834-11839.

Puntervold. T.. Mamonov. A.. Torrijos . I. D. P.. and Strand. S.. 2021. Adsorption of Crude Oil Components onto Carbonate and Sandstone Outcrop Rocks and Its Effect on Wettability: Energy & Fuels. v. 35. no. 7. p. 5738-5747.

Puntervold. T.. Strand. S.. and Austad. T.. 2007. Water Flooding of Carbonate Reservoirs: Effects of a Model Base and Natural Crude Oil Bases on Chalk Wettability: Energy & Fuels. v. 21. no. 3. p. 1606-1616.

Puntervold. T.. Strand. S.. Ellouz. R.. and Austad. T.. 2015. Modified seawater as a smart EOR fluid in chalk: Journal of Petroleum Science and Engineering. v. 133. p. 440-443.

Puntervold. T.. Strand. S.. Torrijos. I. D. P.. Hopkins. P.. and Austad. T.. 2018. Enhancing Oil Recovery from Dolomitic Reservoirs-Investigation of Temperature Limitations. SPE EOR Conference at Oil and Gas West Asia: Muscat. Oman. Society of Petroleum Engineers. p. 15.

Rinderknecht. C. J.. Hasiuk. F. J.. and Oborny. S. C.. 2021. Mg zonation and heterogeneity in low-Mg calcite microcrystals of a depositional chalk: Journal of Sedimentary Research. v. 91. no. 8. p. 795-811.

Risnes. R.. 2001. Deformation and yield in high porosity outcrop chalk: Physics and Chemistry of the Earth. Part A: Solid Earth and Geodesy. v. 26. no. 1. p. 53-57.

Risnes. R.. Haghighi. H.. Korsnes. R. I.. and Natvik. O.. 2003. Chalk–fluid interactions with glycol and brines: Tectonophysics. v. 370. no. 1. p. 213-226.

Risnes. R.. Madland. M.. Hole. M.. and Kwabiah. N.. 2005. Water weakening of chalk—Mechanical effects of water–glycol mixtures: Journal of Petroleum Science and Engineering. v. 48. no. 1-2. p. 21-36.

Robaszynski. F.. Dhondt. A.. and Jagt. J.. 2001. Cretaceous lithostratigraphic units (Belgium): Geologica Belgica. v. 4. p. 121-134.

Romanuka. J.. Hofman. J. P.. Ligthelm. D. J.. Suijkerbuijk. B. M.. Marcelis. A. H.. Oedai. S.. Brussee. N. J.. van der Linde. A.. Aksulu. H.. and Austad. T.. Low Salinity EOR in Carbonates. *in* Proceedings SPE Improved Oil Recovery Symposium2012. Volume All Days: SPE-153869-MS.

Røyne. A.. Bisschop. J.. and Dysthe. D.. 2011. Experimental investigation of surface energy and subcritical crack growth in calcite: Journal of Geophysical Research-Solid Earth. v. 116.

Røyne. A.. Dalby. K. N.. and Hassenkam. T.. 2015. Repulsive hydration forces between calcite surfaces and their effect on the brittle strength of calcite-bearing rocks: Geophysical Research Letters. v. 42. no. 12. p. 4786-4794.

Sachdeva. J. S.. Nermoen. A.. Korsnes. R. I.. and Madland. M. V.. 2020. Effect of Initial Wettability on Rock Mechanics and Oil Recovery: Comparative Study on Outcrop Chalks: Transport in Porous Media. v. 133. no. 1. p. 85-117.

Salathiel. R. A.. 1973. Oil Recovery by Surface Film Drainage In Mixed-Wettability Rocks: Journal of Petroleum Technology. v. 25. p. 1216-1224.

Scholle. P. A.. 1977. Chalk Diagenesis and Its Relation to Petroleum Exploration: Oil from Chalks. a Modern Miracle?1: AAPG Bulletin. v. 61. no. 7. p. 982-1009.

Scholle. P. A.. Hsu. K.. and Jenkyns. H.. 1974. Diagenesis of Upper Cretaceous chalks from England. Northern Ireland and the North Sea. Pelagic Sediments: on Land and under the Sea. Volume 1. Spec. Publs int. Ass. Sediment. p. 177-210.

Scholle. P. A.. and Kinsman. D. J. J.. 1973. Diagenesis of upper Cretaceous chalks from North Sea. England and Northern Ireland: The American Association of Petroleum Geologists Bulletin. v. 57. no. 4. p. 803-804.

Schroeder. C. G.. P. Bergerat. F. Vandycke. S. Coulon. M.. 2006. Faults and matrix deformations in chalk: contribution of porosity and sonic wave velocity measurements: Bulletin de la Société Géologique de France. v. 177. no. 4. p. 203-213.

Schulz. B.. Sandmann. D.. and Gilbricht. S.. 2020. SEM-Based Automated Mineralogy and Its Application in Geo- and Material Sciences: Minerals. v. 10. no. 11. p. 1004.

Shariatpanahi. S. F.. Hopkins. P.. Aksulu. H.. Strand. S.. Puntervold. T.. and Austad. T.. 2016. Water Based EOR by Wettability Alteration in Dolomite: Energy & Fuels. v. 30. no. 1. p. 180-187.

Simonsen. L.. and Toft. J.. 2006. Texture. composition and stratigraphy of volcanic ash beds in lower Palaeocene chalk from the North Sea Central Graben area: Marine and Petroleum Geology. v. 23. p. 767–776.

Skovbjerg. L.. Hassenkam. T.. Makovicky. E.. Hem. C.. Yang. M.. Bovet. N.. and Stipp. S.. 2012. Nano sized clay detected on chalk particle surfaces: Geochimica et Cosmochimica Acta. v. 99. p. 57–70.

Skovbjerg. L.. Okhrimenko. D.. Khoo. J.. Dalby. K.. Hassenkam. T.. Makovicky. E.. and Stipp. S.. 2013. Preferential Adsorption of Hydrocarbons to Nanometer-Sized Clay on Chalk Particle Surfaces: Energy & Fuels. v. 27. p. 3642–3652.

Snow. S. E.. and Brownlee. M. H.. 1989. Practical and Theoretical aspects of Well Testing in the Ekofisk Area Chalk Fields.: SPE Annual Technical Conference and Exibition.

Soleimani. M.. 2017. Naturally fractured hydrocarbon reservoir simulation by elastic fracture modeling: Petroleum Science. v. 14. no. 2. p. 286-301.

Strand. S.. Hjuler. M. L.. Torsvik. R.. Pedersen. J. I.. Madland. M. V.. and Austad. T.. 2007. Wettability of chalk: impact of silica. clay content and mechanical properties: Petroleum Geoscience. v. 13. no. 1. p. 69-80

Strand. S.. Standnes. D. C.. and Austad. T.. 2003. Spontaneous Imbibition of Aqueous Surfactant Solutions into Neutral to Oil-Wet Carbonate Cores: Effects of Brine Salinity and Composition: Energy & Fuels. v. 17. no. 5. p. 1133-1144.

Sulak. R. M.. and Danielsen. J.. 1989. Reservoir Aspects of Ekofisk Subsidence.

Sun. S. Q.. 1995. Dolomite Reservoirs: Porosity Evolution and Reservoir Characteristics1: AAPG Bulletin. v. 79. no. 2. p. 186-204.

Sylte. J. E.. Thomas. L. K.. Rhett. D. W.. Bruning. D. D.. and Nagel. N. B.. Water Induced Compaction in the Ekofisk Field. *in* Proceedings SPE Annual Technical Conference and Exhibition1999. Volume All Days: SPE-56426-MS.

Sylvester. P. J.. 2012. Use of the mineral liberation analyzer (MLA) for mineralogical studies of sediments and sedimentary rocks: Quantitative Mineralogy and Microanalysis of Sediments and Sedimentary Rocks (P. Sylvester. ed.). Mineralogical Association of Canada Short Course Series. v. 42. p. 1-16.

Tanner. R. S.. Udegbunam. E. O.. McInerney. M. J.. and Knapp. R. M.. 1991. Microbially enhanced oil recovery from carbonate reservoirs: Geomicrobiology Journal. v. 9. no. 4. p. 169-195.

Teufel. L. W.. Rhett. D. W.. and Farrell. H. E.. Effect of Reservoir Depletion And Pore Pressure Drawdown On In Situ Stress And Deformation In the Ekofisk Field. North Sea. *in* Proceedings The 32nd U.S. Symposium on Rock Mechanics (USRMS)1991. Volume All Days: ARMA-91-063.

Thomas. S.. 2008. Enhanced Oil Recovery - An Overview: Oil & Gas Science and Technology - Rev. IFP. v. 63. no. 1. p. 9-19.

Van Den Bark. E.. and Thomas. O. D.. 1981. Ekofisk: First of the Giant Oil Fields in Western Europe1: AAPG Bulletin. v. 65. no. 11. p. 2341-2363.

Voorhees. P. W.. 1985. The theory of Ostwald ripening: Journal of Statistical Physics. v. 38. no. 1. p. 231-252.

Wang. W.. zimmermann. U.. Hildebrand-Habel. T.. and Korsnes. R.. 2015. Temperature as Key Factor for Porosity Development in Brine Flooded Chalk at Realistic Reservoir Stress. International Conference and Exhibition. Melbourne. Australia 13-16 September 2015. p. 418-418.

Wen. S. T. S.. 2018. Systematic Specific Surface Area Analysis on Rocks to Implement as a Necessary. Quick. and informative method to understand Geo-Mechanical Parameter in IOR Experiments [Master Thesis]: University of Stavanger. 253 p.

Wirtz. T.. De Castro. O.. Audinot. J.-N.. and Philipp. P.. 2019. Imaging and Analytics on the Helium Ion Microscope: Annual Review of Analytical Chemistry. v. 12. no. 1. p. 523-543.

Woody. R. E.. Gregg. J.. and Koederitz. L. F.. 1996. Effect of texture on petrophysical properties of dolomite: Evidence from the Cambrian-Ordovician of southeastern Missouri: AAPG Bulletin. v. 80.

Wrona. T.. Magee. C.. Jackson. C. A.-L.. Huuse. M.. and Taylor. K. G.. 2017. Kinematics of Polygonal Fault Systems: Observations from the Northern North Sea: Frontiers in Earth Science. v. 5.

Wu. G.. Yang. H.. He. S.. Cao. S.. Liu. X.. and Jing. B.. 2016. Effects of structural segmentation and faulting on carbonate reservoir properties: A case study from the Central Uplift of the Tarim Basin. China: Marine and Petroleum Geology. v. 71. p. 183-197.

Yang. S.-Y.. Hirasaki. G. J.. Basu. S.. and Vaidya. R.. 1999. Mechanisms for contact angle hysteresis and advancingcontact angles: Journal of Petroleum Science and Engineering. v. 24. p. 63–73.

Zahid. A.. Stenby. E.. and Shapiro. A.. 2010. Improved Oil Recovery in Chalk: Wettability Alteration or Something Else?. SPE EUROPEC/EAGE Annual Conference and Exhibition: Barcelona. Spain.

Zhang. H.. Zhong. Y.. Zhang. J.. Zhang. Y.. Kuang. J.. and Yang. B.. 2020. Experimental research on deterioration of mechanical properties of carbonate rocks under acidified conditions: Journal of Petroleum Science and Engineering. v. 185. p. 106612.

Zhang. X.. and Spiers. C. J.. 2005. Effects of phosphate ions on intergranular pressure solution in calcite: An experimental study: Geochimica et Cosmochimica Acta. v. 69. no. 24. p. 5681-5691.

Zhang. X.. Spiers. C. J.. and Peach. C. J.. 2011. Effects of pore fluid flow and chemistry on compaction creep of calcite by pressure solution at 150°C: Geofluids. v. 11. no. 1. p. 108-122.

Zhao. T.. Xu. S.. and Hao. F.. 2023. Differential adsorption of clay minerals: Implications for organic matter enrichment: Earth-Science Reviews. v. 246. p. 104598.

Zhong. S.. and Mucci. A.. 1989. Calcite and aragonite precipitation from seawater solutions of various salinities: Precipitation rates and overgrowth compositions: Chemical Geology. v. 78. no. 3. p. 283-299.

Ziegler. P. A.. 1975. The geological evolution of the North Sea area in the tectonic framework of North Western Europe: AAPG Bulletin 1975;; 59 (7): 1073–1097. .

Zimmermann. U.. Madland. M. V.. Nermoen. A.. Hildebrand-Habel. T.. Bertolino. S. A.. Hiorth. A.. Korsnes. R. I.. Audinot. J.-N.. and Grysan. P.. 2015. Evaluation of the compositional changes during flooding of reactive fluids using scanning electron microscopy. nano-secondary ion mass spectrometry. x-ray diffraction. and whole-rock geochemistryCompositional Changes during Flooding: AAPG Bulletin. v. 99. no. 5. p. 791-805.

Papers

Paper I:

"An Analytical TOOLBOX for the Characterization of Chalks and Other Fine-Grained Rock Types within Enhanced Oil Recovery Research and Its Application – Guideline"

Zimmermann, U., Minde, M. W., Madland, M. V., and Bredal, T. V., 2022,

Energies, v. 15, no. 11, p. 4060.

An Analytical TOOLBOX for the Characterization of Chalks and Other Fine-Grained Rock Types within Enhanced Oil Recovery Research and Its Application—A Guideline

Udo Zimmermann [1,2,*], Mona Wetrhus Minde [2,3], Merete Vadla Madland [4] and Tine Vigdal Bredal [1,2]

1   Department of Energy Resources, University of Stavanger, 4036 Stavanger, Norway; tine.v.bredal@uis.no
2   The National IOR Centre of Norway, University of Stavanger, 4036 Stavanger, Norway; mona.w.minde@uis.no
3   Department of Mechanical and Structural Engineering and Materials Science, University of Stavanger, 4036 Stavanger, Norway
4   Division of Research, University of Stavanger, 4036 Stavanger, Norway; merete.v.madland@uis.no
*   Correspondence: udo.zimmermann@uis.no; Tel.: +47-51-832-270

Abstract: Analyses of fine-grained rocks like shales, cherts, and specifically chalk are challenging with regards to spatial resolution. We propose a "toolbox" to understand mineralogical alteration in chalk, especially those induced by non-equilibrium fluids or polymers and silicates during production of hydrocarbons. These data are fundamental in experiments related to improved/enhanced oil recovery (IOR/EOR) research with the aim to increase hydrocarbon production in a sustainable and environmentally friendly process. The 'toolbox' methods analyse rock–fluid or polymer–rock interaction and can be applied to any fine-grained rock type. In our 'toolbox', we include methods for routine analysis and evaluate the economic side of the usage together with the complexity of application and the velocity of data acquisition. These methods are routine methods for identification and imaging of components at the same time by chemical or crystallographic means and here applied to petroleum geology. The 'toolbox' principle provides a first workflow to develop a road map with clear focus on objectives for maximizing EOR. Most importantly, the methods provide a robust dataset that can identify mineralogical properties and alterations in very fine-grained rocks over several scales (nanometer-decimeter).

Keywords: petroleum geosciences; reservoir characterization; enhanced oil recovery; chalk and fine-grained rocks; rock-fluid chemical interactions; electron microscopy; ion microscopy; Raman spectroscopy

1. Introduction

Chalk is a very fine-grained carbonate and a common Mesozoic reservoir rock in hydrocarbon (HC) fields worldwide but a rock difficult to study because of its small grainsize, wherefore there is a need to demonstrate steps of a feasible analytical study in one paper (Figure 1). The Ekofisk chalk field on the Norwegian Continental Shelf (NCS) is one of the largest oil producers in the North Sea. The study of chalk with the effect of circulating or injected fluids on the primary mineralogy has been of particular interest, as those may affect the oil recovery and compaction of the reservoir. Injection of seawater started during the 1980s with the aim of avoiding pressure depletion and further significant seabed subsidence [1–4]. Therefore, the effects of rock–fluid interactions in chalk have been a widely studied field of research, applicable on a global stage. Processes related to fluid injection, e.g., dissolution, precipitation, sorption, and changes in surface properties at micro- to sub-nanometer scales in chalk affect rock mechanical parameters, which in turn control improved/enhanced oil recovery (IOR/EOR, e.g., [5,6]).

First Step:
Collecting basic data

BASIC BACKGROUND TOOLS FOR FUNDAMENTAL DATABASE INFORMATION

X-RAY DIFFRACTION
OPTICAL MICROSCOPE
WHOLE-ROCK GEOCHEMISTRY
EFFLUENT GEOCHEMISTRY
TRADITIONAL STABLE ISOTOPE GEOCHEMISTRY
ION CHROMATOGRAPHY
PYCNOMETRY

Second Step:
Extending data collecting within the scope of the research

ADVANCED TOOLS FOR EXTENDED DATABASE INFORMATION

ELECTRON MICROSCOPY
 SEM-BSE-EDS
 MLA
RAMAN
SPECIFIC SURFACE ANALYSIS

Third Step:
Applying key analytical techniques to fulfil the objective of the study

SPECIALIZED TOOLS FOR COMPLETE DATA BASE (IDENTIFICATION+IMAGE)

nanoSIMS
(lack of optimal imaging)
TERS-AFM
(challenging sample preparation)
TEM-EDS on FIB-SEM samples
In the nearest future:
Raman-SEM
HIM-SIMS

Figure 1. The 'toolbox' concept with a detailed workflow scheme. TEM-EDS = transmission electron microscopy coupled with energy dispersive X-ray spectroscopy; HIM-SIMS = helium ion microscopy coupled with secondary ion mass spectrometry; nanoSIMS = nano secondary ion mass spectrometry; TERS-AFM = tip enhanced Raman spectroscopy coupled with atomic force microscopy; SEM-BSE-EDS = scanning electron microscopy-back-scattered electron microscopy coupled with energy dispersive X-ray spectroscopy; MLA = mineral liberation analyser; FIB-SEM = focused ion beam scanning electron microscopy.

Chalk is rather simple in terms of its mineralogy, with the major constituent being calcite and minor occurrences (0–10 wt% [weight percent]) of other minerals (e.g., dolomite, quartz, opal, apatite, feldspar, pyrite, oxides, varying clay minerals), depending on location, age, and degree of diagenesis (for the North Sea, see compilations in [7,8]). Chalk is composed mainly of skeletal debris of calcareous micro-fossils (e.g., coccolithophores, calcispheres, foraminifera) along with fragments of macro-fossils (<20 μm), whereas individual coccolith rings can be as small as 0.3 μm (e.g., [9], Figure 2), which exclude optical microscope studies as a useful application, and the lack of suitable routine tools has been a showstopper for many decades in applied petroleum geosciences on chalk. During IOR/EOR related experiments, mineralogical alterations take place mainly at a very small scale (<2 μm). The need for understanding and evaluation of the significance of those processes has been recently shown and is a major focus in IOR/EOR research (e.g., [5,10–12]) and is based on the identification and understanding of the mineralogical processes.

4 μm

Figure 2. SEM micrograph of Liège chalk showing skeletal debris of coccolithophores and other micro-fossils along with minor occurrences of clay minerals.

The major challenge is that analytical methods that can image the alteration, e.g., scanning electron microscopes (SEM), have too large spot-sizes to accurately identify and quantify the chemical composition by, e.g., spectroscopy. Vice versa, routine methods able to identify the mineral species via crystallography (by Raman or X-ray diffraction) are not able to image the analysed area with sufficient resolution. To challenge this catch-22 situation and to deliver applicable methodological recipes to identify the alterations for industry, we propose a "toolbox" that holds sufficient resolution and accuracy for analyses of even brittle very fine-grained sedimentary rocks. We report on the advantages and disadvantages to provide a work-flow model for future research in this field, as sample preparation—especially in the case of chalk—is often a bottleneck, in addition to economic aspects and the velocity of data acquisition. The content of the toolbox (Figure 1) provides the possibility to combine results for a tailored dataset for the needs of the HC industry and its specific issues within IOR/EOR research and application. The selected analytical techniques are a well-combined pool of 'classic' traditional analytical methods as forming the base of further studies and state-of-the-art applications, often for the first time applied to chalk. Similarly, any fine-grained rock type (e.g., shales or chert) can be studied using the here presented workflow. Moreover, the toolbox will be a major guideline to research on various lithotypes of any grain-sizes and may function for research as a guideline based on a thorough combination of several analytical approaches. The background of this contribution is to present for the first time a comprehensive catalogue of methods in one workflow with focus on the technology and applicability behind each non-routine method.

2. Results—The Toolbox Content

The toolbox (Figure 1) is composed of analytical tools that are on one hand well-known in terms of their application to rocks and partly on chalk (including optical microscopy, whole-rock geochemistry, X-ray diffraction, traditional (C and O) stable isotope systems, ion chromatography, pycnometry, and effluent water analysis), and on the other hand new methodological approaches in the study of chalk besides the use of SEM:

- Field emission gun scanning electron microscopy (**FEG-SEM**) with energy dispersive X-ray spectroscopy (**EDS**),
- SEM-based mineral liberation analyzer (**MLA**),
- Focused ion beam (**FIB)-SEM,**
- Transmission electron microscopy (**TEM**),
- Electron microprobe analysis (**EMPA**),
- Nano secondary ion mass spectrometry (**nanoSIMS**),
- Specific surface area (**SSA**),
- Raman spectroscopy,
- Tip enhanced Raman spectroscopy (**TERS**) with atomic force microscopy (**AFM**).

The 'toolbox' concept with a detailed workflow scheme uses a combination of 'classic' traditional analytical methods as the base of data acquisition and state-of-the-art methods to focus on certain issues of interest within EOR research (Figure 1). The paramount basic background information datasets are shown on the left side as step 1 in the workflow (Figure 1). The central column in Figure 1 includes necessary analysis but already dependent on the objective of the research in the hydrocarbon industry. None of the methods fulfill the criteria of providing excellence in imaging and identification. The column to the right names methods that shall be applied for specific objectives (e.g., mineral identification or imaging textural characteristics), with all providing the necessary sub-micron resolution. Those applications are fundamental for up-scale modelling or analysis of wettability therefore they shall be used within EOR research. Some of the analytical methods are not ideal for soft materials like chalk, such as nanoSIMS (nano secondary ion mass spectrometry) or TERS-AFM (tip enhanced Raman spectroscopy coupled with atomic force microscopy), which cause strong sample preparation challenges [13–15]. Methods that can be applied routinely because they have been tested and sample preparation has been developed for the noted issue of resolution and high-resolution imaging at the same time are TEM-EDS

(transmission electron microscopy coupled with energy dispersive X-ray spectroscopy) and MLA (mineral liberation analyser) if the phases are not smaller than 1 micron. In the near future, further developed applications like HIM-SIMS (helium ion microscopy coupled with secondary ion mass spectrometry; [16,17] and RAMAN-SEM (Raman spectroscopy coupled with scanning electron microscopy) will be able to match the same objective [18,19].

With all the noted applications, information can be extracted by progressively increasing resolution of analyses and comparing results from chemical and elemental studies with imaging, mineralogical, and crystallographic data for hydrocarbon research. Using this process, it is possible to identify, map, and quantify the mineralogical alterations from milli- to nanometer scales within a large amount of research applications and especially within those discussed in this special volume.

3. Electron and Ion Microscopy

3.1. Sample Preparation

Electron microscopy demands high quality samples. For chalk, small freshly broken rock-fragments (<1 cm) are often used for analyses in SEM. Polished thin sections and epoxy impregnated mounts have also been used successfully. Sample preparation to yield maximum information for TEM or TERS can be challenging in softer rocks like chalk and shales because mechanical and electrolyte polishing are either difficult or impossible and may alter rock properties. The method found to be most fitting in this study was sample-preparation by FIB-SEM. However, this method is part of the 'classic' analytical techniques, even as data acquisition on chalk is rather rare compared to studies on other rock types, as it requires experience for phase identification because chemical identification using EDS (energy dispersive X-ray spectroscopy) is nearly impossible, as the spotsize is larger than the phases that are in the focus of interest.

3.1.1. Field Emission Gun Scanning Electron Microscope (FEG-SEM)

In a FEG-SEM, electrons are accelerated to create a focused electron beam to scan the sample in an evacuated chamber. When the beam hits the surface of the sample, various energy signals are reflected or produced from the surface that are collected by different detectors like secondary electrons (SE), back-scattered electrons (BSE), and X-rays (energy dispersive X-ray spectroscopy, EDS) as well as, in cases, visible and fluorescent light. The beam 'spot-size' usually lies in the range of 0.5–2 μm as the smallest possible and, at the same time, is the most useful dimension restricting chemical identification to this scale when using EDS. The emission of SE will mainly vary as a function of the topography, enabling imaging of the surface (Figures 2 and 3). A BSE detector collects backscattered, primary electrons dependent on the average atomic number of each phase, where a higher number will yield a brighter shade of grey in the image (Figure 3b). EDS detects characteristic X-rays that are produced during the electron bombardment where the difference in atomic structure of each element causes the release of X-rays differing in energy (or wavelength). Based on the energy spectra of the detected X-rays, quantification of each element is possible, but the accuracy varies based on several factors (e.g., [20]), wherefore the method is often described as semi-quantitative.

3.1.2. Mineral Liberation Analyzer (MLA)

Mineral Liberation Analyzer (MLA) combines imaging by SEM-BSE and X-ray mineral identification to create a spatial spectral color-coded map of the mineralogy or chemical composition of samples. The minerals in the samples are identified and characterised through comparison of their EDS spectra to a list of reference spectra by a "best match" algorithm [21]. Our peer-group developed a particular reference database to enable research on chalk. The resolution of the MLA scanning depends on the size of the area scanned and the time used, but it will always be constrained by the spot-size of the electron beam (c. 1 μm) and the corresponding excitation volume. As grains in the (flooded) chalk often have a grainsize below the beam diameter, signals from adjacent grains may in cases affect

each other (Figure 4). The method is mainly used for heavy minerals within the field of economic geology but with more machines available, it spreads into other geoscientific fields and as well into the hydrocarbon industry for the sake of correlation using specific horizons or to identify trends within quantified components within a stratigraphy [22,23].
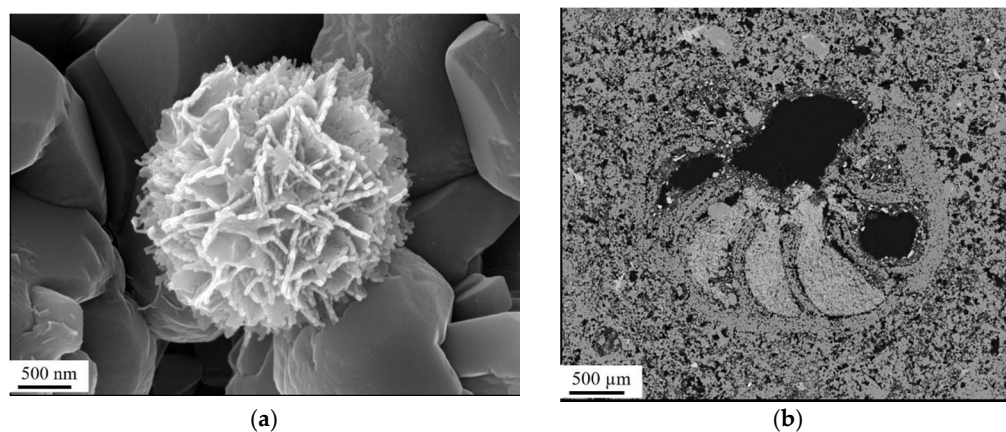
Figure 3. (**a**) SEM micrograph taken with the use of a SE-detector. The imaged object is an opal-CT lepisphere found in Aalborg chalk. (**b**) SEM micrograph of a foraminifera fossil found in chalk from Liège using BSE. The different grey-scales reflects the average atomic number (AAN) of each phase, thereby separating different mineralogical composition.
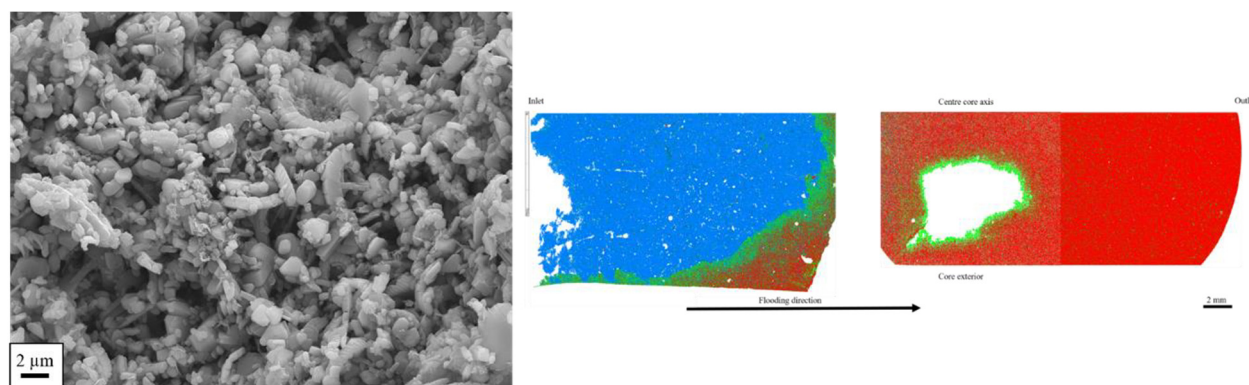
Figure 4. Comparison of scales. Grain-sizes of chalk are smaller than 1 μm, which is more or less the spot-size limit of methods such as MLA where mapping of larger areas in centimeter sizes are possible. Data and modified figure from [10].

3.1.3. Focused Ion Beam Scanning Electron Microscopy (FIB-SEM)

Sample preparation of brittle materials like chalk for TEM is a challenging task because of the demands for extreme thin samples and possible undesired smearing effects by polishing procedures. FIB milling while the sample is mounted in a SEM is a solution. Samples are milled by an ion beam cutting lamellas of approximately 20 μm × 10 μm using a gallium ion-source gun. They are then welded to a 3 mm large copper grid (Figure 5). The FIB lamellas are subsequently thinned to ~100–150 nm by the same ion source. Figure 5 shows the high fragility of the chalk as a consequence of its high porosity with typical low degree of cementation. This technique ideally requires a dual-beam application (ion and electron beams) within the same machine, but this is still rare because of the cost of such an application. Nevertheless, this technique is the base for further detailed studies, especially in material sciences, to identify inhomogenities of materials but also for testing purities of minerals [24]. Nevertheless, the ability to then resolve the challenge of high resolution versus chemical identification enables the method as well for hydrocarbon and EOR research.
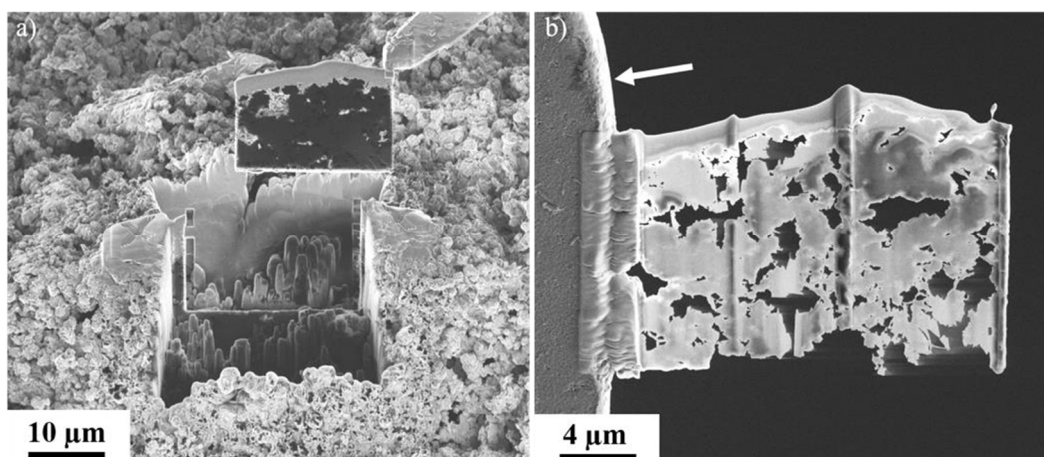
Figure 5. Production of FIB-lamella of MgCl$_2$-flooded chalk: (**a**) cut-out of lamella from the sample surface, (**b**) thinned lamella welded to a copper grid (white arrow).

3.1.4. Transmission Electron Microscope (TEM)

In a TEM, the electron beam is transmitted through the sample, allowing for a much higher resolution than a SEM. This requires acceleration voltage up to 200 kV and extremely thin samples. For our studies, chalk samples are routinely prepared by FIB-SEM but are inclined to be affected by the electron beam, i.e., by burning holes in the samples due to beam damage (Figure 5; [25]), wherefore the microscope set-up and bombardment times need to be calculated carefully. The high acceleration voltage produces an electron beam with shorter wavelengths, allowing for resolutions < 1 nm. A TEM fitted with an EDS detector provides imaging and elemental analyses at high resolution and also offers analyses by electron diffraction, enabling identification of mineral phases based on lattice parameters. In scanning transmission electron microscopy (STEM) mode, elemental identification by EDS can produce multi-coloured maps displaying the elemental composition of grains, where each colour represents an element and not a mineral or phase (Figure 6). The method requires a cost intensive machine and is time consuming but can be used for any small-scale material, even with an EDS [26,27]. Further applications lie in the identification of the atomic composition, which is, for surface charge analysis and subsequently wettability studies, of utmost importance in the hydrocarbon industry and EOR research.
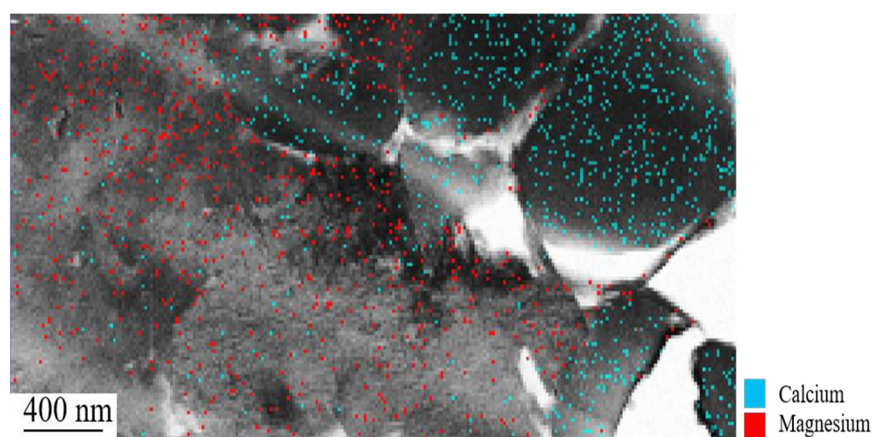
Figure 6. Example of elemental analysis performed on grain-scale by STEM. Blue represents occurrences of calcium, red magnesium. Image modified from [10].

3.1.5. Electron Microprobe Analysis (EMPA)

The principle of EMPA is comparable to the SEM-EDS but here wavelength dispersive X-ray spectroscopy (WDS) instead of EDS is placed in a SEM. By detecting wavelengths instead of the energy of the X-rays, quantitative measurements can be achieved. The reason is simply that WDS analyses identify individual wavelength of X-rays from specific elements and are independent of the effect of partly overlapping energy spectra. The spot-size is limited to c. 1 µm, comparable to the SEM. Therefore, this method is used to determine the number of chemical phases and requires much more meticulous sample preparation compared to SEM-EDS samples. Moreover, the method should be combined with a high-resolution application like a SEM to image the analysed areas, but nevertheless a limit around 1 micron is given. However, the application is used since several decades and much knowledge has been produced to study chemical compositions on a small scale. If the objective is a quantification of a chemical component beyond a doubt and one is not being able to study the material with a TEM-EDS, then EMPA is a very feasible and attractive tool.

3.1.6. Nano Secondary Ion Mass Spectrometry (NanoSIMS)

Secondary ion mass spectrometry (SIMS) uses a primary ion beam that, when sputtering the sample surface, releases secondary ions from the surface to provide information about chemical compositions and structures [28]. The surface is scanned with a focused ion beam (lateral resolution < 100 nm) and has been successfully applied to chalk in IOR/EOR research [12]. The particles produced from the impact of the primary beam are neutral, positively, or negatively charged, depending on the kind of primary ions and the material [29]. The ion-yield varies with respect to the beam type (e.g., Cs, O), ionization energy of the elements, and sample matrix [30]. Using a Time-Of-Flight detector, the number of ejected ions may be measured for several ions simultaneously. Identification of elements in one area is as precise as a resolution of 40 nm. NanoSIMS scanning provides a relative intensity-map for selected ions, oxides, or masses. The intensity values of different images are not directly comparable as the method is not quantitative, but the method is a perfect tool for verification of the existence or absence of a specific element in a phase (Figure 7). NanoSIMS can also create depth profiles and 3D images by sputtering areas (e.g., 10 µm × 10 µm) repeatedly, determining the chemical composition of layers with a thickness of few nm to a depth of approximately 1 µm. This can be visualised as a video or rotatable still image, allowing calculation of porosities (Figure 8). To navigate within the nanoSIMS, an optical camera is used, which is extremely challenging because of the lack of topography and contrast in mineralogical homogeneous fine-grained rocks like chalk. The nanoSIMS requires high vacuum conditions during measurements, which can be time-consuming to reach when studying high-porosity materials. The application is still relatively rare, and only few machines are available compared to other microscopic applications. Studies are often hampered when nanoSIMS are not combined with high-resolution microscopes because then the studied area is not well imaged.
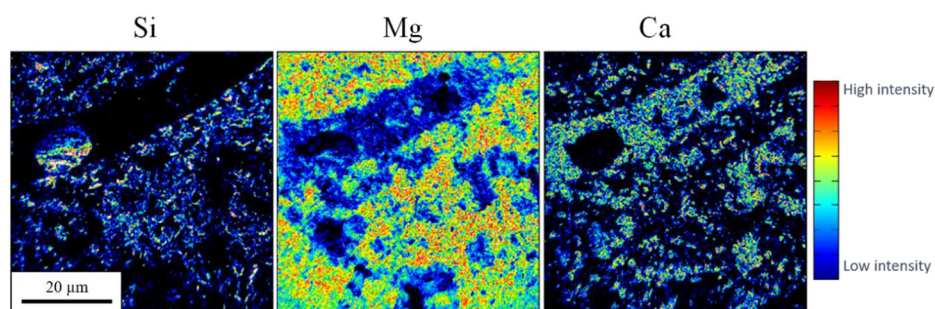
Figure 7. Example of the distribution of silicon (Si), magnesium (Mg), and calcium (Ca) in a chalk sample. The intensity is only relative for each element. Modified from [31].
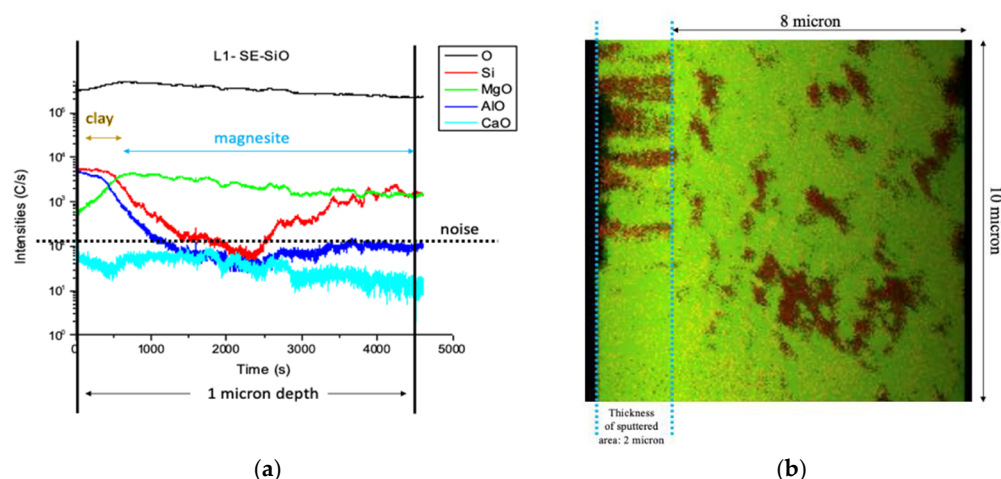
Figure 8. (**a**) A chemical depth profile of 1 micron while sputtering for 4500 s (c. 1.5 h), creating 5000 layers of 0.2 nm showing changes in the chemical composition and the combination of clay minerals and magnesite in a chalk test sample. (**b**) 3D still image from a video created during the sputtering of an area of 8 × 10 micron with a thickness of c. 2 microns. In red, primary calcite and in green, the produced secondary magnesite during flooding experiments for EOR—sample material from a long-term flooding test over 20 months with magnesium chloride in on-shore chalk under reservoir conditions (see [10,12,32]).

3.2. Specific Surface Area (SSA)

The SSA of a sample is a characteristic of solids that relates to the total particle surface per unit of mass, solid, or volume. The results are calculated via the amount of gas adsorbed as a monolayer on the sample surface. Based on the sample weight, the SSA of the sample can be calculated by the Brunauer–Emmett–Teller theory [33]. The SSA of a sample will vary as a function of several factors (e.g., grain size, shape, porosity, permeability), and is therefore a tool to interpret phase changes (e.g., dissolution, precipitation, surface modification) within a sample and a paramount parameter when studying porosity variation. However, there are a variety of methods and sample preparation techniques available, which hamper comparison of rock types or other materials. In-house studies are available, but larger studies that have published a variety of rock samples and their SSA are nearly absent [34,35]. In this field a wide area of improvement for applied science does exist.

3.3. Raman Spectroscopy

Raman spectroscopy is an analytical technique that uses a monochromatic laser beam with a diameter of c. 1 μm penetrating a sample observed using an optical microscope. Most photons scatter with no energy change, but some do and exchange a small amount of energy with the sample, which causes molecules to vibrate within the sample, producing the so-called Raman scattering [36]. The consequence is a shift in frequency of the scattered light, known as material specific 'Raman shift' (linked to lattice parameters, atomic weight, and strength of the atomic bonds of the sample), which enables identification of phases. The advantages of this method are its velocity and low cost compared to nearly all other analytical approaches [37] and the use of crystallography instead of chemical composition for identification. Materials with particles >5 μm are ideal for Raman spectroscopy. Raman application has also been combined within SEM, which then provides the necessary imaging [38], though not enhancing the spot-size.

Tip enhanced Raman spectroscopy coupled with atomic force microscopy has been tested as a method to perform Raman analyses at higher resolution with spot-sizes of 20 nm, producing topography maps of the analysed areas in chalk and allowing identification of phases [39]. However, this method sets extreme demands on sample preparation to produce a smooth surface, nearly impossible for chalk, and the method cannot therefore be recommended at this stage.

Raman spectroscopy is simple and economic, and it is extraordinary how rarely the method has been applied, especially in fields where the velocity of analysis is of importance like in the hydrocarbon industry. Sample preparation is extremely quick, and the method is non-destructive. A major obstacle is the absence of a complete and thorough database for the analytical results. Recent improvements with the development of automated Raman studies [40] and applications combined with electron microscopes to resolve the issue of the imaging of micron or sub-micron sized study areas will hopefully enhance the situation for all interests.

4. Discussion

Analyses of chalk can be challenging to perform when the objective is to identify its mineralogy and at the same time reveal high-resolution first-class images of the samples. Diagenetic processes or, as described in this study, mineralogical changes within experiments in the field of IOR/EOR produce phases on the scale of few microns or even smaller in chalk. Few techniques offer the opportunity for high-resolution images while identifying the mineralogical phases. However, often, analytical methods provide only an excellent image or crystallographic analyses without knowing the exact sampled area. Therefore, we argue that a sound combination of proposed methods provides the best approach. The introduced toolbox yields results at a wide range of scales and combines analyses of textures, chemistry, structures, and crystallography easily applicable like a recipe for very fine-grained reservoir rocks. Coarser rocks (grainsizes > 5 µm) are mostly well-understood by using conventional FEG-SEM-BSE-EDS, stable isotopes, and whole-rock geochemistry along with XRD analyses. Complementary methods, such as density and SSA measurements, are very useful tools to support data from the former noted analyses and are strong gameplayers for the interpretation of processes causing mineralogical modification on the grain-size level. Often, secondary mineral growth can be visualised by SEM analyses, but it is difficult to gain quantification and even identification if grainsizes are straddling 1µm. The δO^{18} isotope values may assist in determining temperatures under which secondary minerals grew, in natural contexts or during laboratory experiments [5]. Raman spectroscopy may support XRD data if the grain-sizes are favourable (>1 µm). For mapping of the mineralogy on micro to core-scale, MLA or equivalent methods may yield good results [10] with the same catch in regard to grainsizes as Raman.

Sub-micron sized minerals in chalk can ideally be identified beyond a doubt with nanoSIMS analytics [12], but imaging remains an issue. In our study, only TEM-EDS and TERS-AFM approaches would allow for both high-resolution imaging and chemical/crystallographic identification on sub-micron scales. Sample-preparation is an issue for TERS-AFM, where good results are dependent on flat surfaces avoiding large differences in topography, which hamper the quality of the study. TEM-EDS analyses are by themselves not extraordinarily time-consuming or expensive, but sample-preparation of brittle high-porous chalk is. Nevertheless, the noted complications are relevant to very fine-grained rocks like shales and chalk, but not an issue for most other rock types, which are harder and coarser grained. Further development on very fine-grained materials needs to include high resolution imaging coupled with chemical/crystallographic tools and less challenging sample preparation for soft very fine-grained rocks. One candidate may be helium microscopy coupled with SIMS technology, but the analysis on chalk has not left the experimental phase [41].

5. Conclusions

We have composed and successfully tested an analytical toolbox useful for a wide field of research on very fine-grained reservoir rocks like chalk for IOR/EOR purposes. The focus has been to find suitable tools to identify in very fine-grained reservoir chalk mineralogical alterations due to rock–fluid interactions at the grain-scale that affect rock mechanics and to implement those technologies for IOR/EOR (e.g., [5,10]). However, the same techniques and the workflow can be used for any fine-grained material, and even

polymer research or other applications that require material studies on a small scale with imaging at the same time at highest resolution. The roadmap using the toolbox (Figure 1) shall also be effective, economic, and fast in order to be attractive for all users. The routine part of the toolbox comprises:

- FEG-SEM-EDS,
- XRD,
- Whole-rock and stable isotope geochemistry,
- Traditional stable isotope geochemistry.
- MLA,
- SSA,
- Pycnometry: depending on the specific focus of the IOR/EOR research and refined by focussed work on representative areas to understand key processes causing mineralogical changes,
- TEM analyses on FIB-SEM samples,
- TERS analyses coupled with AFM imaging,
- NanoSIMS analyses.

All noted methods are positively tested, and detailed methodology recipes exist for chalk [5,6,10,32], ready for application within analytical routines for applied research within the hydrocarbon industry and here focussed on EOR research. The toolbox is designed to enable selecting the quickest and most economic tools to yield necessary datasets for decision making and modelling in this field of HC research and industrial applications (e.g., [5,42]). This concept stresses the need of valuable mineralogical input for simulators to be able to upscale from pore- to core- and field-scale. Beyond a doubt, the noted methods are even more effective and less challenging when applied to harder and coarser grained samples (>5 μm) than shales and chalk. The highest impact for IOR/EOR research, as well as other research objectives, lies—in our opinion—within the combination of carefully selected methodologies from the toolbox in one workflow.

Author Contributions: Conceptualization, U.Z.; methodology, U.Z., M.V.M., M.W.M. and T.V.B.; software, validation, U.Z., M.V.M., M.W.M. and T.V.B.; formal analysis, investigation, U.Z., M.V.M., M.W.M. and T.V.B.; resources, U.Z., M.V.M., M.W.M. and T.V.B.; data curation, U.Z., M.V.M., M.W.M. and T.V.B.; writing—original draft preparation, U.Z.; writing—review and editing, U.Z., M.V.M., M.W.M. and T.V.B.; visualization, M.W.M. and T.V.B.; supervision, U.Z. and M.V.M.; project administration, U.Z.; funding acquisition, M.V.M. All authors have read and agreed to the published version of the manuscript.

Conflicts of Interest: The authors declare no conflict of interest.

References

1. Doornhof, D.; Kristiansen, T.G.; Nagel, N.B.; Pattillo, P.D.; Sayers, C.J.O.R. Compaction and subsidence. *Oilfield Rev.* **2006**, *18*, 50–68.
2. Hermansen, H.; Landa, G.H.; Sylte, J.E.; Thomas, L.K. Experiences after 10 years of waterflooding the Ekofisk Field, Norway. *J. Pet. Sci. Eng.* **2000**, *26*, 11–18. [CrossRef]
3. Nagel, N.B. Ekofisk field overburden modelling. In *SPE/ISRM Rock Mechanics in Petroleum Engineering*; OnePetro: Trondheim, Norway, 1998. [CrossRef]
4. Teufel, L.W.; Rhett, D.W.; Farrell, H.E. *Effect of Reservoir Depletion and Pore Pressure Drawdown on In Situ Stress and Deformation in the Ekofisk Field, North Sea*; American Rock Mechanics Association: Norman, OK, USA, 1991.

5.　Andersen, P.Ø.; Wang, W.; Madland, M.V.; Zimmermann, U.; Korsnes, R.I.; Bertolino, S.R.A.; Minde, M.; Schulz, B.; Gilbricht, S. Comparative Study of Five Outcrop Chalks Flooded at Reservoir Conditions: Chemo-mechanical Behaviour and Profiles of Compositional Alteration. *Transp. Porous Media* **2017**, *121*, 135–181. [CrossRef]

6.　Minde, M.W.; Wang, W.; Madland, M.V.; Zimmermann, U.; Korsnes, R.I.; Bertolino, S.R.A.; Andersen, P.Ø. Temperature effects on rock engineering properties and rock-fluid chemistry in opal-CT-bearing chalk. *J. Pet. Sci. Eng.* **2018**, *169*, 454–470. [CrossRef]

7.　Hjuler, M.L.; Fabricius, I.L. Engineering properties of chalk related to diagenetic variations of Upper Cretaceous onshore and offshore chalk in the North Sea area. *J. Pet. Sci. Eng.* **2009**, *68*, 151–170. [CrossRef]

8.　Kallesten, E.; Zimmermann, U.; Madland, M.V.; Bertolino, S.R.A.; Omdal, E.; Andersen, P.Ø. Mineralogy and geochemistry of reservoir and non-reservoir chalk from the Norwegian continental shelf. *J. Pet. Sci. Eng.* **2021**, *205*, 108914. [CrossRef]

9.　Scholle, P.A.; Kinsman, D.J.J. Diagenesis of Upper Cretaceous chalks from North Sea, England and Northern Ireland. *Am. Assoc. Pet. Geol. Bull.* **1973**, *57*, 803–804.

10.　Minde, M.W.; Zimmermann, U.; Madland, M.V.; Korsnes, R.I.; Schultz, B.; Gilbrich, S. Mineral Replacement in Long-Term Flooded Porous Carbonate Rocks. *Geochim. Cosmochim. Acta* **2020**, *268*, 485–508. [CrossRef]

11.　Skovbjerg, L.L.; Hassenkam, T.; Makovicky, E.; Hem, C.P.; Yang, M.; Bovet, N.; Stipp, S.L.S. Nano sized clay detected on chalk particle surfaces. *Geochim. Cosmochim. Acta* **2012**, *99*, 57–70. [CrossRef]

12.　Zimmermann, U.; Madland, M.V.; Nermoen, A.; Hildebrand-Habel, T.; Bertolino, S.A.R.; Hiorth, A.; Korsnes, R.I.; Audinot, J.-N.; Grysan, P. Evaluation of the compositional changes during flooding of reactive fluids using scanning electron microscopy, nano-secondary ion mass spectrometry, X-ray diffraction, and whole-rock geochemistry. *Am. Assoc. Pet. Geol. Bulletin* **2015**, *99*, 791–805. [CrossRef]

13.　Hrstka, T.; Gottlieb, P.; Skala, R.; Breiter, K.; Motl, D. Automated mineralogy and petrology—Applications of TESCAN Integrated Mineral Analyzer (TIMA). *J. Geosci.* **2018**, *63*, 47–63. [CrossRef]

14.　Pirrie, D.; Rollinson, G.K. Unlocking the applications of automated mineral analysis. *Geol. Today* **2011**, *27*, 226–235. [CrossRef]

15.　Tsikouras, B.; Pe-Piper, G.; Piper, D.J.W.; Schaffer, M. Varietal heavy mineral analysis of sediment provenance, Lower Cretaceous Scotian Basin, eastern Canada. *Sediment. Geol.* **2011**, *237*, 150–165. [CrossRef]

16.　Ball, M.R.; Taylor, R.J.M.; Einsle, J.F.; Khanom, F.; Guillermier, C.; Harrison, R. Helium ion microscope—Secondary ion mass spectrometry for geological materials. *J. Nanotechnol.* **2020**, *11*, 1504–1515. [CrossRef] [PubMed]

17.　Ost, A.D.; Wu, T.; Höschen, C.; Mueller, C.W.; Wirtz, T.; Audinot, J.-N. 4D Surface Reconstructions to Study Microscale Structures and Functions in Soil Biogeochemistry. *Environ. Sci. Technol.* **2021**, *55*, 9384–9393. [CrossRef] [PubMed]

18.　Jiruse, J.; Haničinec, M.; Havelka, M. Integrating focused ion beam–scanning electron microscope with confocal Raman microscope into a single instrument. *J. Vac. Sci. Technol.* **2014**, *32*, 06FC03. [CrossRef]

19.　Wille, G.; Bourrat, X.; Maubec, N.; Lahfid, A. Raman-in-SEM, a multimodal and multiscale analytical tool: Performance for materials and expertise. *Micron* **2014**, *67*, 50–64. [CrossRef]

20.　Borromeo, L.; Zimmermann, U.; Andò, S.; Coletti, G.; Bersani, D.; Basso, D.; Gentile, P.; Schulz, B.; Garzanti, E. Raman Spectroscopy as a tool for magnesium estimation in Mg-calcite. *J. Raman Spectrosc.* **2017**, *48*, 983–992. [CrossRef]

21.　Fandrich, R.; Gu, Y.; Burrows, D.; Moeller, K. Modern SEM-based mineral liberation analysis. *Int. J. Miner. Processing* **2007**, *84*, 310–320. [CrossRef]

22.　Guhl, A.C.; Greb, V.G.; Schulz, B.; Bertau, M. An Improved Evaluation Strategy for Ash Analysis Using Scanning Electron Microscope Automated Mineralogy. *Minerals* **2020**, *10*, 484. [CrossRef]

23.　Keulen, N.; Næsby Malkki, S.; Graham, S. Automated Quantitative Mineralogy Applied to Metamorphic Rocks. *Minerals* **2020**, *10*, 47. [CrossRef]

24.　Andrew, M. A quantified study of segmentation techniques on synthetic geological XRM and FIB-SEM images. *Comput. Geosci.* **2018**, *22*, 1503–1512. [CrossRef]

25.　Hjuler, M.L.; Hansen, V.F.; Fabricius, I.L. Interpretational challenges related to studies of chalk particle surfaces in scanning and transmission electron microscopy. *Bull. Geol. Soc. Den.* **2018**, *66*, 151–165. [CrossRef]

26.　Ohnuki, T.; Yoshida, T.; Ozaki, T.; Samadfam, M.; Kozai, N.; Yubuta, K.; Mitsugashira, T.; Kasama, T.; Francis, A.J. Interactions of uranium with bacteria and kaolinite clay. *Chem. Geol.* **2005**, *220*, 237–243. [CrossRef]

27.　Yuan, P.; Liu, D.; Tian, Q.; Song, Y.; Wei, H.; Wang, S.; Zhou, J.; Deng, L.; Du, P. Identification of the occurrence of minor elements in the structure of diatomaceous opal using FIB and TEM-EDS. *Am. Mineral.* **2019**, *104*, 1323–1335. [CrossRef]

28.　Hirata, K.; Saitoh, Y.; Chiba, A.; Yamada, K.; Takahashi, Y.; Narumi, K. Secondary ion counting for surface-sensitive chemical analysis of organic compounds using time-of-flight secondary ion mass spectroscopy with cluster ion impact ionization. *Rev. Sci. Instrum.* **2011**, *82*, 033101. [CrossRef]

29.　Griffiths, J. Secondary Ion Mass Spectrometry. *Anal. Chem.* **2008**, *80*, 7194–7197. [CrossRef]

30.　Handley, J. Product Review: Secondary Ion Mass Spectrometry. *Anal. Chem.* **2002**, *74*, 335A–341A. [CrossRef]

31.　Minde, M.W.; Zimmermann, U.; Madland, M.V.; Korsnes, R.I.; Schulz, B.; Audinot, J.N. Fluid-flow During EOR Experiments in Chalk: Insights using SEM-MLA, EMPA and NanoISMS Applications. In Proceedings of the International Symposium of the Society of Core Analysts, Snowmass, CO, USA, 21–26 August 2016; p. 7.

32.　Minde, M.W.; Madland, M.V.; Zimmermann, U.; Egeland, N.; Korsnes, R.I.; Nakamura, E.; Kobayashi, K.; Ota, T. Mineralogical alterations in calcite powder flooded with MgCl₂ to study Enhanced Oil Recovery (EOR) mechanisms at pore scale. *Microporous Mesoporous Mater.* **2019**, *304*, 109402. [CrossRef]

33. Brunauer, S.; Emmett, P.H.; Teller, E. Adsorption of Gases in Multimolecular Layers. *J. Am. Chem. Soc.* **1938**, *60*, 309–319. [CrossRef]

34. Kuila, U.; Prasad, M. Specific surface area and pore-size distribution in clays and shales. *Geophys. Prospect.* **2013**, *61*, 341–362. [CrossRef]

35. Macht, M.; Eusterhues, K.; Pronk, G.J.; Totsche, K.-U. Specific surface area of clay minerals: Comparison between atomic force microscopy measurements and bulk-gas (N2) and -liquid (EGME) adsorption methods. *Appl. Clay Sci.* **2011**, *53*, 20–26.

36. Raman, C.V. A new radiation. *Indian J. Phys.* **1928**, *2*, 387–398. [CrossRef]

37. Borromeo, L.; Egeland, N.; Minde, M.W.; Zimmermann, U.; Andò, S.; Madland, M.V.; Korsnes, R.I. Quick, Easy, and Economic Mineralogical Studies of Flooded Chalk for EOR Experiments Using Raman Spectroscopy. *Minerals* **2018**, *8*, 221. [CrossRef]

38. Aksenov, Y. Raman Microscopy in an Electron Microscope: Combining Chemical and Morphological Analyses. Ph.D. Thesis, University of Twente, Enschede, Switzerland, 2003.

39. Borromeo, L.; Toccafondi, C.; Minde, M.W.; Zimmermann, U.; Andò, S.; Madland, M.V.; Korsnes, R.I.; Ossikovski, R. Application of Tip-Enhanced Raman Spectroscopy for the nanoscale characterization of flooded chalk. *J. Appl. Phys.* **2018**, *124*, 173101. [CrossRef]

40. Lünsdorf, N.K.; Kalies, J.; Ahlers, P.; Dunkl, I.; von Eynatten, H. Semi-Automated Heavy-Mineral Analysis by Raman Spectroscopy. *Minerals* **2019**, *9*, 385. [CrossRef]

41. Bredal, T.V.; Zimmermann, U.; Madland, M.V.; Minde, M.W.; Ost, A.D.; Wirtz, T.; Audinot, J.-N.; Korsnes, R.I. High-Resolution Topographic and Chemical Surface Imaging of Chalk for Oil Recovery Improvement Applications. *Minerals* **2022**, *12*, 356. [CrossRef]

42. Kallesten, E.; Andersen, P.Ø.; Berawala, D.S.; Korsnes, R.I.; Madland, M.V.; Omdal, E.; Zimmermann, U. SPE Modelling of Permeability and Strain Evolution in Chemical Creep Compaction Experiments with Fractured and Unfractured Chalk Cores Conducted at Reservoir Conditions. *SPE Reserv. Eval. Eng. Reserv. Eng.* **2020**, *25*, 2710–2728. [CrossRef]

Paper II:

"High-Resolution Topographic and Chemical Surface Imaging of Chalk for Oil Recovery Improvement Applications"

Bredal, T. V., Zimmermann, U., Madland, M. V., Minde, M. W., Ost, A. D., Wirtz, T., Audinot, J.-N., and Korsnes, R. I., 2022,

Minerals, v. 12, no. 3, p. 356.

High-Resolution Topographic and Chemical Surface Imaging of Chalk for Oil Recovery Improvement Applications

Tine Vigdel Bredal [1,2,*], Udo Zimmermann [1,2], Merete Vadla Madland [3], Mona Wetrhus Minde [2,4], Alexander D. Ost [5,6] , Tom Wirtz [5] , Jean-Nicolas Audinot [5] and Reidar Inge Korsnes [1,2]

[1] Department of Energy Resources, University of Stavanger, Ullandhaug, 4036 Stavanger, Norway; udo.zimmermann@uis.no (U.Z.); reidar.i.korsnes@uis.no (R.I.K.)

[2] The National IOR Centre of Norway, University of Stavanger, Ullandhaug, 4036 Stavanger, Norway; mona.w.minde@uis.no

[3] Division of Research, University of Stavanger, Ullandhaug, 4036 Stavanger, Norway; merete.v.madland@uis.no

[4] Department of Mechanical and Structural Engineering and Materials Science, University of Stavanger, Ullandhaug, 4036 Stavanger, Norway

[5] Advanced Instrumentation for Nano-Analytics, Department of Materials Research and Technology, Luxembourg Institute of Science and Technology, 4362 Esch-sur-Alzette, Luxembourg; alexander.ost@list.lu (A.D.O.); tom.wirtz@list.lu (T.W.); jean-nicolas.audinot@list.lu (J.-N.A.)

[6] Faculty of Science, Technology and Medicine, University of Luxembourg, 2 Av. de l'Universite, 4365 Esch-sur-Alzette, Luxembourg

* Correspondence: tine.v.bredal@uis.no

Abstract: Chalk is a very fine-grained carbonate and can accommodate high porosity which is a key characteristic for high-quality hydrocarbon reservoirs. A standard procedure within Improved Oil Recovery (IOR) is seawater-injection which repressurizes the reservoir pore pressure. Long-term seawater-injection will influence mineralogical processes as dissolution and precipitation of secondary minerals. These secondary minerals (<1 micrometer) precipitate during flooding experiments mimicking reservoir conditions. Due to their small sizes, analysis from traditional scanning electron microscopy combined with energy dispersive X-ray spectroscopy is not conclusive because of insufficient spatial resolution and detection limit. Therefore, chalk was analyzed with high-resolution imaging by helium ion microscopy (HIM) combined with secondary ion mass spectrometry (SIMS) for the first time. Our aim was to identify mineral phases at sub-micrometer scale and identify locations of brine–rock interactions. In addition, we wanted to test if current understanding of these alteration processes can be improved with the combination of complementary imaging techniques and give new insights to IOR. The HIM-SIMS imaging revealed well-defined crystal boundaries and provided images of excellent lateral resolution, allowing for identification of specific mineral phases. Using this new methodology, we developed chemical identification of clay minerals and could define their exact location on micron-sized coccolith grains. This shows that it is essential to study mineralogical processes at nanometer scale in general, specifically in the research field of applied petroleum geology within IOR.

Keywords: helium ion microscopy; secondary ion mass spectrometry; chalk; clay mineral; chemistry; nano-scale imaging; mineralogical alteration

1. Introduction

Chalk is a marine sedimentary rock that comprises mainly calcium carbonate ($CaCO_3$) which is primarily composed of micron-sized coccolithophore fragments (coccoliths) and nano-sized fossil debris. The size of individual coccolith rings ranges between 0.3 and 5 μm [1]. Precipitation and deposition of chalk typically occur in deep marine settings, where clastic input is secondary if not absent. Accessory minerals may be silicate-rich microfossils or clay minerals related to aerial transport from volcanic eruptions. Due to the

characteristic texture of the chalk (Figure 1), the rock is also highly porous, nevertheless, its softness may cause compaction during diagenesis. This pronounced porosity is vital for the oil industry as it provides great potential as reservoirs for hydrocarbons. Water injection into carbonate reservoirs, such as the giant Ekofisk on the Norwegian Continental Shelf (NCF), is performed as a method known as Improved Oil Recovery (IOR) to gain more hydrocarbon from existing reservoirs instead of developing new fields [2–7]. This technique is essential in the transition process to a greener energy production in the future. The injected brine will alter the wettability of the grain surface from oil-wet to water-wet such that additional oil will be released [5]. However, this process will additionally alter the properties of the reservoir, initiate dissolution and precipitation of minerals, consequently influencing porosity and permeability [8–12]. Non-carbonate phases are suspected to influence the entire rock–fluid interaction and the identification is obviously the first step [11,13–16].
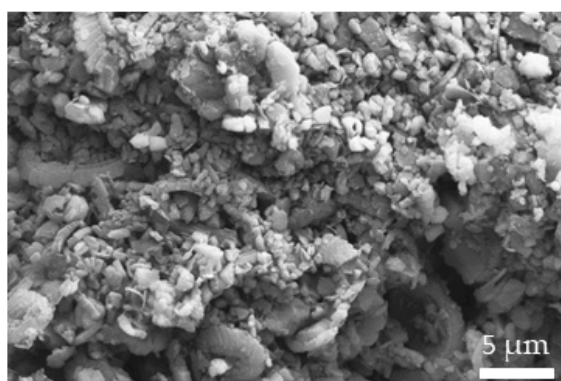
Figure 1. Typical texture of an Upper Cretaceous onshore chalk sample derived from the St. Vaast Formation from Obourg quarry close to Mons (Belgium; sample OBSV 12.3) imaged by SEM showing abundant coccolith rings and high porosity.

Magnesium is one of the most reactive ions in seawater. Seawater injection causes brine–rock interactions which normally involve calcium dissolution and magnesium precipitation. To identify secondary mineralogical and textural alteration of chalk, various methods of analytical tools have been applied [17]. The small size of these chalk constituents challenges the resolution of most of these techniques. Scanning Electron Microscopy (SEM) combined with elemental analysis using energy dispersive X-ray spectroscopy (EDS) is widely used on a regular basis for the purpose of performing reservoir characterization of chalk. This method can, however, not achieve sufficient spatial resolution and analytical sensitivity to resolve and identify mineral phases on sub-micron level as the acquired signal originates from an interaction volume of ~1 μm^3 in the sample [18,19]. Specific approaches within reservoir characterization on submicron scale needs state-of-the-art resolution in the field of imaging and mineral or component identification using crystallographic techniques or chemical data. The lack of these two data sets acquired at the same time, hampers the interpretation of mineralogical processes related to fluid injection as new grown minerals related t flooding experiments are in the nm size range [10,20,21]. The use of Transmission Electron Microscopy (TEM) has also been employed, however, sample preparation for this method is often challenging.

The main objective here is to provide high-resolution morphology images plus the mineral identification based on chemical surface analyses. Within three decades of IOR research we developed several methodological approaches to tackle this objective [17,22] (Minde et al., 2019a, b). Most of the analytical solutions turned out to be highly time consuming with significant challenges on sampling [20]. Crystallographic studies with tip-enhanced Raman spectroscopy (TERS) combined with atomic force microscopy (AFM) are extremely tedious and sample preparation is very challenging [22].

The novel combination of helium ion microcopy (HIM) with secondary ion mass spectrometry (SIMS) [23,24] allows to solve these issues for a variety of mineralogical and thus geological problems, especially in the field of rock–fluid interactions in IOR research. In the context of chalk analysis, we demonstrate in this manuscript for the first time the advantages of this method compared to those mentioned above and commence new and more advanced studies within this field.

2. Sample Material and Experimental Setup

The sample (OBSV 12) is Upper Cretaceous chalk from the St. Vaast Formation (Obourg quarry, Mons Belgium) [25–27]. The St. Vaast Formation has a high carbonate concentration with traces of glauconite, chlorite, and pyrite [28]. The chalk samples discussed here were cored with a cylindrical shape of 38.1 mm in diameter and a length of about 70 mm out of an un-weathered chalk block. A 2 mm drill bit was used to produce an artificial fracture without contaminating the sample. The size of the fracture aperture measured 2.25 mm (± 0.05 mm) and ran parallel to the flooding direction in the central core (Figure 2a). The aim was to mimic fractured chalk in reservoirs such as Ekofisk on the NCS. In unflooded material the average amount of calcite was around 95% (Table 1). These cores were used for flooding experiments when different fluids were tested under reservoir conditions to provoke mineralogical changes which affect rock mechanics [29,30]. The main average abundances of the non-carbonate material (in weight percent) were SiO_2 (3.42 wt.%), followed by Al_2O_3 (1.01 wt.%), Fe_2O_3 (0.39 wt.%), and K_2O (0.23 wt.%) (Table 1). The experiment was conducted in a triaxial cell at high temperature (130 °C) with confining and pore pressure of 12 and 0.7 MPa, respectively. The test sample was initially flooded with NaCl during loading and the primary week during creep (deformation at constant stress) and was subsequently flooded for 53 days with synthetic seawater (SSW). The composition of this fluid is described in detail in [13] and comprises mainly sodium, chlorine, magnesium, calcium, potassium, and sulphur. For more information about the set-up of the triaxial cells, the reader is referred to [9]. The chalk sample was cleaned with distilled water after the experimental test, dried, and sliced into six units from OBSV 12.1 (inlet) to OBSV 12.6 (outlet).

(a)   (b)   (c)
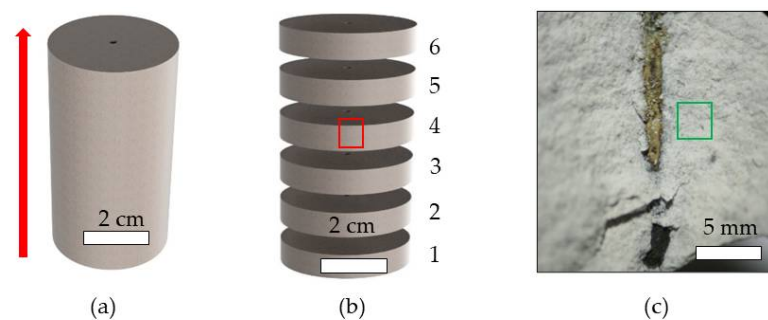
Figure 2. (**a**) The chalk sample (OBSV 12.4) before testing with the location of the drilled fracture (diameter: 2.25 ± 0.05 mm). The red arrow indicates the flooding direction. (**b**) The core was sliced after flooding, where number one is the "inlet", where the fluids were injected, and the "outlet" is number six. The red square in slice four shows the exact sample location for this study. (**c**) Optical microscopy image of the fracture fill from the sampling area after flooding of the sample. HIM-SIMS analysis was performed from sample material (green square) extracted from the matrix very close to the fracture fill.

Table 1. Bulk chemical composition of unflooded reference samples including the end piece of the flooded sample which has not been flooded (REF.6) and the flooded chalk samples of OBSV 12. Analysis with HIM-SIMS was performed on OBSV 12.4. wt.% indicates weight percent. The complete data set is available in Supplementary Table S1.

Content/ Sample	SiO_2 wt.%	Al_2O_3 wt.%	Fe_2O_3 wt.%	MgO wt.%	CaO wt.%	Na_2O wt.%	K_2O wt.%
REF.1	3.32	0.97	0.34	0.29	52.06	0.04	0.22
REF.2	3.39	1.00	0.54	0.27	51.90	0.04	0.22
REF.3	3.44	1.01	0.39	0.29	51.97	0.04	0.22
REF.4	3.38	1.00	0.34	0.28	52.29	0.04	0.22
REF.5	3.40	1.03	0.33	0.30	51.89	0.04	0.23
REF.6	3.58	1.05	0.40	0.28	51.89	0.04	0.24
OBSV 12#1	3.61	1.07	0.47	0.44	51.93	0.04	0.24
OBSV 12#2	3.52	1.05	0.38	0.48	52.05	0.04	0.22
OBSV 12#3	3.56	1.07	0.40	0.53	51.93	0.03	0.23
OBSV 12#4	3.64	1.08	0.43	0.52	51.88	0.04	0.22
OBSV 12#5	3.60	1.06	0.39	0.49	51.67	0.04	0.23
OBSV 12#6	3.62	1.08	0.43	0.40	51.94	0.04	0.24

3. Methods

3.1. Whole-Rock Geochemistry Characterization

In total, 5 g of sample material was milled in an agate mill to a fine mesh. The geochemical data were obtained by inductively coupled plasma–mass spectrometry (ICP-MS) analysis at ACME laboratory (Vancouver, BC, Canada). The milled sample was mixed with $LiBO_2/Li_2B_4O_7$ flux in crucibles and fused in a furnace. The cooled bead was dissolved in the American Chemical Society (ACS) grade nitric acid and analyzed by ICP-MS. Loss on ignition (LOI) was determined by igniting a sample split then measuring the weight loss. A 1 g sample was weighed into a tarred crucible and ignited to 1000 °C for 1 h, then cooled and weighed again. Total carbon and sulphur were determined using the LECO method. Here, induction flux was added to the prepared sample then ignited in an induction furnace. A carrier gas swept up released carbon to be measured by adsorption in an infrared spectrometric cell. Results are quantitative and give the concentrations of carbon and sulphur in all components. An additional 14 elements were measured after dilution in Aqua Regia. The prepared sample was digested with a modified Aqua Regia solution of equal parts concentrated HCl, HNO_3, and DI-H_2O for 1 h in a heating block or hot water bath. The sample volume was increased with dilute HCl solution and splits of 0.5 g were analyzed. The accuracy and precision are between 2 and 3%.

3.2. Helium Ion Microscopy–Secondary Ion Mass Spectroscopy (HIM-SIMS)

Secondary electron (SE) image acquisitions were performed in a Zeiss ORION NanoFab Helium Ion Microscope (HIM) [31] (Figure 3). HIM uses a very finely focused He^+ or Ne^+ ion beam, produced by a gas field ion source (GFIS), to raster-scan the sample under investigation and to create SEs collected by an Everhart–Thornley (ET) detector. He^+ ions are typically used to produce SE images to limit sputtering of the surface during the imaging process due to the low sputtering yield of He^+ versus Ne^+ [32]. This gives spatial resolutions down to 0.5 nm [33,34] thanks to the high-brightness of the GFIS and the very small interaction volume between the impinging He^+ ions and the sample in the near surface region, from which SEs are emitted [31]. For more technical details about HIM the reader can refer to [24,31]. Chemical images were acquired by using a Secondary Ion Mass Spectrometer (SIMS) system installed on the HIM, which was developed by the Luxembourg Institute of Science and Technology (LIST) to provide analytical information of specimen on the HIM (called "HIM-SIMS") [23,24,33]. For SIMS, Ne^+ primary ions are used to enhance sputtering of the surface (up to a few nanometers of depth) and therefore to increase the secondary ion (SI) yield to achieve adequate signal statistics. The spatial resolution of the SIMS mode is better than 20 nm, which makes it a record in SIMS imaging [23,24].
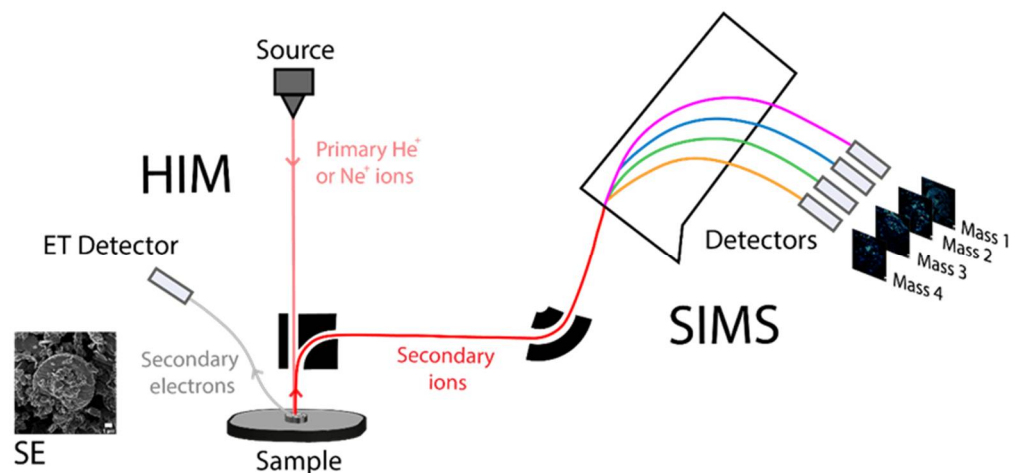
Figure 3. Schematic view of the HIM-SIMS instrument. The central part consists of the helium ion microscope (HIM) used primarily for topographic SE imaging, while the left part is showing the coupled secondary ion mass spectrometer (SIMS) add-on system dedicated for elemental analysis.

In situ analysis using both techniques, HIM for topographic SE imaging and SIMS for visualization of elemental distribution, firstly allows an efficient data acquisition workflow minimizing contamination of the sample and secondly facilitates image correlation of the same ROI in the data treatment process. Correlation of 2-dimensional topographic SE images and even 3D SE reconstructions using a photogrammetry method [35,36] and chemical images from SIMS, visualize complementary information in a single representation, thus enabling a deeper comprehension of a ROI with respect to its structural and chemical properties.

In this work, HIM-SE images were acquired with a He$^+$ primary current of 2 pA at 25 keV acceleration energy for a scanning of 2048 $\times$ 2048 pixels and a counting time of 10 μs/pixel averaged over 8 lines. For SIMS analysis, the surface of the same ROIs was scanned with a 10 pA (25 keV) Ne$^+$ beam with 512 $\times$ 512 pixels at a counting time of 2 ms/pixel. The instrument was tuned to map the distribution of the positive ion of magnesium (^{24}Mg$^+$), aluminum (^{27}Al$^+$), silicon (^{28}Si$^+$), potassium (^{39}K$^+$), and calcium (^{40}Ca$^+$) (^{24}Mg, ^{28}Si, ^{39}K in a first run and ^{27}Al and ^{40}Ca in a second run). The negative ions recorded were carbon (^{12}C$_2{}^-$) and oxygen (^{16}O$^-$).

4. Results

4.1. Geochemical Bulk Data

Bulk analysis results were acquired from un-flooded end pieces (where the endpiece of OBSV 12 is REF.6) and six flooded units of OBSV 12 (Table 1). The sample experienced an increase in magnesium concentration from 0.28 wt.% in the unflooded sample to 0.52 wt.% for OBSV 12.4 flooded with SSW. However, no significant loss of other elements was observed.

4.2. Helium Ion Microscopy Combined with Secondary Ion Mass Spectrometry (HIM-SIMS)

The HIM provided a high-resolution secondary electron (SE) image of a fresh surface chalk sample with detailed topographical features of the coccolith grains (Figure 4a). Elemental maps of the same ROI were acquired using SIMS (Figure 4b–h). ^{40}Ca was found correspondingly to the occurrence of the coccolith (Figure 4a), along with ^{12}C$_2$ and ^{16}O which shows the calcite (CaCO$_3$) distribution. However, there are a few locations on the coccolith surface where these ions are not detected: ^{24}Mg, ^{27}Al, ^{28}Si, and ^{39}K are distributed in areas of less than 1 μm^2, coinciding with the absence of ^{16}O, ^{40}Ca, and partly ^{12}C$_2$ signals (Figure 4e–h).
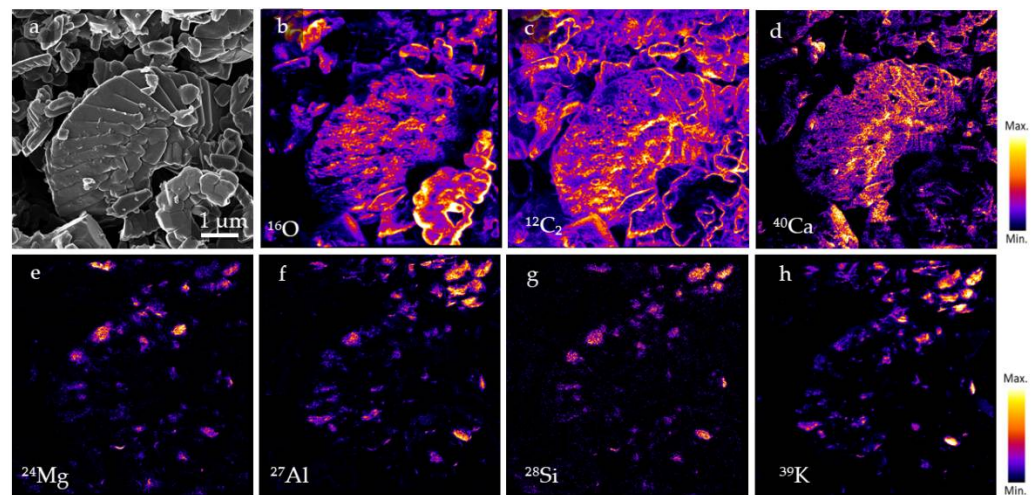
Figure 4. HIM-SIMS images of sample OBSV 12.4. (**a**) SE image of a ROI obtained by HIM focusing on a coccolith fragment. (**b–d**) Chemical images obtained by SIMS of ^{16}O, ^{12}C$_2$, and ^{40}Ca are presented with a scalebar at the right, representing the intensity of each element. (**e–h**) Elemental distribution of ^{24}Mg, ^{27}Al, ^{28}Si, and ^{39}K.

Separate clay grains were not identified in the selected SE image. An SE image overlayed with the SIMS maps of ^{24}Mg, ^{27}Al, ^{28}Si, and ^{39}K, in red, clearly defines locations and topography of clay coating the coccolith surface (Figure 5a). Increased magnification of the SE image allowed us to observe various surface roughness (Figure 5b,d,f) and the corresponding distribution of calcite in Figure 5c,e,g.
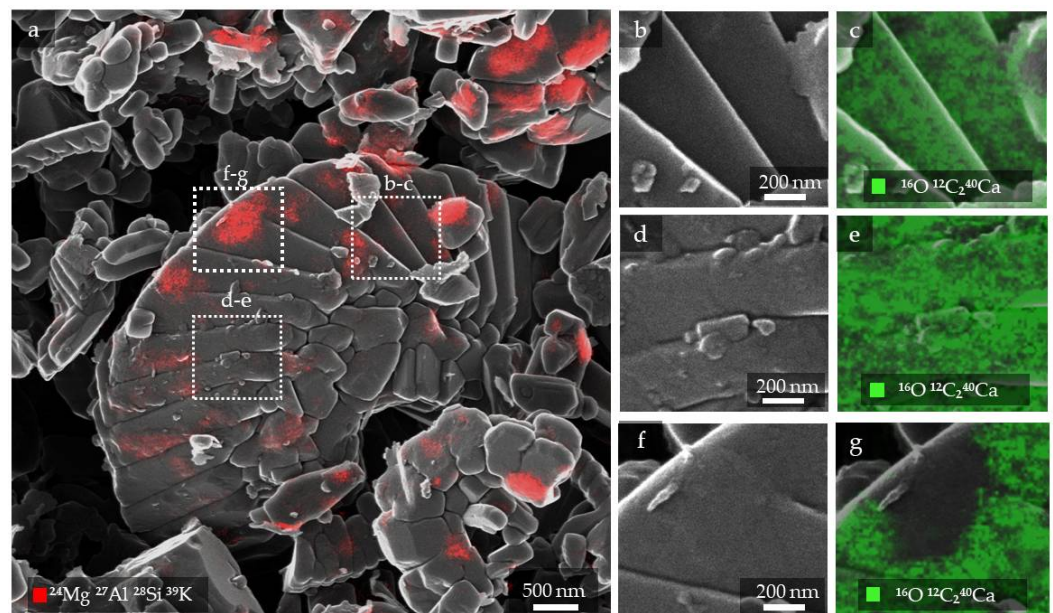
Figure 5. SE images with identified calcite distribution versus clay coating linked to topography of the coccolith grain and fragments. (**a**) The SE image is overlayed by the coinciding distribution of ^{24}Mg, ^{27}Al, ^{28}Si, and ^{39}K in red, representing clay. Three white boxes are marked and presented with increased magnification to highlight surface topography versus chemistry (**b–g**). (**b**) Smooth, yet stepwise surface (**c**) with distribution of ^{16}O, ^{12}C$_2$, and ^{40}Ca in green combined with the corresponding SE image. (**d**) Irregular surface. (**e**) The irregular surface in (**d**) is identified as calcite. (**f**) SE image with smooth surface which covers and evens out the steplike structure. (**g**) The overlay of (**f**) with the SIMS image presents a calcite dominated background.

Two clay minerals with different shapes on the same ROI were magnified to highlight possible compositional differences. A clay mineral was coating the surface and the second had a sheetlike appearance (Figures 6a–d and 6e–h). The second clay was thicker and lacked calcite distribution in the center. The ^{24}Mg concentration versus ^{27}Al, ^{28}Si and ^{39}K reflected a higher ^{24}Mg concentration on the sheetlike clay (Figure 6e–h).
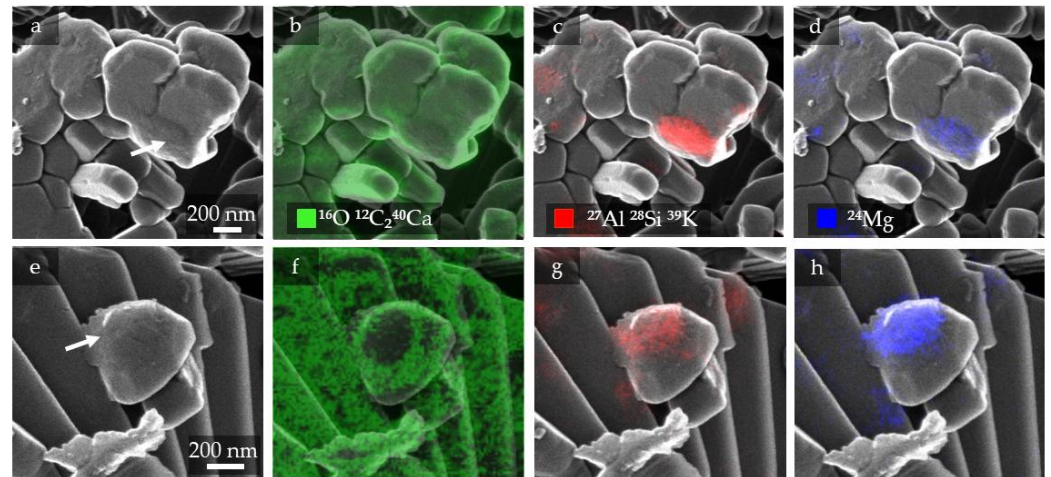
Figure 6. Series of SE and overlay of SE with SIMS results showing mineral phases of coccolith fragments and coating mineral phases, highlighting ^{24}Mg distribution. (**a**) SE image of a coccolith fragment highlighting a location with a slightly different roughness marked by a white arrow. (**b**) Calcite distribution (^{16}O, ^{12}C$_2$, and ^{40}Ca) overlaying the corresponding SE image. (**c**) SIMS detection of ^{27}Al, ^{28}Si, and ^{39}K overlapped with the corresponding SE image. These elements form a sub-micron phase of clay. (**d**) ^{24}Mg distribution. (**e**) SE image discloses a sheetlike feature covering a fragment marked by an arrow. (**f**) SIMS identification of calcite (^{16}O, ^{12}C$_2$, and ^{40}Ca) distribution, overlapping the corresponding SE image. Central absence of calcite. (**g**) The sheetlike mineral has presence of ^{27}Al, ^{28}Si, and ^{39}K representing clay. (**h**) ^{24}Mg is abundant on the sheetlike feature.

5. Discussion

High resolution imaging of chalk by HIM reveals detailed textural information of nanosized grains or coating adhered to the surface of the coccolith fragment. Altered surfaces may be a result of diagenetic processes in the reservoir or experimental flooding processes. Surface locations dominated by calcite are possible sites of calcite dissolution or potential calcite reprecipitation which is a common process during diagenesis [15]. In the analyzed ROIs, clay mineral phases are detected mainly as sub-micron sized particles filling cracks, adhering to the coccolith surface, or as sheetlike features.

Imaging and chemical identification by HIM-SIMS allows to identify nanosized mineral phases chemically and provides high-quality, both topographical and chemical, images. Identification of primary or secondary minerals on this scale is important for interpretation regarding wettability. Most of these phases are not possible to distinguish using SEM-EDS, hence, erroneous conclusions may be drawn. HIM results will clearly identify locations where mineral phases cover the coccolith, and the combination with SIMS will additionally provide chemical information and confirm the presence of non-carbonate phases, such as clay minerals (Figure 5a). However, when acquiring data for mass m/z 56, in the attempt to map ^{56}Fe, it is ambiguous, as the SIMS system (providing a mass resolution power $m/\Delta m \approx 400$) [33], could not differentiate the compound ^{40}Ca ^{16}O from ^{56}Fe due to mass interference (mass resolution of at least 2500 necessary). Glauconite (K,Na)(Fe^{3+},Al,Mg)$_2$(Si,Al)$_4$O$_{10}$(OH)$_2$ is present in St. Vaast Formation [28] and is likely to be identified in this sample, besides the presence of 0.4 wt.% Fe (Table 1) can enhance the probability of glauconite presence. Based on shape and data acquired by SIMS, the mineral phase identified is more likely illite (K,H$_3$O)(Al,Mg,Fe)$_2$(Si,Al)$_4$O$_{10}$[(OH)$_2$·(H$_2$O)].

MgO was the only element that was enriched in the sample during the flooding experiment, showing values of 0.4–0.6 wt.% after flooding compared to <0.3 wt.% in unflooded samples. The increase in Mg^{2+} has been demonstrated in numerous flooding experiments, leading to growth of magnesite [9,10]. In the ROI studied with HIM-SIMS (Figure 4e) magnesite ($MgCO_3$) could not be identified. The increased amount of Mg^{2+} (Table 1), derived from the injected fluid, is possibly retained in the sample by increasing the magnesium concentration in present clay minerals. However, this requires further studies on clays before and after flooding experiments. Two clay minerals identified with different shapes (Figure 6) may have different concentrations of magnesium. By comparing the distribution of ^{24}Mg versus ^{27}Al, ^{28}Si, and ^{39}K for 6d-c and 6h-g it is likely that the clay mineral in 6h has a higher ^{24}Mg concentration. SIMS may nevertheless not reflect accurate quantification and additional data, either with the use of standards or by a different method, is needed.

6. Conclusions

An Upper Cretaceous outcrop chalk sample, where calcite is the most abundant phase (up to 95 %) with an artificial fracture of a diameter of 2.25 ($\pm$0.05) mm, was flooded by SSW under reservoir conditions (T = 130 °C; p = 12 MPa) at the Norwegian Continental Shelf over approximately two months. This is a routine experiment regarding IOR research [2,9]. Mg^{2+} is one of the most reactive ions in SSW and the sample increased the bulk MgO concentration from 0.28 to 0.52 wt.% (Table 1) as expected, e.g., [9,37]. The combination of high-resolution SE imaging by HIM combined with elemental maps obtained by SIMS, showed that calcite was in numerous areas covered by other phases, challenging to resolve with traditional analytical methods such as SEM-EDS. In various research studies within this field, this observation had not previously been described or monitored ([9,10]) wherefore the presented study is novel and highlights the need of such analytical approach. In our case study, we could show that the HIM can identify phases covering the coccolith surface thoroughly and that high-resolution SIMS imaging allowed us to characterize those phases chemically which is the major advance using the combined HIM-SIMS. Moreover, most of the phases can be identified with chemical tools and, in cases, a secondary nature can even be interpreted. This has tremendous impact on further aspects of wettability processes and imbibition, as we can now show that calcite surfaces are heterogeneously covered by other mineral phases. These are novel data for modeling of wettability or other rock–fluid interaction processes. HIM-SIMS is a highly recommended method in reservoir characterization of fine-grained rocks when key processes take place on sub-micron and even nano-scale level. Moreover, sample preparation is very rapid, similar to traditional SEM-EDS studies. Hence, this technique, HIM-SIMS, opens new horizons for a variety of research fields within IOR and petroleum geosciences.

Author Contributions: Conceptualization, U.Z., J.-N.A.; Methodology, T.W., A.D.O., J.-N.A., R.I.K., U.Z.; Software, T.W., A.D.O.; Validation, All; Formal Analysis, T.V.B., T.W., J.-N.A., A.D.O.; Investigation: All; Resources, U.Z., M.V.M., J.-N.A.; Data Curation, All; Writing—Original Draft Preparation, T.V.B.; Writing—Review & Editing, All; Visualization. All; Supervision, U.Z., M.W.M., R.I.K., M.V.M.; Project Administration, U.Z.; Funding Acquisition: U.Z., J.-N.A. All authors have read and agreed to the published version of the manuscript.

Data Availability Statement: All data supporting the results are mentioned in the text or download-able with the Supplementary Materials.

Acknowledgments: The authors would like to thank the editor and reviewers for their inspiring and insightful comments which improved the manuscript.

Conflicts of Interest: The authors declare no conflict of interest.

References

1. Scholle, P.A.; Hsu, K.; Jenkyns, H. Diagenesis of Upper Cretaceous chalks from England, Northern Ireland and the North Sea. In *Pelagic Sediments: On Land and under the Sea*; John Wiley & Sons, Inc.: Hoboken, NJ, USA, 1974; pp. 177–210.
2. Strand, S.; Standnes, D.C.; Austad, T. Spontaneous Imbibition of Aqueous Surfactant Solutions into Neutral to Oil-Wet Carbonate Cores: Effects of Brine Salinity and Composition. *Energy Fuels* **2003**, *17*, 1133–1144. [CrossRef]
3. Korsnes, R.I.; Strand, S.; Hoff, Ø.; Pedersen, T.; Madland, M.V.; Austad, T. Does the chemical interaction between seawater and chalk affect the mechanical properties of chalk?. In *Eurock 2006: Multiphysics Coupling and Long Term Behaviour in Rock Mechanics*; Taylor & Francis: London, UK, 2006; pp. 427–434. ISBN 00415410010.
4. Korsnes, R.; Madland, M.V.; Austad, T. Impact of brine composition on the mechanical strength of chalk at high Temperature. In *Eurock 2006: Multiphysics Coupling and Long Term Behaviour in Rock Mechanics*; Taylor & Francis: London, UK, 2006; pp. 133–140, ISBN 0415410010.
5. Zhang, P.; Tweheyo, M.T.; Austad, T. Wettability alteration and improved oil recovery by spontaneous imbibition of seawater into chalk: Impact of the potential determining ions Ca^{2+}, Mg^{2+}, and $SO4^{2-}$. *Colloids Surf. A Physicochem. Eng. Asp.* **2007**, *301*, 199–208. [CrossRef]
6. Madland, M.V.; Midtgarden, K.; Manafov, R. The effect of temperature and brine composition on the mechanical strength of Kansas chalk. In Proceedings of the International Symposium of the Society of Core Analysts, Abu Dhabi, United Arab Emirates, 29 October–2 November 2008; p. 6.
7. Newman, G.H. The Effect of Water Chemistry on the Laboratory Compression and Permeability Characteristics of Some North Sea Chalks. *J. Pet. Technol.* **1983**, *35*, 976–980. [CrossRef]
8. Nermoen, A.; Korsnes, R.; Aursjø, O.; Madland, M.; Kjørslevik, T.A.; Østensen, G. How Stress and Temperature Conditions Affect Rock-Fluid Chemistry and Mechanical Deformation. *Front. Phys.* **2016**, *4*. [CrossRef]
9. Andersen, P.Ø.; Wang, W.; Madland, M.V.; Zimmermann, U.; Korsnes, R.I.; Bertolino, S.R.A.; Minde, M.; Schulz, B.; Gilbricht, S. Comparative Study of Five Outcrop Chalks Flooded at Reservoir Conditions: Chemo-mechanical Behaviour and Profiles of Compositional Alteration. *Transp. Porous Media* **2018**, *121*, 135–181. [CrossRef]
10. Zimmermann, U.; Madland, M.V.; Nermoen, A.; Hildebrand-Habel, T.; Bertolino, S.A.R.; Hiorth, A.; Korsnes, R.I.; Audinot, J.-N.; Grysan, P. Evaluation of the compositional changes during flooding of reactive fluids using scanning electron microscopy, nano-secondary ion mass spectrometry, x-ray diffraction, and whole-rock geochemistryCompositional Changes during Flooding. *AAPG Bull.* **2015**, *99*, 791–805. [CrossRef]
11. Megawati, M.; Andersen, P.Ø.; Korsnes, R.I.; Evje, S.; Hiorth, A.; Madland, M.V. The Effect of Aqueous Chemistry pH on the Time-Dependent Deformation Behaviour of Chalk-Experimental and Modelling Study. In Proceedings of the Pore2Fluid International IFP Energies Nouvelles, Paris, France, 16–18 November 2011.
12. Hellmann, R.; Renders, P.; Gratier, J.; Guiguet, R. Experimental pressure solution compaction of chalk in aqueous solutions Part 1. Deformation behavior and chemistry. In *Water–Rock Interactions, Ore Deposits, and Environmental Geochemistry*; Hellmann, R., Wood, S.A., Eds.; Geochemical Society: Washington, DC, USA, 2002; Volume 7, pp. 129–152.
13. Madland, M.V.; Hiorth, A.; Omdal, E.; Megawati, M.; Hildebrand-Habel, T.; Korsnes, R.I.; Evje, S.; Cathles, L.M. Chemical Alterations Induced by Rock–Fluid Interactions When Injecting Brines in High Porosity Chalks. *Transp. Porous Media* **2011**, *87*, 679–702. [CrossRef]
14. Fabricius, I.L.; Borre, M.K. Stylolites, porosity, depositional texture, and silicates in chalk facies sediments. *Ontong Java-Plateau—Gorm Tyra Fields North Sea Sedimentol.* **2007**, *54*, 183–205.
15. Hjuler, M.L.; Fabricius, I.L. Engineering properties of chalk related to diagenetic variations of Upper Cretaceous onshore and offshore chalk in the North Sea area. *J. Pet. Sci. Eng.* **2009**, *68*, 151–170. [CrossRef]
16. Megawati, M.; Madland, M.V.; Hiorth, A. Mechanical and physical behavior of high-porosity chalks exposed to chemical perturbation. *J. Pet. Sci. Eng.* **2015**, *133*, 313–327. [CrossRef]
17. Zimmermann, U.; Madland, M.V.; Minde, M.; Borromeo, L.; Egeland, N. Tools to Determine and Quantify Mineralogical Changes During EOR Flooding Experiments on Chalk. In Proceedings of the Abu Dhabi International Petroleum Exhibition & Conference, Abu Dhabi, United Arab Emirates, 13–16 November 2017.
18. Priebe, A.; Barnes, J.-P.; Edwards, T.E.J.; Pethö, L.; Balogh, I.; Michler, J. 3D Imaging of Nanoparticles in an Inorganic Matrix Using TOF-SIMS Validated with STEM and EDX. *Anal. Chem.* **2019**, *91*, 11834–11839. [CrossRef] [PubMed]
19. Notte, J.; Goetze, B. Imaging with the Helium Ion Microscope. In *Surface Analysis and Techniques in Biology*; Smentkowski, V.S., Ed.; Springer International Publishing: Cham, Switzerland, 2014; pp. 171–194.
20. Minde, M.W.; Zimmermann, U.; Madland, M.V.; Korsnes, R.I.; Schulz, B.; Gilbricht, S. Mineral Replacement in Long-Term Flooded Porous Carbonate Rocks. *Geochim. Cosmochim. Acta* **2019**, *268*, 485–508. [CrossRef]

21. Minde, M.W.; Madland, M.V.; Zimmermann, U.; Egeland, N.; Korsnes, R.I.; Nakamura, E.; Kobayashi, K.; Ota, T. Mineralogical alterations in calcite powder flooded with MgCl$_2$ to study Enhanced Oil Recovery (EOR) mechanisms at pore scale. *Microporous Mesoporous Mater.* **2019**, *304*, 109402. [CrossRef]

22. Borromeo, L.; Egeland, N.; Minde, M.W.; Zimmermann, U.; Andò, S.; Madland, M.V.; Korsnes, R.I. Quick, Easy, and Economic Mineralogical Studies of Flooded Chalk for EOR Experiments Using Raman Spectroscopy. *Minerals* **2018**, *8*, 221. [CrossRef]

23. Audinot, J.-N.; Philipp, P.; De Castro, O.; Biesemeier, A.; Hoang, Q.H.; Wirtz, T. Highest resolution chemical imaging based on secondary ion mass spectrometry performed on the helium ion microscope. Reports on progress in physics. *Rep. Prog. Phys.* **2021**, *84*, 105901. [CrossRef]

24. Wirtz, T.; De Castro, O.; Audinot, J.-N.; Philipp, P. Imaging and Analytics on the Helium Ion Microscope. *Annu. Rev. Anal. Chem.* **2019**, *12*, 523–543. [CrossRef]

25. Schroeder, C.; Gaviglio, P.; Bergerat, F.; Vandycke, S.; Coulon, M. Faults and matrix deformations in chalk: Contribution of porosity and sonic wave velocity measurements. *Bull. Soc. Geol. Fr.* **2006**, *177*, 203–213. [CrossRef]

26. Dusar, M.; Lagrou, D. Cretaceous flooding of the Brabant Massif and the lithostratigraphic characteristics of its chalk cover in northern Belgium. *Geol. Belg.* **2007**, *10*, 27–38.

27. Robaszynski, F.; Dhondt, A.; Jagt, J. Cretaceous lithostratigraphic units (Belgium). *Geol. Belg.* **2001**, *4*, 121–134. [CrossRef]

28. Briart, F.L.C. Saint-Vaast Chalk Formation—SVA. 2000. Available online: https://ncs.naturalsciences.be/cretaceous/2114-saint-vaast-chalk-formation-sva (accessed on 7 January 2022).

29. Abubeker, E. Water Weakening of Chalks—Comparsion of Intact and Fractured Cores. Master's Thesis, Faculty of Science and Technology, University of Stavanger, Stavanger, Norway, 2013; p. 88. Available online: https://uis.brage.unit.no/ (accessed on 13 December 2021).

30. Geitle, K. Chemically Induced Compaction in Fractured and Intact Chalk Cores. Master's Thesis, Institute for Energy and Resources (IER), University of Stavanger, Stavanger, Norway, 2013; p. 78. Available online: https://uis.brage.unit.no/uis (accessed on 13 December 2021).

31. Hlawacek, G.; Gölzhäuser, A. (Eds.) *Helium Ion Microscopy*; Springer International Publishing: Cham, Switzerland, 2016; p. 526.

32. Pillatsch, L.; Vanhove, N.; Dowsett, D.; Sijbrandij, S.; Notte, J.; Wirtz, T. Study and optimisation of SIMS performed with He$^+$ and Ne$^+$ bombardment. *Appl. Surf. Sci.* **2013**, *282*, 908–913. [CrossRef]

33. Dowsett, D.; Wirtz, T. Co-registered in situ secondary electron and mass spectral imaging on the helium ion microscope demonstrated using lithium titanate and magnesium oxide nanoparticles. *Anal. Chem.* **2017**, *89*, 8957–8965. [CrossRef] [PubMed]

34. Kim, S.; Trofimov, A.; Khanom, F.; Stern, L.; Lamberti, W.; Colby, R.; Abmayr, D.; Belianinov, A.; Ovchinnikova, O.S. High Resolution Multimodal Chemical Imaging Platform for Organics and Inorganics. *Anal. Chem.* **2019**, *91*, 12142–12148. [CrossRef] [PubMed]

35. Vollnhals, F.; Wirtz, T. Correlative Microscopy in 3D: Helium Ion Microscopy-Based Photogrammetric Topography Reconstruction Combined with in situ Secondary Ion Mass Spectrometry. *Anal. Chem.* **2018**, *90*, 11989–11995. [CrossRef] [PubMed]

36. Ost, A.D.; Wu, T.; Höschen, C.; Mueller, C.W.; Wirtz, T.; Audinot, J.-N. 4D Surface Reconstructions to Study Microscale Structures and Functions in Soil Biogeochemistry. *Environ. Sci. Technol.* **2021**, *55*, 9384–9393. [CrossRef] [PubMed]

37. Minde, M.W.; Wang, W.; Madland, M.V.; Zimmermann, U.; Korsnes, R.I.; Bertolino, S.R.; Andersen, P. Temperature effects on rock engineering properties and rock-fluid chemistry in opal-CT-bearing chalk. *J. Pet. Sci. Eng.* **2018**, *169*, 454–470. [CrossRef]

Paper III:

"4D surface reconstruction of micron-sized organic calcite for characterization of chemical heterogeneity of chalk surfaces".

Bredal, T. V., Ost, A. D, Wirtz, T., Audinot, J.-N., Zimmermann, U., Madland, M. V., Minde, M. W., Puntervold, T., 2023,

Energy and Fuels

Paper III

Article

4D Surface Reconstruction of Micron-Sized Organic Calcite for the Characterization of Chemical Heterogeneity of Chalk Surfaces

Tine V. Bredal,* Alexander D. Ost, Tom Wirtz, Jean-Nicolas Audinot, Udo Zimmermann, Merete V. Madland, Mona W. Minde, and Tina Puntervold

Cite This: https://doi.org/10.1021/acs.energyfuels.2c04047

Read Online

ACCESS | Metrics & More | Article Recommendations | Supporting Information

ABSTRACT: Seawater injection into chalk reservoirs is a method for improved oil recovery (IOR) at the Norwegian Continental Shelf (NCS). During the injection of fluids for IOR, complex physicochemical interactions between the injected fluid and the reactive rock surface will take place, such as compaction and alterations of rock properties (e.g., porosity, permeability, wettability). The distribution of noncarbonate mineral phases in the reservoir and on the surface of the chalk will dictate wettability properties. Yet, the identification and quantification of nanometer-sized mineral phases on calcite surfaces have been challenging due to insufficient spatial resolution and sensitivity of the analytical methods used. On-shore chalk was used in this study. Helium ion microscopy (HIM) combined with *in situ* secondary ion mass spectrometry (SIMS) was used to produce secondary electron images for mapping surface morphology and topography correlated with chemical maps from SIMS. First, a 3D surface model was created from a series of secondary electron images acquired

Surface chemistry of coccoliths

from different perspectives around the coccolith. A chemical image obtained by SIMS was developed on the same region of interest and projected onto the 3D surface model to create a 4D surface reconstruction (3D+1 concept). This includes surface chemistry information on sub-micron-sized noncarbonate phases on calcite grains. The surface distribution of noncarbonate phases added up to a minimum of 6.3%, where no ^{40}Ca had been detected. Moreover, 39.8% of the entire area is characterized by ^{40}Ca and ^{27}Al plus ^{28}Si. Compared with 5 wt % noncarbonate phases identified by whole-rock geochemistry, we identify at least 200−300% higher noncarbonate phase abundance than expected based on bulk geochemistry. This has a significant implication for the modeling of mineral surface charges, the major criteria for wettability calculations. Therefore, HIM-SIMS studies allow nanoscale mapping and mineral phase identification, which will enhance the knowledge of fluid−rock interactions for purposes related to IOR, carbon capture, and storage as well as for hydrogen storage.
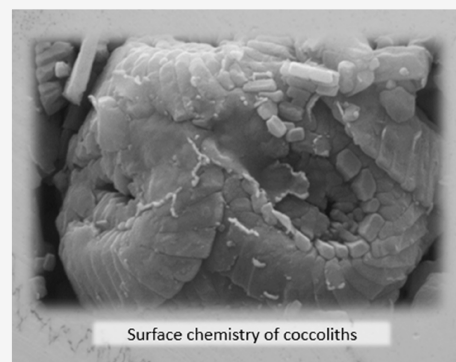
INTRODUCTION

Ekofisk is a giant chalk reservoir on the Norwegian Continental Shelf (NCS). Seawater injection was first performed in 1987 at Ekofisk to sustain pore pressure and prevent seabed subsidence following declined hydrocarbon production, initially produced by pressure depletion.[1] Seawater injection allowed not only to sustain but also to increase the oil production beyond initial predictions. The instant increase in oil production was related to spontaneous imbibition, which was confirmed by laboratory experiments.[1] The initial mixed-wet chalk surface became more water-wet due to the sulfate ions present in the injection brine, which adsorbed to the chalk surface and catalyzed the wettability alteration process, hence releasing additional oil.[2] The seawater injection did, however, not prevent further seabed subsidence, but stimulated compaction due to the water-weakening of chalk.[3] Seawater injection is implemented as a standard method for improved oil recovery (IOR) from chalk reservoirs.[4]

Chalk is a deep marine sedimentary rock consisting mainly of highly porous calcareous micro- and nanofossils, but mostly

coccolithophores, which degrade to individual skeletal plates of micron-sized coccoliths with increasing burial. Due to its deposition at large distances from the shore, the presence of detrital grains (noncarbonate) is normally minor. Grain surface properties (e.g., chemistry) impact oil recovery by changing the surface wettability to being more water-wet (hydrophilic surface) by injecting seawater into the reservoir. Current models for wettability alterations are based on simplified models that consider the calcite surface as either water-wet, oil-wet, fractional, or mixed-wet controlled by the chemistry.[5] Atomic force microscopy (AFM) measurements have shown that within Danish North Sea oil fields, chalk presented heterogeneous properties, revealing a physical and chemical

complexed chalk surface.[6] The mineralogical distribution of the rock surface, determines surface charges and adsorption of polar organic crude oil components.[7] Water-wet rock surfaces allow spontaneous imbibition of water into the rock matrix and expelling the oil therein, thus increasing the total oil recovery. Seawater injection into chalk reservoirs causes alteration of the wettability condition of the reservoir rock.[4] Due to its unique chemical composition, with ions such as SO_4^{2-}, Mg^{2+}, and Ca^{2+} in addition to Na^+, Cl^-, and K^+, the chemical equilibrium in the reservoir between crude oil, brine, and rock is disturbed, and wettability is altered to more water-wet conditions.[8] Additional oil is produced due to the generation of positive capillary forces, hence improving sweep efficiency.

Helium ion microscopy (HIM) coupled with secondary ion mass spectrometry (SIMS)[9−11] was used to image *in situ* nanosized mineral phases located on the calcite surfaces at ultrahigh spatial resolution (secondary electron mode: 0.5 nm, SIMS: <20 nm).[10−12] This combination of methods appeared to be superior in comparison to several others that have been applied to analyze nanoscaled newly grown mineral phases in chalk.[12,13] Surface chemistry of sub-micron-sized minerals was identified on flooded analogue chalk. A recently developed analytical method is used to create 4D surface reconstructions using the HIM-SIMS, by creating a 3D surface model from multiview SE images with photogrammetry software and overlaying them with a SIMS image acquired from the same region of interest (ROI).[14,15] In this study, we aim to evaluate the surface chemistry in unflooded chalk by creating a 4D surface reconstruction of coccoliths. The distribution of the noncarbonate mineral concentration at the surface will be compared to the noncarbonate mineral abundance obtained by bulk geochemical data. The expression "noncarbonate" will hereon denote *only* mineral phases not organic compounds, etc. The applied method combination of HIM and SIMS, along with the visualization of the 4D reconstruction, will improve the understanding of noncarbonate mineral distribution within the chalk. Petrographic and mineralogical identification of the sample on a microscale is performed to complement the interpretation on a nanoscale and the bulk geochemistry of the sample. Mineralogical analyses are paramount as the composition within a reservoir rock influences the type of oil components adsorbed on the surfaces and therefore also wettability alteration processes. Mapping the distribution and extension of noncarbonate phases is essential for evaluating wettability alterations and spontaneous imbibition when a fluid injection is implemented in impure chalk reservoirs. This should be followed by using the findings presented here and especially applying the proposed methodology. Additionally, the 4D surface mapping of the surface chemistry will increase the understanding of brine−rock interactions that affect geomechanical processes in the reservoir.

MATERIALS AND METHODOLOGY

Sample Material. Due to the difficulty of collecting reservoir samples, analogue on-shore quarried chalks have previously been used to study the IOR process.[16,17] In this study, chalk from the Mons basin in Belgium was used, which is located in the northern extension of the Paris Basin. The chalk was deposited during the Upper Cretaceous (Coniacian) and belongs to the St. Vaast Formation.[18−20] The deep basin consists of the accumulation of fine-grained carbonate dominated by coccolithophores and fragments of coccoliths, as well as foraminifers. Several shifts in sedimentation and deformation events have formed the chalk succession into major sedimentary and

structural units. A thin bed of glauconitic sediments marks the lower, transgressive sequence of the chalk deposits from the Coniacian onward in the Mons region. Early Cretaceous facies are locally covered by calcirudites, sandstones, and conglomerates rich in glauconite and ferriferous illite. The basal unit, St. Vaast Formation is followed by the Trivières, Obourg, Nouvelles, and Spiennes Formations,[19] where the latter four were deposited during Early-Late Campanian to Late Campanian. The basin may be considered a "syncline" developed on a folded and faulted Devonian-Carboniferous basement[21] characterized by extension during the entire Upper Cretaceous.[18]

The St. Vaast Formation contains more than 95% calcium carbonate, with impurities of quartz and traces of glauconite, chlorite, and pyrite.[22] This chalk formation possesses high specific surface areas of 4.52 ($\pm$0.14) g/m^2.[23] The chalk sample discussed here along with several cores for supplementary references were extracted from a chalk block for the identification of chemical homogeneity. Earlier research showed that the sampled chalk drilled from cubic-meter-large freshly broken blocks from the quarries do not show any hints of alteration controlled by careful electron microscopy, whole-rock geochemistry, and stable isotope measurements.[16] The sample has not been cleaned and has not been in contact with hydrocarbons.

Whole-Rock Geochemistry. The sample material was milled in an agate beaker to very fine mesh. The geochemical data was obtained by inductively coupled plasma-mass spectrometry (ICP-MS) analysis. The milled sample was mixed with the $LiBO_2/Li_2B_4O_7$ flux in crucibles and fused in a furnace. The cooled bead was dissolved in the American Chemical Society (ACS) grade nitric acid and analyzed by ICP-MS. Loss on ignition (LOI) was determined by igniting a sample split before measuring the weight loss after being ignited at 1000 °C for 1 h. The sample was cooled and weighed again. The total carbon and sulfur concentrations were determined by the LECO method. Here, an induction flux was added to the prepared sample and then it was ignited in an induction furnace. A carrier gas swept up the released carbon to be measured by adsorption in an infrared spectrometric cell. Fourteen additional elements were measured after dilution in Aqua Regia. The prepared sample was treated with a modified Aqua Regia solution with equal parts of concentrated HCl, HNO_3, and $DI-H_2O$ for 1 h in a heating block. The sample volume was increased with dilute HCl solutions and splits of 0.5 g were analyzed. The accuracy and precision are between 2 and 3% per element, respectively.

Scanning Electron Microscopy and Energy-Dispersive X-ray Spectroscopy (SEM-EDS). Fresh surfaced samples were mounted on aluminum holders, followed by coating with gold (Au). A Zeiss Supra 35-VP SEM was used for high-magnification topographical imaging and elemental composition was obtained by an EDS detector. Images were acquired by using the secondary electron (SE) detector at a fixed working distance of 10 mm, accelerating voltage of 15 kV, and an aperture size of 30 μm. The energy-dispersive X-ray spectroscopy (EDS) data was used for the interpretation of minerals. Backscatter electron microscopy (BSE) images were acquired to identify the texture, separate elements with atomic numbers higher than that of calcite, and resolve the intraporous conditions. BSE imaging was performed on carbon-coated polished mounts swept in epoxy.

Helium Ion Microscopy−Secondary Ion Mass Spectrometry (HIM-SIMS) and 4D Surface Reconstruction. SE images were acquired in a Zeiss ORION NanoFab helium ion microscope (HIM).[24,10] Forty-eight SE images were acquired with 2048 pixels × 2048 pixels, 25 keV He$^+$, 1 pA, dwell time of 10 μs/pixel, 4 lines average, and polar angle of 45° with sample stage rotation steps every 10 and 50° and polar angle with rotation steps of 30° for each image. The in situ chemical analysis of the specimen was acquired by using a secondary ion mass spectrometer (SIMS) system developed for HIM (HIM-SIMS).[9−11] Ne$^+$ ions are used for SIMS to enhance the sputtering of the surface and therefore to increase the secondary ion (SI) yield and hence signal statistics. The following parameters were used during the SIMS acquisition: 8.5 × 8.5 μm^2 field of view, 512 pixels × 512 pixels, 25 keV Ne$^+$, 2.5 pA, and a dwell time of 2.5 ms/

Table 1. Bulk Geochemical Data from Selected Locations in the Same Outcrop Block of Chalk Used for Sampling in This Study, Demonstrating the Homogeneous Distribution of Major Elements within the Sample (in Weight %)[a]

element (wt %)	SiO_2	Al_2O_3	Fe_2O_3	MgO	CaO	Na_2O	K_2O	TiO_2	P_2O_5	MnO	LOI	sum
detection limit	0.01	0.01	0.04	0.01	0.01	0.01	0.01	0.01	0.01	0.01	-	-
OBSV 4	3.32	0.97	0.34	0.29	52.06	0.04	0.22	0.04	0.06	0.02	42.5	99.86
OBSV REF 1	3.50	1.03	0.37	0.28	52.01	0.04	0.23	0.05	0.05	0.02	42.3	99.85
OBSV REF 2	3.38	1.00	0.34	0.28	52.29	0.04	0.22	0.05	0.06	0.02	42.2	99.84
OBSV REF 3	3.40	1.03	0.33	0.30	51.89	0.04	0.23	0.05	0.09	0.02	42.5	99.84
OBSV REF 4	3.44	1.01	0.39	0.29	51.97	0.04	0.22	0.05	0.10	0.02	42.3	99.85
OBSV REF 5	3.59	1.05	0.47	0.28	52.00	0.04	0.23	0.05	0.07	0.02	42.0	99.84
OBSV REF 6	3.58	1.05	0.40	0.28	51.89	0.04	0.24	0.05	0.06	0.02	42.2	99.84
OBSV REF 7	3.39	1.00	0.54	0.27	51.90	0.04	0.22	0.05	0.10	0.02	42.3	99.83

[a]Please find the complete geochemical data set in Supplementary Material Appendix 1.
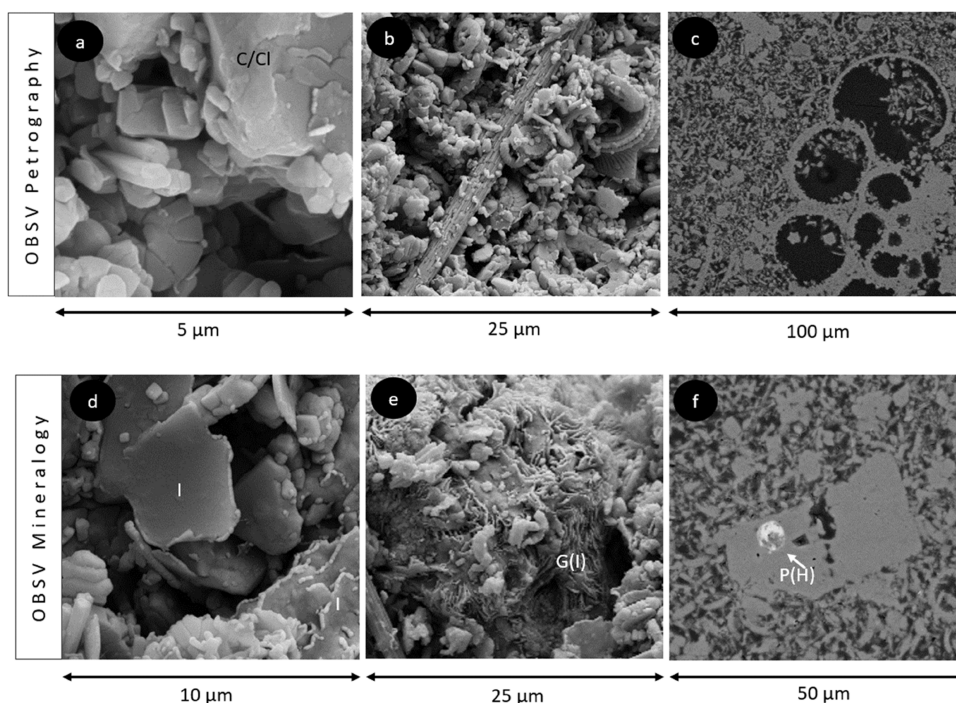
Figure 1. Secondary electron (SE) images combined with EDS acquisitions obtained from OBSV 4 f (St. Vaast Formation): (a) calcite (C) and clay (Cl) on the calcite surface containing oxides of Si, Al, and Mg; (b) well-preserved nanofossils and coccoliths; (c) BSE image of abundant foraminifera without significant intrafossil cementation or new growth; (d) flaky authigenic illite (I); (e) glauconite (G) or possibly illite within the sample; and (f) BSE image of framboidal pyrite (P) inside a large calcite grain.

pixel. A 3D surface model was created from the series of multiview SE images acquired around the same ROI from different perspectives. A chemical image obtained by SIMS was acquired at the selected location and projected onto the 3D surface model, creating a 4D surface reconstruction.[14,15] A MATLAB code was used to calculate the relative surface of each ion, where the ion was detected with respect to the entire surface of the coccolith from the SIMS image. ^{40}Ca (representing calcite) was counted separately, whereas the number of pixels with ^{27}Al and ^{28}Si was counted collectively, representing clay (noncarbonate). The surface distribution of ^{24}Mg presented a very localized distribution (in the form of a hotspot composed of Mg-rich carbonate) and was processed separately.

RESULTS

Whole-Rock Geochemistry. Major elements for OBSV 4 and seven additional samples collected from the same outcrop block of chalk are presented in Table 1. The concentrations of noncarbonate minerals were 5 wt % in OBSV 4. The

determined values are typical for relatively clean chalk (Andersen et al.[16]).

Electron Microscopy. The SE images of the chalk sample of the St. Vaast Formation reveal the presence of well-preserved coccoliths (Figure 1a), where complete rings are normally around 1−5 μm (Figure 1b) and only rarely exceed 10 μm. SE images showed a preserved intrafossil porosity and only limited cementation (Figure 1c). Minerals observed in the images were identified as alkali feldspar, illite, glauconite, and pyrite determined by texture (SEM) and composition (EDS) as well as atomic number discrepancy (BSE) presented in Figure 1d−f.

Helium Ion Microscopy−Secondary Ion Mass Spectrometry. The HIM-SE image of a coccolith was acquired to show in detail its topographical structure (Figure 2a). Elemental maps of the same ROI were imaged using SIMS (Figure 2b−f). ^{40}Ca was detected widely on the coccolith surface (Figure 2f) and correlated with the expected calcite
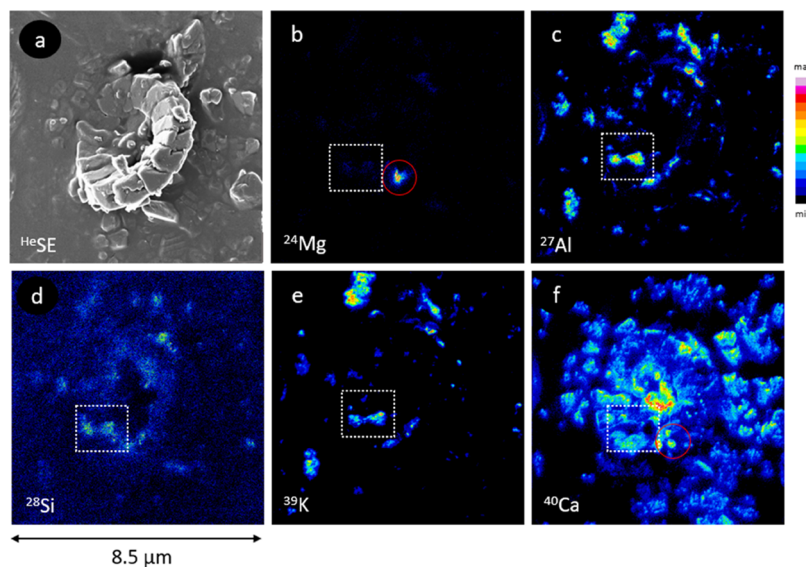
Figure 2. Coccolith from OBSV 4 analyzed with HIM-SIMS. A white rectangle highlights the occurrence of ^{27}Al, ^{28}Si, ^{39}K, and ^{24}Mg (b−f). (a) HIM-SE top-view image of the coccolith structure. (b) ^{24}Mg "hotspot" is marked by a red circle. (c)−(e) Elemental distributions of ^{27}Al, ^{28}Si, and ^{39}K, respectively. (f) Distribution of ^{40}Ca. The red circle highlights the area with a high abundance of ^{40}Ca, corresponding to the red circle in (b).
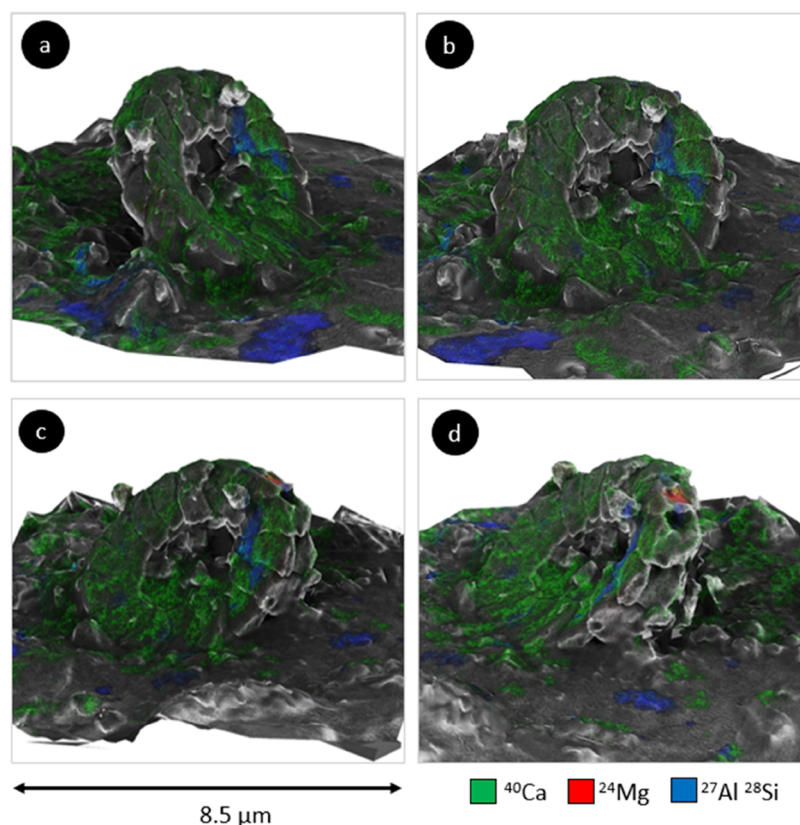
Figure 3. 4D surface reconstruction of the coccolith grain presented from different perspectives with azimuthal angles of 0, 45, 60, and 90° (a−d). ^{40}Ca is represented by green, ^{24}Mg by red, and ^{27}Al−^{28}Si compound by blue pointing to silicates.

(CaCO$_3$) distribution. The high-resolution chemical distribution accurately separates calcite from noncarbonate, possibly silicate mineral phases (^{24}Mg, ^{27}Al, ^{28}Si, and ^{39}K) on a nanoscale, which are identified as clays according to their morphologies (Figure 2a). The highlighted area of approximately 500 × 500 nm^2 (red circle in Figure 2b) displayed an accumulation of ^{24}Mg. The so-called Mg "hotspot" showed absence of ions typical for noncarbonate phases.

The final 4D surface reconstruction visualizes the distribution of different chemical phases linked to the topography of the selected coccolith (Figure 3).

Chemical Surface Distribution. The total number of pixels in the selected raw SIMS images (Figure 2b−f) was 512 × 512, which covered 72.25 μm^2 of the surface, and ^{40}Ca, ^{24}Mg, ^{27}Al, and ^{28}Si were measured. ^{40}Ca was detected within

the analyzed surface covering a total area of 89.8%. In 46.1% of the pixels, ^{24}Mg, ^{27}Al, ^{28}Si, or all three elements were present. As each pixel can contain several ions, the data set is categorized into groups: (i) calcite ^{40}Ca (locations occupied by calcite only), (ii) ^{24}Mg hotspot, (iii) ^{27}Al and/or ^{28}Si (locations occupied by noncarbonate only), and (iv) "mix" composed of ^{40}Ca and ^{27}Al/^{28}Si. The mix of the latter covered 39.8% of the area, while calcite (indicated by ^{40}Ca only) covered 50.0% of the sampled region and noncarbonate and noncalcite areas accounted for more than 10% of the surface (Table 2). ^{24}Mg

Table 2. Relative Surface Distribution of Detected Elements with Respect to the Entire Surface of the Coccolith (Figure 2b−d,f)

	area	%
^{40}Ca only	50.00	%
^{24}Mg (dominantly present at hotspot)	1.40	%
^{27}Al and/or ^{28}Si or (noncarbonate)	6.30	%
"Mix": ^{40}Ca and ^{27}Al and/or ^{28}Si (or all)	39.80	%
locations with no detection (^{40}Ca, ^{27}Al, ^{28}Si, ^{24}Mg)	2.50	%
total field of view	100.00	%

hotspot was detected in 1.4% of the pixels and mostly in one area only. However, the "mix" contains not necessarily only minerals composed of ^{40}Ca, ^{27}Al, and ^{28}Si but also minerals either composed of ^{40}Ca or ^{27}Al and ^{28}Si or a combination of the elements. This enlarges the number of noncarbonate phases covering the coccolith.

■ DISCUSSION

The noncarbonate minerals in the matrix of the selected sample identified by SEM-EDS were alkali feldspar, illite, and glauconite, in addition to other nonclassified clay minerals (Figure 1a,d−f). The high-resolution chemical distribution obtained by SIMS presents a detailed ion composition of the coccolith grain surface. The noncarbonate composition on the surface is represented by Mg-rich carbonate and abundant clay minerals, according to the identified chemistry likely belonging to the smectite-illite group (S-I) or the illite-chlorite group (I-C). The chemical distribution (^{24}Mg, ^{27}Al, ^{28}Si, and/or ^{39}K) is in accordance with the presence of detrital grains identified in the matrix and the overall elemental composition measured in the bulk geochemistry (Figure 2a−f). A common process during burial diagenesis is the new growth of authigenic clay minerals such as illite, altering from glauconite[25] depending on the pressure and temperature conditions. Glauconite is abundant in the St. Vaast Formation;[22] hence, illite surface detection is likely. For a more accurate determination of the mineral type, additional methods that allow the identification of crystallographic properties such as TEM[26] or TERS combined with AFM may be used for supporting these results.[27] However, at this stage, the abundance of the identified phases is of extraordinary importance. The mineralogical identification provided indicates mineral surface variation not recognized in such a quantitative amount, which is in turn of importance for modeling purposes for rock−fluid interaction in chalk (e.g.,[16]). Surface mineral composition, charge, and ion-exchange capacity as well as brine pH and ionic composition are some of the rock and fluid properties that impact initial wettability establishment and wettability alteration and spontaneous imbibition potential during water injection.[7] The noncarbonate surface distribution showed 6.3%

in addition to a fraction of the 39.8% chemically mixed area together with the abundance of minute Mg-rich carbonate (Table 2). The bulk geochemistry showed on the other hand abundance of only 5% noncarbonate phases (Table 1), which demonstrates the much wider distribution of noncarbonate phases on the coccolith surface than expected. The combined high-resolution HIM-SIMS results provided not only the surface chemical composition but also the distribution of these elements and subsequently minerals visualized in the 4D surface reconstruction (Figure 3). The 4D surface reconstruction shows not only a wider distribution of noncarbonate, most probably clay minerals coating coccolith surfaces, but also so-called "hotspots," here dominated by ^{24}Mg (Figures 2b and 3), which are challenging to be recognized by conventional SEM-EDS studies.[12] The distribution of the noncarbonate phases is heterogeneous at this high resolution and correlates with the heterogeneous distribution of adhesion properties on the calcite surface obtained by AFM studies.[6,28] Hassenkam et al. (2009) found that wettability and elasticity were inhomogeneously distributed over scales of 10s of nanometers on the surface of chalk and interpreted mixed wet surface in patches with different physiochemical properties. It was suggested that these were relicts from material originally present during sedimentation or a result of diagenesis.

The whole-rock geochemistry of the various samples collected from the outcrop block (Table 1) showed comparable geochemical compositions for all reference samples. This implies that the noncarbonate concentration is homogeneously distributed on the core scale. However, additional acquisitions are necessary to increase the value of these observations, which suggest an unexpectedly extensive distribution of noncarbonate phases on the surface of calcite grains in patches. Waterflooding of reservoirs may cause mineralogical changes, such as dissolution of Opal-CT, reprecipitation of Mg−Si-bearing minerals[16] and the dissolution of calcite, followed by the precipitation of magnesite.[29−32] These processes are dependent on the composition of the injection water, present formation water, and its pH, reservoir temperature, and stress conditions but strongly dependent on the mineralogical composition[26,32,33] and their surface charges. As fluid−rock interactions occur at the spatial scale of single pores, it is essential to understand chemical processes on the nanoscale related to diagenetic characteristics.[34]

The application of HIM-SIMS in our first 4D study on chalk shows that the abundance of noncarbonate phases is more widespread than earlier modeled or expected.[26,32,35] As the presence, composition, and distribution of noncarbonate mineral phases influence the surface charge, surface wetting, and crude oil adhesion in carbonate rock, this observation affects one key area for improving the oil recovery by wettability alteration methods. Experimental work has shown that crude oil acids have a stronger affinity to a pure chalk surface than to crude oil bases.[36] Other experimental work has shown that for a sandstone surface, where the chemistry is different from that of chalk, the crude oil bases adsorbed readily over the crude oil acids. Thus, when the chalk contained noncarbonate mineral impurities, in the form of Opal-CT (hydrated silica), the preferences of the chalk changed slightly. When chalk contains noncarbonate minerals, it prefers crude oil acids over bases, but the affinity of bases to the surface increases.[7,37] Therefore, when waterflooding a reservoir, the crude oil−brine−rock interactions taking place in

the pore space may be influenced by noncarbonate mineral phases at the pore surfaces. If wettability alteration is believed to be a mechanism for the improved oil recovery observed by low salinity or Smart Water flooding, then interactions between the crude oil components, ions in the brine phase, and the actual pore surface minerals are very important.

Heterogeneous surface charge areas, related to varying surface mineral distribution, hamper the predictions in the field of wettability. Here, we image submicron-sized noncarbonate phases in patches on a 4D surface reconstruction (Figure 3) that are smaller than a single droplet.[38] Current wettability models are based on bulk geochemistry and subsequently bulk mineralogy with an even distribution throughout the sample. Nevertheless, recent studies in regard to wettability s.l. emphasized the role of fluid−fluid interaction[39] and the role of droplets within a porous material,[40] which is suspected to have a higher impact on EOR than proposed earlier.

A more extensive and heterogeneous distribution of noncarbonate phases than expected of 6.3% noncarbonate plus a fraction of 39.8% mixed composition (Table 2) will impact wettability alteration processes and the potential for spontaneous imbibition. Future quantification of the abundance of noncarbonate phases covering calcite or dolomite surfaces in carbonate reservoirs is essential to increase the understanding of brine−rock interaction mechanisms.

■ CONCLUSIONS

A 4D surface reconstruction model, consisting of a 3D reconstruction has been obtained from a series of HIM-SE images overlaid with chemical maps generated by high-resolution SIMS of a single coccolith grain in outcrop chalk. The details of the surface chemistry linked to topography has not been presented this way before. The 4D surface model demonstrated that the presence of noncarbonate minerals (composed of mainly ^{27}Al, ^{28}Si, and ^{39}K, interpreted as smectite-illite or illite-chlorite group members) was inhomogeneously distributed at the micron scale. Surface distribution calculations showed 6.3% coverage by noncarbonate minerals in addition to unknown amounts of a total of 39.8% of the surface characterized by an elemental mix of ^{27}Al, ^{28}Si, and ^{40}Ca. This amount surpasses strongly estimates of noncarbonate mineral abundance based on bulk geochemistry. Our data indicates that the distribution of noncarbonate phases covering the calcite mineral surface is more than doubled because clay minerals occur abundantly as thin films on calcite surfaces.

The wide distribution has significant impacts on the evaluation of wettability and spontaneous imbibition during IOR procedures and seawater injection in reservoir rocks, as wettability depends on the mineral surface charge/composition. If, as in our study, minerals with different surface charges are more widespread than expected, modeling exercises would be erroneous.

HIM-SIMS is a key technology to identify mineral surfaces at an ultrahigh spatial resolution in the range of nano- or even sub-nanometer level. 4D surface reconstruction is an excellent method for sample visualization that combines surface topography and chemical distribution information. This recent insight will enable us to refine methods for fluid injection to increase hydrocarbon recovery in mature reservoirs. HIM-SIMS is an essential tool to elaborate and fine-tune wettability modeling by mapping minerals within a reservoir.

■ ASSOCIATED CONTENT

ⓢ Supporting Information

The Supporting Information is available free of charge at https://pubs.acs.org/doi/10.1021/acs.energyfuels.2c04047.

Geochemical data set (PDF)

■ AUTHOR INFORMATION

Corresponding Author

Tine V. Bredal − *Department of Energy Resources, University of Stavanger, Ullandhaug 4036 Stavanger, Norway; The National IOR Centre of Norway, University of Stavanger, Ullandhaug 4036 Stavanger, Norway;* ⓘ orcid.org/0009-0004-6634-185X; Email: tine.v.bredal@uis.no

Authors

Alexander D. Ost − *Advanced Instrumentation for Nano-Analytics (AINA), Materials Research and Technology (MRT) Department, Luxembourg Institute of Science and Technology, 4362 Esch-sur-Alzette, Luxembourg; Faculty of Science, Technology and Medicine, University of Luxembourg, 4365 Esch-sur-Alzette, Luxembourg;* ⓘ orcid.org/0000-0002-7465-2541

Tom Wirtz − *Advanced Instrumentation for Nano-Analytics (AINA), Materials Research and Technology (MRT) Department, Luxembourg Institute of Science and Technology, 4362 Esch-sur-Alzette, Luxembourg*

Jean-Nicolas Audinot − *Advanced Instrumentation for Nano-Analytics (AINA), Materials Research and Technology (MRT) Department, Luxembourg Institute of Science and Technology, 4362 Esch-sur-Alzette, Luxembourg;* ⓘ orcid.org/0000-0002-4966-7653

Udo Zimmermann − *Department of Energy Resources, University of Stavanger, Ullandhaug 4036 Stavanger, Norway; The National IOR Centre of Norway, University of Stavanger, Ullandhaug 4036 Stavanger, Norway*

Merete V. Madland − *Division of Research, University of Stavanger, Ullandhaug 4036 Stavanger, Norway*

Mona W. Minde − *The National IOR Centre of Norway and Department of Mechanical and Structural Engineering and Materials Science, University of Stavanger, Ullandhaug 4036 Stavanger, Norway*

Tina Puntervold − *Department of Energy Resources, University of Stavanger, Ullandhaug 4036 Stavanger, Norway; The National IOR Centre of Norway, University of Stavanger, Ullandhaug 4036 Stavanger, Norway;* ⓘ orcid.org/0000-0002-5944-7275

Complete contact information is available at:
https://pubs.acs.org/10.1021/acs.energyfuels.2c04047

Schlumberger Norge AS, and Wintershall Dea Norge AS, of The National IOR Centre of Norway. They are thankful for the thoughtful comments of three anonymous reviewers and the kind handling of the chief editor.

■ REFERENCES

(1) Hermansen, H.; Landa, G. H.; Sylte, J. E.; Thomas, L. K. Experiences after 10 years of waterflooding the Ekofisk Field, Norway. *J. Pet. Sci. Eng.* **2000**, *26*, 11−18.

(2) Strand, S.; Hjuler, M. L.; Torsvik, R.; Pedersen, J. I.; Madland, M. V.; Austad, T. Wettability of chalk: impact of silica, clay content and mechanical properties. *Pet. Geosci.* **2007**, *13*, 69−80.

(3) Sylte, J. E.; Thomas, L. K.; Rhett, D. W.; Bruning, D. D.; Nagel, N. B. *Water Induced Compaction in the Ekofisk Field*, SPE Annual Technical Conference and Exhibition, vol. All Days, SPE-56426-MS, 1999.

(4) Austad, T.; Strand, S.; Madland, M. V.; Puntervold, T.; Korsnes, R. I. Seawater in Chalk: An EOR and Compaction Fluid. *SPE Reservoir Eval. Eng.* **2008**, *11*, 648−654.

(5) Yang, S.-Y.; Hirasaki, G. J.; Basu, S.; Vaidya, R. Mechanisms for contact angle hysteresis and advancingcontact angles. *J. Pet. Sci. Eng.* **1999**, *24*, 63−73.

(6) Hassenkam, T.; Skovbjerg, L.; Stipp, S. Probing the intrinsically oil-wet surfaces of pores in North Sea chalk at subpore resolution. *Proc. Natl. Acad. Sci. U.S.A.* **2009**, *106*, 6071−6076.

(7) Puntervold, T.; Mamonov, A.; Torrijos, I. D. P.; Strand, S. Adsorption of Crude Oil Components onto Carbonate and Sandstone Outcrop Rocks and Its Effect on Wettability. *Energy Fuels* **2021**, *35*, 5738−5747.

(8) Zhang, P.; Tweheyo, M. T.; Austad, T. Wettability alteration and improved oil recovery by spontaneous imbibition of seawater into chalk: Impact of the potential determining ions Ca2+, Mg2+, and SO42−. *Colloids Surf., A* **2007**, *301*, 199−208.

(9) Dowsett, D.; Wirtz, T. Co-registered in situ secondary electron and mass spectral imaging on the helium ion microscope demonstrated using lithium titanate and magnesium oxide nanoparticles. *Anal. Chem.* **2017**, *89*, 8957−8965.

(10) Wirtz, T.; De Castro, O.; Audinot, J.-N.; Philipp, P. Imaging and Analytics on the Helium Ion Microscope. *Annu. Rev. Anal. Chem.* **2019**, *12*, 523−543.

(11) Audinot, J.-N.; Philipp, P.; De Castro, O.; Biesemeier, A.; Hoang, Q. H.; Wirtz, T. Highest resolution chemical imaging based on secondary ion mass spectrometry performed on the helium ion microscope. *Rep. Prog. Phys.* **2021**, *84*, 10591.

(12) Bredal, T. V.; Zimmermann, U.; Madland, M. V.; Minde, M. W.; Ost, A. D.; Wirtz, T.; Audinot, J-N.; Korsnes, R. I. High-Resolution Topographic and Chemical Surface Imaging of Chalk for Oil Recovery Improvement Applications. *Minerals* **2022**, *12*, 356.

(13) Zimmermann, U.; Minde, M. W.; Madland, M. V.; Bredal, T. V. An Analytical TOOLBOX for the Characterization of Chalks and Other Fine-Grained Rock Types within Enhanced Oil Recovery Research and Its Application-A Guideline. *Energies* **2022**, *15*, 4060.

(14) Vollnhals, F.; Wirtz, T. Correlative Microscopy in 3D: Helium Ion Microscopy-Based Photogrammetric Topography Reconstruction Combined with in situ Secondary Ion Mass Spectrometry. *Anal. Chem.* **2018**, *90*, 11989−11995.

(15) Ost, A. D.; Wu, T.; Höschen, C.; Mueller, C. W.; Wirtz, T.; Audinot, J.-N. 4D Surface Reconstructions to Study Microscale Structures and Functions in Soil Biogeochemistry. *Environ. Sci. Technol.* **2021**, *55*, 9384−9393.

(16) Andersen, P. Ø.; Wenxia, W.; Madland, M. V.; Zimmermann, U.; Korsnes, R. I.; Bertolino, S.; Schulz, B.; Gilbricht, S.; Minde, M. W. Comparative Study of Five Outcrop Chalks Flooded at Reservoir Conditions: Chemo-mechanical Behaviour and Profiles of Compositional Alteration. *Transp. Porous Media* **2018**, *121*, 135−181.

(17) Kallesten, E. I.; Zimmermann, U.; Madland, M. V.; Bertolino, S.; Omdal, E.; Andersen, PØ. Mineralogy and geochemistry of

reservoir and non-reservoir chalk from the Norwegian continental shelf. *J. Pet. Sci. Eng.* **2021**, *205*, 108914.

(18) Schroeder, C.; Gaviglio, P.; Bergerat, F.; Vandycke, S.; Coulon, M. Faults and matrix deformations in chalk: contribution of porosity and sonic wave velocity measurements. *Bulletin Société Géologique France* **2006**, *177*, 203−213.

(19) Dusar, M.; Lagrou, D. Cretaceous flooding of the Brabant Massif and the lithostratigraphic characteristics of its chalk cover in northern Belgium. *Geol. Belg.* **2007**, *10*, 27−38.

(20) Robaszynski, F.; Dhondt, A.; Jagt, J. Cretaceous lithostratigraphic units (Belgium). *Geol. Belg.* **2002**, *4*, 121−134.

(21) Pirson, S.; Spagna, P.; Baele, J.-M.; Damblon, F. G.; Vanbrabant, Y.; Yans, J. An overview of the Geology of Belgium. *Memoirs Geological Survey Belgium* **2008**, *55*, 5−25.

(22) Cornet, F. L.; Briart Saint-Vaast Chalk Formation - SVA. https://ncs.naturalsciences.be/cretaceous/2114-saint-vaast-chalk-formation-sva. (accessed 21 Jan, 2022).

(23) Wen, S. T. S. Systematic Specific Surface Area Analysis on Rocks to Implement as a Necessary, Quick, and informative method to understand Geo-Mechanical Parameter in IOR Experiments. University of Stavanger, 2018, https://uis.brage.unit.no/uis-xmlui/handle/11250/2570740.

(24) Hlawacek, G.; Gölzhäuser, A. *Helium Ion Microscopy*, In Hlawacek, G.; Gölzhäuser, A., Eds.; Springer International Publishing, 2016; p 526.

(25) Lindgreen, H.; Drits, V.; Sakharov, Boris.; Jakobsen, H.; Salyn, A.; Dainyak, L.; Krøyer, H. The structure and diagenetic transformation of illite-smectite and chlorite-smectite from North Sea Cretaceous-Tertiary chalk. *Clay Miner.* **2002**, *37*, 429−450.

(26) Minde, M. W.; Zimmermann, U.; Korsnes, R.; Schulz, B.; Gilbricht, S.; et al. Mineral Replacement in Long-Term Flooded Porous Carbonate Rocks. *Geochim. Cosmochim. Acta* **2019**, *268*, 485.

(27) Borromeo, L.; Minde, M. W.; Toccafondi, C. Z.; Udo Andò, S.; Ossikovski, R. A New Frontier Technique for Nano-analysis on Flooded Chalk - TERS (Tip Enhanced Raman Spectroscopy), 2017, https://www.earthdoc.org/content/papers/10.3997/2214-4609.201700290.

(28) Skovbjerg, L.; Hassenkam, T.; Makovicky, E.; Hem, C.; Yang, M.; Bovet, N.; Stipp, S. Nano sized clay detected on chalk particle surfaces. *Geochim. Cosmochim. Acta* **2012**, *99*, 57−70.

(29) Austad, T.; Strand, S.; Puntervold, T. *Is Wettabilty Alteration of Carbonates by Seawater Caused by Rock Dissolution?* International Symposium of the Society of Core Analysts, Noordwijk, The Netherlands, 27−30 September, 2009.

(30) Madland, M. V.; Hiorth, A.; Omdal, E.; Megawati, M.; Hildebrand-Habel, T.; Korsnes, R. I.; Evje, S.; Cathles, L. M. Chemical Alterations Induced by Rock−Fluid Interactions When Injecting Brines in High Porosity Chalks. *Transp. Porous Med.* **2011**, *87*, 679−702.

(31) Megawati, M.; Andersen, P. Ø.; Korsnes, R. I.; Evje, S.; Hiorth, A.; Madland, M. V. The Effect of Aqueous Chemistry pH on the Time-Dependent Deformation Behaviour of Chalk- Experimental and Modelling Study," presented at the Les Rencontres scientifiques d'IFP Energies Nouvelles, Flows and Mechanics in Natural Porous Media From Pore To Field Scale Paris, 16−18 November, 2011.

(32) Minde, M. W.; Madland, M. V.; Zimmermann, U.; Egeland, N.; Korsnes, R. I.; Nakamura, E.; Kobayashi, K.; Ota, T. Mineralogical alterations in calcite powder flooded with MgCl2 to study Enhanced Oil Recovery (EOR) mechanisms at pore scale. *Microporous Mesoporous Mater.* **2020**, *304*, 109402.

(33) Minde, M. W.; Wang, W.; Madland, M. V.; Zimmermann, U.; Korsnes, R. I.; Bertolino, S.; Andersen, PØ. Temperature effects on rock engineering properties and rock-fluid chemistry in opal-CT-bearing chalk. *J. Pet. Sci. Eng.* **2018**, *169*, 454−470.

(34) Skovbjerg, L. L.; Okhrimenko, D.; Khoo, J.; Dalby, K.; Hassenkam, T.; Makovicky, E.; Stipp, S. Preferential Adsorption of Hydrocarbons to Nanometer-Sized Clay on Chalk Particle Surfaces. *Energy Fuels* **2013**, *27*, 3642−3652.

(35) Hjuler, M. L.; Fabricius, I. L. Engineering properties of chalk related to diagenetic variations of Upper Cretaceous onshore and offshore chalk in the North Sea area. *J. Pet. Sci. Eng.* **2009**, *68*, 151−170.

(36) Puntervold, T.; Strand, S.; Austad, T. Water Flooding of Carbonate Reservoirs: Effects of a Model Base and Natural Crude Oil Bases on Chalk Wettability. *Energy Fuels* **2007**, *21*, 1606−1616.

(37) Mamonov, A.; Kvandal, O. A.; Strand, S.; Puntervold, T. Adsorption of Polar Organic Components onto Sandstone Rock Minerals and Its Effect on Wettability and Enhanced Oil Recovery Potential by Smart Water. *Energy Fuels* **2019**, *33*, 5954−5960.

(38) Mercado, K. P.; Radhakrishnan, K.; Stewart, K.; Snider, L.; Ryan, D.; Haworth, K. J. Size-isolation of ultrasound-mediated phase change perfluorocarbon droplets using differential centrifugation. *J. Acoust. Soc. Am.* **2016**, *139*, EL142−EL148.

(39) Chai, R.; Liu, Y.; He, Y.; Liu, Q.; Xue, L. Dynamic behaviors and mechanisms of fluid-fluid interaction in low salinity waterflooding of carbonate reservoirs. *J. Pet. Sci. Eng.* **2022**, *208*, 109256.

(40) Cunha, L. H.; Siqueira, I.; Albuquerque, E. L.; Oliveira, T. Flow of emulsion drops through a constricted microcapillary channel. *Int. J. Multiphase Flow* **2018**, *103*, 141−150.

Paper IV:

"Unconsolidated artificial calcite and dolomite core flooding tests under reservoir conditions"

Bredal, T. V., Zimmermann, U., Korsnes, I.R, Madland, M. V., Minde, M.

Under review in Geoenergy Science and Engineering.

Paper IV

Not availabe in the repository because it is still under review

Paper V:

"Water Weakening of Artificially Fractured Chalk, Fracture Modification and Mineral Precipitation during Water Injection; An Experimental Study"

Bredal, T. V., Korsnes, R. I., Zimmermann, U., Minde, M. W., and Madland, M. V., 2022,

Energies, v. 15, no. 10, p. 3817.

Water Weakening of Artificially Fractured Chalk, Fracture Modification and Mineral Precipitation during Water Injection—An Experimental Study

Tine Vigdel Bredal [1,2,*], **Reidar Inge Korsnes** [1,2], **Udo Zimmermann** [1,2], **Mona Wetrhus Minde** [2,3] **and Merete Vadla Madland** [2,4]

1   Department of Energy Resources, University of Stavanger, Ullandhaug, 4036 Stavanger, Norway; reidar.i.korsnes@uis.no (R.I.K.); udo.zimmermann@uis.no (U.Z.)
2   The National IOR Centre of Norway, University of Stavanger, Ullandhaug, 4036 Stavanger, Norway; mona.w.minde@uis.no (M.W.M.); merete.v.madland@uis.no (M.V.M.)
3   Department of Mechanical and Structural Engineering and Materials Science, University of Stavanger, Ullandhaug, 4036 Stavanger, Norway
4   Division of Research, University of Stavanger, Ullandhaug, 4036 Stavanger, Norway
*   Correspondence: tine.v.bredal@uis.no

Abstract: This experiment was designed to study the water-weakening effect of artificially fractured chalk caused by the injection of different compositions of brines under reservoir conditions replicating giant hydrocarbon reservoirs at the Norwegian Continental Shelf (NCS). NaCl, synthetic seawater (SSW), and $MgCl_2$, with same ionic strength, were used to flood triaxial cell tests for approximately two months. The chalk cores used in this experiment originate from the Mons basin, close to Obourg, Belgium (Saint Vast Formation, Upper Cretaceous). Three artificially fractured chalk cores had a drilled central hole parallel to the flooding direction to imitate fractured chalk with an aperture of 2.25 ($\pm$0.05) mm. Two additional unfractured cores from the same sample set were tested for comparison. The unfractured samples exposed a more rapid onset of the water-weakening effect than the artificially fractured samples, when surface active ions such as Ca^{2+}, Mg^{2+} and SO_4^{2-} were introduced. This instant increase was more prominent for SSW-flooded samples compared to $MgCl_2$-flooded samples. The unfractured samples experienced axial strains of 1.12% and 1.49% caused by $MgCl_2$ and SSW, respectively. The artificially fractured cores injected by $MgCl_2$ and SSW exhibited a strain of 1.35% and 1.50%, while NaCl showed the least compaction, at 0.27%, as expected. Extrapolation of the creep curves suggested, however, that artificially fractured cores may show a weaker mechanical resilience than unfractured cores over time. The fracture aperture diameters were reduced by 84%, 76%, and 44% for the SSW, $MgCl_2$, and NaCl tests, respectively. Permeable fractures are important for an effective oil production; however, constant modification through compaction, dissolution, and precipitation will complicate reservoir simulation models. An increased understanding of these processes can contribute to the smarter planning of fluid injection, which is a key factor for successful improved oil recovery. This is an approach to deciphering dynamic fracture behaviours.

Keywords: geo-mechanical compaction; water-weakening effect; artificial fracture; mineral dissolution; mineral precipitation; fracture modification; improved oil recovery (IOR)

1. Introduction

About 40% of the world's oil is produced from chalk and carbonate rocks [1]. North Sea carbonate reservoirs have great potential to accumulate oil, as the porosity may often be very high, reaching 40–50% [2]. However, carbonate reservoirs are often characterised by low permeability and tend not to be water-wet, which challenges primary oil production. Matrix permeability for chalk is often in the range of 1–5 mD [2]. The recovery factor on

Ekofisk, a giant chalk reservoir on the Norwegian continental shelf (NCS), is over 50% [3], and there is still great potential for improved oil recovery (IOR) methods. By implementing enhanced oil recovery (EOR), or tertiary recovery, immobile oil that remains in the reservoir after production by conventional methods are prone to be recovered.

Ekofisk started oil production in 1971 by pressure depletion. Water injection was introduced in 1987 to create pressure support and to prevent seabed subsidence. The field subsequently experienced a substantial increase in oil recovery. Experience proved that water displaced the oil much more effectively than anticipated. Another consequence of the seawater injection was the deformation of the chalk matrix, hence the further compaction of the soft chalk despite the stabilization of pore pressure. This is referred to as a water-weakening effect and has been widely studied in laboratory experiments [4–7].

Geo-mechanical responses related to the water weakening of chalk are mainly a result of surface chemistry and chemical alterations which lead to calcite dissolution and the precipitation of new mineral phases associated with surface-active ions present in seawater Ca^{2+}, Mg^{2+}, and SO_4^{2-} [6,8]. Dissolution and precipitation processes are also dependent on effective stresses, temperatures, porosity, chemistry, and diagenetic processes such as cementation [9]. Precipitated magnesite ($MgCO_3$) is identified in experiments where Mg^{2+} is present in the injected brine [10]. It has a smaller crystal size compared to the dissolved calcite, and thereby it may reduce the solid volume. These brine–rock interaction processes that take place are also dependent on noncarbonate minerals [11]. Madland et al. (2011) [11] observed that pure chalk experienced a lower compaction rate compared to chalk with impurities of silicate and clay minerals. Andersen et al. (2017) [4] suggested that reprecipitation of Si-bearing minerals advances the dissolution of calcite, which justified the high compaction in $MgCl_2$-flooded chalk. SO_4^{2-} is also present in seawater and in injected brine (SSW). It's presence will cause additional strain by adsorbing to the calcite surface and cause a reduction in the bulk modulus and yield points compared to experiments where NaCl is injected under the same conditions. The disjoining pressure in granular contacts is increased by the interaction between charged surfaces and, furthermore, net repulsive forces that act as normal forces in the grains' vicinity, will counteract the cohesive forces and enhance pore collapse during loading [12].

NaCl is the major constituent in seawater. Geochemical analysis following laboratory experiments on chalk at 130 °C has shown that, without the presence of surface-active ions, precipitation of new mineral phases has not been observed in pure systems [11,13]. NaCl is therefore expected to be inert. However, calcite dissolution has been identified in laboratory experiments with prolonged test duration under elevated stress states, which has caused morphological changes such as the smoothing of grain surfaces [4]. This surface grain rounding has been suggested to weaken mechanical intergranular friction and provoke additional compaction [14].

During pressure depletion, the reservoir experience increased effective overburden stresses, seabed subsidence, and reduced matrix permeability. On the other hand, compaction may also induce fractures [15]. Since chalk reservoirs have a combination of high porosity and rather low permeability, fractures and high permeable zones are of great importance to sustain an effective fluid flow [16]. The presence of a naturally fractured system will increase the potential for fluid transportation, hence the oil recovery. The naturally fractured system on Ekofisk Field is believed to increase reservoir permeability by a factor of 50 [2]. A high intensity of fractures can create a spatially distinct, permeable zone [17]. The single fracture's contribution to reservoir fluid flow depends on size features, which include length, height, aperture, and aspect ratio [18]. This may change if fractures seal and may help to obtain a better sweep of the reservoir if the injected water is forced into the matrix instead of flowing throught the fractures. To better understand the complexity of reservoir fluid behaviour and petrophysical properties, it is beneficial to consider the details of a fault zone, and to categorize the zones with distinct hydrogeological units as barriers, conduits, or combined conduits and barriers [19]. The fault core is a narrow zone that commonly forms between major slip surfaces. The original host rock is here

destroyed by mechanical and chemical processes such as the dissolution and precipitation of minerals. The inner core of the fault zone has experienced the highest strain and thus reduced the porosity to a degree that permeability is so decreased that the inner core acts as a barrier [20,21]. The adjacent damaged zone is a wider zone of deformation with numerous fractures and smaller faults. The fracture network, fracture density, and orientation will ultimately control bulk permeability in these damage zones. The continuous flood behaviour is dependent on the fracture's ability to seal [22]. For carbonate reservoirs, isolated fractures may even affect the bulk permeability [18].

A laboratory experiment demonstrated that a core sample from the damaged zone presented permeability of several orders higher than that of samples extracted from the fault core [23]. Their experiment was performed on core scale but suggested that these microfractures (micron to centimetre scale) and the heterogeneous density distribution could be upscaled, and similar observations for macro fractures (up to meters) could be expected in the reservoir. However, microfractures are more prone to becoming sealed. During the water injection and depletion of the reservoir, the altered stress state and the induced water-weakening effect may modify reservoir properties dramatically. Mechanical and chemical alterations may induce or enhance natural fractures and reactivate faults, which can alter matrix permeabilities. The faulting and fracturing of carbonate reservoirs have major implications for hydrocarbon fluid pathways [24]. These processes will collectively cause additional compaction in the reservoir and provide extra drainage and increased recovery. However, injection may over time cause precipitation, which seals off minor fractures and reduce local permeability and alter fluid transportation. Matrix permeability may be further diminished by pore collapse due to increased effective stress during depletion of the reservoir. By studying the link between water weakening and the composition of brine, and by further comparing these geo-mechanical responses with the ability to seal smaller fractures, one can improve the prediction of seawater injection and thereby maximize production. Here, we present geo-mechanical responses to artificially fractured cores versus unfractured cores and further report how these responses differ depending on the ion composition of the injected brine. Beside studying the geo-mechanical response and ion concentration in the effluent, we study textural characteristics obtained by Scanning Electron Microscope combined with Energy Dispersive Spectroscopy (SEM-EDS) and specific surface area (SSA) adjacent fracture in addition to bulk geochemistry. This study demonstrates changes in terms of dissolution and precipitation processes for artificially fractured samples as an analogue to reservoir conditions at the NCS. Furthermore, this study links fracture aperture modification to the composition of the injected brine in addition to the experienced strain for fractured samples. By characterizing fracture geometry and spatial distribution related to mechanical properties, input data for reservoir flooding models to predict fluid flow properties may be refined.

2. Samples, Sample Preparation and Methodology

An Upper Cretaceous succession (Coniacian) from the Obourg quarry within the St. Vaast Formation of the Mons basin (OBSV) was chosen as an analogue to Ekofisk reservoir chalk due to the accessibility of onshore chalk and earlier studies (e.g., [4,25]). Five samples were cored parallel from the same outcrop block with a diameter of 38.1 mm and a length of about 70 mm. The average porosity was 41 ($\pm$1)%, and the permeability ranged around 0.56 mD on intact cores (Table 1). A 2 mm drill bit was used to produce cylindrical holes along the flooding axis, mimicking fractures in three cores. The size of the fractures measured 2.25 ($\pm$0.05) mm in diameter. Two supplementary intact cores were added to the experiment as reference. Three different brines were used in the experiment to detect results related to different concentration of surface-active ions. Synthetic seawater (SSW) is a laboratory mixed brine, reproducing the ion concentration in seawater, which is used for IOR purposes in the reservoir. The composition of this fluid is described in detail in Madland et al. (2011) [11] and is comprised of Na^+, Cl^-, Mg^{2+}, Ca^{2+}, K^+, and SO_4^{2-}. Mg^{2+} is one of the most reactive ions in SSW, and in these experiments, a higher and isolated

concentration of $MgCl_2$ in addition to NaCl was selected such that all brines had equal ion strength to SSW in the experiment. NaCl was added as a reference, as it is expected to be inert with chalk. The concentrations are presented in Table 1.

Table 1. Ion concentration of the brine used in the experiment. * The ion is not present in the brine.

Brine/mol/L	Cl^-	Na^+	K^+	Mg^{2+}	Ca^{2+}	SO_4^{2-}
$MgCl_2$	0.438	*	*	0.219	*	*
SSW	0.525	0.450	0.010	0.0445	0.013	0.024
NaCl	0.657	0.657	*	*	*	*

The experiments were conducted in a triaxial cell, simulating reservoir conditions at Ekofisk reservoir with a temperature of 130 °C and constant hydrostatic pressure (effective overburden) of 12 MPa while flooding the cores. Replication of actual reservoir conditions have been implemented in laboratory routines and has been demonstrated to be highly representative [4–6,11]. The triaxial cell is connected to three high pressure pumps (Gilson Pump-Model 307 HPLC), where two provided axial and confining pressure and the last was a fluid pump to provide brine injection through the core. The triaxial cell system is arranged such that the confining pressure also supplied pressure in axial direction. Moreover, the piston providing axial pressure only supplied an additional threshold pressure to keep the piston in contact with the sample. The axial displacement in this test set-up, was therefore not purely hydrostatic because of the additional pressure supplied in the axial direction causing a slightly higher stress in axial versus lateral direction. The confining pressure was gradually increased to 12 MPa, with a stable piston pressure at 0.7 MPa, just above the friction pressure, to simulate hydrostatic test conditions. The quantity of axial compaction was detected by a linear variable differential transformer (LVTD), tracking the movement of the piston in contact with the chalk core. The triaxial cells were not equipped to measure radial strain. The cores were injected with a flow rate corresponding to one pore volume a day based on the original pore volume. Pore pressure was kept constant at 0.7 MPa by using a back-pressure regulator. The triaxial cells were equipped with a Backer 1500 W heating Jacket, covering the triaxial cell, and a regulating system (Omron E5CN), which allowed a stable test temperature of 130 (±0.1) °C that was continuously monitored by a Pt100 sensor inside the cell. LabView software was used to log all real time data recorded from the experiments. Drainage discs allow for even distribution of the brine at inlet and outlet surfaces. For fractured cores, the drainage disk will not work as intended, since brine follows the easiest path with the least resistance in the central fracture. Permeability will, for these three tests, therefore be irrelevant. The reader is referred to Geitle K. (2013) [26] and Abubeker E. (2013) [27] for additional information regarding these tests.

All five samples (Figure 1) were initially saturated and flooded by NaCl during loading, and the primary creep phase lasted six days. In the second phase, the two unfractured cores, OBSV 9 SSW and OBSV 6 $MgCl_2$, were followed by injection of SSW and $MgCl_2$, respectively. Two of the artificially fractured samples, OBSV 12 AF-SSW and OBSV 4 AF-$MgCl_2$, were injected with SSW and $MgCl_2$, respectively. The third artificially fractured core was flooded with NaCl during the complete test period. The total number of flooding days ranged between 18 and 60 days (Table 2). The cores were sliced after the test, where the inlet was given the number one, and the outlet was given the highest number (Figure 1), ex: OBSV 4.1 is the inlet of OBSV 4 AF-$MgCl_2$. End slices were kept for reference analysis.

Figure 1. Selected samples and associated fluid composition versus flooding condition (artificial fractured cores have small holes in the center). Flooding direction indicates slice one being the so-called "inlet" followed by slice two, etc., until slice six, which is named the "outlet".

Table 2. The table distributes porosity, permeability, strain, yield strength, bulk modulus, and test duration. * No data available.

Sample	Porosity [%]		Permeability [mD]		Strain [%]				Yield Strength [MPa]	Bulk Modulus [GPa]	Duration [Days]
	Pre-Test	Post-Test	Start	Stop	Loading	Creep 1	Creep 2	Total			
OBSV 4 AF-MgCl$_2$	40.49	37.95	*	*	0.81	1.25	1.35	3.41	9.4	0.750	62
OBSV 6 MgCl$_2$	40.81	38.60	0.53	0.17	0.80	1.16	1.12	3.08	9.9	0.685	46
OBSV 9 SSW	41.34	37.02	0.59	0.00	0.90	1.06	1.49	3.45	9.1	0.696	18
OBSV 12 AF-SSW	41.34	37.15	*	*	1.07	1.59	1.50	4.16	9.4	0.625	53
OBSV 18 AF-NaCl	40.18	*	*	*	0.86	1.38	0.27	2.51	9.4	0.730	27

2.1. Axial Strain, Yield Strength, and Bulk Modulus

Axial strain (Equation (1)) is compaction given in [%], where ΔL is the change in length from the original core length (L).

$$\text{Axial Strain } = \frac{\Delta L}{L} \times 100 \tag{1}$$

Yield point is, in this study, determined as the intersection of two tangent lines that follows the elastic and the plastic phase of the loading curve. The yield strength is the stress [MPa] applied to the core where the elastic strain is passed. The bulk modulus (K) is an elastic coefficient used to determine the relationship between stress and volumetric strain during hydrostatic loading. The bulk modulus reflects the material's ability to resist compression (Equation (2)) and is given in [GPa], where σ_h is hydrostatic stress and ε_v is volumetric strain under hydrostatic test conditions.

$$K = \frac{\sigma_h}{\varepsilon_v} \tag{2}$$

A logarithmic formula (Equation (3)) was used for extrapolation of creep, where A and t_0 are constants that were determined by adjustment to the experimental creep curve. ε_{creep} is the logarithmic creep behavior and t is the endpoint of the observed creep phase. For detailed descriptions, the reader is referred to Madland et al., 2006 [28].

$$\varepsilon_{creep} = A \ln (1 + t/t_0) \tag{3}$$

2.2. Porosity and Permeability

Porosity is the ratio of pore volume (PV) to its bulk volume (BV), (Equation (4)). Porosities were simply measured by weight analysis. The samples were dried in a heating chamber to evaporate the remaining moisture before applying vacuum to approximately 0.04 kPa followed by saturation with distilled water. PV was determined by the dry and

the fully saturated weight of the cores, and BV was calculated from the dimensions of the cores, where φ is porosity:

$$\varphi = \frac{PV}{BV} \times 100 \qquad (4)$$

Porosity calculations post-test were calculated based on strain (where φ_0 is the original porosity and ε_v is volumetric strain) in addition to mass, where BV is measured by gas pycnometer and derived densities, where Ms is solid mass and $\mathcal{P}$ is density of the core (Equation (5)).

$$\varphi = (1 - \frac{Ms}{\mathcal{P}BV}) \qquad (5)$$

Permeabilities were calculated using Darcy's law, (Equation (6)), where k is permeability (mD), q is flow rate (cm^2/s), μ is viscosity (cp), L is core length (cm), A is core area (cm^2), and ΔP is differential pressure (atm).

$$k = \frac{q\mu L}{A\Delta P} \qquad (6)$$

2.3. Ion Chromatography (IC)

Water samples were frequently collected throughout the experiments. Effluent samples were prepared by diluting the samples 500 times by using the Gilson Gx-271 dilution system. They were further filtered before chemical analyses were performed by using the Dionex ICS-3000 Ion Chromatography System. The ion concentrations of the produced fluid were analysed and verified by external standards. Ion deviation in the effluent, from the ion concentration in the original brine injected, contributed to our understanding of the non-equilibrium status of the rock–fluid interactions during the test. These changes were used to predict the dissolution and precipitation of minerals inside the core.

2.4. Optical Light Microscopy (OLM) and Fracture Modification

The optical light microscope, Zeiss Stemi DV4, has a maximum of 20 times magnification. This was used to observe textural differences and enabled the study of colour variations. Magnification allowed for the measurement of the final fracture diameters.

2.5. Geochemistry

Method 1: Sample material was milled in an agate beaker to a fine mesh. The milled sample was mixed with $LiBO_2/Li_2B_4O_7$ flux in crucibles and fused in a furnace. The cooled bead was dissolved in American Chemical Society (ACS) grade nitric acid. The geochemical data were then obtained by using Inductively Coupled Plasma-Mass Spectrometry (ICP-MS) at the ACME laboratory (Vancouver, Canada). Loss on ignition (LOI) was determined by igniting a sample split then measuring the weight loss after being ignited at 1000 °C for 1 h and was then cooled and weighed again. Total amounts of carbon and sulphur were determined by the LECO® method. Here, induction flux was added to the prepared sample then ignited in an induction furnace. A carrier gas sweeps up released carbon to be measured by adsorption in an infrared spectrometric cell. Additional 14 elements were measured after dilution in Aqua Regia. The prepared sample was processed with a modified Aqua Regia solution of equal parts concentrated HCl, HNO_3, and DI-H_2O for 1 h in a heating block. The sample volume was increased with dilute HCl-solutions, and splits of 0.5 g were analysed. Accuracy and precision are between 2 and 3% per element. Detection limits are found in Table 3.

Method 2: Major elements for samples < 5 g were analysed geochemically by Fusion Inductively Coupled Plasma (FUS-ICP) without the detection of LOI and were processed at Actlabs (Canada).

Table 3. Major element geochemistry for reference material, flooded samples, and central fill (CF) from OBSV 4 AF-MgCl$_2$.

Element wt.%	SiO$_2$	Al$_2$O$_3$	Fe$_2$O$_3$	MgO	CaO	Na$_2$O	K$_2$O	TiO$_2$	P$_2$O$_5$	LOI	Sum
Detection limit LF 200	0.01	0.01	0.04	0.01	0.01	0.01	0.01	0.01	0.01		
OBSV 4 REF IN	3.32	0.97	0.34	0.29	52.06	0.04	0.22	0.04	0.06	42.5	99.84
OBSV 4 AF-MgCl$_2$ #1	3.38	0.99	0.31	0.66	51.81	0.03	0.18	0.04	0.05	42.4	99.85
OBSV 4 AF-MgCl$_2$ #3	3.39	1.00	0.36	0.97	51.37	0.03	0.16	0.05	0.07	42.4	99.80
OBSV 4 AF-MgCl$_2$ #4	3.32	0.98	0.34	0.99	51.73	0.03	0.15	0.04	0.09	42.1	99.77
OBSV 4 AF-MgCl$_2$ #6	3.37	0.98	0.34	0.98	51.67	0.03	0.16	0.04	0.06	42.2	99.83
OBSV 4 AF-MgCl$_2$ #7	3.32	0.98	0.35	0.95	51.68	0.03	0.15	0.04	0.06	42.2	99.76
OBSV 4 REF OUT	3.50	1.03	0.37	0.28	52.01	0.04	0.23	0.05	0.05	42.3	99.86
OBSV 6 REF IN	3.38	1.00	0.34	0.28	52.29	0.04	0.22	0.05	0.06	42.2	99.86
OBSV 6 MgCl$_2$ #2	3.19	1.00	0.34	1.50	51.24	0.03	0.15	0.05	0.07	42.2	99.77
OBSV 6 MgCl$_2$ #3	3.37	1.02	0.36	1.43	51.21	0.03	0.15	0.05	0.08	42.1	99.80
OBSV 6 MgCl$_2$ #4	3.27	1.00	0.34	1.28	51.38	0.04	0.16	0.05	0.09	42.2	99.81
OBSV 6 MgCl$_2$ #5	3.31	1.02	0.41	1.08	51.68	0.03	0.17	0.05	0.08	42.0	99.83
OBSV 6 MgCl$_2$ #6	3.52	1.05	0.38	0.96	51.50	0.04	0.17	0.05	0.10	42.0	99.77
OBSV 6 MgCl$_2$ #7	3.54	1.03	0.40	1.01	51.86	0.04	0.18	0.05	0.08	41.6	99.79
OBSV6 REF OUT	3.40	1.03	0.33	0.30	51.89	0.04	0.23	0.05	0.09	42.5	99.86
OBSV9 REF IN	3.44	1.01	0.39	0.29	51.97	0.04	0.22	0.05	0.10	42.3	99.81
OBSV 9 SSW #1	3.37	1.04	0.36	0.55	51.88	0.04	0.21	0.05	0.10	42.2	99.80
OBSV 9 SSW #2	3.43	1.03	0.40	0.51	51.64	0.04	0.22	0.05	0.09	42.4	99.81
OBSV 9 SSW #3	3.52	1.04	0.38	0.48	51.50	0.04	0.23	0.05	0.08	42.5	99.82
OBSV9 SSW #4	3.45	1.04	0.39	0.45	51.65	0.05	0.22	0.05	0.08	42.5	99.88
OBSV 9 SSW #5	3.49	1.02	0.42	0.43	51.80	0.05	0.23	0.05	0.07	42.3	99.86
OBSV 9 SSW #6	3.55	1.04	0.42	0.40	51.60	0.05	0.24	0.05	0.06	42.4	99.81
OBSV9 REF OUT	3.59	1.05	0.47	0.28	52.00	0.04	0.23	0.05	0.07	42.0	99.78
OBSV 12 REF IN	3.58	1.05	0.40	0.28	51.89	0.04	0.24	0.05	0.06	42.2	99.79
OBSV 12 AF-SSW #1	3.61	1.07	0.47	0.44	51.93	0.04	0.24	0.05	0.08	41.9	99.83
OBSV 12 AF-SSW #2	3.52	1.05	0.38	0.48	52.05	0.04	0.22	0.05	0.07	42.0	99.86
OBSV 12 AF-SSW #3	3.56	1.07	0.40	0.53	51.93	0.03	0.23	0.05	0.08	41.9	99.78
OBSV 12 AF-SSW #4	3.64	1.08	0.43	0.52	51.88	0.04	0.22	0.05	0.06	41.9	99.82
OBSV 12 AF-SSW #5	3.60	1.06	0.39	0.49	51.67	0.04	0.23	0.05	0.07	42.2	99.80
OBSV 12 AF-SSW #6	3.62	1.08	0.43	0.40	51.94	0.04	0.24	0.05	0.08	42.0	99.88
OBSV 18 AF-NaCl #1	3.49	1.02	0.39	0.28	52.21	0.06	0.22	0.05	0.09	42.0	99.81
OBSV 18 AF-NaCl #2	3.30	0.98	0.38	0.27	52.52	0.06	0.21	0.04	0.10	42.0	99.86
OBSV 18 AF-NaCl #3	3.21	0.98	0.36	0.27	52.46	0.06	0.21	0.04	0.09	42.1	99.78
OBSV 18 AF-NaCl #4	3.30	1.00	0.38	0.27	52.46	0.07	0.21	0.04	0.07	42.0	99.80
OBSV 18 AF-NaCl #5	3.28	0.99	0.39	0.27	52.38	0.07	0.21	0.04	0.07	42.1	99.80
OBSV 18 AF-NaCl #6	3.39	1.09	0.43	0.28	52.94	0.06	0.22	0.05	0.11	41.6	100.16
OBSV 18 REF IN	3.39	1.00	0.54	0.27	51.90	0.04	0.22	0.05	0.10	42.3	99.81
Detection limit FUS-ICP	0.01	0.01	0.01	0.01	0.01	0.01	0.01	0.001	0.01		
OBSV 4 AF-MgCl$_2$ CF #1	8.77	1.55	0.77	41.05	1.95	<0.01	0.24	0.074	0.12		54.55
OBSV 4 AF-MgCl$_2$ CF #7	4.96	1.14	0.44	42.68	4.11	<0.01	0.16	0.05	0.1		53.69

2.6. Field Emission Gun Scanning Electron Microscopy (SEM) and Energy Dispersive X-ray Spectroscopy (EDS)

Fresh surfaced samples were mounted on aluminum holders, followed by coating with palladium (Pd) or gold (Au). A Zeiss Supra 35-VP FEG-SEM at the University of Stavanger (UiS) was used for the high magnification of morphological differences and to obtain elemental composition by using an Energy dispersive X-ray spectroscopy (EDS) detector. Images were acquired by using the secondary electron (SE) detector at a fixed working distance of 10 mm, accelerating voltage of 15.00 kV and using an aperture size of 30 μm. EDS was performed on squared areas of 2 × 2 μm.

2.7. Specific Surface Area (SSA)

Approximately two grams of sample material was ground in an agate mortar. The samples were heated in a tube at a temperature of 80 °C and kept under vacuum for 4.5 h. A Micromeritics TriStar II was utilized for the purpose of measuring Brunauer–Emmett–Teller (BET) surface area based on the BET theory [29]. Nitrogen gas was introduced to the sample continuously under a vacuum of around 20–30 mTorr. The sample tube was submerged in liquid nitrogen (LN_2) for cooling during measurement. At increased partial pressures, nitrogen gas filled a greater area of the micro-pores, which adsorbed as a monolayer on the surface of the grains. The change in pressure is a measure of the amount of gas that was adsorbed on the surface. Along with the exact sample weight, the SSA was calculated by TriStar II 3020 Software, and the resulting surface extension is given in m^2/g.

3. Results

3.1. Geo-Mechanical Responses

Axial strain rates were continuously measured throughout the experiment. The average axial strain during loading under injection of NaCl was 0.85 (±0.16)% for intact samples (Figure 2). OBSV 12 AF-SSW showed a higher compaction, just outside the expected range, with 1.08%. The two other cores with an artificial fracture experienced a similar strain (0.81% and 0.86%) as the two flooded unfractured cores. The yield stress was similar for all cores, ranging from 9.1 to 9.9 MPa (Table 1).
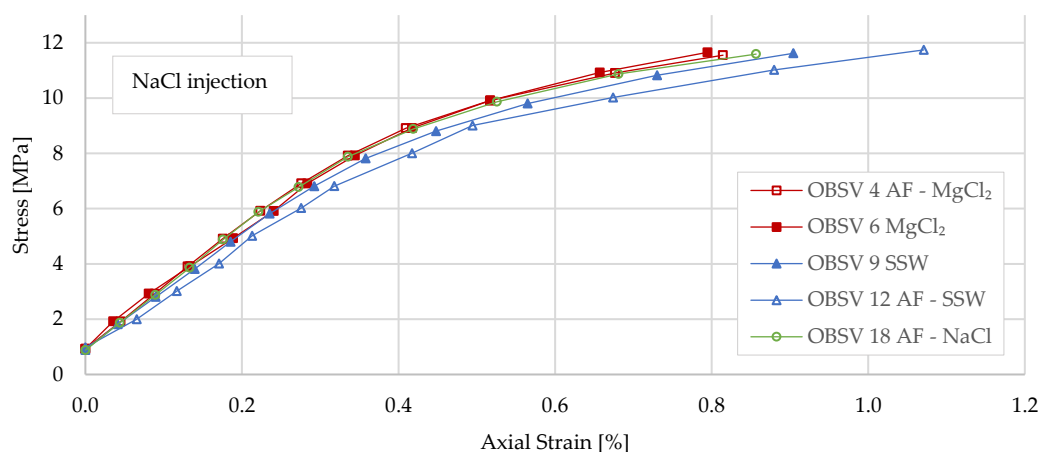
Figure 2. Axial creep strain during loading with injection of NaCl.

The average axial creep strain for both unfractured and the artificially fractured cores following the 6-day period of NaCl injection (Creep 1) was 1.29% (Figure 3a). Unfractured cores showed an average axial strain of 1.11 (±0.17)%. The artificially fractured cores, on the other hand, OBSV 4 AF-MgCl$_2$, OBSV 12 AF-SSW, and OBSV 18 AF-NaCl, experienced a higher strain of 1.25%, 1.59%, and 1.38% respectively, with an average for the three of 1.40%. OBSV 12 AF-SSW and OBSV 18 AF-NaCl exhibitedd significantly higher compaction rates compared to the intact reference samples (both outside the expected range).

In Creep 2, after six days of the creep with injection of NaCl, four of the samples changed brine: OBSV 9 SSW and OBSV 12 AF-SSW to SSW and OBSV 4 AF-MgCl$_2$, and OBSV 6 MgCl$_2$ to MgCl$_2$. OBSV 18 AF-NaCl continued the injection of NaCl throughout the entire test duration. During Creep 2, starting after six days, the five different samples experienced distinct axial strain rates (Figure 3b). The most dramatic increase in strain rate was observed for OBSV 9 SSW. It had the highest strain rate of 0.302%/day on day eight. When the test passed 16 days of duration, OBSV 9 SSW experienced a dramatic increase in differential pressure, and the test had to be terminated. A lower and later onset of increased compaction rate was identified for the artificially fractured core, OBSV 12 AF-SSW, which reached the highest strain rate of 0.089%/day on the 12th day of the test

duration. The MgCl$_2$-flooded samples experienced a lower compaction rate compared to the SSW-flooded cores. A distinct rate and onset of increased compaction was also noted for the two MgCl$_2$-flooded samples. The difference between the artificially fractured core and the unfractured core was however less significant than observed for the two SSW-flooded cores. OBSV 6 MgCl$_2$ distributed a maximum strain rate of 0.074%/day on the 12th day of testing, and OBSV 4 AF-MgCl$_2$ reached the highest compaction rate of 0.054%/day on the 13th day. The lowest strain rate was observed for OBSV 18 AF-NaCl, with a stable and maximum axial strain rate close to 0.027%/day at the start of Creep 2, decreasing towards 0.018%/day on the last test day.

(a)

(b)
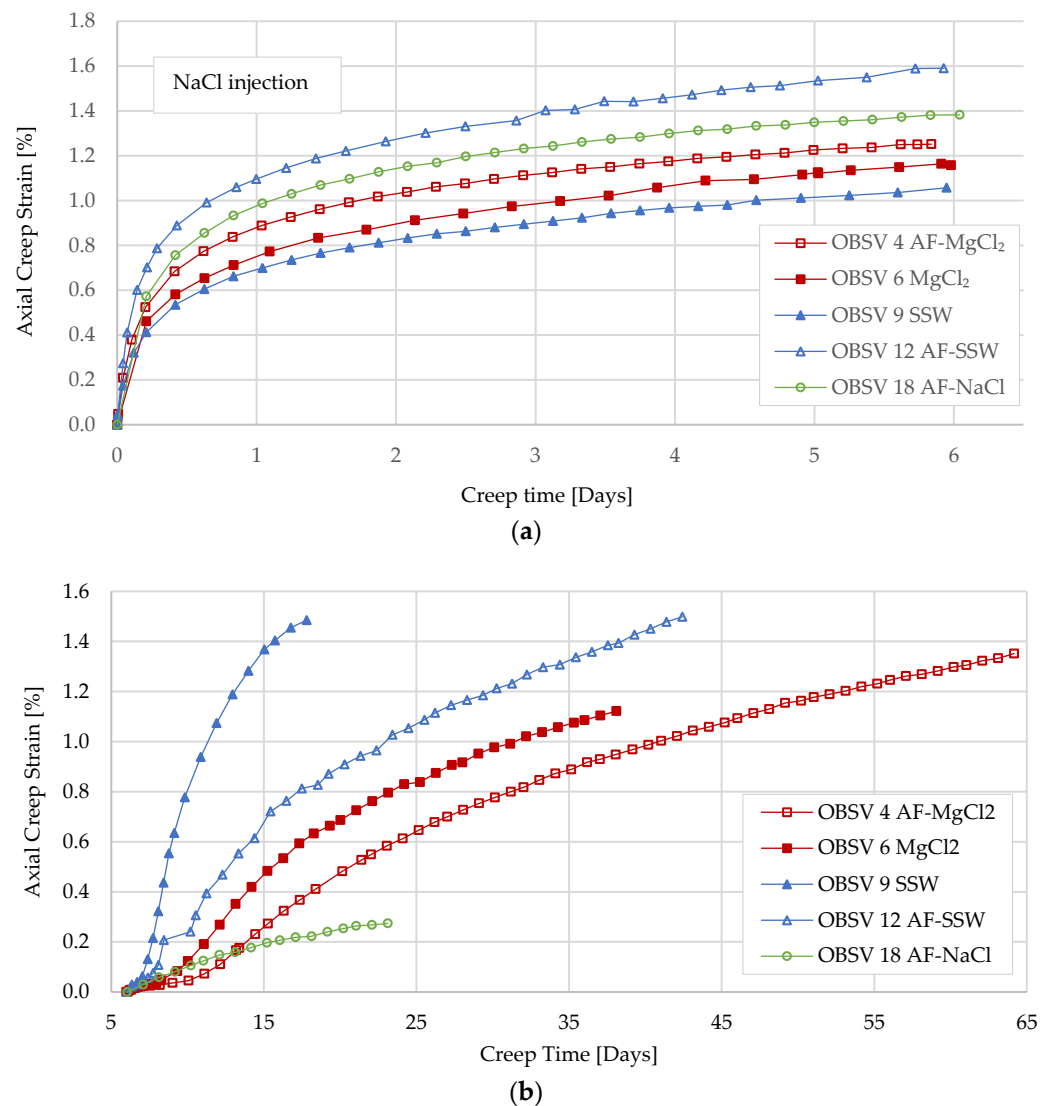
Figure 3. The graphs distribute the axial creep strain for Creep 1 and Creep 2: (**a**) Axial creep strain for five cores during Creep 1 with six days of NaCl injection for all samples. (**b**) Compaction behaviour during Creep 2 starting at day six, when the injected brine changed from NaCl to MgCl$_2$ and SSW, and OBSV 18 AF-NaCl continued with NaCl injection throughout the entire test period.

3.2. Porosity, Permeability, and Mechanical Strength Data

Porosity measurements were performed both before and after the experiment (Table 2) in addition to permeability calculations. Pre-test average porosity of the five samples was 40.83 ($\pm$1.38)%. All samples flooded with SSW and MgCl$_2$ distributed significantly reduced porosities. The two cores flooded with SSW experienced a reduction of 4.19% and 4.32% for OBSV 12 AF-SSW and OBSV 9 SSW, respectively. The two cores flooded with MgCl$_2$

showed a lower porosity reduction of 2.21% and 2.54% for OBSV 6 MgCl$_2$ and OBSV 4 AF-MgCl$_2$. Both artificially fractured cores showed lower porosity reduction compared to its reference intact core.

3.3. Ion Chromatography and Analysis of Effluent

The ion concentration of Ca^{2+}, Mg^{2+}, Na$^+$, and Cl$^-$ for OBSV 4 AF-MgCl$_2$ and OBSV 6 MgCl$_2$ oscillated around the original values of the injected brines during Creep 1 (Figure 4). The accuracy of the ion chromatography results is within 3%. A significant deviation from original concentrations was observed after brine change for both samples when the injected brine was switched to MgCl$_2$ on the sixth day (Creep 2). The unfractured core, OBSV 6 MgCl$_2$, spent 24 h before breakthrough of Mg^{2+} was observed, whereas the artificially fractured sample showed a breakthrough a few hours after brine change (Figure 4a). Both samples constantly lost Mg^{2+} to the core after brine change. Both samples showed a constant deviation from the injected concentration of Mg^{2+}, which flattened out over time and showed 0.205 M MgCl$_2$ for the unfractured sample and 0.213 M MgCl$_2$ for OBSV 4 AF-MgCl$_2$ at 45 days of testing. The artificially fractured OBSV 4 AF-MgCl$_2$ instantly produced 0.010 M Ca^{2+}, gradually increasing to a maximum level of 0.015 M Ca^{2+} 12 days after the brine change. The intact core (OBSV 6 MgCl$_2$) started; however, production one day after brine change with a maximum level of 0.064 M Ca^{2+} was followed by a reduction of 0.018 M. The production gradually reduced yet kept a slightly higher production compared to the fractured core (OBSV 4 AF-MgCl$_2$). Na$^+$ and Cl$^-$ gradually decreased towards the concentration of the injected brine within two days for the unfractured core (OBSV 6 MgCl$_2$) (Figure 4b). The artificially fractured core (OBSV 4 AF-MgCl$_2$) showed an instant drop in Na$^+$ concentration when MgCl$_2$ was injected but spent nine days until reaching the same concentration as the intact sample (the same injection rate was used for all tests (1 PV/day) based on matrix volume). A similar trend, yet less significant was observed for Cl$^-$.

SSW-flooded samples (OBSV 9 SSW and OBSV 12 AF-SSW) experienced a similar yet less significant response of Ca^{2+} dissolution and Mg^{2+} retention observed for the unfractured and artificially fractured cores flooded with MgCl$_2$ in start of Creep 2 (Figure 5). Mg^{2+} breakthrough was observed instantly for the artificially fractured core flooded with SSW (OBSV 12 AF-SSW) and showed 0.036 M Mg^{2+} 24 h into Creep 2 (whereas it was 0.044 M Mg^{2+} in SSW). OBSV 9 SSW showed breakthrough after two days, with a more prominent loss of 0.021 M Mg^{2+}. Ca^{2+} showed an instant breakthrough for OBSV 12 AF-SSW yet did not pass original concentrations until one week into Creep 2. A relative constant Ca^{2+} production of 0.0015 M persisted throughout the remaining test period. The SSW 9 SSW experienced a breakthrough of Ca^{2+} production again after two days with a maximum of 0.025 M, which gradually reduced. SO$_4{}^{2-}$ showed an instant breakthrough for OBSV 12 AF-SSW and reached original values after one week into Creep 2 and oscillated around original values thereafter. Again, a two-day delayed breakthrough was observed for OBSV 9 SSW, with a maximum level of 0.022 M SO$_4{}^{2-}$, which rapidly reduced. SO$_4{}^{2-}$ loss is often linked with the precipitation of anhydrite (CaSO$_4$), which in turn will lead to the same concentration of Ca^{2+} loss, a process that is corrected for in Figure 5.

Na$^+$ and Cl$^-$ oscillated around its original concentration during the first creep phase with NaCl injection. The intact core rapidly reduced the concentrations of Na$^+$ and Cl$^-$ to zero starting after only one day (earlier than the divalent ions) and returned to zero within two days during Creep 2 (Figure 5b), whereas the artificially fractured core, OBSV 12-SSW, Na$^+$, and Cl$^-$ spent five days to reduce concentration to zero.

3.4. Textural and Morphological Observation OLM

The three artificially fractured cores were sliced parallel and perpendicular to the flooding direction (Figure 6). OBSV 4 AF-MgCl$_2$ presented a distinct boarder with empty space between the core matrix and the fracture "fill". The filling (diameter of 2.75 mm) was not completely attached to the remaining core and has a white appearance (Figure 6d). The central part of the core (OBSV 12 AF-SSW) showed longitudinal accumulation of

brownish green precipitate (Figure 6b,e), measuring a width < 1 mm. The border between the original core wall and new precipitated or redeposited minerals from the core was not possible to detect with optical light microscopy. The inner surface of the fracture (OBSV 18 AF-NaCl) presented a sheet-like texture with a beige colour, which stood out from the remaining pale grey core (Figure 6c).

The fracture aperture diameter measured approximately 2.25 mm before testing. The three artificially fractured cores, OBSV 4 AF-MgCl$_2$, OBSV 12 AF-SSW, and OBSV 18 AF-NaCl, presented different values of vacant space after flooding (Figure 7). OBSV 18 AF-NaCl shows, on average, the lowest magnitude of aperture reduction, at 44%. OBSV 12 AF-SSW showed almost complete closure of the fracture aperture, with the first four slices being completely diminished, and an average reduction of 84%. OBSV 4 AF-MgCl$_2$ reduced the aperture diameter by 76%. The vacant spaces varied depending on the distance from inlet.
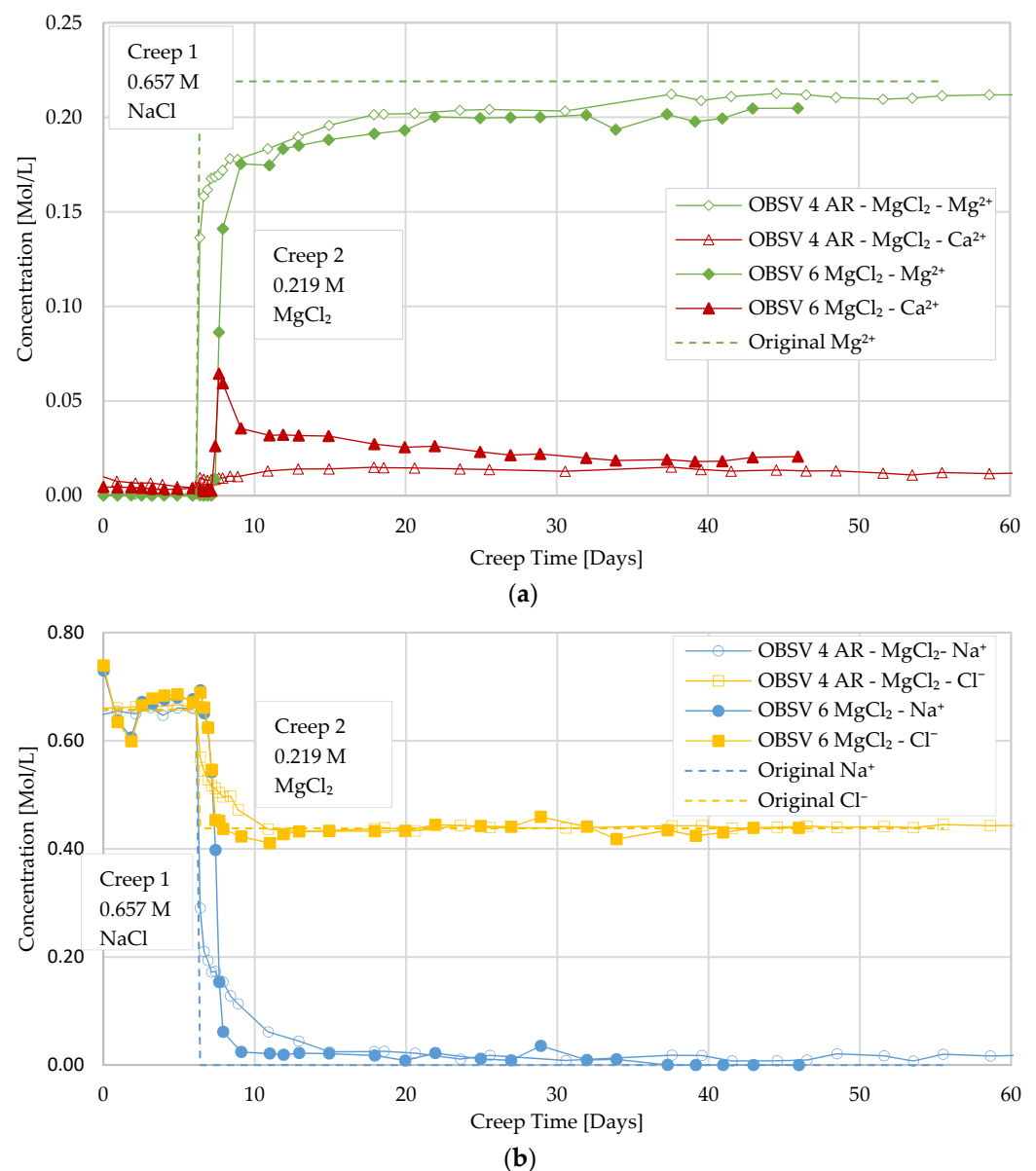
Figure 4. Effluent concentration for OBSV 4 AF-MgCl$_2$ and OBSV 6 MgCl$_2$: (**a**) Effluent concentration of Mg^{2+} and Ca^{2+} for the artificially fractured and intact sample flooded with MgCl$_2$ (OBSV 4 AF-MgCl$_2$ and OBSV 6 MgCl$_2$). (**b**) Effluent concentration of Na$^+$ and Cl$^-$ for the artificially fractured and intact sample flooded with MgCl$_2$ (OBSV 4 AF-MgCl$_2$ and OBSV 6 MgCl$_2$).
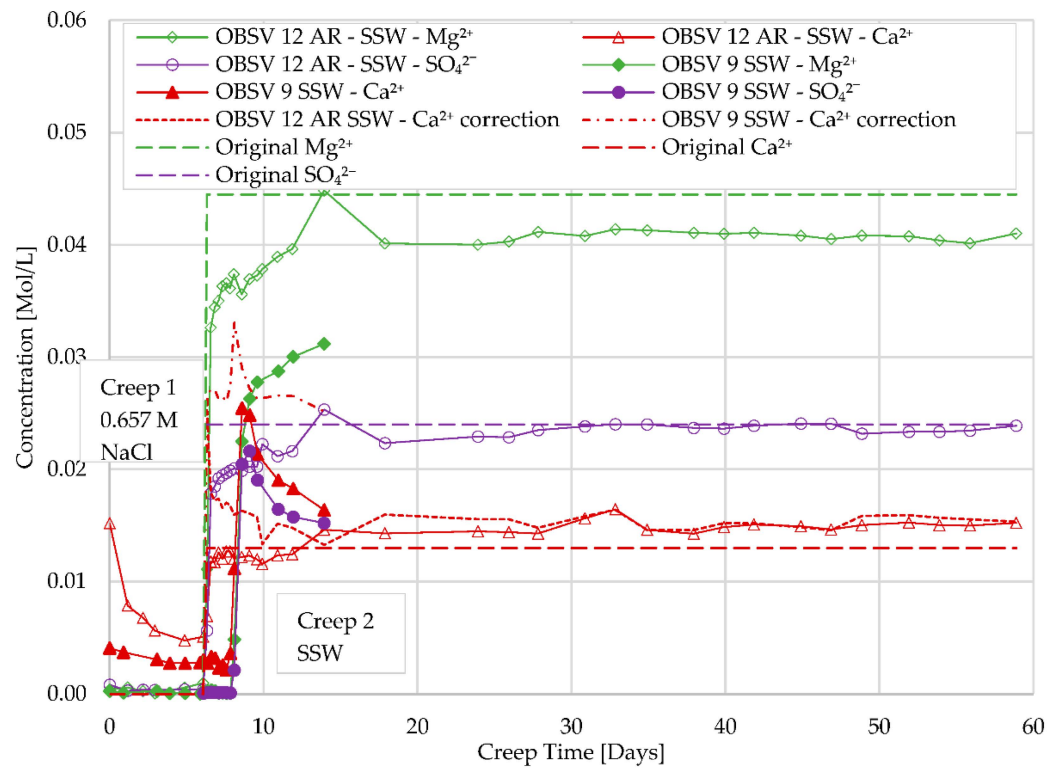
(**a**)
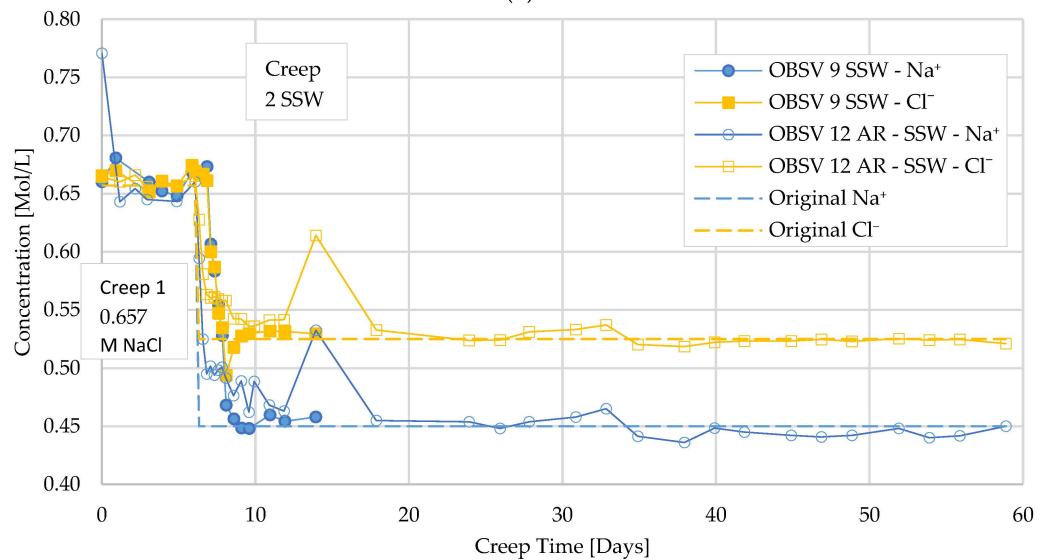
(**b**)

Figure 5. Effluent data for OBSV 9 SSW and OBSV 12 AF-SSW: (**a**) Mg^{2+}, Ca^{2+}, and SO_4^{2-} concentrations for the intact and artificially fractured sample flooded with SSW (OBSV 9 SSW and OBSV 12 AF-SSW) Ca^{2+} correction reflects potential Ca^{2+} production without anhydrite ($CaSO_4$) precipitation. (**b**) Effluent data for Na^+ and Cl^- is presented for samples as in Figure 5a.
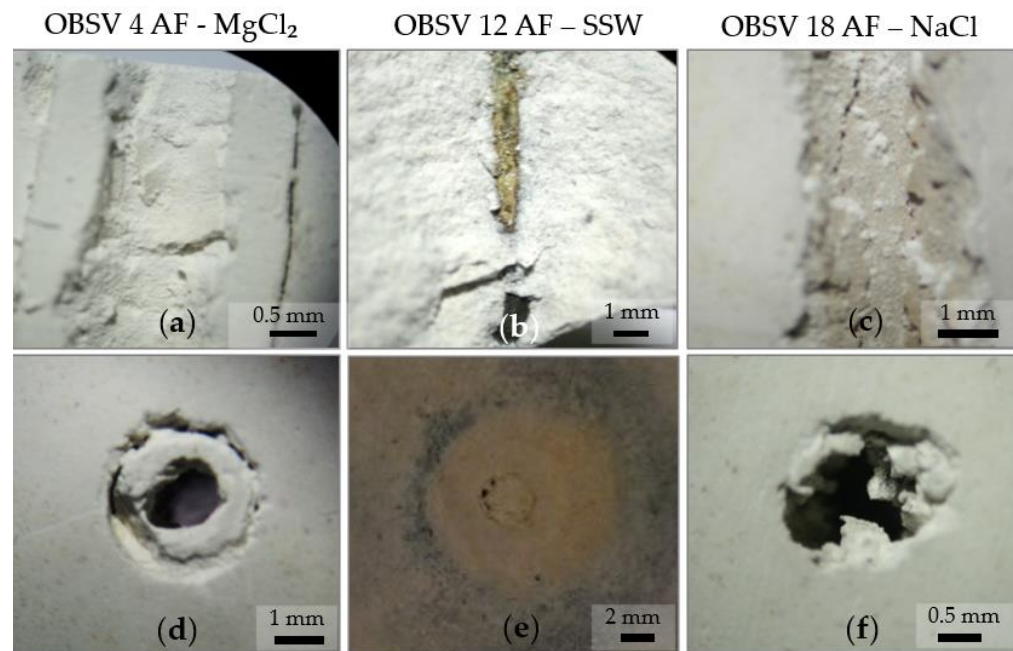
Figure 6. Photographs of textural characteristics of the three artificially fractured cores: (**a**) OBSV 4 AF-MgCl$_2$ #4 parallel to flooding direction. (**b**) OBSV 12 AF-SSW #5 parallel to flooding direction. (**c**) OBSV 18 AF-NaCl #1, parallel to flooding direction. The black arrow points to beige surface of the fracture precipitate. (**d**) OBSV 4 AF-MgCl$_2$ #1 perpendicular to flooding direction. Black arrow points to the void space between matrix and fracture precipitate. (**e**) Wet condition of OBSV 12 AF-SSW #1 perpendicular to flooding direction. (**f**) OBSV 18 AF-NaCl #3 perpendicular to flooding direction.
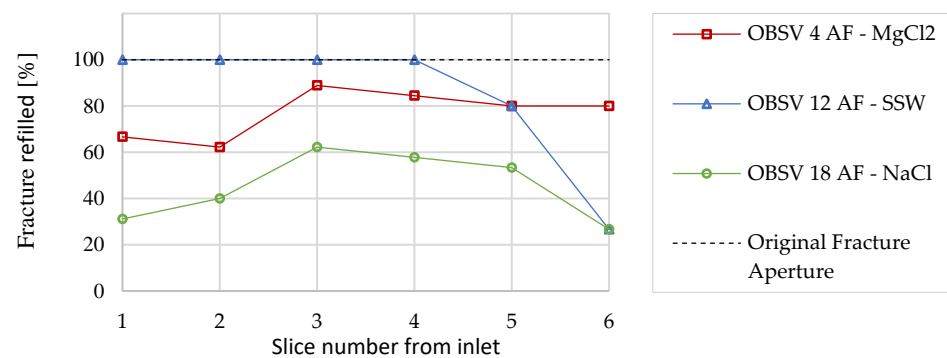
Figure 7. Distribution of artificially fractured aperture diameter reduction (mm) for the three fractured samples from inlet to outlet.

3.5. Geochemistry

Geochemistry was measured on unflooded end slices and flooded core material (Figure 1). The unflooded end samples showed 5 wt.% (weight percent) noncarbonate material (summing Si, Al, Na, and K) (Table 3). Among those, the most abundant component was SiO$_2$ (3.45 wt.%), followed by Al$_2$O$_3$ (1.02 wt.%). The average calcium concentration for reference samples was 52.00 ($\pm$0.37) wt.%. After testing, a reduction in CaO was measured for most slices in sample OBSV 6 MgCl$_2$, with the most significant decrease occurring in the first few slices (Table 3). OBSV 4 AF-MgCl$_2$ and OBSV 9 SSW also showed CaO reduction, but only the third slice in OBSV 4 AF-MgCl$_2$ in addition to two slices in OBSV 9 SSW experienced a significant reduction in CaO concentration. The average MgO concentration was 0.28 wt.% for the reference samples. The highest concentration is observed for OBSV 6 MgCl$_2$, with 1.50 wt.% in the second slice, with an almost linear reduction throughout the sample, measuring 1.01 wt.% for the outlet sample (OBSV 6 MgCl$_2$ #7) (Table 3). OBSV

4 AF-MgCl$_2$ experienced an increase of MgO concentration with a maximum of 0.99 wt.% in slice 4 (central core) and the lowest in the inlet slice (0.66 wt.%). MgO concentration increased in both cores flooded with SSW, but to a lesser extent than observed for the MgCl$_2$-flooded cores. The unfractured core, OBSV 9 SSW, experienced the highest precipitation of MgO in the inlet slice of 0.55 wt.%, which linearly reduced towards the outlet. The artificially fractured core, OBSV 12 AR-SSW, showed the same trend as the artificially fractured core flooded with MgCl$_2$ (OBSV 4 AF-MgCl$_2$), with the highest concentration of 0.53 wt.% in slice three. The central fill in sample OBSV 4 AF-MgCl$_2$ showed a completely different content compared to the matrix. Its inlet and outlet slices of the central fill showed a dominance of MgO of 41.01 and 42.68 wt.% and a CaO concentration of 1.95 and 4.11 wt.%, respectively (Table 3). The noncarbonate concentration was above ten and five percent for the inlet and outlet central fill, respectively.

3.6. Field Emission Gun Scanning Electron Microscopy (SEM) and Energy Dispersive X-ray Spectroscopy (EDS)

Secondary electron (SE) images disclosed gross morphological and compositional variation when focusing on the surface of the fractures or the fracture fill (right column Figure 8) compared to the unflooded matrix (left column Figure 8). Coccoliths were not identified on the fracture surface of OBSV 4.3 AF-MgCl$_2$ (Figure 8b). The most frequently present mineral was square-shaped with sizes up to seven μm and with a high concentration of Mg. OBSV 6.1 MgCl$_2$ did not disclose any significant textural changes compared to its unflooded reference (Figure 8c). OBSV 9.1 SSW was dominated by coccolithophore debris, such as the unflooded material (Figure 8e). No significant textural differences were observed for the fracture fill in OBSV 12.4 AF-SSW compared to its unflooded reference. The inner surface of the fracture of OBSV 18.1 AF-NaCl was dominated by flaky shaped minerals with high concentrations of Si, Mg, Fe, and Al (Figure 8j).

3.7. Specific Surface Area (SSA)

SSA for unflooded reference slices held an average of 4.60 m^2/g with a high normal distribution of ±1.35, which is related to a different cleaning procedure than flooded samples. An average of 4.52 (±0.16) m^2/g was measured for the same samples in a larger SSA study by Wen S.T.S. (2018) [30]. For flooded samples, material from the outer rim of the core was sampled. OBSV 6 MgCl$_2$ showed the highest surface area for the second slice with 5.89 m^2/g, followed by a linear decrease towards the outlet of the core (slice 7) (Table 4), which held 4.25 m^2/g. OBSV 4 AF-MgCl$_2$ showed a maximum of 4.97 m^2/g in the third slice and lowest in slice four (3.67 m^2/g). OBSV 9 SSW showed stable values (averagely 3.53 m^2/g), with significantly lower SSA compared to the unflooded samples. OBSV 12 AF-SSW showed a reduction only in the first slice (3.32 m^2/g) and a few slices with increased SSA, with a maximum of 5.40 m^2/g in the fourth slice. OBSV 18 AF-NaCl distributed stable (3.16 m^2/g) and significantly lower SSA compared to the reference.

Table 4. Measured SSA for flooded unfractured and artificially fractured samples. For the fractured cores (OBSV 4 AF-MgCl$_2$, OBSV 12 AF-SSW, and OBSV 18 AF-NaCl), the material is extracted from the peripheral parts of the cores, not in touch with the fracture. * Data not acquired.

	OBSV 4 AF-MgCl$_2$ m^2/g	OBSV 6 MgCl$_2$ m^2/g	OBSV 9 SSW m^2/g	OBSV 12 AF-SSW m^2/g	OBSV 18 AF-NaCl m^2/g
Slice 1	4.58	5.49	3.64	3.32	3.09
Slice 2	*	5.89	3.49	5.08	3.25
Slice 3	4.97	5.29	3.60	*	3.19
Slice 4	3.67	4.98	3.46	5.40	3.12
Slice 5	*	4.74	3.46	*	3.13
Slice 6	4.95	*	3.56	4.67	*
Slice 7	*	4.25	*	*	*
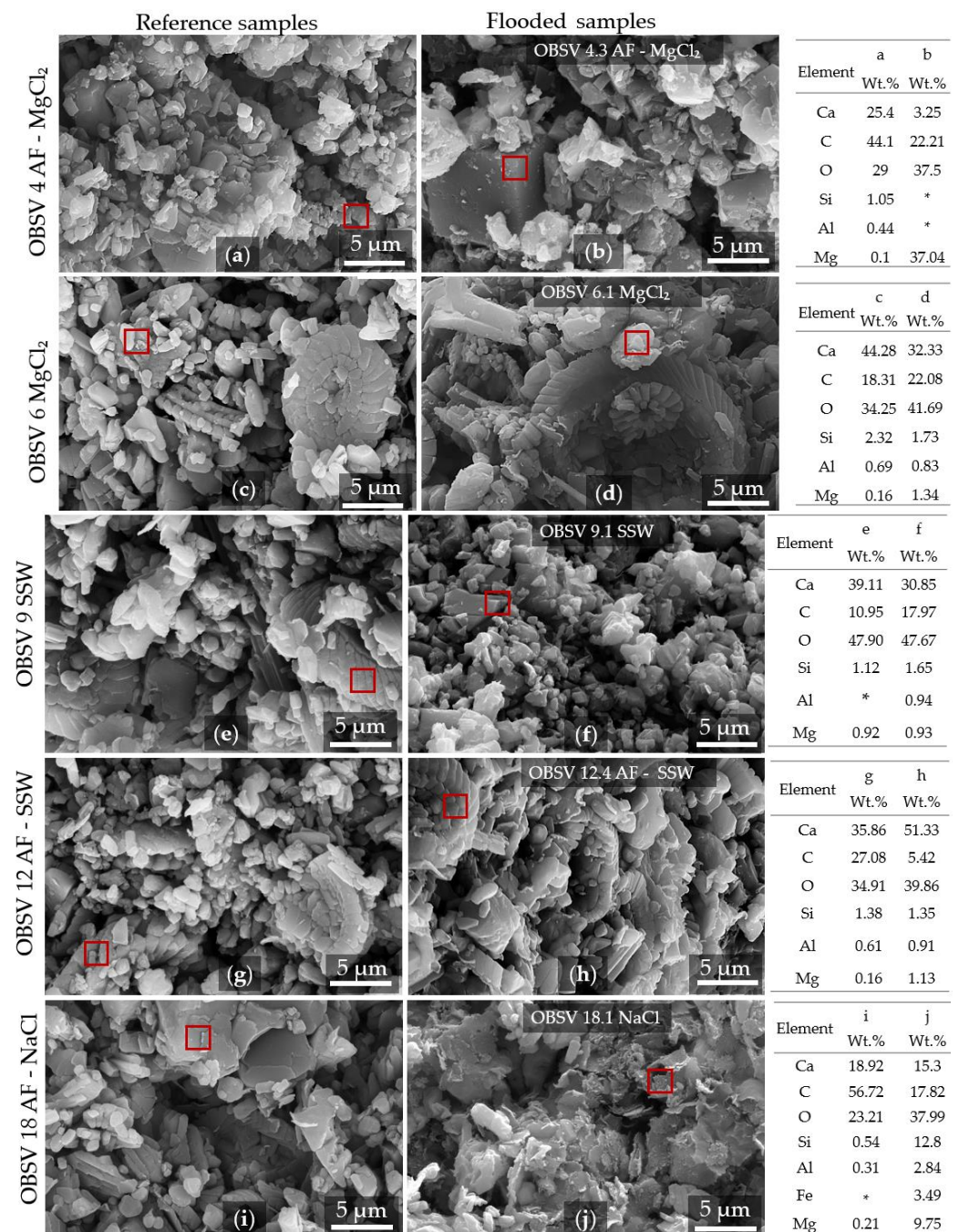
Figure 8. (**a**–**j**) SEM-EDS analysis highlights morphological and elemental differences between reference samples (left column) and flooded samples (right column). The artificially fractured samples were extracted from the surface of the fracture fill (Figure 6a,c). The EDS analysis was extracted from a two-time two μm area marked with a red square on each SEM image. The corresponding elemental composition is presented to the right of the images (semi-quantitative). See text for more detailed descriptions. * Element not detected.

4. Discussion

4.1. Water-Weakening Effect versus Composition of Brine Injected

OBSV 18 AF-NaCl experienced the lowest compaction rate during Creep 2, as expected, since NaCl is inert to chalk. Both the MgCl$_2$-flooded cores (OBSV 4 AF-MgCl$_2$ and OBSV 6 MgCl$_2$) experienced a more prominent compaction rate than the OBSV 18 AF-NaCl sample. In an experimental study by Megawati et al. (2011) [14], a link between the increased compaction rate and the dissolution of Ca^{2+} with the simultaneous precipitation

of Mg^{2+} was observed while flooding chalk cores with brine-containing Mg^{2+}. Researchers have discussed that the weakening of chalks, when injecting Mg^{2+}, may be related to the dissolution of calcite and the precipitation of secondary minerals such as magnesite and magnesium carbonate-bearing clay minerals [31,32]. Madland et al. (2011) [11] discussed the hypothesis that the precipitation of secondary minerals enhanced dissolution, which will lead to increased creep. The higher compaction rate and lowering of porosity for SSW-flooded cores compared to $MgCl_2$-flooded cores (Figure 3b) may be linked to the dissolution and reprecipitation of noncarbonate minerals, possibly clays, which enhanced the compaction for SSW-flooded cores. The two cores flooded with SSW surpassed the strain rate of the two samples flooded with $MgCl_2$. This difference in compaction (related to composition of the injected brine) was evidenced despite the SSW-flooded samples producing lower amounts of Ca^{2+} and a modest retention of Mg^{2+} compared to the $MgCl_2$-flooded samples. All samples showed homogeneous properties in terms of strength (yield and bulk modulus) and geochemistry. The distinct compaction rates (Creep 2) for the various brine points to effects caused by different ions in the injected brine, hence the dissimilar chemical and chemo-physical processes. Adsorption of SO_4^{2-} to calcite surfaces is believed to play a key role in water weakening. Madland et al. (2008) [33] showed that Kansas chalk samples (with purity of 99% calcite) flooded with SSW without the presence Mg^{2+} experienced a considerable amount of compaction; however, experiments performed with SSW without SO_4^{2-} experienced a lower compaction rate than the SSW-flooded samples. Megawati et al. (2013) [12] showed that SO_4^{2-} ions present in a brine to adsorb the chalk surface, resulting in a negative surface charge, which triggers the occurrence of repulsive forces at granular contacts, thus reducing the cohesion between grains. They also reported a link between the escalating strain and the increased concentration of SO_4^{2-} in the injecting brine and test temperature. Kallesten et al., 2020 [34], however, observed in reservoir samples that a $MgCl_2$-flooded sample compacted more than a sample flooded with SSW. This may imply that the presence of noncarbonate phases influence chemo-physical processes, and that the role of SO_4^{2-} is yet not completely understood in the presence of clays.

4.2. Compaction Rate in Artificially Fractured Samples versus Unfractured

The artificial fractures had no significant effect on the mechanical strength during hydrostatic loading with NaCl injection and distributed similar strength in terms of yield and bulk modulus (Table 2 and Figure 2). During Creep 1, still injected with NaCl, ion chromatography analysis identified concentrations that straddled original values. This points to no or minimal chemical interaction with the tested rock samples and strengthened the interpretation that NaCl is inert (compilation in Andersen et al., 2017 [4]). However, all three artificially fractured cores showed a higher strain rate (Figure 3a) than the two intact cores during Creep 1. This lowering of mechanical strength above yield stress may indicate that the artificial fracture is significant despite a small aperture of 2.25 ($\pm$0.05) mm versus a total diameter of 38.1 mm and thereby present a lower bulk volume to withstand the effective overburden pressure. The cores became shorter, and the artificially fractured diameter reduced as a result of axial and radial strain forcing the matrix into void space.

The injection fluid was changed from NaCl to SSW and $MgCl_2$ for two fractured and two intact cores in Creep 2 (Figure 3b). The result demonstrated an increased compaction rate for all cores injected by either $MgCl_2$ or SSW. At the start of the brine change, the two unfractured samples (OBSV 6 $MgCl_2$ and OBSV 9 SSW) showed a higher creep rate compared to their paired artificially fractured samples injected with the same brine (OBSV 4 AF-$MgCl_2$ and OBSV 12 AF-SSW). The increased deformation rate observed for the unfractured cores is suggested to be a result of the entire core matrix being immediately in contact with the flooding brine. For the cores containing an artificial fracture, the ions in the brine spent longer time to diffuse into the matrix and used the open fracture as a "highway" through the core. This delayed fluid transport to peripheral parts of the sample and is reflected in the ion chromatography results, where two of the artificially fractured cores

(OBSV 4 AF-MgCl$_2$ and OBSV 12 AF-SSW) showed Ca$^+$ production/Mg$^+$ retention similar to unfractured cores (OBSV 6 MgCl$_2$ and OBSV 9 SSW), albeit in a lower rate and with a later onset (Figures 4 and 5). The ion concentration (Na$^+$ and Cl$^-$) lasted approximately seven days until the effluent achieved the same composition as the injected brine. The unfractured cores returned, however, to stable levels after one day, which reflects the injection rate of one PV/day and an immediate contact with matrix (Figures 4 and 5). The higher creep rate observed for OBSV 4 AF-MgCl$_2$ and OBSV 12 AF-SSW, compared to OBSV 18 AF-NaCl, which showed a lower compaction rate (Figure 3b) and NaCl is believed to be chemically inert to chalk, evidencing that chemical water-weakening is certainly present in peripheral locations despite the low matrix permeability and was therefore caused by ion diffusion (Table 2).

4.3. Extrapolation of Compaction

The results showed that artificially fractured cores were mechanically weaker when no (or limited) brine–rock interactions took place during the primary creep phase under NaCl injection (Creep1). On the contrary, we observed a predominant compaction for unfractured samples during Creep 2, when brines with surface active ions such as Mg^{2+} and SO$_4^{2-}$ were injected. However, unfractured and artificially fractured compaction behaviour, along with effluent data (Figures 4 and 5), showed that these creep rates stagnated most evidently for the two unfractured cores (OBSV 6 MgCl$_2$ and OBSV 9 SSW). An extrapolated logarithmic behaviour (Equation (3)) of the geo-mechanical response (Figure 9) illustrates that artificially fractured cores, with the same composition of the injected brine, may be geomechanically weaker after ruffly four to six months despite the experimental creep rates showing the opposite (complete description of methodology in Madland et al. (2006) [28] and statistical references for applicability in [4,10,11]). Regardless of the delayed ions' diffusion from the high permeable fracture to the matrix, water weakening will eventually take place in the entire core. It is therefore possible that an unfractured sample will experience less creep over time than an artificially fractured sample, despite an instant onset of water weakening when surface-active ions are injected. Moreover, the artificially fractured sample experienced lower mechanical resilience caused by the presence of the fracture, showing water weakening in peripheral locations by ion diffusion from the main fluid transport through the fracture. This process is dependent on matrix permeability, the size of the fracture aperture, the distance of the ion diffusion from the fracture and duration of brine injection. A longer test duration in future experiments may verify if artificially fractured samples or unfractured samples are most prone to compact in the long run.
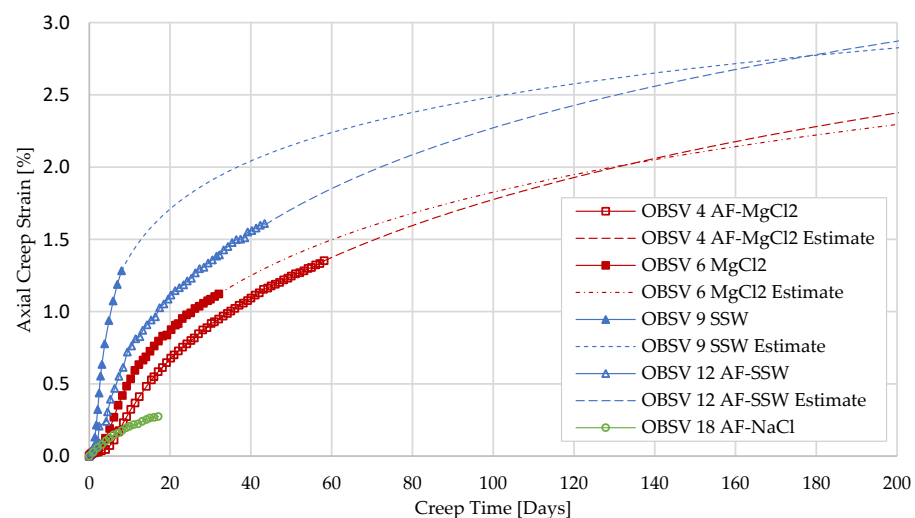
Figure 9. Extrapolation of the geo-mechanical response of creep rates for two artificially fractured samples (OBSV 4 AF-MgCl$_2$ and OBSV 12 AF-SSW) and two unfractured samples (OBSV 6 MgCl$_2$ and OBSV 9 SSW) over a period of 200 days.

These results may be considered as a primary approach to decipher dynamic reservoir conditions caused by fracture alterations. Future laboratory experiments may repeat testing for the verification of test results and include geological evolution, including different formation properties related to a hydrocarbon play and identify its statistical significance and modification of hydrocarbon production. This also refers to a thorough evaluation with a variety of analytical techniques to describe the reservoir [35], which, in the next phase, would be applied for modelling fracture behaviour [36].

4.4. Textural Alterations versus Mineral Precipitation

OBSV 18 AF-NaCl was added to the experiment as a reference sample as it is expected to produce minute mineralogical changes [11,13]. Geochemistry did not disclose chemical differences from unflooded samples. The SSA measurements showed, however, a reduced SSA (Table 4). A similar reduction in SSA was observed by Andersen et al. (2017) [4] in Aalborg chalk (Maastrichtian Cretaceous) rich in opal CT, where SSA reduced from 4.9 to 2.1 m^2/g for the inlet slice and identified a reduction in opal CT. The core was flooded with NaCl at 130 °C. For pure chalk samples, reduction in SSA was, however, not significant. Samples with higher noncarbonate content also showed the highest dissolution of Ca^{2+} of 0.004 M (near the detection limit) in the effluent compared to chalk samples with purer concentrations of $CaCO_2$. Another study on Aalborg samples, also flooded under a temperature of 130 °C, (Minde et al., 2018) [10], showed the same SSA reduction when flooding with NaCl. Additionally, they observed the rounding of calcite grains. Since chemical alteration is in this study unexpected, the SSA reduction is interpreted to be related to the rounding of grain surfaces by dominantly physio-mechanical forces.

OBSV 6 $MgCl_2$ experienced the most significant precipitation of MgO-containing phases, predominantly in the inlet slices, which gradually decreased towards the outlet (Table 3). Simultaneously, OBSV 6 $MgCl_2$ also experienced the greatest increase in SSA, again with the most significant SSA alteration in the inlet and decreasing towards the outlet slice (Table 4). The link between the abundance of phases enriched in MgO and increased SSA (Figure 10) supports the interpretation that these phases are secondary products that are also present in previous EOR experiments [4,37]. Another possible reason for increased SSA (OBSV 6 $MgCl_2$) could be a stepwise chemical dissolution of coccoliths (calcite) producing a rougher surface, thus increasing the SSA (or, potentially the reprecipitation of small calcite particles). The fractured OBSV 12 AF-SSW showed similar precipitation of MgO-containing phases as the intact OBSV 9 SSW; however, the SSA is generally higher for the fractured OBSV 12 AF-SSW. The higher SSA in OBSV 12 AF-SSW could be related to the crystallization of ions in the brine despite a thorough cleaning procedure passing three times the volume used in standard cleaning procedures.
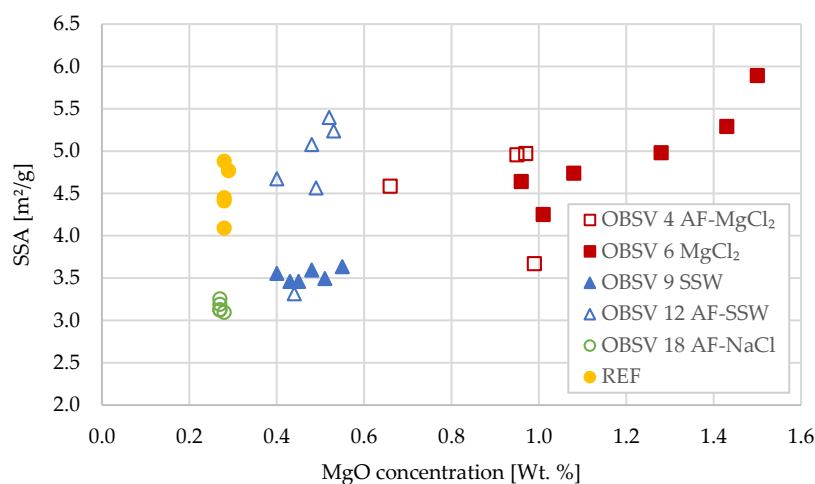
Figure 10. A presentation of the link between precipitation of MgO and SSA for all flooded samples compared with unflooded reference samples.

4.5. Aperture Modification versus Strain

Bulk permeability estimates depend on anisotropy as fracture density, orientation, aperture size distribution, and fracture versus matrix permeability. Seawater injection will introduce water weakening, altering matrix permeability. Fracture aperture modification may change fracture permeability and complicate the prediction of flow behaviour through a reservoir. Here, permeability was calculated for the two intact cores, which experienced a reduction as water weakening proceeded (Table 2). Porosity reduction was observed for all samples (Table 2). Textural (Table 2) and bulk geochemistry data (Table 3) suggest also that the peripheral matrix, adjacent to the fracture fill, has been changed, which could indicate reduced matrix permeability for artificially fractured cores despite the great permeability difference between fracture versus matrix. Caine et al. (1996) [20] suggested that, despite low matrix permeability, it may not necessarily act as a barrier to flow, especially during compaction. All three samples reduced the overall fracture aperture in this experiment to different extents. Gale et al., 2010 [38], showed that cement accumulated gradually at rates governed by temperature history. They suggested that cement patterns in fractures are a consequence of the surface areas and volumes of the fractures of various sizes. Fracture connectivity may reduce by filling the narrow tips of fractures and small fractures in addition to cement reducing overall open-fracture length and connectivity [18]. The geochemistry result of the fracture fill, which was detached from the surrounding matrix in OBSV 4 AF-MgCl$_2$, showed a predominance of MgO (42 wt.%) and higher SiO$_2$ and Al$_2$O$_3$ compared to the matrix (Table 3). This indicates a higher concentration of noncarbonate phases in the fracture fill compared to the surrounding matrix. The exact mineralogy present in the fracture fill will be further analysed and discussed in a follow up article. Mainly coccoliths with an abundance of a flaky noncarbonate phase were identified (Figures 6 and 8) in the fracture fill of OBSV 12 AF-SSW and OBSV 18 AF-NaCl. The presence of intact coccoliths in the fracture fill (Figure 8) may be related to an aperture reduction caused by mechanical forces, pushing the matrix to void spaces in the fracture during creep (Figure 11).
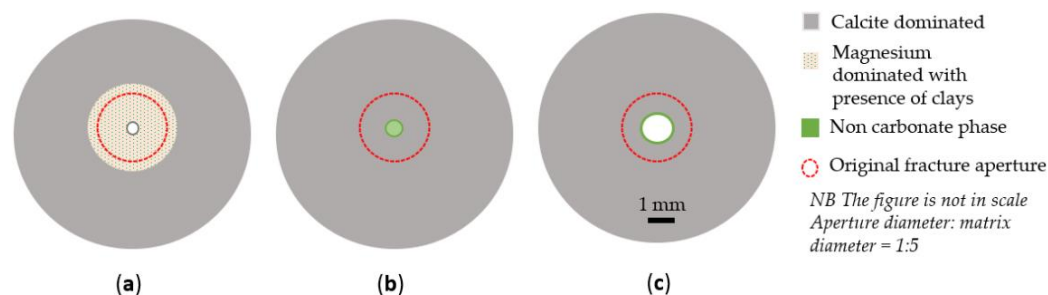
Figure 11. The sketch simplifies aperture modification and mineralogy in a cross-section for the three artificially fractured cores. All samples represent the third slice, where the apertures are most significantly reduced. The red circle symbolizes the original aperture size. (**a**) OBSV 4 AF-MgCl$_2$; (**b**) OBSV 12 AF-SSW; (**c**) OBSV 18 AF-NaCl.

The overall fracture apertures were reduced for all three artificially fractured samples throughout the cores, from inlet to outlet, and have been suggested to be caused by a combination of mechanical and chemical consequences. The experiment was performed under hydrostatic test conditions, where radial strain was not measured, yet was expected to execute the similar strain as identified in the axial direction and thereby contribute to the fracture modification. OBSV 12 AF-SSW experienced the most significant aperture diameter reduction of 84%, which also experienced the highest total strain of 4.16%, where 2.66% compacted during loading and Creep 1 (NaCl injection) and 1.50% compacted during Creep 2 under injection of SSW (Table 2). On average, OBSV 4 AF-MgCl$_2$ reduced the aperture diameter by 76%. Moreover, OBSV 4 AF-MgCl$_2$ experienced a total axial strain of 3.41% (Table 2), where 2.06% strain was identified during loading and Creep 1 (NaCl

injection), and 1.35% strain was detected during $MgCl_2$ injection in Creep 2. The OBSV 18 AF-NaCl experienced the lowest total strain (2.51%) (where 2.24% was related to loading and Creep 1 and only 0.27% strain was detected during Creep 2) and showed the smallest aperture reduction of 44% (Figure 7). A relationship between strain and aperture reduction is very likely. A linear relationship was drawn from origo through the reference sample of OBSV 18 AF-NaCl, representing the relationship between increased strain and a reduction in aperture diameter caused by mechanical forces alone, as NaCl did not cause any chemical alteration (Figure 12). This demonstrates that the additional reduction (deviation from the linear relationship) may indicate additional aperture reduction caused by chemical alteration. The deviation indicated that OBSV 4 AF-$MgCl_2$ experienced the steepest curve for Creep 2, which was caused by mineral precipitation. Furthermore, OBSV 12 AF-SSW also showed an additional reduction (steeper curve) than the OBSV 18 AF-NaCl caused by dissolution and precipitation processes. Ion chromatography strengthen this relationship, with a more prominent ion exchange (dissolution of Ca^{2+} and precipitation of Mg^{2+}) present in OBSV 4 AF-$MgCl_2$ compared to OBSV 12 AF-SSW (Figures 4 and 5). Higher precipitation of MgO in OBSV 4 AF-$MgCl_2$ compared to OBSV 12 AF-SSW was also confirmed by geochemistry (Table 3), which enhances this theory. Future experiments with several fracture diameters flooded with primarily NaCl could confirm a more accurate relation between creep and fracture modification before adding several experiments with brines expected to generate dissolution and precipitation processes contributing to the additional reduction of an aperture.
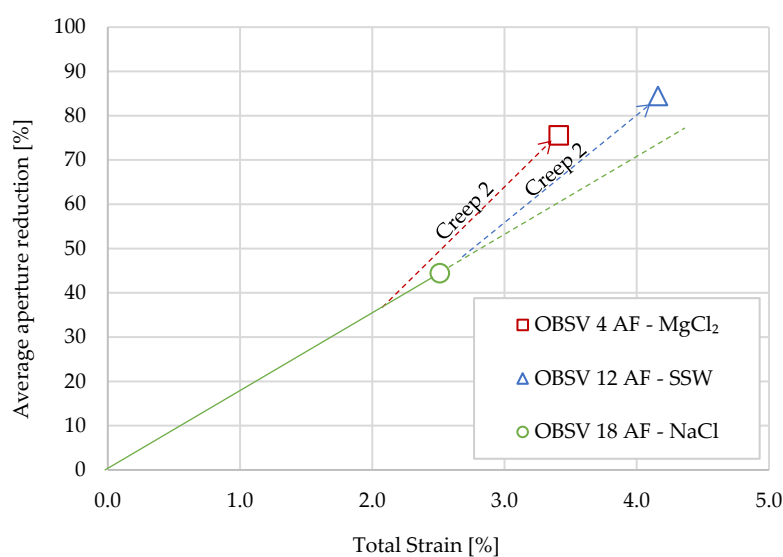
Figure 12. The graph presents the link between the average aperture reduction [%] and the total axial strain [%] experienced during Loading, Creep 1, and Creep 2 for the three artificially fractured cores (radial strain was not identified in this hydrostatic test; however, the aperture reduction is necessarily a result of the combined strain). A linear relationship between total strain [%] and aperture reduction [%] for OBSV 18 AF-NaCl is marked from origo through the final point of axial strain and aperture reduction (the reduction is expected to be related to mechanical forces only). The deviation above the linear relationship for OBSV 4 AF-$MgCl_2$ and OBSV 12 AF-SSW are ambiguous estimations related to aperture reduction caused by mineral precipitation during Creep 2.

The detached fracture fill of OBSV 4 AF-$MgCl_2$ (Figure 6a,d) was dominated by MgO (Table 3) and measured a larger diameter of 2.75 mm (Figure 11) compared to the initial aperture of 2.25 ($\pm$0.05) mm. Two simultaneous processes have been identified for OBSV 4 AF-$MgCl_2$ affecting the modification of the artificial fracture: reduction of the fracture aperture caused by axial and radial strain, simultaneously with Ca^{2+} dissolution/Mg^{2+} precipitation (Figure 4) predominantly along the fracture wall.

5. Conclusions

- Flooded samples showed no significant difference in yield strength during loading when comparing unfractured with artificially fractured samples;
- Compaction during NaCl injection showed that artificially fractured cores experienced significantly higher axial strain compared to unfractured samples;
- Water weakening was identified during injection of SSW and $MgCl_2$ for unfractured and artificially fractured cores. Geo-mechanical response indicated that water weakening is activated shortly after injecting brines with surface-reactive ions (SSW and $MgCl_2$) for unfractured samples. The artificially fractured samples showed a later onset of the increased compaction rate compared to the unfractured samples. Effluent data supported the water-weakening effect;
- A delayed water-weakening effect was observed for artificially fractured cores and is suggested to be linked to a later onset of brine–rock interaction processes in peripheral matrix locations caused by the diffusion of surface-active ions from the fracture despite a low permeable matrix. Geochemistry data identified MgO precipitation in unfractured samples besides the peripheral locations of artificially fractured samples;
- SSW-flooded samples experienced axial strain beyond $MgCl_2$-flooded cores during the test phase when different brines were injected (Creep 2). Unfractured samples compacted 1.12% and 1.49%, caused by $MgCl_2$ and SSW, respectively. The artificially fractured SSW-flooded core experienced a total strain of 1.50%, $MgCl_2$ exhibited 1.35%, and NaCl showed the least compaction, at 0.27% (samples had different test duration);
- Extrapolation of the geo-mechanical response indicated that unfractured samples over time will be mechanically weaker than artificial fractured samples; despite that, the results obtained in this time-limited experiment showed that unfractured samples experienced the highest strain. The extrapolation suggests that the water-weakening effect will stagnate for intact cores and be delayed to the peripheral matrix in artificially fractured cores due to diffusion. A longer test duration of a similar setup is suggested to confirm the theory;
- The original fracture aperture of 2.25 (±0.05) mm was reduced in all three artificially fractured samples. The average aperture diameter reduction throughout the samples were 84%, 76%, and 44% for SSW, $MgCl_2$, and NaCl, respectively;
- A relationship between strain and aperture reduction was identified. The artificial aperture reduction is believed to be caused by a combination of mechanical forces, where axial and radial strains drive the matrix towards void spaces besides mineral precipitation, causing additional aperture reduction, which is dependent on the brine composition and mineral present in the sample.

The degree of water weakening of the matrix adjacent to a fracture will depend on the fracture density and connectivity and the travel distance from the permeable zone, as well as on porosity and permeability differences. Nevertheless, the experiment showed the potential of aperture diameter reduction and a link to a water-weakening effect. When smaller fractures reduce, the injected brine may be forced into the adjacent matrix and find new paths throughout the more compacted reservoir, and further complex EOR processes will develop. If those yield in higher hydrocarbon production, it is left to be substantiated.

References

1. Tanner, R.S.; Udegbunam, E.O.; McInerney, M.J.; Knapp, R.M. Microbially enhanced oil recovery from carbonate reservoirs. *Geomicrobiol. J.* **1991**, *9*, 169–195. [CrossRef]
2. Sulak, R.; Danielsen, J. Reservoir aspects of Ekofisk subsidence. *J. Pet. Technol.* **1989**, *41*, 709–716. [CrossRef]
3. NPD. Available online: https://factpages.npd.no/en/field/pageview/all/43506 (accessed on 13 July 2018).
4. Andersen, P.; Wang, W.; Madland, M.V.; Zimmermann, U.; Korsnes, R.I.; Bertolino, S.R.A.; Minde, M.; Schulz, B.; Gilbricht, S. Comparative Study of Five Outcrop Chalks Flooded at Reservoir Conditions: Chemo-mechanical Behaviour and Profiles of Compositional Alteration. *Transp. Porous Media* **2017**, *121*, 135–181. [CrossRef]
5. Korsnes, R.; Madland, M.; Austad, T. Impact of brine composition on the mechanical strength of chalk at high Temperature. In *Eurock 2006*; CRC Press: Boca Raton, FL, USA, 2006; pp. 133–140. [CrossRef]
6. Korsnes, R.I.; Madland, M.V.; Austad, T.; Haver, S.; Røsland, G. The effects of temperature on the water weakening of chalk by seawater. *J. Pet. Sci. Eng.* **2008**, *60*, 183–193. [CrossRef]
7. Nermoen, A.; Korsnes, R.I.; Aursjø, O.; Madland, M.V.; Kjørslevik, T.A.; Østensen, G. How stress and temperature conditions affect rock-fluid chemistry and mechanical deformation. *Front. Phys.* **2016**, *4*, 2. [CrossRef]
8. Strand, S.; Standnes, A.D.C.; Austad, T. Spontaneous imbibition of aqueous surfactant solutions into neutral to oil-wet carbonate cores: Effects of brine salinity and composition. *Energy Fuels* **2003**, *17*, 1133–1144. [CrossRef]
9. Bjørlykke, K.; Høeg, K. Effects of burial diagenesis on stresses, compaction and fluid flow in sedimentary basins. *Mar. Pet. Geol.* **1997**, *14*, 267–276. [CrossRef]
10. Minde, M.W.; Wang, W.; Madland, M.V.; Zimmermann, U.; Korsnes, R.I.; Bertolino, S.R.; Andersen, P. Temperature effects on rock engineering properties and rock-fluid chemistry in opal-CT-bearing chalk. *J. Pet. Sci. Eng.* **2018**, *169*, 454–470. [CrossRef]
11. Madland, M.V.; Hiorth, A.; Omdal, E.; Megawati, M.; Hildebrand-Habel, T.; Korsnes, R.I.; Evje, S.; Cathles, L.M. Chemical alterations induced by rock–fluid interactions when injecting brines in high porosity chalks. *Transp. Porous Media* **2011**, *87*, 679–702. [CrossRef]
12. Megawati, M.; Hiorth, A.; Madland, M.V. The impact of surface charge on the mechanical behavior of high-porosity chalk. *Rock Mech. Rock Eng.* **2012**, *46*, 1073–1090. [CrossRef]
13. Megawati, M.; Madland, M.; Hiorth, A. Mechanical and physical behavior of high-porosity chalks exposed to chemical perturbation. *J. Pet. Sci. Eng.* **2015**, *133*, 313–327. [CrossRef]
14. Megawati, M.; Andersen, P.Ø.; Korsnes, R.I.; Evje, S.; Hiorth, A.; Madland, M.V. The effect of aqueous chemistry pH on the time-dependent deformation behaviour of chalk- experimental and modelling study. Les Rencontres scientifiques d'IFP Energies Nouvelles. Flows and mechanics in natural porous media from pore to field scale. In Proceedings of the Pore2Fluid IFP Energies Nouvelles Paris, Aussois, France, 16–18 November 2011.
15. Mukherjee, H.; Poe, B.J.; Heidt, J.H.; Watson, T.B.; Barree, R.D. Effect of Pressure Depletion on Fracture-Geometry Evolution and Production Performance. *SPE Prod. Facil.* **2000**, *15*, 144–150. [CrossRef]
16. Snow, S.E.; Brownlee, M.H. Practical and theoretical aspects of well testing in the Ekofisk area chalk fields. In *SPE Annual Technical Conference and Exibition*; OnePetro: Richardson, TX, USA, 1989.
17. Michie, E.; Haines, T.; Healy, D.; Neilson, J.; Timms, N.; Wibberley, C. Influence of carbonate facies on fault zone architecture. *J. Struct. Geol.* **2014**, *65*, 82–99. [CrossRef]
18. Philip, Z.G.; Jennings, J.W.; Olson, J.E.; Laubach, S.E.; Holder, J. Modeling coupled fracture-matrix fluid flow in geomechanically simulated fracture networks. *SPE Reserv. Eval. Eng.* **2005**, *8*, 300–309. [CrossRef]
19. Chester, F.M.; Evans, J.P.; Biegel, R.L. Internal structure and weakening mechanisms of the San Andreas Fault. *J. Geophys. Res. Earth Surf.* **1993**, *98*, 771–786. [CrossRef]
20. Caine, J.S.; Evans, J.P.; Forster, C.B. Fault zone architecture and permeability structure. *Geology* **1996**, *24*, 1025–1028. [CrossRef]

21. Goddard, J.V.; Evans, J.P. Chemical changes and fluid-rock interaction in faults of crystalline thrust sheets, northwestern Wyoming, U.S.A. *J. Struct. Geol.* **1995**, *17*, 533–547. [CrossRef]

22. Laubach, S.E. Practical approaches to identifying sealed and open fractures. *AAPG Bull.* **2003**, *87*, 561–579. [CrossRef]

23. Wibberley, C.A.; Shimamoto, T. Internal structure and permeability of major strike-slip fault zones: The Median Tectonic Line in Mie Prefecture, Southwest Japan. *J. Struct. Geol.* **2003**, *25*, 59–78. [CrossRef]

24. Agosta, F.; Prasad, M.; Aydin, A. Physical properties of carbonate fault rocks, fucino basin (Central Italy): Implications for fault seal in platform carbonates. *Geofluids* **2007**, *7*, 19–32. [CrossRef]

25. Hjuler, M.; Fabricius, I. Engineering properties of chalk related to diagenetic variations of Upper Cretaceous onshore and offshore chalk in the North Sea area. *J. Pet. Sci. Eng.* **2009**, *68*, 151–170. [CrossRef]

26. Geitle, K. Chemically Induced Compaction in Fractured and Intact Chalk Cores in Institute for Energy and Resources (IER). Master's Thesis, University of Stavanger, Stavanger, Norway, 2013; p. 78. Available online: https://uis.brage.unit.no/uis (accessed on 13 December 2021).

27. Abubeker, E. Water weakening of chalks-comparsion of intact and fractured cores, in Faculty of Science and Technology. Master's Thesis, University of Stavanger, Stavanger, Norway, 2013; p. 88. Available online: https://uis.brage.unit.no/ (accessed on 13 December 2021).

28. Madland, M.V.; Finsnes, A.; Alkafadgi, A.; Risnes, R.; Austad, T. The influence of CO_2 gas and carbonate water on the mechanical stability of chalk. *J. Pet. Sci. Eng.* **2006**, *51*, 149–168. [CrossRef]

29. Brunauer, S.; Emmett, P.H.; Teller, E. Adsorption of gases in multimolecular layers. *J. Am. Chem. Soc.* **1938**, *60*, 309–319. [CrossRef]

30. Wen, S.T.S. Systematic Specific Surface Area Analysis on Rocks to Implement as a Necessary, Quick, and Informative Method to Understand Geo-Mechanical Parameter in IOR Experiments, in Faculty of Science and Technology. Master's Thesis, University of Stavanger, Stavanger, Norway, 2018; p. 253. Available online: https://uis.brage.unit.no/uis-xmlui/handle/11250/2570740 (accessed on 3 February 2022).

31. Minde, M.W.; Zimmermann, U.; Madland, M.V.; Korsnes, R.I.; Schulz, B.; Gilbricht, S. Mineral replacement in long-term flooded porous carbonate rocks. *Geochim. Cosmochim. Acta* **2019**, *268*, 485–508. [CrossRef]

32. Kallesten, E.; Zimmermann, U.; Madland, M.; Bertolino, S.; Omdal, E.; Andersen, P. Mineralogy and geochemistry of reservoir and non-reservoir chalk from the Norwegian continental shelf. *J. Pet. Sci. Eng.* **2021**, *205*, 108914. [CrossRef]

33. Madland, M.V.; Midtgarden, K.; Manafov, R.; Korsnes, R.I.; Kristiansen, T.; Hiorth, A. The effect of temperature and brine composition on the mechanical strength of Kansas chalk. In Proceedings of the International Symposium of the Society of Core Analysts, Abu Dhabi, United Arab Emirates, 29 October–2 November 2008; p. 6. Available online: scaweb.org (accessed on 16 April 2022).

34. Kallesten, E.; Andersen, P.; Berawala, D.S.; Korsnes, R.I.; Madland, M.V.; Omdal, E.; Zimmermann, U. Modeling of Permeability and Strain Evolution in Chemical Creep Compaction Experiments with Fractured and Unfractured Chalk Cores Conducted at Reservoir Conditions. *SPE J.* **2020**, *25*, 2710–2728. [CrossRef]

35. Shahbazi, A.; Monfared, M.S.; Thiruchelvam, V.; Fei, T.K.; Babasafari, A.A. Integration of knowledge-based seismic inversion and sedimentological investigations for heterogeneous reservoir. *J. Southeast Asian Earth Sci.* **2020**, *202*, 104541. [CrossRef]

36. Soleimani, M. Naturally fractured hydrocarbon reservoir simulation by elastic fracture modeling. *Pet. Sci.* **2017**, *14*, 286–301. [CrossRef]

37. Zimmermann, U.; Madland, M.V.; Nermoen, A.; Hildebrand-Habel, T.; Bertolino, S.A.; Hiorth, A.; Korsnes, R.I.; Audinot, J.-N.; Grysan, P. Evaluation of the compositional changes during flooding of reactive fluids using scanning electron microscopy, nano-secondary ion mass spectrometry, X-ray diffraction, and whole-rock geochemistry Compositional Changes during Flooding. *AAPG Bull.* **2015**, *99*, 791–805. [CrossRef]

38. Gale, J.F.; Lander, R.H.; Reed, R.M.; Laubach, S. Modeling fracture porosity evolution in dolostone. *J. Struct. Geol.* **2010**, *32*, 1201–1211. [CrossRef]

Paper VI:

"Comprehensive Characterization of Mineral Precipitation in Artificially Fractured Chalk during flooding Experiments"

Bredal, T.V., Zimmermann, U., Korsnes, I.R, Minde, M., Tucho, W.M. Audinot, J.-N., Madland M. V., 2023

Paper VI
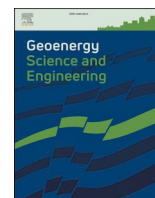
Characterization of mineral precipitation in artificially fractured chalk during flooding experiments for IOR research

Tine Vigdel Bredal [a,b,*], Udo Zimmermann [a,b], Reidar Inge Korsnes [a,b], Mona Wetrhus Minde [b,c], Wakshum Mekonnen Tucho [c], Jean-Nicolas Audinot [d], Merete Vadla Madland [e]

[a] Department of Energy Resources, University of Stavanger, Ullandhaug, 4036, Stavanger, Norway
[b] The National IOR Centre of Norway, University of Stavanger, Ullandhaug, 4036, Stavanger, Norway
[c] Department of Mechanical and Structural Engineering and Materials Science, University of Stavanger, Ullandhaug, 4036, Stavanger, Norway
[d] Luxembourg Institute of Science and Technology, Luxembourg
[e] Division of Research, University of Stavanger, Ullandhaug, 4036, Stavanger, Norway

ARTICLE INFO

ABSTRACT

Natural fractures in carbonate reservoirs are essential to effectively transport hydrocarbon in an otherwise low permeable matrix. However, they can reduce the wanted effect of water injection and Improved Oil Recovery (IOR), as the injected water mainly runs through the fractures. We have investigated chemical and textural alteration in and adjacent to an artificial fracture with an aperture of 2.25 ($\pm$0.05) mm in Upper Cretaceous chalk from the St. Vaast Formation (Mons Basin, Belgium). The sample has been injected mainly with 0.219 M $MgCl_2$ under reservoir conditions over two months. The fracture aperture reduced averagely by 76%. The analysis performed by Transmission Electron Microscopy (TEM) and X-ray Diffraction (XRD) show that, magnesite is the dominating precipitate in the fracture with sizes ranging from 0.5 to 5 μm. The abundance of magnesium phases in the fracture fill was also confirmed by Scanning Electron Microscopy (SEM) coupled with Energy-dispersive X-ray spectroscopy (EDS) and bulk geochemistry (Inductively Coupled Plasma Mass Spectrometry ICP-MS). Besides magnesite, phyllosilicates were observed by TEM and Helium Ion Microscopy combined with Secondary Ion Mass Spectrometry (HIM-SIMS). The newly formed material, precipitates, and possible reworked minerals are characterized by magnesite crystals being covered occasionally by phyllosilicates. This material has formed a distinct area bounded to the surrounding matrix. The final diameter of the precipitate measures about 2.75 ($\pm$0.15) mm, which indicates an incremental widening of the original fracture aperture. Calcite along fracture wall dissolved. Effluent concentration supports dissolution by an increase in Ca^{2+} and precipitation of magnesite by the loss of Mg^{2+}. As either silica or aluminium is a component of the fluids, the origin of these elements is necessarily from the matrix of the chalk. It is yet unknown if phyllosilicates precipitated or was reworked, or both. Formation and concentration of magnesite and phyllosilicates in reservoir fractures can reduce fracture permeability over time and lead to subsequent propagation through the matrix of the reservoir rock. This in-depth mineralogical study of artificial fracture changes has the utmost importance for the implementation of techniques in fractured reservoirs.

1. Introduction

Chalk (CaCO₃) reservoirs on the Norwegian Continental Shelf (NCS) have great potential to accumulate oil (Korsnes et al., 2006) due to the often high porosity of 40–50% (Sulak and Danielsen, 1989). Nevertheless, the ultimate oil recovery is usually low for carbonate reservoirs because of low matrix permeability (1–5 mD Ekofisk) (Sulak and Danielsen, 1989). Ekofisk is the largest carbonate reservoir found on the NCS and located in the southern part of the Norwegian Central Graben (NCG) which represents the southern branch of the North Sea triple rift system. Oil production started in 1971 by pore pressure depletion. The pore pressure depletion caused increased effective stress facilitating compaction in the reservoir. Hydrocarbon was expulsed from the porous chalk, initiating seafloor subsidence (Sulak and Danielsen, 1989; Hermansen et al., 2000). Following a peak production rate during primary recovery, the production rate decreased significantly. A substantial increase in oil recovery followed implementation of water injection, an established method, which started in 1987 and continued in subsequent years. Experience proved that water displaced the oil much more effectively than anticipated. Seawater injections alter the calcite surface characteristics by modifying the surface from being oil wet to become more water wet, consequently oil is more easily released from the surface (Puntervold et al., 2007; Austad et al., 2008, 2009). Deformation of chalk matrix and compaction of the soft chalk are secondary effects of seawater injection and caused by surface chemical alterations involving calcite dissolution and precipitation of new mineral phases. This is referred to as the water weakening effect of chalk (Risnes et al., 2005; Korsnes et al., 2006, 2008; Megawati et al., 2011). These processes provide extra force to drainage of a field. Geo-mechanical responses related to water weakening of chalk are linked to the composition of present mineralogy and the brine injected where surface-active ions present as Ca^{2+}, Mg^{2+} and SO_4^{2-} may provoke dissolution of calcite and secondary mineral precipitation (Strand et al., 2003; Korsnes et al., 2008). Precipitated magnesite (MgCO₃) is identified in experiments where Mg^{2+} is present in the injected brine (Minde et al., 2018, 2019a, 2019b). NaCl is the major constituent in seawater. Geochemical analysis following laboratory experiments on chalk at 130 °C, has shown that without presence of surface-active ions, precipitation of new mineral phases has not been observed in pure systems (Madland et al., 2011; Megawati et al., 2015). NaCl is therefor expected to be chemically inert to calcite.

An efficient oil and gas production is characterized by a naturally fractured system, with well-connected network which enhances the overall permeability in the reservoir. Prominent oil production from the Ekofisk field is believed to be significantly influenced by the presence of connected fault and fracture networks (Hermansen, 2008; Boersma et al., 2020). The actual basin has experienced a complex geological and tectonic history with extensional and compressional forces, as well as transpression with subsequent fault development. Subsidence was accompanied by several compressive pulses resulting in the inversion of major basement faults with additionally salt movement and finally development of a giant dome. The reservoir has for this reason naturally developed an extensive and well-connected fractured system. Fracture network characterization of the southern Ekofisk field indicated that fractures mainly occur in clusters which concentrated in larger separated zones showing relatively high fracture intensity (Boersma et al., 2020). A naturally fractured system may be distinguished into three distinct geometrically zones, an extensively deformed inner core, an adjacent damaged zone and the surrounding undamaged matrix. The inner core has experienced the highest strain in the fault zone where the porosity is extensively reduced by brittle deformation (Chester et al., 1993). The damage zones exhibit a network of secondary structures including smaller faults, fractures, cleavage, and folds surrounding the fault core and is, together with the core, a distinct hydrogeological unit (Caine et al., 1996). The permeability in the inner core is such diminished that it may act as a barrier (Goddard and Evans, 1995; Caine et al.,

1996). The damage zones comprise anisotropic, yet high permeable fractures and faults along the fault plane, enhancing fluid flow (Paul et al., 2007; Wibberley and Shimamoto, 2003) performed permeability measurements on samples collected from major strike-slip fault zones in the Median Tectonic Line in Mie Prefecture, Southwest Japan. They disclosed that the structural core of the fault had more complicated hydrological behaviours than anticipated using the simplified model of (Caine et al., 1996). They found superior permeability variations and high degree of continuity and connectivity between the low and high permeability zones in the fault core. Reservoir fracture apertures may alter over time during water-injection. Brine-rock interactions can either increase the fracture aperture in carbonates by calcite dissolution, or gradually accumulate cements and diminish pore throats and fracture apertures. By filling small fractures, cement reduces fracture porosity and subsequently permeability (Tokan-Lawal et al., 2014). High effective overburden may over time force matrix into void spaces in fractures and thereby reduce fracture aperture (Bredal et al., 2022a).

We have therefore studied synthetic fracture modification in terms of fracture geometry but most importantly in regard of mineralogical alterations, when the sample was flooded under simulated reservoir conditions at the world-class hydrocarbon deposit of Ekofisk (130 °C and 12 MPa isotropic effective stress) at the Norwegian continental shelf. The sample has been injected by 0.657 M NaCl followed by 0.219 M MgCl₂, in a triaxial cell experiment over 60 days. The different fluid concentrations were selected to mimic the same ionic strength as seawater. The main aim was to record changes from the original fracture aperture and identify different mineral phases within the fracture and adjacent to it. A selection of reference samples was chemically and mineralogically analysed to determine chemical alterations in and adjacent the fracture. We used therefore a variety of different state-of-the-art methods for an in-depth study on tested samples using Focussed-Ion Beam Scanning Electron Microscopy (FIB-SEM) samples in Transmission Electron Microscopy (TEM) and Helium Ion Microscopy combined with Secondary Ion Mass Spectrometry (HIM-SIMS), which have been applied successfully to the extreme fine grained chalk (nano fossils) (Minde et al., 2019a; Bredal et al., 2022b) besides traditional methods which provide basic mineralogical data like whole-rock geochemistry, X-ray Diffraction (XRD) and Scanning Electron Microscopy (SEM) coupled with Energy-dispersive X-ray Spectroscopy (EDS). The study of laboratory modified fracture using complementary methods including high resolution imaging and chemical detection provides insight to precipitation and dissolution caused by specific component in seawater and how it affects fracture modification. The experiment and analytical workflow will provide new paths within research on fractured chalk to enhance the effect of IOR. The data may be utilized in upscaling and modelling of bulk fluid transportation in naturally fractured reservoirs.

2. Experimental setup

The chalk sample studied, was part of a larger experiment with several samples, (Bredal et al., 2022a). The cored samples were drilled parallel from the same block. Reference samples did not have an artificial fracture (Fig. 1a). A 2 mm drill bit was used to produce the fracture in the drilled cores. The size of the fracture measured 2.25 (±0.05) mm in diameter (Fig. 1b) and ran parallel to the flooding direction in the central core.

The experiment has been conducted as described by (Abubeker, 2013; Geitle, 2013; Bredal et al., 2022a). The experiment was carried out in a triaxial cell simulating reservoir conditions at elevated temperature (130 °C) and hydrostatic pressure (12 MPa) while flooding the cores. The triaxial cell is equipped with three high pressure pumps (Gilson Pump - Model 307 HPLC) where two provides axial and confining pressure and the last is a fluid pump to provide brine injection through the core. Axial deformation was measured with a Linear Variable Differential Transformer (LVTD) following the movement of the
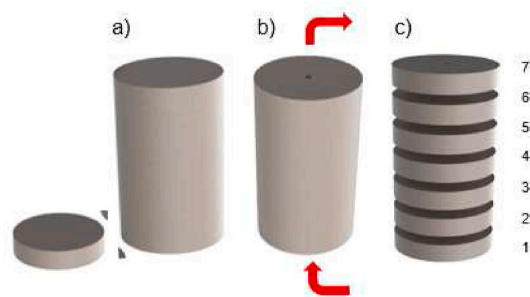
Fig. 1. a) Cylinder illustrating the cored chalk sample. A trim (bottom slice) was removed for reference analysis.; b) an artificial fracture of 2.25 ($\pm$0.05) mm was drilled in the central core with red arrows showing flow direction during flooding; c) the flooded core was cut into seven slices, where the inlet slice is labelled '1' and outlet slice is labelled '7'. The samples are named OBSV 4-AF MgCl$_2$. The number after '#' assigns the slice within the drilled core: OBSV 4-AF MgCl$_2$ #1 indicates the inlet etc (AF = artificial fracture).

piston in contact with the chalk core. The core was flooded at a flow rate corresponding to one pore volume a day based on the original matrix pore volume. Pore pressure was kept constant at 0.7 MPa by using a back-pressure regulator. The triaxial cells were equipped with a Backer 1500W heating Jacket, covering the triaxial cell and a regulating system (Omron E5CN) which allowed a stable test temperature of 130 ($\pm$0.1) °C that was continuously monitored by Pt100 sensor inside the cell. LabView software was used to log all real time data recorded from the experiments. The sample was initially saturated by 0.657 M NaCl during loading and the primary creep phase during the first week. The second phase followed by injection of 0.219 M MgCl$_2$ (Table 1). The total flooding experiment lasted 62 days. Effluent was collected throughout the experiment to supervise ion deviation from the original injected brine. For more detailed description of the experimental procedure the reader is referred to (Abubeker, 2013; Geitle, 2013; Bredal et al., 2022a).

After testing, the sample was dried for 24 h in a heating cabinet and further cut into seven slices from inlet (slice one) to outlet (slice seven) as shown in Fig. 1c. The sample name is OBSV 4-AF MgCl$_2$ (AF = artificial fracture), and OBSV 4-AF MgCl$_2$ #1 indicates the inlet slice until no 7 (Fig. 1c). The size of the artificially fracture aperture was measured using optical light microscopy. The material selected for FIB-SEM, TEM, SEM-EDS and HIM-SIMS were swept in epoxy under vacuum followed by polishing.

3. Methodologies

A selection of various methodologies has been used for the purpose of imaging and identification of chemistry and mineralogy which will complement one another on different scales (see Zimmermann et al., 2022).

3.1. Sample material

Due to limited access to offshore samples, Santonian to Campanian (Schroeder et al., 2006) chalk with comparable characteristics have been collected from the Saint Vaast Formation deposited close to Mons in Belgium. The basal unit, the St-Vaast Formation (pre-Campanian) is followed by the Trivières, Obourg, Nouvelles and the Spiennes Formations (Dusar and Lagrou, 2007). The chalk succession is located in the

southeast of Belgium, a northern extension of the Paris Basin, characterized by extension during the entire Upper Cretaceous (Schroeder et al., 2006). The chalk has been deposited in a deep basin and is composed of fine-grained carbonate dominated by coccolithophores and fragments of those, as well as foraminifer shells and few other nanofossils. The St. Vaast Formation overlies the Maisières Formation, which is a granular, glauconitic green chalk (Robaszynski et al., 2002).

3.2. Axial strain, porosity, and ion chromatography

The original experimental set up is available in (Bredal et al., 2022a) for detailed descriptions of methodologies and calculation for axial strain, porosity and ion chromatography.

3.3. Optical light microscopy

The optical light microscope, Zeiss Stemi DV4 with a maximum magnification of 20 was used to image textural differences and to measure the fracture aperture diameter of the various slices.

3.4. Scanning Electron Microscopy (SEM) energy dispersive X-ray spectroscopy (EDS)

Samples were prepared by sputtering palladium (Pd) in a vacuum chamber to prevent charging on selected fragments of the core. A Zeiss Supra 35-VP FEG-SEM was used for high magnification studies of morphological differences and obtain semi-quantitative elemental composition from a location not smaller than 1 μm^2 by using the Octane Elite EDS detector. Secondary Electron (SE) images were acquired by using Everhart-Thornley detector (EDT) at a fixed working distance of 10 mm, EHT at 15.00 kV and aperture size of 30 μm. A reference sample is selected for SEM-EDS in addition to slice #5 as well as SEM of slice #4.

3.5. Whole-rock geochemistry

Method 1: (LF 200) Approximately 5 g sample material was milled in an agate beaker to a fine mesh. The milled sample was mixed with LiBO$_2$/Li$_2$B$_4$O$_7$ flux in crucibles and fused in a furnace. The cooled bead was dissolved in the American Chemical Society (ACS) grade nitric acid. The geochemical data were then obtained by using Inductively Coupled Plasma-Mass Spectrometry (ICP-MS) at ACME laboratory (Vancouver, Canada). Loss on ignition (LOI) was determined by igniting a sample split then measuring the weight loss after being ignited at 1000 °C for 1 h, then cooled and weighed again. Total Carbon and Sulphur were determined by the LECO® method. Here, induction flux was added to the prepared sample then ignited in an induction furnace. A carrier gas sweeps up released carbon to be measured by adsorption in an infrared spectrometric cell. An additional 14 elements were measured after dilution in Aqua Regia. The prepared sample was digested with a modified Aqua Regia solution of equal parts concentrated HCl, HNO$_3$, and DI-H$_2$O for 1 h in a heating block. The sample volume was increased with dilute HCl-solutions and splits of 0.5 g were analysed. Accuracy and precision are between 2 and 3% per element. Detection limits are found in Table 2. Six additional reference samples were selected for comparison.

Method 2: Major elements for samples <5 g were analysed geochemically by Fusion Inductively Coupled Plasma (FUS-ICP) without detection of LOI was processed at Actlabs (Canada). Precipitated material inside the fracture in slice #1 and #7 were analysed.

3.6. X-ray diffraction (XRD)

Phase analysis was performed using powder X-ray diffractograms recorded on Bruker D8 Endeavor X-Ray diffraction (XRD) with a Lynxeye XE-T detector. The XRD operated at 40 kV and 25 mA during data collection. The diffractograms were recorded between 5° and 70° two-

Table 1
Ion concentration of the brine used in the experiment. *Ions not present.

Brine/Mol/L	Cl$^-$	Na$^+$	Mg^{2+}
MgCl$_2$	0.438	*	0.219
NaCl	0.657	0.657	*

Table 2
Data set for porosity, strain and test duration on the selected sample for the synthetic fracture.

Sample	Porosity [%]		Strain [%]					Duration [Days]
	1. Pre-test	Post-test	Loading	Creep 1	Creep 2	Total	2.	
OBSV 4 AF-MgCl₂	40.49	37.95	0.81	1.25	1.35	3.41		60

Theta at a step size of 0.015° two-Theta at a time step of 0.5 s. ICDD PDF-4+ - database was available (Powder Diffraction Files). MDI Jade Pro – software was used for interpretation. Slice #3 was selected for XRD analysis.

3.7. Helium Ion Microscopy – Secondary Ion Mass Spectrometry (HIM-SIMS)

A Zeiss ORION NanoFab Helium Ion Microscope (HIM) with add-on Secondary Ion Mass Spectrometry (SIMS) (Wirtz et al., 2019) at Luxembourg Institute of Science and Technology (LIST) was used for high-resolution SE-HIM imaging and chemical identification on polished chalk samples. The sample was coated with 5 nm gold (Au) to create electrical conductivity surface. In a Gas Field Ion Source (GFIS), a 25 keV helium ion source was first used to obtain secondary electron (SE) image of the region of interest (ROI). The SE detection was done with an ETD detector with a primary beam-current at 2 pA. A neon source at 3 pA was subsequently applied through the GFIS of the HIM and allowed sputtering of the sample surface and then the emission of secondary ions. The SIMS run positive and negative modes separately. A magnetic sector with separate detectors collected single ions according to their mass. Each element was assigned a colour map that represented the surface chemical distribution. A subsequent procedure involving Fiji software, enabled images of the combined information of the SE-HIM with the assigned chemical distribution obtained by SIMS. A polished section of #5 was selected for HIM-SIMS analysis.

3.8. Transmission Electron Microscopy (TEM) and energy dispersive X-ray spectroscopy (EDS)

Further studies of the microstructure and phase identification of sample material from #5 were performed using Transmission Electron Microscopy (TEM), JEOL-2100 (LaB6 filament, JEOL) operating at 200 kV. The TEM is equipped with EDAX energy dispersive X-ray Spectroscopy (EDS) for elemental analysis, bright-field and dark-field detectors for Scanning TEM (STEM) mode. Samples were prepared by FIB-SEM processes as described above. The lattice (d-) spacing of the diffraction spots were measured using RADIUS software based on calibrated system. The measured d-spacing for spots of the diffraction pattern were compared with known values obtained from crystal structure database, AMCSD (Oh et al., 1973). The diffraction pattern was indexed with JEMS software [JEMS] using crystal structure data (Oh et al., 1973).

4. Results

4.1. Ion chromatography (IC) and axial strain rate

The Ion chromatography results show no significant deviation from the original ion concentration of the injected brine during loading and the primary week of creep (Creep 1) when the core was injected by NaCl (Fig. 2). Reduction of Na⁺ and Cl⁻ concentrations were observed when MgCl₂ was injected after the first week (Creep 2). Five days later, Cl⁻ reached original levels. Na⁺ decreased during nine days and oscillated around original values of 0.01 M (showed a minute production of 0.005
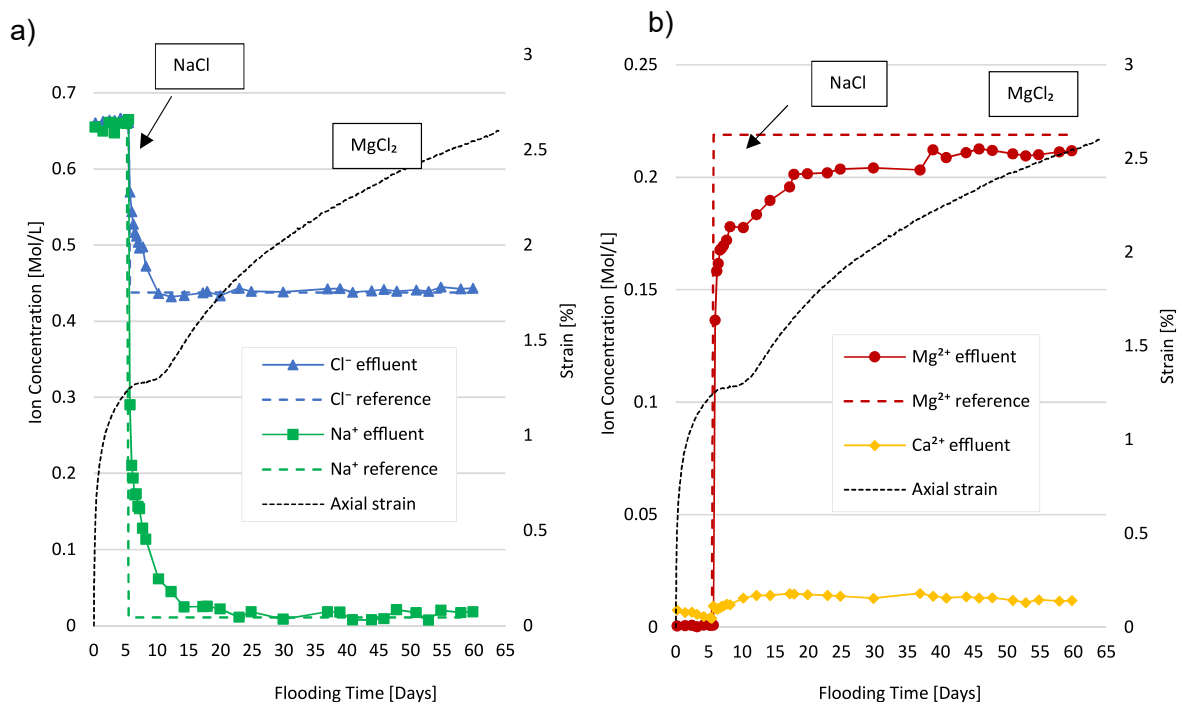
Fig. 2. Ion detection of major elements using ion-chromatography in OBSV 4 AF-MgCl₂ flooded with NaCl during the initial week (Creep 1) followed by MgCl₂ injection in the last test phase (Creep 2). a) Na⁺ and Cl⁻ versus strain. b) Mg²⁺ and Ca²⁺ versus strain for the same time duration (second y-axis).

M averagely). Mg^{2+} experienced an instant breakthrough, gradually increasing for two weeks until it stagnates and finally stabilizes after three weeks of $MgCl_2$ injection at a loss of 0.01 M Ca^{2+} production was observed instantly when $MgCl_2$ was injected. It reached the maximum production of 0.015 M after five days of flooding $MgCl_2$ and gradually decreased the production after day 40. The initial strain rate gradually reduced over the first week and was not instantly affected by the brine change from NaCl to $MgCl_2$. An increase in the compaction rate, was, however, observed five days after the brine change, while Cl^- reached original levels.

4.2. Porosity and geo-mechanical data

Porosity measurements were performed both, pre- and post-experimental (Table 2). Pre-test porosity measured 40.49% (the average sample in the original experiment was 40.83 ($\pm$1.38) %; (Bredal et al., 2022a). The porosity was reduced by 2.54% (from 40.49% to 37.95%) during the experiment. Unfractured reference samples showed permeability of about 0.56 ($\pm$0.09) mD (Bredal et al., 2022a).

4.3. Optical light microscopy and fracture size

The unflooded artificial fracture aperture (Fig. 3a) in OBSV 4 AF-$MgCl_2$ measured a diameter of 2.25 ($\pm$0.05) mm. After the flooding experiment, all slices showed a reduced fracture aperture (Table 3). The reduction was most prominent for slice three, opposed to the second slice which was least effected. The aperture diameter reduced averagely throughout the core by 77%.

The wet dismantled inlet showed a concentric circle in the fracture which appeared less grey than the surrounding matrix (Fig. 3b). The inner concentric white circle detached from the matrix when the sample has been dried (Fig. 3c). The precipitated material showed uneven

Table 3
Aperture measurements presented in % reductions throughout the core of OBSV 4 AF-$MgCl_2$ for slices one to six (data not available for slice seven). The final apertures are non-uniform and the reduction in % is an average. The original aperture diameter measured 2.25 ($\pm$0.05) mm. The middle part of the core experienced the most prominent reduction of fracture aperture. *Data not available.

Slice number	1	2	3	4	5	6	7
Aperture diameter reduction [%]	67	62	89	84	80	80	*

distribution along the fracture wall (Fig. 3d). Matrix adjacent to the hollow cylinder was more infiltrated by epoxy compared to peripheral parts of the slices (Fig. 3e), thus holding a higher permeability nearby fracture compared to the otherwise low permeable matrix. The sample distributed various degree of epoxy penetration, which reflects distinct permeability (Fig. 3f).

4.4. X-ray diffraction

XRD measurements of the fracture fill of OBSV 4 AF-$MgCl_2$ #3 (Fig. 4) show dominance of magnesite. Calcite exists only in traces. Illite, halloysite (kaolinite-serpentine group) and lizardite (serpentine group) are identified, yet at very low counts.

4.5. Whole rock geochemistry

The most abundant elements, except CaO, for the unflooded inlet (U. I) of OBSV4-U.I were SiO_2 (3.32 wt%, where wt.% stands for weight percent), followed by Al_2O_3 (0.97 wt%), Fe_2O_3 (0.34 wt%) and K_2O (0.22 wt%). Comparable data was obtained from unflooded reference samples (Table 4). A homogeneous distribution of not more than a maximum of
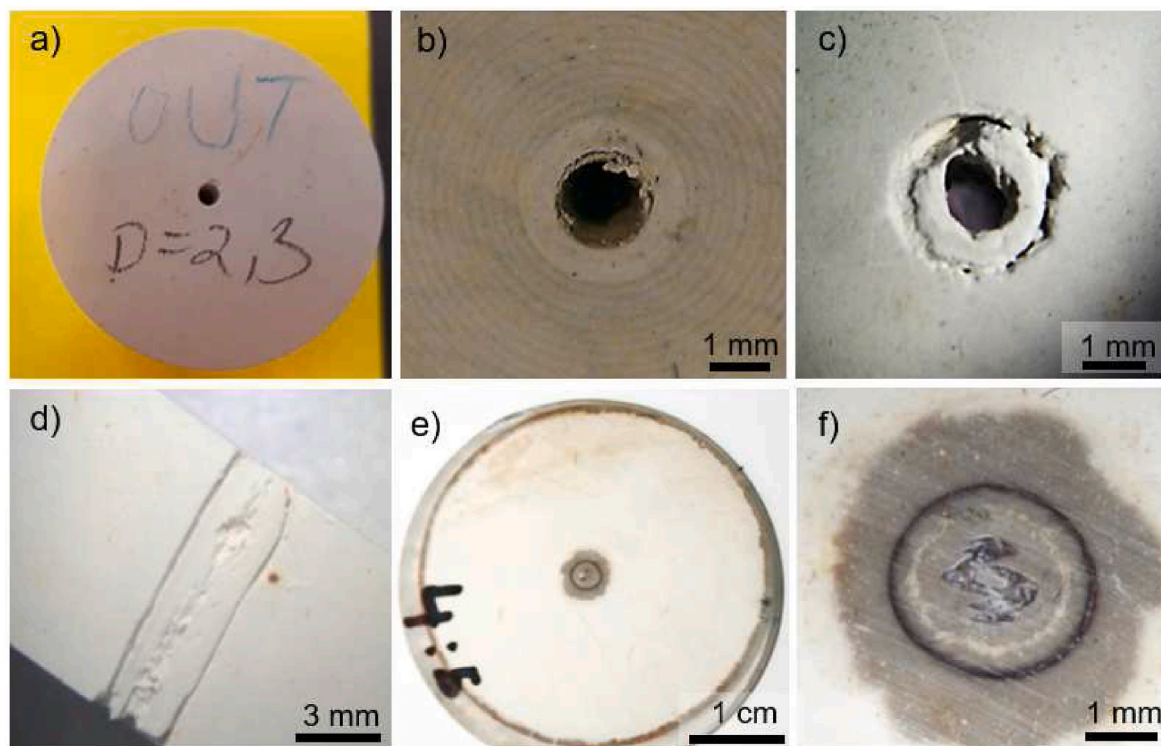
Fig. 3. a) an artificial fracture of 2.25 ($\pm$0.05) mm was drilled to imitate a natural fracture (unflooded sample); b) OBSV 4 AF-$MgCl_2$ #1 in a wet condition after dismantelling from the triaxial cell with a concentric inner circle appears cleaner than the surrounding matrix; c) fracture fill detached from matrix OBSV 4 AF-$MgCl_2$ #1 in dry condition; d) OBSV 4 AF-$MgCl_2$ #1 cut parallel to flood direction distributes heterogenous distribution of fracture-fill; e) OBSV 4 AF-$MgCl_2$ #5 perpendicular to flood direction with darker areas in central and peripheral parts (penetrated by epoxy); f) high magnification of the fracture fill shown in e). The darker grey locations have been swept by epoxy. White locations have lower permeability and not infiltrated by epoxy.
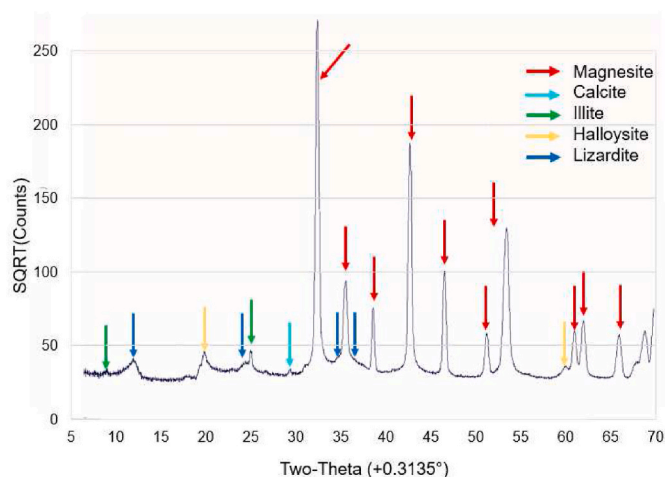
Fig. 4. Mineral identification of fracture fill in OBSV 4 AF-MgCl₂ #3 by XRD.

5 wt% of non-carbonate minerals for the entire chalk was assessed. Other elements show low concentrations and are not relevant for the current study. Two samples of fracture fill were analysed for bulk geochemistry of major and minor elements (Table 4). Interestingly, the fracture fill contains SiO_2 as high as 8.77 and 4.96 wt% for sample OBSV 4 AF-MgCl₂ #1 -fracture fill and OBSV 4 AF-MgCl₂ #7 -fracture fill respectively. This is significantly higher concentration compared to unflooded chalk ranging between 3.32 and 3.58 wt% (Table 4). Similar trends can be observed for Al_2O_3 and partly for Fe_2O_3. The K_2O value in the fracture fill samples showed 0.16/0.24 wt% for OBSV 4 AF-MgCl₂ #1 -fracture fill and OBSV 4 AF-MgCl₂ #7 -fracture fill respectively and is comparable to the reference value of 0.23 wt%. However, the concentration of MgO is dominant (up to 40 wt%) and CaO is depleted to less than 4.2 and 2.0 wt%, respectively, for the two sliced samples (Table 4).

4.5.1. Scanning Electron Microscopy and energy dispersive X-ray spectroscopy (SEM-EDS)

The unflooded carbonate material is, as in most chalks (Hjuler and Fabricius, 2009; Andersen et al., 2018) dominated by fragments with grain sizes down to 0.5 μm. Non-carbonate minerals are only accessory, glauconite (Fig. 5a) alkali feldspar (Fig. 5b) and iron-oxides as pyrite (Fig. 5c). The appearance of pyrite varied from intact spheroidal shaped clusters with high sulphur-iron ratio to framboidal grains. Authigenic clay minerals were also observed as single "platy" units or as coating on coccolith grains (Bredal et al., 2022b). These minerals were interpreted, based on EDS and XRD data, as illite (Fig. 5d).

SEM combined with EDS analysis provide detailed information of the

size, shape and composition of newly precipitated grains inside the fracture. The surface of the fracture fill did not display distinct crystal features (Fig. 6 a-c) and its concentration is dominated by Mg, C and O. Rhombohedral grains of various sizes, ranging from 0.5 to 3 μm were observed in the mid fracture fill (Fig. 6 e-h) and interpreted as magnesite crystals. A clustered sheet-like mineral (Fig. 6 i-k) was frequently observed on the peripheral part of the fracture fill adjacent to the matrix.

An EDS mapping of the fracture fill and adjacent matrix were acquired on the polished surface of OBSV 4 AF-MgCl₂ #5 (Fig. 7). The image shows that the matrix is dominated by Ca (turquoise), whereas the fracture fill by Mg (red). However, a few, but scattered, areas with high abundance of Ca can be observed in the fracture fill. The central part of the fracture fill is organized by bridge-like structures that has been connecting peripheral parts of the fill.

A SEM-EDS line scan disclosed the transition from differently chemically composed zones in the surrounding fracture fill area (Fig. 8). Four different zones were determined based on chemical concentrations and distribution (Fig. 8): (i) matrix, (ii) a separate transition zone (1 mm) which is located between matrix and the near zone, (iii) a 'near zone' adjacent to the fracture and (iv) the fracture precipitate itself. The matrix exhibited the highest Ca concentration (EDS-counts) which are reduced remarkably towards the transition zone (Fig. 8a). The enrichment of Mg (33%) and Si (21%) (Fig. 8a) is high in the near zone compared to the matrix. The Ca content decreased significantly in the defined near zone (0.2 mm) and was outweighed by Mg abundances. The highest abundance of Mg was however in the central fill with slightly lower accumulation in the peripheral parts of the fill. Si accumulated more noticeably in the peripheral fracture fill than in the central precipitation fill. C and O are identified in the physical gap between matrix and fracture fill which are linked to the composition of epoxy ($C_{21}H_{25}(Cl)O_5$).

4.6. Helium Ion Microscopy – Secondary Ion Mass Spectrometry

To overcome the challenges of insufficient spatial resolution of SEM-EDS for chemical identification, further analysis by HIM-SIMS was performed on a polished thin section of OBSV 4 AF-MgCl₂ #5. A ROI of 20×20 μm² was studied to determine chemical compositions of present minerals (Fig. 9a). Elements are presented individually. $^{12}C^+$, $^{16}O^-$, $^{24}Mg^+$, ^{12}C, $^{27}Al^+$, and $^{28}Si^+$ (Fig. 9b, c, d, e f and g). $^{40}Ca^+$ showed inhomogeneous distribution (Fig. 9h) with highest accumulation in isolated particles (e.g., objects resembling coccoliths). The major distribution of calcium is present with lower counts and coincides with the distribution of $^{12}C^-$.Several elements are overlain in one single colour map to mimic potential mineral phases. $^{12}C^-$, $^{16}O^-$ and $^{24}Mg^+$ are combined and represent the presence of magnesite ($MgCO_3$) (Fig. 9i). $^{27}Al^+$ and $^{28}Si^+$ occur at corresponding locations and represent a clay

Table 4
Geochemistry of major elements of studied samples. LOI = loss on ignition, not available for fracture fill samples due to very small sample quantities. *Data not available/acquired.

| Elements/ Samples	SiO₂ wt. %	Al₂O₃ wt. %	Fe₂O₃ wt. %	MgO wt. %	CaO wt. %	Na₂O wt. %	K₂O wt. %	TiO₂ wt. %	P₂O₅ wt. %	LOI wt. %	Sum wt. %
Method 1											
Detection limit	0.01	0.01	0.04	0.01	0.01	0.01	0.01	0.01	0.01		
OBSV 4-U.I	3.32	0.97	0.34	0.29	52.06	0.04	0.22	0.04	0.06	42.50	99.84
OBSV 12-U.I	3.58	1.05	0.40	0.28	51.89	0.04	0.24	0.05	0.06	42.20	99.79
OBSV 18-U.I	3.39	1.00	0.54	0.27	51.90	0.04	0.22	0.05	0.10	42.30	99.81
OBSV 9-U.I	3.44	1.01	0.39	0.29	51.97	0.04	0.22	0.05	0.10	42.30	99.81
OBSV 6-U.I	3.38	1.00	0.34	0.28	52.29	0.04	0.22	0.05	0.06	42.20	99.86
OBSV 6-U.O	3.40	1.03	0.33	0.30	51.89	0.04	0.23	0.05	0.09	42.50	99.86
Method 2											
Detection limit	0.01	0.01	0.01	0.01	0.01	0.01	0.01	0.00	0.01		
OBSV 4 AF-MgCl₂ #1- fracture fill	8.77	1.55	0.77	41.05	1.95	<0.01	0.24	0.07	0.12	*	54.52
OBSV 4 AF-MgCl₂ #7-fracture fill	4.96	1.14	0.44	42.68	4.11	<0.01	0.16	0.05	0.10	*	53.64
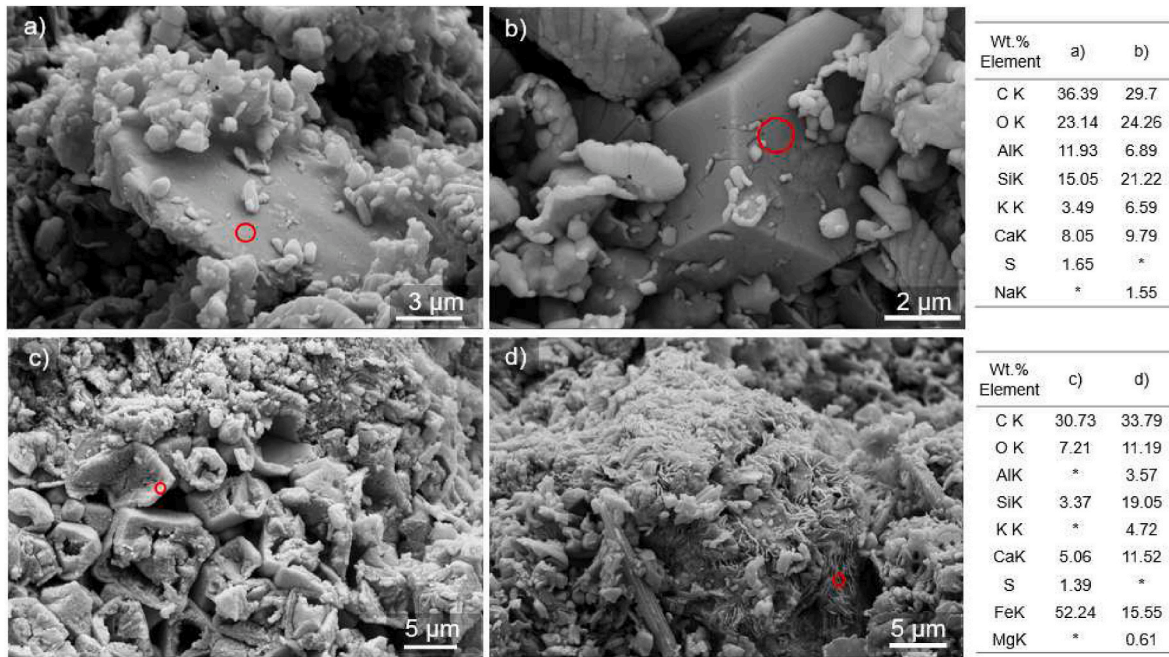
Fig. 5. SE-SEM image of one of the reference samples (OBSV 18-U.I see Table 4) combined with EDS analysis were aquired from a red circle (spotsize 1 μm). a) Glauconite or phlogopite/biotite; b) alkali-feldspar (microline/orthoclase); c) mix of pyrite, calcite and quartz because of spotsize limitation) and d) illite on a calcite grain.
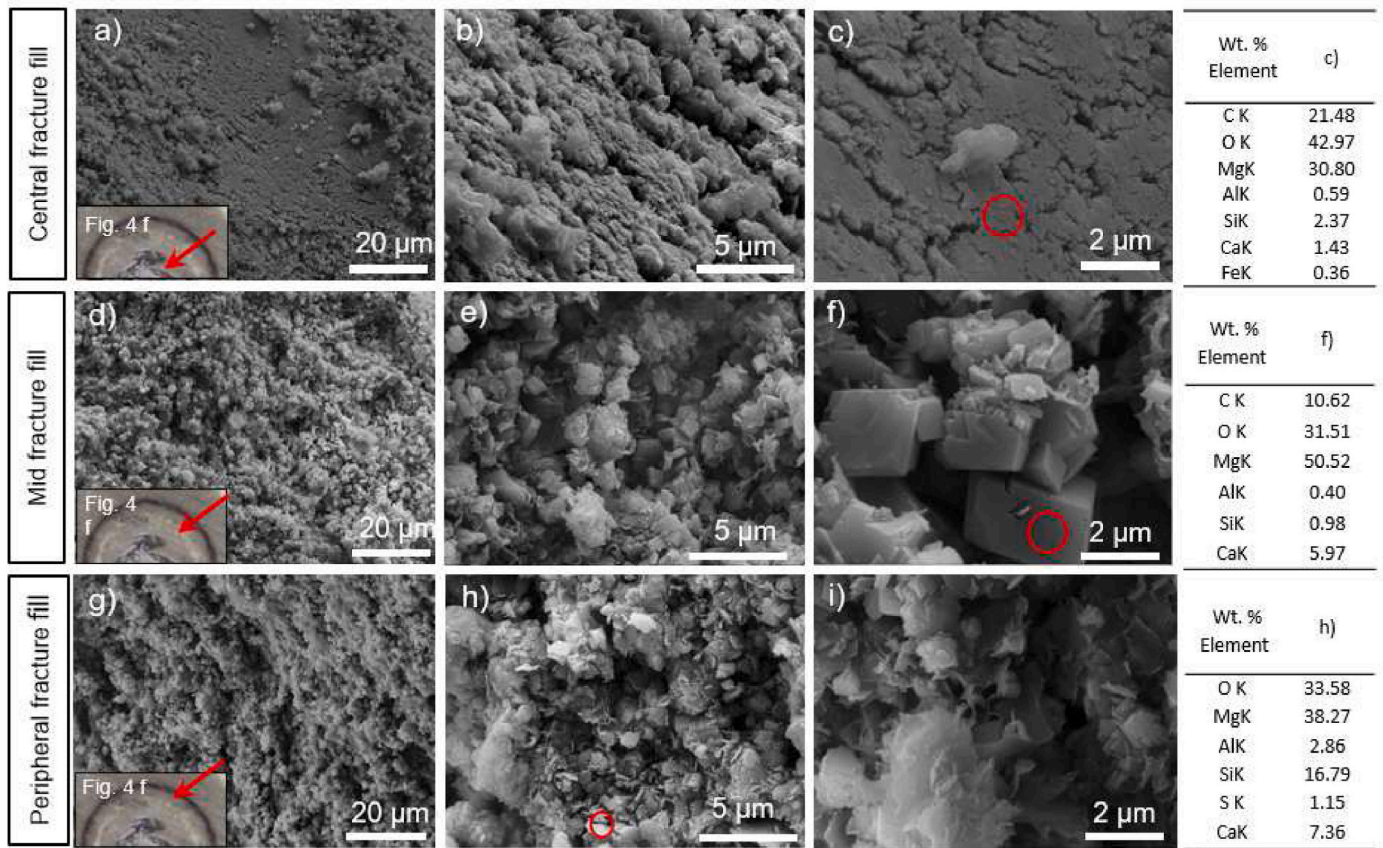

Fig. 6. SEM and EDS acquisitions of OBSV 4 AF-MgCl₂ #4 at three different locations of the fracture fill (see Fig. 3f) marked by red arrows: a-c) central fracture fill; d-f) mid fracture fill with rhombohedral shaped mineral precipitated in the mid fracture fill, shows a relative pure concentration of Mg with traces of Ca acquired in f); g-i) peripheral fracture fill adjacent matrix showing a platy shaped mineral showing abundances of Mg, Si and Ca (see Fig. 3f for location).
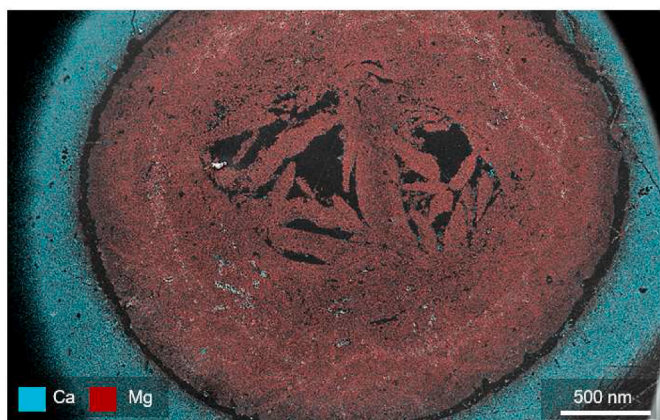
Fig. 7. SEM-EDS map of the fracture fill and adjacent matrix of OBSV 4 AF-MgCl₂ #5 showing only Ca and Mg and black areas are pores.

mineral (Fig. 9j). A combined image of MgCO₃ and the clay (²⁷Al⁺ and ²⁸Si⁺ allocation) (Fig. 9k) demonstrates that the clay (²⁷Al⁺ and ²⁸Si⁺ allocation) essentially surrounds the MgCO₃ and bridges. Fig. 9l illustrates that ⁴⁰Ca⁺⁻ and ¹²C⁻ appears in porous spaces (epoxy (C₂₁H₂(Cl)O₅)) as relocated calcite particles with low ⁴⁰Ca⁺ counts of (mixed with epoxy).

4.7. Transmission Electron Microscopy and energy dispersive X-ray spectroscopy

The sample for observation with TEM was prepared using FIB-SEM from the peripheral part of the fracture fill, located approximately at the border between fracture fill and original matrix (OBSV 4 AF-MgCl₂ #5: see Methodology). The sample is composed of very small particles, often below one micron (Fig. 10) surrounded by epoxy (C and O). Two mineral groups were identified based on shape and chemical composition. A clay mineral was identified based on the appearance of thin sheetlike bands with dark appearance (possibly different densities). The corresponding elements are Si, Al, Mg, Fe, Na, C, and O in various

quantities and traces of K (measurements 1–6; Fig. 10). The second mineral was rhombohedral shaped crystals (Fig. 11a) with various amounts of Mg, C and O, identified as magnesite (measurements 7–12 Fig. 10). The sizes of single magnesite crystals range between 200 and 800 nm and are occasionally observed surrounded by clay minerals.

A more detailed approach to the two different minerals in Fig. 10 with TEM, confirmed different crystallographic structures (Fig. 11). Fig. 11a shows a rhombohedral shaped crystal structure (1), revealed as magnesite according to the diffraction presented in (Fig. 11c) and confirmed by EDS data (Fig. 11d - column 1). The micro-graphed clay mineral showed the typically black sheetlike band in the centre surrounded by grey substances (Fig. 11b). The table (Fig. 11d) distributes the elemental composition acquired from the black (2) and grey areas (3) (Fig. 11b). The grey area (3) distributed higher concentration of C compared to the black area (2), while the ratio of the remaining elements was relative stable. As C and O are related to epoxy filling void spaces this reflects a higher density of clay elements in darker locations.

Magnesite belongs to a space group of R-3c, and has a trigonal crystal structure with hexagonal axis (a = 4.637 Å, c = 15.023 Å) (Oh et al., 1973). The selected area diffraction pattern (SADP) shown in Fig. 11c, is indexed to [110] zone axis. The reflections from the planes corresponding to the diffraction spots are given in Table 5. The measured d-spacing of magnesite (Table 5) for the ROI analysed areas of the diffraction pattern shown in Fig. 11c are very closely matching the values reported in the literature (AMCSD) (Oh et al., 1973). The TEM analysis thus reveals the presence of magnesite phase and confirms the results obtained by EDS and XRD analysis.

5. Discussion

5.1. Mechanical processes and reduced fracture aperture

During loading and the initial week under NaCl injection (Creep 1) for the previously described IOR experiment, the sample experienced compaction where axial and radial strain caused matrix into void space hence reduced the artificially aperture diameter (Bredal et al., 2022a). A reference sample (flooded with NaCl throughout the experiment) and OBSV 4 AF-MgCl₂ showed similar compactional behaviour until Creep 2;
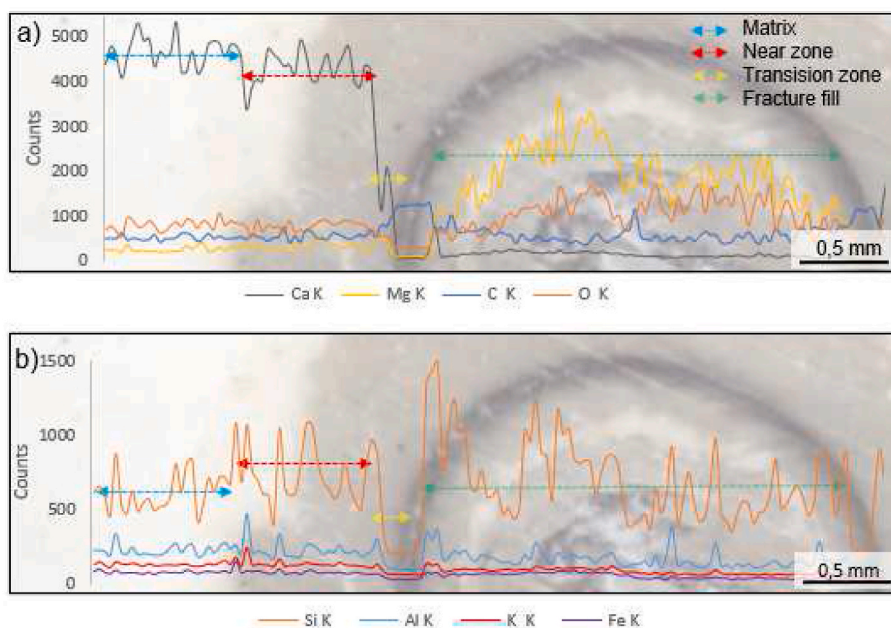

Fig. 8. SEM-EDS line scan acquired from OBSV 4 AF-MgCl₂ #5 through the adjacent matrix (blue arrow), a transition zone (red arrow) a near zone (yellow arrow) and the fracture itself, marked by the green arrow. a) Major elements show distribution of Ca, Mg, C and O within the different zones; b) Si distributed higher abundance in the peripheral parts of the fracture fill and adjacent zones.
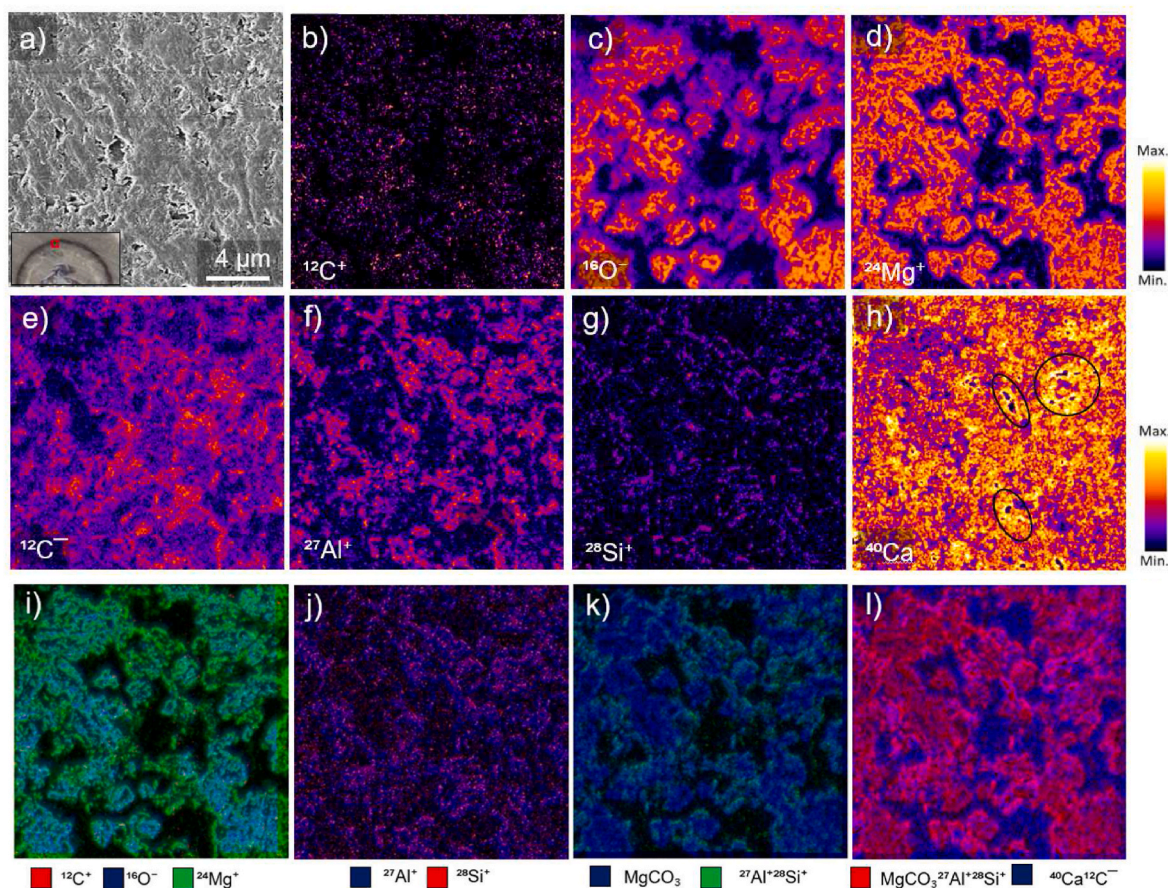
Fig. 9. HIM-SIMS analysis of OBSV 4 AF-MgCl₂ #5. A SE-HIM image with its respective chemical identification obtained by SIMS. a) The SE-HIM image of a polished surface sample of the studied area; b - h) elemental distribution of single elements obtained by SIMS and presented in colour maps; h) inhomogeneous distribution of $^{40}Ca^+$ (see text for detailed description). A few locations are marked with black circles highlighting coccolith particles (removed from matrix); i) magnesite ($MgCO_3$); j) distribution of $^{28}Si^+$ and $^{27}Al^+$ points to a silicate phase (clay); k) combined distribution of the silicate phase associated with magnesite crystals; l) magnesite and silicate phases combined with distribution of $^{40}Ca^+$ and $^{12}C^-$. $^{40}Ca^+$ and $^{12}C^-$ occupy porous space (mixed with epoxy and linked to adsorbed surface ions).
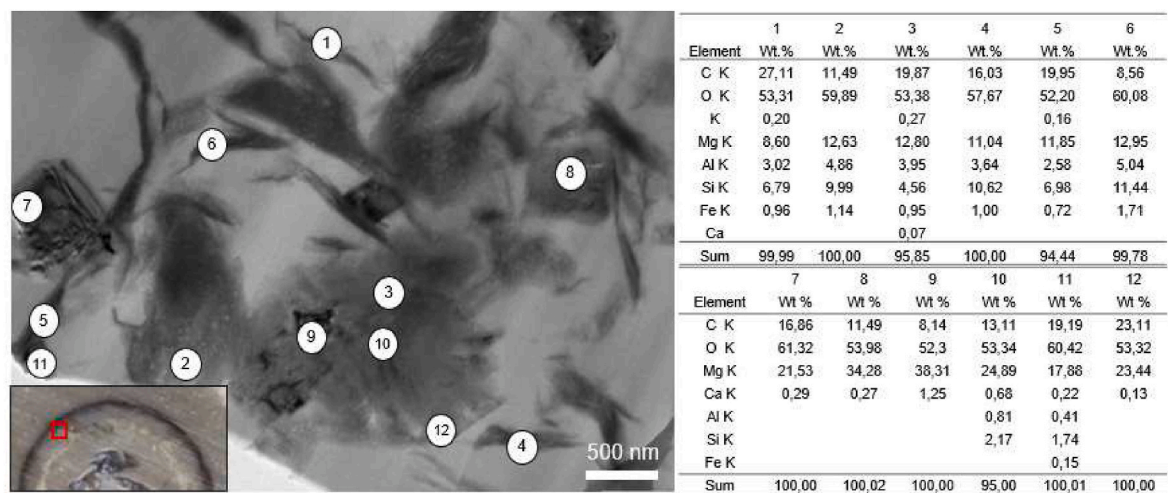
Fig. 10. TEM-EDS analysis of a FIB-SEM sample (OBSV 4 AF-MgCl₂ #5) detected basically two different minerals which were identified based on their texture and composition. Mineral 1–6 is interpreted as clay with occasionally platy shapes (various amounts of C and O are linked to the surrounding epoxy). Dark and/or rhombohedral shaped minerals 7–12, are identified as magnesites.

as the brine was switched from NaCl to MgCl₂ for OBSV 4 AF-MgCl₂ (Bredal et al., 2022a). It is therefore possible that the fracture aperture was already narrowed for OBSV 4 AF-MgCl₂ when MgCl₂ was injected and chemical processes commenced. Additional water weakening was observed during Creep 2. Furthermore, it is likely that increased compaction processes may have continued forcing matrix into the void space, hence narrowing the fracture aperture.
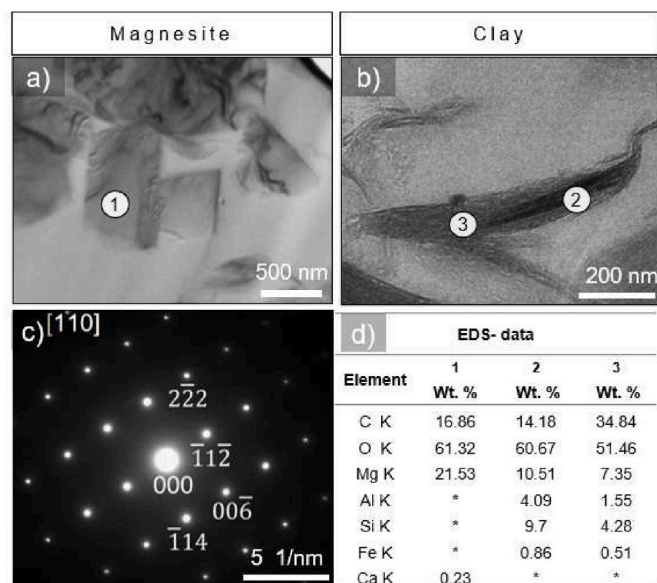
Fig. 11. High resolution TEM studies on two minerals extracted from the fracture fill of OBSV 4 AF-MgCl₂ #5 adjacent matrix and identified by crystallographic pattern and/or chemical composition. a) Brightfield image of a rombohedral mineral (1); b) bright field image of clay mineral presenting dark sheets in the central part surrounded by brighter grey matrix; location of aquired EDS point from a central dark area (1) and the surrounding grey area (2); c) well developed crystallographic diffraction pattern aquired in (1); d) EDS data for location (1–3); e) d-spacing of diffraction pattern shown in c) of sheet-like Si-Al rich phases.

Table 5
d-spacing of diffraction pattern shown in Fig. 12c of sheet-like, dark Si-Al rich phases.

Measured (Å)	Ref []	hkl
3.56	–	112
2.77	2.742	114
2.51	2.503	006
1.95	1.939	222
1.7	1.7	118

5.2. Calcium dissolution and temporary fracture widening

Despite an overall final reduction of the fracture aperture, it is likely that the sample experienced temporary incremental widening. The detached fracture fill measures approximately 2.8 mm in diameter, although the original drilled fracture diameter measured only 2.25 ($\pm$ 0.05) mm. Furthermore it is dominated by magnesite with some clay and holds only minute amounts of calcite, despite a process of matrix being forced into the void space during creep caused by hydrostatic pressure (Bredal et al., 2022a). This may indicate that the fracture experienced dissolution of calcite dominantly along fracture walls during injection of MgCl₂ in addition to calcite dissolution in adjacent zones. The zone surrounding the fracture showed a lower Ca density and increased Si values (Fig. 9). The adjacent zone is also penetrated by epoxy, demonstrating locally higher permeability compared to the matrix (Fig. 4eandf). This supports a pronounced mineralogical dissolution adjacent to the fracture compared to the matrix which experienced a delayed transportation of injected fluid to peripheral matrix locations. The instant, yet relatively weak increase of Ca^{2+} in the effluent (Fig. 3) when MgCl₂ was injected, suggests that CaCO₃ dissolution primarily takes place along the fractured wall as often observed during IOR experiments (Andersen et al., 2018). This experiment showed a significantly lower fraction of Ca^{2+} in effluent compared with a reference test

with the identical test conditions, but without a fracture (Bredal et al., 2022a). This reinforce that dissolution is scarcely present in the matrix and the injected brine is mainly transported through a fracture which operates as a 'highway'.

5.3. Precipitation of magnesite and fracture aperture reduction

The instant loss of Mg^{2+} in the effluent was possibly related to MgCl₂ replacing free Na^+ in the pore volume and Na^+ adsorbed on the calcite surface through ion-exchange (Fig. 3). A simultaneous reduction of Cl^- concentration is observed in the effluent. A fraction of the Mg^{2+} loss is related to an instant precipitation of magnesite (MgCO₃) which is often linked to the production of Ca^{2+} in the effluent (e.g. Andersen et al., 2018). Cl^- reached its original concentration five days after brine changed. This may indicate that the injected fluid (MgCl₂) had completely displaced NaCl that preoccupied the pores and surfaces (Fig. 3). After five days, the creep curve experienced a boost which indicated initiation of enhanced water weakening and reinforced that MgCl₂ had reached peripheral parts of the matrix (Bredal et al., 2022a). Precipitation of magnesite (MgCO₃) was dominantly employed in the fracture where the main fluid transportation took place. The detached fracture fill is identified as magnesite by XRD measurements (Fig. 5). Magnesite crystals ranged in sizes from 0.5 to 5 μm depending on the location of precipitation. The largest minerals could be recognized in mid-fracture fill (Fig. 7f) and the smallest in the adjacent matrix (Fig. 12a). Various sizes of magnesite may indicate different onset of crystallization or reflect different conditions (e.g., pore space, fluid composition, etc.) for precipitation. As the largest crystals were identified in the mid fracture fill, it is likely that the primary magnesite crystals precipitated out of solution. In addition, they have not been limited by available space (at initial phase) which allowed crystal growth to a larger scale. Magnesite crystals located at the rim of the fracture fill are smaller in size and may indicate precipitation at a later stage in the flooding experiment compared to larger central crystals and could be influenced by less space and a different composition of the fluid. Moreover, surface charge may also affect growth of grains and control final sizes. Additionally, the smaller sizes may also reflect space limitations. This hypothesis coincides with the expected incremental calcite dissolution at fracture walls subsequently being replaced by magnesite precipitation. Precipitates in sedimentary rocks are commonly found in localized cement deposits (bridges) in otherwise open fractures (Gale et al., 2010). If fractures become wide enough (2 mm), the cement does not span fracture widths between aperture increments and bridges will be absent (Hooker et al., 2012). In this experiment, after a certain level of precipitation, the favoured location of accumulation was along fracture walls. Minde et al. (2019a) observed transformation from calcite to magnesite in a long-term flooding experiment over several years on outcrop-chalk from Liège (Belgium, injected by 0.219 M MgCl₂ under reservoir conditions). The finding demonstrated that the transformation was related to alteration processes driven by dissolution with subsequent precipitation and not by solid-state diffusion. This is evidenced in slice one (OBSV 4 AF-MgCl₂ #1) with precipitation alongside the fracture wall and absence of bridges. After a certain reduction of the aperture, the bridges have developed further towards the outlet (OBSV 4-AF MgCl₂ #5) and can be shown in Figs. 4 and 8. The inlet slice showed, however, no bridges (Fig. 4b). Fracture closure tends to bridge at fracture diameters measuring 1 mm or smaller only. A crucial factor directing precipitation and bridging may be the velocity of fluid transport. However, the ability and realisation of cement growth is obviously depending on a variety of preconditions. In particular, as we have shown in this study a rather rapid and complete growth has taken place and diminished the fracture aperture. This aspect may be the utmost important for IOR deliveries in fractured reservoirs.

5.4. Clay minerals in fracture fill and near fracture locations

Detrital and/or authigenic minerals (Fig. 6) in matrix have possibly dissolved and re-precipitated in the fracture void indicated by the higher concentration of SiO_2, Al_2O_3 and Fe_2O_3 in the fracture fill shown in Table 2. The observed clay minerals exhibit platy shapes (Fig. 7h and i) and relatively uniform composition which is dominated by magnesium (Fig. 11). The clay texturally and chemically resemble the magnesium rich end member of chlorite, which is clinochlore $(Mg,Fe^{2+})_5Al_2Si_3O_{10}$ $(OH)_8$. Another possibility could be illite (XRD), but potassium was not detected in significant amounts in clays as measured by TEM-EDS (Fig. 11). The low chemical concentrations within these clay minerals in the fracture fill hampers an exact determination of the mineral phase.

5.5. The source of clays

Magnesite crystals were identified in the fracture frequently surrounded by clays observed by HIM-SIMS (Fig. 10) and TEM (Fig. 11). The observation suggests that magnesite precipitated first, followed by precipitation of clay. Precipitation of clay may also have contributed to the bridging process observed by HIM-SIMS where ^{27}Al and ^{28}Si phase were found surrounding and connecting magnesite crystals (Fig. 10k). Firstly, this implies a certain mobility of silica and aluminium within the chalk during the experiment. The highest concentration of SiO_2 was identified in peripheral parts of the fracture fill in addition to increased quantities in the transition and near zones adjacent to the fracture fill (Figs. 7h and 9). This enhanced fraction of silicate in the surrounding matrix (Fig. 9b), may simply be a result of amplified calcite dissolution. The ratio of SiO_2/Al_2O_3 and SiO_2/Fe_2O_3 is higher in the fracture fill versus unflooded matrix samples (Table 4) which indicates mobility of silicate. Minde et al. (2018) studied Aalborg chalk samples tested under reservoir conditions with $MgCl_2$. They found traces of Si^{4+} in the effluent obtained by inductively coupled plasma-optical emission spectrometry (ICP-OES). The unflooded Alborg samples were Opal CT bearing and after subsequent fluid injection they found dissolved Opal-CT and precipitated flaky Si-Mg bearing minerals confirmed by FEG-SEM. However, at this stage, dissolution of minerals in matrix and precipitation in void spaces are not more than a working hypothesis as thorough studies with a large range of datasets are necessary to confirm these processes. Nevertheless, as the injected fluids were devoid of silicon and aluminium, the discovered clay minerals in the fracture fill were necessarily related to the original minerals in the chalk matrix. This in turn indicates a mineralogical change of the matrix which leaves room for further studies in regard of wettability and hydrocarbon release.

5.6. Cementing and fracture sealing followed by altered fluid behaviours in chalk reservoir

Gale et al. (2010) suggested that the sealing process in dolostone during fracture growth can act as competing forces between rates of fracture aperture opening and syn-kinematic cement precipitation. Similarly, in this experiment $MgCl_2$ injection is linked with primarily dissolution of fracture walls and adjacent matrix concurrently with magnesite precipitation in the fracture void space. Moreover, the continuous compaction of the reservoir during injection under high temperature and pressure can enhance the reduction of aperture by forcing matrix into the fracture (Bredal et al., 2022a). Aperture reducing processes are dependent on several factors such as temperature, kinetics and chemical composition of the brine and matrix. The fracture size, the fracture network and the nature of the secondary minerals growing in the fracture fill are also determining factors. Dissolution and precipitation processes identified here was caused by injection of $MgCl_2$. Injection of seawater may develop differently in the reservoir as the concentration of reactive Mg^{2+} is lower. A similar process was observed with synthetic seawater (SSW) injection (Bredal et al., 2022a) which could be expected to arise also in the reservoir (Kallesten et al., 2021). Compaction and cementing may cause clogging of minor fractures and reduce fracture connectivity, hence force injected seawater into matrix. Seawater transportation into matrix will alter wettability and release previously captured hydrocarbons and increase the recovery rate.

6. Conclusions

The two-month lab experiment on artificially fractured Upper Cretaceous outcrop chalk, flooded with NaCl followed by $MgCl_2$ under reservoir condition, resulted in an overall reduced aperture diameter from 2.25 ($\pm$0.05) mm to an average of 1.1 mm. The fracture aperture has, however, experienced an incremental widening due to calcite dissolution primarily along the fracture wall. The final detached fracture precipitate measured averagely 2.8 mm and superiors the width of the artificial fracture diameter. The incremental widening of the fracture aperture implies complex fracture development and validates a dominant fluid transportation through the fracture – 'a 'fluid highway'. A prolonged test duration would possibly produce a larger detached diameter and a complete aperture reduction caused by geo-mechanical compaction and precipitation of secondary minerals. Consequentially, the injected brine will be forced in new directions.

A transition zone, or a concentric circle of approximately one mm surrounding the fracture showed lower Ca, but increased Si concentration. The same area was penetrated by epoxy demonstrating locally higher permeability compared to matrix. This indicates a major fluid transport through the fracture, with primary dissolution of calcite along fracture walls. Slightly increased Mg concentration in this transition zone compared to matrix, supports the route of water transport.

The fracture fill precipitates consist primarily of magnesite, but with abundant clay mineral(s) and only minute amounts of calcite. The presence of calcite was identified as coccolith and coccoliths particles eroded in the matrix and transported. Magnesite crystals showed well developed crystallographic pattern (TEM) which was indexed and identified. Magnesite was also identified by XRD in addition to elemental identification of magnesium in SEM-EDS as well as HIMS-SIMS. New grown magnesite crystals show different sizes depending on their precipitation location inside the fracture fill. Mid-fracture fill attained the largest sized crystals whereas the smallest were located at peripheral locations of the precipitated matter/adjacent matrix. Magnesite dominates especially the central fracture fill, while clay minerals were mainly observed in clusters in peripheral parts of the fracture fill closest to the matrix and show mineral growth as bridging. Clay mineral(s) were identified as possibly illite based on texture (SEM), (crystallographic structure by XRD) in addition to the chemical composition obtained by TEM-EDS. Chlorite (clinochlore) is suggested based on the chemical composition and the mineral is likely to coexist with illite. Halloysite and lizardite were identified by XRD, but at insignificantly low counts. Only trace values of calcite were identified. Precipitation of clay minerals were occasionally identified surrounding magnesite crystals (HIM-SIMS and TEM-EDS). The order of precipitation is identified as initial precipitation of magnesite followed by a secondary growth of clay. The transport and appearance of clay minerals in the fracture is not yet completely understood (dissolution-precipitation or transported) but silica and aluminium are sourced from the matrix chalk. The quantity of clay mineral precipitation along the fracture wall needs further investigation.

The dynamic process of fracture aperture alteration in the reservoir may be considered two-folded as external and internal processes. Decreasing pore-pressures during depletion and water-weakening effect during seawater injection will cause compaction and increased stresses which will cause reduction of a fracture aperture (external). Surface active ions in the seawater injected will simultaneously trigger dissolution (dominantly adjacent fracture wall) and precipitation of secondary minerals in the fracture (internal). The processes may be determined by local conditions as temperature, rates, stresses and chemistry of matrix and brine injected as well as aperture size. Smaller fractures will

eventually clog and force injected fluid into matrix. Hydrocarbons will be released and cause increased recovery factor. By deciphering the impact of the surface-active ions present in seawater in the fracture and the adjacent matrix, we may refine IOR methods to improve control of fracture development.

Declaration of competing interest

Data availability

Data will be made available on request.

Acknowledgement

Appendix

Focused Ion Beam - Secondary Electron Microscopy (FIB-SEM)

Samples for TEM analysis were prepared at *Norges teknisk-naturvitenskapelige universitetet* (NTNU) using a Focused Ion Beam- Secondary Electron Microscopy (FIB-SEM) (a Helios G4 UX FEI) instrument. The FIB-SEM combination allows a simultaneous monitoring of the preparation process of ultrathin FIB-samples (100 nm). The original sample was coated with 30 nm gold (Au) to create electrical conductivity. The beam of ionized gallium (Ga^+) was accelerated (30 keV) and focused onto the specimen surface. This initiated atom sputtering and removal of layer by layer which produced a pool around the area of interest (Fig. 12). A sharp wolfram needle was attached to a carbon cord on top of the sample. Naphthalene, $C_{10}H_8$, diffused into the chamber, enhanced the needle welding to the sample. The sample (2 μm) was pulled out at a speed of 1 μm/s and attached to an omniprobe (sample holder) of copper (Cu). A final thickness of 100 nm was achieved by a time-consuming sputtering process at a constant working distance of 4 mm.
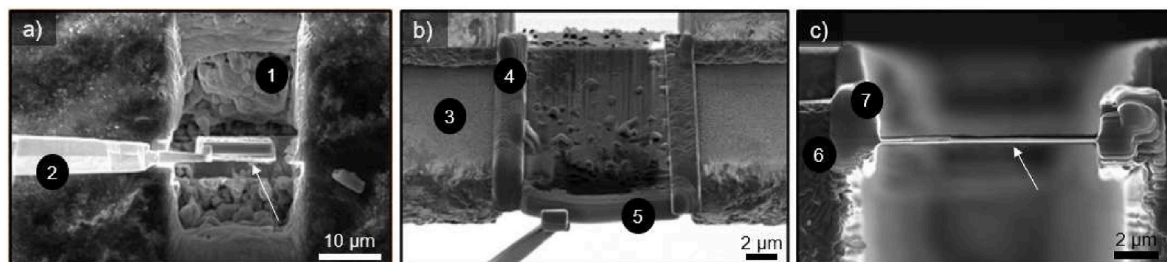
Fig. 12. An image series that visualize the steps in FIB preparation. a) The white arrow indicates the chalk sample. A pool (1) was formed around the sample by sputtering around it using a beam of gallium ions attached to a tungsten needle (2); b) the tungsten needle moved the sample to an omniprobe (3); applied carbon (4) connected the sample to the omniprobe and a carboncord (5) to attach the sample to the needle; c) the white arrow points to the final result after thinning the sample by sputtering. The sample reached a thickness of 100 nm, has a dimension of 10 × 12 μm, and is glued to carbon (7) which connects the sample to the omniprobe (6).

References

Abubeker, E., 2013. Water Weakening of Chalks - Comparsion of Intact and Fractured Cores [Master of Science Master Thesis]. University of Stavanger, p. 88.

Andersen, P.Ø., Wang, W., Madland, M.V., Zimmermann, U., Korsnes, R.I., Bertolino, S. R.A., Minde, M., Schulz, B., Gilbricht, S., 2018. Comparative study of five outcrop chalks flooded at reservoir conditions: chemo-mechanical behaviour and profiles of compositional alteration. Transport Porous Media 121 (1), 135–181.

Austad, T., Strand, S., Madland, M.V., Puntervold, T., Korsnes, R.I., 2008. Seawater in chalk: an EOR and compaction fluid. SPE Reservoir Eval. Eng. 11 (4), 648–654.

Austad, T., Strand, S., Puntervold, T., 2009. Is wettability alteration of carbonates by seawater caused by rock dissolution?. In: International Symposium of the Society of Core Analysts. Noordwijk, The Netherlands, 27-30 September, 2009.

Boersma, Q., Athmer, W., Haege, M., Etchebes, M., Haukås, J., Bertotti, G., 2020. Natural fault and fracture network characterization for the southern Ekofisk field: a case study integrating seismic attribute analysis with image log interpretation. J. Struct. Geol. 141, 104197.

Bredal, T.V., Korsnes, R.I., Zimmermann, U., Minde, M.W., Madland, M.V., 2022a. Water weakening of artificially fractured chalk, fracture modification and mineral

precipitation during water injection—an experimental study. Energies 15 (10), 3817.

Bredal, T.V., Zimmermann, U., Madland, M.V., Minde, M.W., Ost, A.D., Wirtz, T., Audinot, J.-N., Korsnes, R.I., 2022b. High-resolution topographic and chemical surface imaging of chalk for oil recovery improvement applications. Minerals 12 (3), 356.

Caine, J.S., Evans, J.P., Forster, C.B., 1996. Fault zone architecture and permeability structure. Geology 24 (11), 1025–1028.

Chester, F.M., Evans, J.P., Biegel, R.L., 1993. Internal structure and weakening mechanisms of the san andreas fault. J. Geophys. Res. Solid Earth 98 (B1), 771–786.

Dusar, M., Lagrou, D., 2007. Cretaceous flooding of the Brabant Massif and the lithostratigraphic characteristics of its chalk cov. er in northern Belgium: Geol. Belg. 10, 27–38.

Gale, J.F.W., Lander, R.H., Reed, R.M., Laubach, S.E., 2010. Modeling fracture porosity evolution in dolostone. J. Struct. Geol. 32 (9), 1201–1211.

Geitle, K., 2013. Chemically Induced Compaction in Fractured and Intact Chalk Cores [Master Master of Science. University of Stavanger, p. 78.

Goddard, J.V., Evans, J.P., 1995. Chemical changes and fluid-rock interaction in faults of crystalline thrust sheets, northwestern Wyoming. U.S.A: J. Struct. Geol. 17 (4), 533–547.

Hermansen, H., 2008. The Ekofisk field: achieving three times the original value. In: Proceedings 19th World Petroleum Congress. Volume All Days: WPC-19-3966.

Hermansen, H., Landa, G.H., Sylte, J.E., Thomas, L.K., 2000. Experiences after 10 years of waterflooding the Ekofisk field, Norway. J. Petrol. Sci. Eng. 26 (1), 11–18.

Hjuler, M.L., Fabricius, I.L., 2009. Engineering properties of chalk related to diagenetic variations of Upper Cretaceous onshore and offshore chalk in the North Sea area. J. Petrol. Sci. Eng. 68 (3), 151–170.

Hooker, J., Gomez, L., Laubach, S., Gale, J., Marrett, R., 2012. Effects of diagenesis (cement precipitation) during fracture opening on fracture aperture-size scaling in carbonate rocks. Geol. Soc. London, Special Publ. 370 (1), 187–206.

Kallesten, E.I., Cherif, Y., Madland, M.V., Korsnes, R.I., Omdal, E., Andersen, P.Ø., Zimmermann, U., 2021. Validation study of water weakening research from outcrop chalks performed on Eldfisk reservoir cores. J. Petrol. Sci. Eng. 198, 108164.

Korsnes, R., Madland, M.V., Austad, T., 2006. Impact of Brine Composition on the Mechanical Strength of Chalk at High Temperature. Taylor & Francis, pp. 133–140.

Korsnes, R., Madland, M.V., Austad, T., Haver, S., Røsland, G., 2008. The effects of temperature on the water weakening of chalk by seawater. J. Petrol. Sci. Eng. 60, 183–193.

Madland, M.V., Hiorth, A., Omdal, E., Megawati, M., Hildebrand-Habel, T., Korsnes, R.I., Evje, S., Cathles, L.M., 2011. Chemical alterations induced by rock–fluid interactions when injecting brines in high porosity chalks. Transport Porous Media 87 (3), 679–702.

Megawati, M., Andersen, P., Korsnes, R., Evje, S., Hiorth, A., Madland, M.V., 2011. The Effect of Aqueous Chemistry pH on the Time-dependent Deformation Behaviour of Chalk- Experimen- Tal and Modelling Study.

Megawati, M., Madland, M.V., Hiorth, A., 2015. Mechanical and physical behavior of high-porosity chalks exposed to chemical perturbation. J. Petrol. Sci. Eng. 133, 313–327.

Minde, M., Wang, W., Madland, M.V., Zimmermann, U., Korsnes, R., Bertolino, S., Andersen, P., 2018. Temperature effects on rock engineering properties and rock-fluid chemistry in opal-CT-bearing chalk. J. Petrol. Sci. Eng. 169.

Minde, M., Zimmermann, U., Madland, M., Korsnes, R., Schulz, B., Gilbricht, S., 2019a. Mineral Replacement in Long-Term Flooded Porous Carbonate Rocks, vol. 268. Geochimica et Cosmochimica Acta.

Minde, M.W., Madland, M.V., Zimmermann, U., Egeland, N., Korsnes, R.I., Nakamura, E., Kobayashi, K., Ota, T., 2019b. Mineralogical Alterations in Calcite Powder Flooded with MgCl2 to Study Enhanced Oil Recovery (EOR) Mechanisms at Pore Scale: Microporous and Mesoporous Materials.

Oh, K.D., Morikawa, H., Iwai, S., Aoki, H., 1973. The crystal structure of magnesite. Am. Mineral. 58, 1029–1033.

Paul, P.K., Zoback, M.D., Hennings, P.H., 2007. Fluid flow in a fractured reservoir using a geomechanically-constrained fault zone damage model for reservoir simulation. In: Proceedings SPE Annual Technical Conference and Exhibition. Volume All Days: SPE-110542-MS.

Puntervold, T., Strand, S., Austad, T., 2007. Water flooding of carbonate reservoirs: effects of a model base and natural crude oil bases on chalk wettability. Energy Fuel. 21 (3), 1606–1616.

Risnes, R., Madland, M., Hole, M., Kwabiah, N., 2005. Water weakening of chalk—mechanical effects of water–glycol mixtures. J. Petrol. Sci. Eng. 48 (1–2), 21–36.

Robaszynski, F., Dhondt, A.V., Jagt, J.W.M., 2002. Cretaceous lithostatigraphic units (Belgium). In: Dejonghe, B. (Ed.), Guide to a Revised Lithostratigraphic Scale of Belgium, vol. 4. Belgium, Geologica Belgica, pp. 121–134.

Schroeder, C., Gaviglio, P., Bergerat, F.o., Vandycke, S., Coulon, M., 2006. Faults and matrix deformations in chalk: contribution of porosity and sonic wave velocity measurements. Bull. Soc. Geol. Fr. 177 (4), 203–213.

Strand, S., Standnes, D.C., Austad, T., 2003. Spontaneous imbibition of aqueous surfactant solutions into neutral to oil-wet carbonate cores: effects of brine salinity and composition. Energy Fuel. 17 (5), 1133–1144.

Sulak, R.M., Danielsen, J., 1989. Reservoir Aspects of Ekofisk Subsidence.

Tokan-Lawal, A., Landry, C., Prodanović, M., Eichhubl, P., 2014. Understanding Tortuosity and Permeability Variations in Naturally Fractured Reservoirs. Niobrara Formation.

Wibberley, C.A.J., Shimamoto, T., 2003. Internal structure and permeability of major strike-slip fault zones: the median tectonic line in Mie prefecture, Southwest Japan. J. Struct. Geol. 25 (1), 59–78.

Wirtz, T., Castro, O.D., Audinot, J.-N., Philipp, P., 2019. Imaging and analytics on the helium ion microscope. Annu. Rev. Anal. Chem. 12 (1), 523–543.

Zimmermann, U., Minde, M.W., Madland, M.V., Bredal, 2022. An Analytical TOOLBOX for the Characterization of Chalks and Other Fine-Grained Rock Types within Enhanced Oil Recovery Research and Its Application-A Guideline. Energies 15 (11), 4060.